
Electronic Thesis and Dissertation Repository

1-22-2015 12:00 AM

The Influence of Long-Term Gamma-Radiation and Initially Dissolved Chemicals on Aqueous Kinetics and Interfacial Processes

Pamela A. Yakabuskie
The University of Western Ontario

Supervisor
Dr. Jungsook Clara Wren
The University of Western Ontario

Graduate Program in Chemistry
A thesis submitted in partial fulfillment of the requirements for the degree in Doctor of Philosophy
© Pamela A. Yakabuskie 2015

Follow this and additional works at: <https://ir.lib.uwo.ca/etd>

 Part of the [Physical Chemistry Commons](#)

Recommended Citation

Yakabuskie, Pamela A., "The Influence of Long-Term Gamma-Radiation and Initially Dissolved Chemicals on Aqueous Kinetics and Interfacial Processes" (2015). *Electronic Thesis and Dissertation Repository*. 2669.

<https://ir.lib.uwo.ca/etd/2669>

This Dissertation/Thesis is brought to you for free and open access by Scholarship@Western. It has been accepted for inclusion in Electronic Thesis and Dissertation Repository by an authorized administrator of Scholarship@Western. For more information, please contact wlsadmin@uwo.ca.

**THE INFLUENCE OF LONG-TERM γ -RADIATION AND INITIALLY DISSOLVED
CHEMICALS ON AQUEOUS KINETICS AND INTERFACIAL PROCESSES**

(Thesis format: Integrated Article)

by

Pamela A. Yakabuskie

Graduate Program in Chemistry

A thesis submitted in partial fulfillment
of the requirements for the degree of
Doctor of Philosophy

The School of Graduate and Postdoctoral Studies
The University of Western Ontario
London, Ontario, Canada

© Pamela A. Yakabuskie 2014

Abstract

This thesis presents work focusing on the long-term effect of γ -radiation on aqueous solution kinetics. Ionizing radiation drives the decomposition of water to form both oxidizing ($\bullet\text{OH}$, O_2 , H_2O_2) and reducing ($\bullet\text{e}_{\text{aq}}^-$, $\bullet\text{O}_2^-$, $\bullet\text{H}$, H_2) chemical species. Over time, these radiolysis products can react with dissolved solutes and participate in interfacial reactions. This can lead to significant changes in the eventual solution redox condition, and gas phase composition, and in certain cases result in the formation of solid species. Understanding the long-term solution kinetics for radiolysis systems is particularly important for the improvement of chemistry control and activity transport models, such as those employed in the nuclear power industry.

In order to study the chemical changes induced by exposing these aqueous systems to γ -radiation, species in the aqueous, gaseous and solid phases (where applicable) were monitored by a variety of techniques as a function of irradiation time. Chemical kinetics modeling was performed to both validate obtained experimental results, as well as aid in the interpretation of these results. The presence of dissolved solutes was found to impact the steady-state concentrations of the molecular water radiolysis products by competing with them for reaction with radical species. This radical scavenging lowers the rate of removal of the molecular products and allows their concentrations to reach higher levels, however the relative increase observed relative to pure water is dependent on pH and solute concentration. Redox active solutes that can undergo pseudo-catalytic reaction cycles with the radical species can also significantly affect the concentrations of water radiolysis products without experiencing a significant change in their net speciation.

Irradiation studies with transition metal solutes were shown to generate uniform sized colloidal species in solution. The radiolytic oxidation of soluble ferrous ions to less soluble ferric species leads to the homogeneous condensation of primary particles out of solution. Prolonged irradiation leads to growth at the particle surface, with the final size determined by the steady state balance of redox reactions occurring on the particle surface. Irradiation was also shown to increase the relative metal oxidation rate on a carbon steel coupon in aqueous solutions, with dissolution dominating over oxide growth at low pH. However, the initial presence of dissolved iron suppresses the metal oxidation rate. The deposition of

radiolytically produced iron oxide/oxyhydroxide particles contributes to enhanced oxide film growth on these coupon surfaces, effectively decreasing the driving force for ongoing metal oxidation.

Keywords

Radiation chemistry, water radiolysis, kinetics, mass transport, interfacial reactions, colloid formation, carbon steel, stainless steel, corrosion

Co-Authorship Statement

This thesis includes data that has been previously published elsewhere (Chapters 3, 5, and 6). Significant portions of these publications have been reproduced with permission. For all research chapters, I was the lead investigator and author. Individuals who provided support with respect to the collection of experimental data (e.g., surface science analysis) are acknowledged in individual chapters where appropriate.

Acknowledgments

As every graduate student knows, the completion of a Ph.D. thesis is a collaborative effort – both technically and emotionally. While it is impossible to individually thank every person who has contributed in one way or another to this collection of work, I will attempt to single out those that have provided unique or exceptional levels of guidance and support.

Without question, the first and most important person I would like to acknowledge is my supervisor, Dr. J. Clara Wren. As both mentor and friend, she has been a tremendous tutor, always available for help, ideas, and reassurance. I am indebted for the opportunities I had as a graduate student – the experiences I gained from travelling to international conferences throughout North America and Europe, and the opportunity to work as a visiting researcher at the University of Notre Dame are truly unforgettable. Clara, you are a leader whose qualities I can hope to mirror as my career progresses.

Over the years, all members of the Wren research group, and colleagues in the Shoesmith research group have provided input, support, humour and friendship. In particular, my labmates made coming in to the lab everyday enjoyable and rewarding. I would specifically like to thank Drs. Jamie Noël, Jiju Joseph, and Sriya Peiris for providing immense technical and/or writing support throughout this project, Dr. Dave Shoesmith for always providing help and a quick wit when required, as well as Dr. Dave Wren for his thorough, but always helpful, editorial efforts. I would also like to thank co-authors from Atomic Energy of Canada Ltd., Drs. Craig Stuart, Glenn Glowa, and Dave Guzonas for their contributions in the preparation of various manuscripts, Dr. David Bartels from the University of Notre Dame Radiation Lab for his patience and laboratory support during my time there, as well as Dr. Ian Muir for providing me with the opportunity to begin my career prior to the full completion of this thesis.

Finally, I would be remiss if I did not mention my family and friends. To my parents, Elmer and Monica, and my sister, Tammy, thank you for your unwavering love and support throughout my time at Western. And to Dr. Brad Payne, my sounding board, partner, and best friend, I could not have finished this and maintained my sanity without you.

Table of Contents

Abstract	ii
Co-Authorship Statement.....	iv
Acknowledgments.....	v
Table of Contents	vi
List of Symbols and Acronyms.....	xii
List of Tables	xv
List of Figures	xvi
Chapter 1 Introduction	1-1
1.1 Thesis Objectives and Methods.....	1-1
1.2 Radiation Chemistry.....	1-3
1.2.1 Radiation-Matter Interaction.....	1-3
1.2.1.1 The Linear Energy Transfer Rate	1-4
1.2.2 Water Radiolysis by Low LET Radiation.....	1-6
1.2.2.1 Primary Radiolysis Processes	1-6
1.2.2.2 Bulk Phase Chemistry and the Steady State	1-10
1.3 Irradiated Aqueous Systems in a Nuclear Reactor	1-11
1.3.1 Heat Transport System.....	1-12
1.3.1.1 Corrosion and Activity Transport.....	1-12
1.3.1.2 Chemistry Control.....	1-15
1.3.2 Moderator System	1-16
1.3.3 End Shield Cooling System	1-18

1.3.4	Radiation Chemistry Considerations under other Conditions.....	1-18
1.3.4.1	Radiolysis of Chemical Impurities	1-18
1.3.4.2	Air Radiolysis in Humid Environments.....	1-19
1.4	References	1-20
Chapter 2 Experimental Principles and Details		2-1
2.1	Analytical and Imaging Methods	2-1
2.1.1	UV-Visible (UV-Vis) Spectrophotometry	2-1
2.1.2	Gas Chromatography	2-2
2.1.3	Transmission Electron Microscopy (TEM)	2-3
2.1.4	Selected Area Electron Diffraction (SAED)	2-4
2.1.5	Scanning Electron Microscopy (SEM)	2-5
2.1.6	Energy Dispersive X-ray (EDX) Spectroscopy	2-6
2.1.7	X-Ray Photoelectron Spectroscopy (XPS)	2-6
2.1.8	Fourier Transform Infrared (FTIR) Spectroscopy	2-7
2.1.9	Raman Spectroscopy	2-8
2.2	General Experimental Design and Set-up	2-9
2.2.1	Solution Preparation and Degassing	2-9
2.2.2	Irradiation Technique	2-10
2.2.3	Solution Analysis	2-11
2.2.4	Gas Composition Analysis.....	2-12
2.3	The Radiolysis Kinetic Model.....	2-12
2.4	References	2-18

Chapter 3	The Effect of Interfacial Mass Transport on Steady-State Water Radiolysis	
	Radiolysis	3-1
3.1	Introduction	3-1
3.2	Experimental Procedure	3-3
3.3	Interfacial Mass Transfer in the Radiolysis Model	3-3
3.3.1	Aqueous-Gas Interfacial Transfer	3-3
3.4	Results and Discussion	3-6
3.4.1	General Observations	3-6
3.4.2	Radiolytic Production of Hydrogen in the Cover Gas	3-10
3.4.3	Effect of Interfacial Transfer of Volatile Species on Aqueous Products	3-14
3.4.3.1	pH 6.0	3-16
3.4.3.2	pH 10.6	3-21
3.5	Conclusions	3-23
3.6	References	3-24
Chapter 4	The Effect of Initially Added Oxygen on Steady-State Water Radiolysis Kinetics	4-1
4.1	Introduction	4-1
4.2	Experimental Procedure	4-2
4.3	The Water Radiolysis Model	4-3
4.4	Results and Discussion	4-3
4.4.1	Time-Dependent Behaviour of Water Radiolysis Products	4-3
4.4.1.1	Time-Dependent Behaviour in Initially Deaerated Water	4-7
4.4.1.2	Time-Dependent Behaviour in Initially Oxygenated Water	4-10
4.4.2	Effect of Initially Dissolved O ₂ on Steady-State Radiolysis Behaviour	4-11

4.4.2.1	Hydrogen Behaviour as a Function of pH	4-11
4.4.2.2	Hydrogen Peroxide Behaviour as a Function of pH	4-17
4.4.2.3	Effect of Dissolved Oxygen for Samples with No Headspace	4-19
4.5	Conclusions	4-22
4.6	References	4-23
Chapter 5 Long term γ-Radiolysis Kinetics of NO_3^- and NO_2^- Solutions		5-1
5.1	Introduction	5-1
5.2	Experimental Procedure	5-3
5.3	Water Radiolysis Model	5-4
5.4	Experimental Results	5-6
5.5	Model Simulation Results	5-9
5.6	Discussion of Results	5-10
5.6.1	Water Radiolysis in the Absence of Dissolved Nitrate and Nitrite.....	5-10
5.6.2	Radiolysis of Aqueous Solutions Initially Containing Nitrate or Nitrite.....	5-13
5.6.2.1	Production of H_2 and H_2O_2	5-13
5.6.2.2	Nitrogen speciation, $[\text{NO}_3^-]$ and $[\text{NO}_2^-]$	5-19
5.6.2.3	Assessment of Nuclear Reactor Data.....	5-20
5.7	Conclusions	5-22
5.8	Acknowledgements	5-22
5.9	References	5-23
Chapter 6 Iron Oxy-Hydroxide Colloid Formation by γ-Radiolysis		6-1
6.1	Introduction	6-1
6.2	Experimental Procedure	6-3

6.3	Experimental Results	6-5
6.4	Discussion of Results	6-14
6.5	Conclusions	6-21
6.6	Acknowledgements	6-22
6.7	References	6-22

Chapter 7 The Effect of Initially Dissolved Ferrous Iron on Steel Corrosion under γ -Irradiation

7.1	Introduction	7-1
7.2	Experimental Procedure	7-3
7.3	Experimental Results.....	7-5
7.3.1	Behaviour Observed for Different Initial Ferrous Ion Concentrations	7-5
7.3.1.1	Visual Appearance of Solutions and Coupon Surfaces	7-5
7.3.1.2	Dissolved Ferrous and Ferric Iron Concentrations	7-6
7.3.1.3	Gas Phase H ₂ and O ₂ Concentrations	7-9
7.3.1.4	Surface Analysis of Steel Coupons.....	7-11
7.3.2	Behaviour Observed as a Function of Time.....	7-14
7.3.2.1	Visual Appearance of Solutions and Coupon Surfaces with Irradiation .	7-14
7.3.2.2	Time-Dependent Ferric/Ferrous Behaviour.....	7-20
7.3.2.3	Time-Dependent Hydrogen Behaviour.....	7-22
7.3.2.4	UV-Visible Spectra of Irradiated Solutions.....	7-24
7.3.3	Effect of Organic Contamination on Radiolytic Behaviour.....	7-29
7.4	Mechanism of Corrosion in Irradiated Systems	7-34
7.4.1	Carbon Steel Corrosion in the Absence of Initially Dissolved Fe ²⁺	7-37

7.4.2	Carbon Steel Corrosion in the Presence of Initially Dissolved Fe ²⁺	7-38
7.4.3	Corrosion of Stainless Steel	7-39
7.5	Conclusions	7-40
7.6	Acknowledgements	7-41
7.7	References	7-41
Chapter 8	Summary and Future Work.....	8-1
8.1	Summary.....	8-1
8.2	Future Work.....	8-4

List of Symbols and Acronyms

Acronyms

AECL	Atomic Energy of Canada Limited
BE	Binding Energy
BWR	Boiling Water Reactor
CANDU	CANada Deuterium Uranium
CHC	Critical Hydrogen Concentration
CS	Carbon Steel
ECD	Electron Capture Detector
ECP	Electrochemical Corrosion Potential
ED	Electron Diffraction
EDX	Energy Dispersive X-ray
ESC	End Shield Cooling
FTIR	Fourier Transform Infrared
HS	Headspace
HTS	Heat Transport System
HWC	Hydrogen Water Chemistry
IR	Infrared
KE	Kinetic Energy
GC	Gas Chromatography
LET	Linear Energy Transfer
MSD	Mass Selective Detector
m ox	Metal/Oxide Interface
NC	No Coupon
NRU	National Research Universal
ox sol	Oxide/Solution Interface
PHWR	Pressurized Heavy Water Reactor
PTFE	Polytetrafluoroethylene
PWR	Pressurized Water Reactor
SAED	Selected Area Electron Diffraction

SCC	Stress Corrosion Cracking
SEM	Scanning Electron Microscopy
SS	Steady State
SS	Stainless Steel
TCD	Thermal Conductivity Detector
TEM	Transmission Electron Microscopy
UV(-Vis)	Ultraviolet (-Visible)
XPS	X-ray Photoelectron Spectroscopy
XRD	X-Ray Diffraction

Symbols – Alphanumeric

A	Absorbance
A_{int}	Aqueous-gas interfacial surface area
c	Concentration
C^i	Concentration of species <i>i</i>
C_R	Unit conversion constant
°C	Degrees Celsius
D	Diffusivity
D_R	Dose rate
E^0	Standard potential
G_i	G-value (radiation chemical yield) of a species <i>i</i>
Gy	Gray
h	Planck's constant
I	Light intensity
k_{app}^i	Net mass transfer coefficient of species <i>i</i>
k_{rad}^i	Primary radiolytic production rate of species <i>i</i>
k_x	Reaction rate constant
K_p^i	Partition coefficient of species <i>i</i> (dimensionless Henry's law constant)
<i>l</i>	Path length
M^x	Metal with oxidation state x

r	Radius
t	Time
v	Vibrational energy state
V	Volume
x	Dimensionless scattering size parameter

Symbols – Greek

δ	Thickness of the boundary layer
$\Delta E_{\text{vibration}}$	Vibrational energy gap
ε	Molar absorption coefficient
λ	Wavelength of light
ν	Light frequency
ρ	Density
v_{app}^i	Overall interfacial transfer coefficient of species i
v_x	Resistance to diffusion through a film layer x
Φ	Work function

Iron Oxides

$\alpha\text{-FeOOH}$	Goethite
$\gamma\text{-FeOOH}$	Lepidocrocite
$\alpha\text{-Fe}_2\text{O}_3$	Hematite
$\gamma\text{-Fe}_2\text{O}_3$	Maghemite
Fe_3O_4	Magnetite

List of Tables

Table 1.1: The primary α - and γ -radiolysis yields (G-values, $\mu\text{mol}\cdot\text{J}^{-1}$) at 25 °C for liquid water [1].	1-10
Table 2.1: The G-values, reactions and rate constants, and equilibria that form the basic water radiolysis kinetic model.....	2-16
Table 5.1: The reactions and rate constants that comprise the simplified nitrogen reaction set of the radiolysis kinetic model.....	5-4

List of Figures

- Figure 1.1: Schematic representation of the clusters of ions and excited molecules along the radiation track for different types of ionizing radiation [1]. 1-6
- Figure 1.2: A representation of the spur distribution in water along the radiation track for γ -radiation [1]..... 1-7
- Figure 1.3: Schematic of water radiolysis events as a function of time following absorption of radiation energy. The right hand panel shows the expansion of spurs with time [5]. 1-9
- Figure 1.4: Overview of the layout of a CANDU pressurized heavy water reactor. 1-12
- Figure 1.5: The feedback relationship of corrosion and radiolysis for an irradiated aqueous system in contact with iron. 1-15
- Figure 1.6: Simplified overview of the separated coolant system, moderator system and end shield cooling system in a CANDU nuclear reactor. 1-17
- Figure 2.1: Differences in the imaging (left) and electron diffraction (right) modes for a transmission electron microscope. 2-4
- Figure 2.2: The sample vial holder (a) custom designed to fit into the irradiation chamber of the MDS Nordion 220 Gamma Cell (b). 2-11
- Figure 3.1: $H_2(g)$ concentration in the headspace as a function of irradiation time for a volume ratio ($V_g:V_{aq}$) of 1:1 and a dose rate of $2.5 Gy \cdot s^{-1}$ 3-7
- Figure 3.2: H_2 concentrations in the headspace (a) and H_2O_2 concentrations in the aqueous phase (b) as a function of irradiation time for aerated water at pH 6.0 at $2.5 Gy \cdot s^{-1}$. The symbols represent the experimental data and the lines the radiolysis model results..... 3-8
- Figure 3.3: H_2 concentrations in the headspace (a) and H_2O_2 concentrations in the aqueous phase (b) as a function of irradiation time for deaerated water at pH 10.6 at $2.5 Gy \cdot s^{-1}$. The symbols represent the experimental data and the lines the radiolysis model results..... 3-9

- Figure 3.4: H_2 concentrations in the aqueous phase as a function of irradiation time for aerated water at pH 6.0 (a) and deaerated water at pH 10.6 (b) at $2.5 \text{ Gy}\cdot\text{s}^{-1}$ 3-12
- Figure 3.5: H_2O_2 concentrations in the aqueous phase as a function of irradiation time for aerated water at pH 6.0 (a) and deaerated water at pH 10.6 (b) at $2.5 \text{ Gy}\cdot\text{s}^{-1}$ 3-13
- Figure 3.6: The log of ($V_g \times \text{slope of } [H_2(g)] \text{ vs time}$) is shown as a function of $\log[H_2(aq)]_{ss}$ for aerated water at pH 6.0 and deaerated water at pH 10.6. 3-14
- Figure 3.7: Full model predictions for the steady-state concentrations of H_2 and O_2 along with $[\bullet OH]_{ss}$ (a) and H_2O_2 along with $[\bullet OH]_{ss}$ and $[\bullet e_{aq}^-]_{ss}$ (b), as a function of pH for deaerated water. 3-15
- Figure 3.8: Model predictions for the steady-state concentrations of $\bullet OH$, $\bullet e_{aq}^-$ and $\bullet O_3^-$ (a) and $H_2(aq)$, H_2O_2 , $O_2(aq)$ and $\bullet O_2^-$ (b) for aerated water at pH 6.0 as a function of time at $2.5 \text{ Gy}\cdot\text{s}^{-1}$. The radiolysis model results are shown for $V_g:V_{aq}$ ratios of 4:1 (— —) and 1:1 (— - —) and for water with no headspace ($V_g = 0$) (—). 3-20
- Figure 3.9: Model predictions for the steady-state concentrations of $\bullet OH$, $\bullet e_{aq}^-$ and $\bullet O_3^-$ (a) and $H_2(aq)$, H_2O_2 , $O_2(aq)$ and $\bullet O_2^-$ (b) for deaerated water at pH 10.6 as a function of time at $2.5 \text{ Gy}\cdot\text{s}^{-1}$. The radiolysis model results are shown for $V_g:V_{aq}$ ratios of 4:1 (— —) and 1:1 (— - —) and for water with no headspace ($V_g = 0$) (—). 3-22
- Figure 4.1: Model predictions of water radiolysis product behaviour at pH 6.0 (a) and pH 10.6 (b) for deaerated water as a function of time at $2.5 \text{ Gy}\cdot\text{s}^{-1}$ 4-5
- Figure 4.2: Model predictions of water radiolysis product behaviour at pH 6.0 (a) and pH 10.6 (b) for water with $2.3 \times 10^{-4} \text{ mol}\cdot\text{dm}^{-3}$ of initially dissolved O_2 as a function of time at $2.5 \text{ Gy}\cdot\text{s}^{-1}$ 4-6

- Figure 4.3: The $[H_2(g)]$ (a) and $[H_2(aq)]$ (b) concentrations shown as a function of irradiation time for headspace samples at pH 6.0 at a dose rate of $2.5 \text{ Gy}\cdot\text{s}^{-1}$ 4-12
- Figure 4.4: The $[H_2(g)]$ (a) and $[H_2(aq)]$ (b) concentrations shown as a function of irradiation time for headspace samples at pH 10.6 at a dose rate of $2.5 \text{ Gy}\cdot\text{s}^{-1}$ 4-13
- Figure 4.5: Radiolysis model predictions for the concentrations of $\bullet\text{OH}$ (a) and $\bullet\text{e}_{\text{aq}}^-$ (b) as a function of irradiation time for headspace samples at pH 6.0 at a dose rate of $2.5 \text{ Gy}\cdot\text{s}^{-1}$ for different initial O_2 concentrations: 35% (\cdots , $-$), 23% (\cdots , $-$), 10% (\cdots , $-$) and 0% (Ar purged) (\cdots , $-$). 4-15
- Figure 4.6: Radiolysis model predictions for the concentrations of $\bullet\text{OH}$ (a) and $\bullet\text{e}_{\text{aq}}^-$ (b) as a function of irradiation time for headspace samples at pH 10.6 at a dose rate of $2.5 \text{ Gy}\cdot\text{s}^{-1}$ for different initial O_2 concentrations: 35% (\cdots , $-$), 23% (\cdots , $-$), 10% (\cdots , $-$) and 0% (Ar purged) (\cdots , $-$). 4-16
- Figure 4.7: The H_2O_2 concentrations shown as a function of irradiation time for headspace samples at pH 6.0 (a) and pH 10.6 (b) at a dose rate of $2.5 \text{ Gy}\cdot\text{s}^{-1}$. The solid symbols represent the experimental data and the lines show the radiolysis model results for different initial O_2 concentrations: 35% (\blacktriangle , $-$), 23% (\bullet , $-$), 10% (\blacksquare , $-$) and 0% O_2 (Ar purged) (\blacktriangledown , $-$). 4-18
- Figure 4.8: The $\text{H}_2(aq)$ concentrations shown as a function of irradiation time for full samples at pH 6.0 (a) and pH 10.6 (b) at a dose rate of $2.5 \text{ Gy}\cdot\text{s}^{-1}$. The solid symbols represent the experimental data and the lines show the radiolysis model results for different initial O_2 concentrations: 35% O_2 (\blacktriangle , $-$), 23% O_2 (\bullet , $-$), 10% O_2 (\blacksquare , $-$) and 0% O_2 (Ar purged) ($-$). 4-20
- Figure 4.9: The H_2O_2 concentrations shown as a function of irradiation time for full samples at pH 6.0 (a) and pH 10.6 (b) at a dose rate of $2.5 \text{ Gy}\cdot\text{s}^{-1}$. The solid symbols represent the experimental data and the lines show the radiolysis model results for different initial O_2 concentrations: 35% O_2 (\blacktriangle , $-$), 23% O_2 (\bullet , $-$), 10% O_2 (\blacksquare , $-$) and 0% O_2 (Ar purged) ($-$). 4-21

- Figure 5.1: The time-dependent concentrations of H_2 (■, —), H_2O_2 (●, ---) and O_2 (⋯) (top) and the time-dependent speciation of NO_3^- (▼, —) and NO_2^- (▲, —), along with the overall mass balance of nitrogen species (◇, ---) (bottom) for deaerated pH 6.0 water containing (a) $1 \times 10^{-3} \text{ mol} \cdot \text{dm}^{-3} [\text{NO}_3^-]_0$ and (b) $1 \times 10^{-3} \text{ mol} \cdot \text{dm}^{-3} [\text{NO}_2^-]_0$. Data points represent the experimental data for irradiations at $2.1 \text{ Gy} \cdot \text{s}^{-1}$ and the lines are the model simulation results..... 5-7
- Figure 5.2: The time-dependent concentrations of H_2 (■, —), H_2O_2 (●, ---) and O_2 (⋯) (top) and the time-dependent speciation of NO_3^- (▼, —) and NO_2^- (▲, —), along with the overall mass balance of nitrogen species (◇, ---) (bottom) for deaerated pH 10.6 water containing (a) $1 \times 10^{-3} \text{ mol} \cdot \text{dm}^{-3} [\text{NO}_3^-]_0$ and (b) $1 \times 10^{-3} \text{ mol} \cdot \text{dm}^{-3} [\text{NO}_2^-]_0$. Data points represent the experimental data for irradiations at $2.1 \text{ Gy} \cdot \text{s}^{-1}$ and the lines are the model simulation results..... 5-8
- Figure 5.3: The time-dependent concentrations of H_2 (■, —), H_2O_2 (●, ---) and O_2 (⋯) for deaerated water at (a) pH 6.0 and (b) pH 10.6. Data points represent the experimental data for irradiations at $2.1 \text{ Gy} \cdot \text{s}^{-1}$ and the lines are the model simulation results. At pH 6.0 the measured concentrations of H_2 and H_2O_2 were below the detection limits of $1 \times 10^{-5} \text{ mol} \cdot \text{dm}^{-3}$ and $3 \times 10^{-6} \text{ mol} \cdot \text{dm}^{-3}$, respectively. 5-9
- Figure 5.4: The model simulation results for the time-dependent concentrations of $\cdot\text{OH}$, $\cdot\text{e}_{\text{aq}}^-$, and $\cdot\text{O}_2^-$ achieved in the radiolysis of deaerated solutions of pure water (—), $[\text{NO}_3^-]_0 = 1 \times 10^{-3} \text{ M}$ (---), and $[\text{NO}_2^-]_0 = 1 \times 10^{-3} \text{ M}$ (⋯), at pH 6.0 (a) and pH 10.6 (b)..... 5-15
- Figure 5.5: The behaviour of water radiolysis products at pH 6.0 (a) and pH 10.6 (b) shown for deaerated water as a function of time. 5-16
- Figure 5.6: The behaviour of water radiolysis products at pH 6.0 (a) and pH 10.6 (b) shown as a function of time for a deaerated $1 \times 10^{-3} \text{ mol} \cdot \text{dm}^{-3} \text{NO}_3^-$ solution. 5-18

- Figure 5.7: The speciation of NO_3^- (▼) and NO_2^- (▲), in the end shield cooling system (pH 10) at Point Lepreau Generating Station. 5-21
- Figure 6.1: (a) Optical images of the test solutions arranged in order of irradiation duration and (b) TEM images showing the size and morphology of iron nanoparticles formed by the irradiation of $[\text{Fe}^{2+}]_0 = 5 \times 10^{-4} \text{ mol}\cdot\text{dm}^{-3}$ deaerated solution at pH 5.5 and a dose rate of $1.9 \text{ Gy}\cdot\text{s}^{-1}$ shown as a function of irradiation time. 6-6
- Figure 6.2: TEM images showing the size and morphology of iron nanoparticles formed by the irradiation of a $[\text{Fe}^{2+}]_0 = 1 \times 10^{-4} \text{ mol}\cdot\text{dm}^{-3}$ deaerated solution at pH 5.5 and a dose rate of $1.9 \text{ Gy}\cdot\text{s}^{-1}$, shown as a function of irradiation time..... 6-7
- Figure 6.3: The concentration profiles of Fe^{2+} (▲) and Fe^{3+} (▼) in pH 5.5 deaerated solutions of (a) $[\text{Fe}^{2+}]_0 = 1 \times 10^{-4} \text{ mol}\cdot\text{dm}^{-3}$, and (b) $[\text{Fe}^{2+}]_0 = 5 \times 10^{-4} \text{ mol}\cdot\text{dm}^{-3}$ at a dose rate of $1.9 \text{ Gy}\cdot\text{s}^{-1}$ as a function of irradiation time. 6-9
- Figure 6.4: The dissolved H_2 concentration measured as a function of irradiation time for deaerated solutions initially containing $1 \times 10^{-4} \text{ mol}\cdot\text{dm}^{-3}$ (■); and $5 \times 10^{-4} \text{ mol}\cdot\text{dm}^{-3}$ (●) at pH 5.5 and a dose rate of $1.9 \text{ Gy}\cdot\text{s}^{-1}$ 6-10
- Figure 6.5: The FTIR spectrum obtained for iron nanoparticles formed by the radiolysis of a $[\text{Fe}^{2+}]_0 = 5 \times 10^{-4} \text{ mol}\cdot\text{dm}^{-3}$ deaerated solution at pH 5.5, at a dose rate of $1.9 \text{ Gy}\cdot\text{s}^{-1}$. The reference spectrum of $\alpha\text{-FeOOH}$ is displayed upwards for easier viewing. 6-11
- Figure 6.6: The SAED ring pattern and the associated diffraction spectrum (inset) of iron nanoparticles formed by the radiolysis of a $[\text{Fe}^{2+}]_0 = 5 \times 10^{-4} \text{ mol}\cdot\text{dm}^{-3}$ deaerated solution at pH 5.5, at a dose rate of $1.9 \text{ Gy}\cdot\text{s}^{-1}$ for 5 hours..... 6-11
- Figure 6.7: UV-Vis spectra of irradiated $[\text{Fe}^{2+}]_0 = 5 \times 10^{-4} \text{ mol}\cdot\text{dm}^{-3}$ deaerated solutions at pH 5.5 and a dose rate of $1.9 \text{ Gy}\cdot\text{s}^{-1}$. (a) Spectra of irradiated ferrous sulphate solutions (solid lines, irradiation times from bottom to top are 0, 20, 40, 60, 120, 240 and 300 minutes) along with the spectrum for an unirradiated ferric nitrate solution (dashed line). (b) Spectra of the irradiated ferrous sulphate

- solutions with the absorption contribution of the hydrated ferric ion removed (irradiation times from bottom to top are 20, 40, 60, 120, 240 and 300 minutes)..... 6-13
- Figure 6.8: Proposed three stage growth mechanism of γ -FeOOH particles induced by the γ -irradiation of deaerated FeSO₄ solutions at pH 5.5..... 6-16
- Figure 7.1: Photographs of the test vials after 64 h for 2.5×10^{-4} mol·dm⁻³ FeSO₄ solutions at pH 6.0 that were (a) not irradiated and (b) irradiated at a dose rate of 1.4 Gy·s⁻¹. Photographs for pH 6.0 solutions after 64 h of irradiation without initially added iron (c) are also presented. 7-5
- Figure 7.2: Aqueous concentrations of Fe²⁺ (gray) and Fe³⁺ (purple) determined for test solutions at pH 6.0 with various concentrations of initially dissolved ferrous sulfate following 64 h of irradiation at a dose rate of 1.4 Gy·s⁻¹. The labels CS, SS, and NC represent tests with carbon steel, stainless steel and no coupon..... 7-7
- Figure 7.3: The total concentration of iron species measured in the aqueous phase (solid lines) and hydrogen measured in the gas phase (dashed lines) for pH 6.0 ferrous sulfate solutions in contact with carbon steel (■), stainless steel (●) and no coupon (▲) following 64 h of irradiation at a dose rate of 1.4 Gy·s⁻¹.. 7-8
- Figure 7.4: A representative survey spectrum and a high resolution Fe 2p band (inset) from the XPS analysis of a carbon steel coupon..... 7-12
- Figure 7.5: XPS analysis results for carbon steel surfaces displaying the relative contributions of metallic Fe⁰ and iron oxide phases to the Fe 2p band after 64 h irradiation tests. Carbon steel samples were in contact with: pH 6.0 water without irradiation (left), irradiated pH 6.0 water (middle), and irradiated pH 6.0 FeSO₄ solutions at 2.5×10^{-4} mol·dm⁻³ 7-13
- Figure 7.6: The SEM images of (a) a carbon steel coupon and (b) a stainless steel coupon following 64 h of irradiation in 2.5×10^{-4} M [FeSO₄]₀..... 7-14

- Figure 7.7: Optical images of the irradiated test solutions for carbon steel in (a) water, and (b) 5×10^{-4} M FeSO₄, and for irradiated 5×10^{-4} M FeSO₄ in contact with (c) a stainless steel coupon, and (d) no coupon. From left to right, the irradiation times increase from 20, 40, 64, to 138 h. 7-15
- Figure 7.8: SEM images showing the surface morphology of stainless steel coupons irradiated in contact with 5×10^{-4} M FeSO₄ for 20, 40, 64, and 138 h. 7-17
- Figure 7.9: SEM images showing the surface morphology of carbon steel coupons irradiated in contact with 5×10^{-4} M FeSO₄ for 20, 40, 64, and 138 h. 7-18
- Figure 7.10: (a) An SEM image for a carbon steel coupon irradiated for 64 h in ferrous solution. EDX spectra is shown for the pearlite ridged area (b) and the flatter amorphous region (c). 7-19
- Figure 7.11: The Raman spectra of selected iron oxide standards along with a representative spectra of a carbon steel surface after irradiation in a ferrous solution. 7-20
- Figure 7.12: The aqueous concentrations of Fe²⁺ (grey) and Fe³⁺ (purple) species measured for tests with carbon steel (CS), stainless steel (SS), or no coupon (NC) in contact with a 5×10^{-4} M FeSO₄ solution as a function of irradiation time (at a dose rate of 1.4 Gy·s⁻¹). From left to right, the sets of bars represent times of 20, 40, 64, and 138 h. 7-21
- Figure 7.13: The aqueous concentrations of Fe²⁺ (grey) and Fe³⁺ (purple) species measured for tests with carbon steel (CS) and stainless steel (SS) in pure water as a function of irradiation time (at a dose rate of 1.4 Gy·s⁻¹). From left to right, the sets of bars represent times of 20, 40, 64, and 138 h. 7-22
- Figure 7.14: The concentrations of hydrogen measured in the gas phase for pH 6.0 5×10^{-4} M FeSO₄ solutions (solid lines) and pH 6.0 water (dashed lines) in contact with carbon steel (■), stainless steel (●) and no coupon (▲) following 64 h of irradiation at a dose rate of 1.4 Gy·s⁻¹. 7-24

- Figure 7.15: The UV-Visible spectra of irradiated $[\text{Fe}^{2+}]_0 = 5 \times 10^{-4} \text{ mol} \cdot \text{dm}^{-3}$ deaerated solutions at pH 6.0 and a dose rate of $1.4 \text{ Gy} \cdot \text{s}^{-1}$ with the absorption contribution of the hydrated ferric ion removed. (a) Ferrous solutions irradiated in the absence of a coupon and (b) ferrous solutions irradiated in contact with a stainless steel coupon. 7-26
- Figure 7.16: The UV-Visible spectra collected for pH 6.0 deaerated (a) water ($[\text{Fe}^{2+}]_0 = 0 \text{ mol} \cdot \text{dm}^{-3}$), and (b) ferrous solution ($[\text{Fe}^{2+}]_0 = 5 \times 10^{-4} \text{ mol} \cdot \text{dm}^{-3}$), that were irradiated in contact with a carbon steel coupon at a dose rate of $1.4 \text{ Gy} \cdot \text{s}^{-1}$. The absorption contribution of the hydrated ferric ion was removed..... 7-27
- Figure 7.17: Optical images of 1st trial test solutions following 136 h of (a) irradiation at a dose rate of $1.4 \text{ Gy} \cdot \text{s}^{-1}$, or (b) no irradiation, with a carbon steel coupon (left), a stainless steel coupon (middle) and no coupon (right), where $[\text{Fe}^{2+}]_0 = 5 \times 10^{-4} \text{ mol} \cdot \text{dm}^{-3}$ 7-29
- Figure 7.18: The concentrations of H_2 (solid lines) and O_2 (dashed lines) measured in the gas phase for 1st trial test vials containing carbon steel, stainless steel, or no coupon in contact with a $5 \times 10^{-4} \text{ mol} \cdot \text{dm}^{-3}$ ferrous solution as a function of (a) irradiation time (at a dose rate of $1.4 \text{ Gy} \cdot \text{s}^{-1}$), or (b) contact time outside of a radiation field. 7-31
- Figure 7.19: The relative concentrations of Fe^{2+} (grey) and Fe^{3+} (purple) species measured in the aqueous phase for test vials containing carbon steel (CS), stainless steel (SS), or no coupon (NC) in contact with a $5 \times 10^{-4} \text{ mol} \cdot \text{dm}^{-3}$ ferrous solution as a function of irradiation time (at a dose rate of $1.4 \text{ Gy} \cdot \text{s}^{-1}$). From left to right, the sets of bars represent times of 21, 41, 64, 138, and 183 h. ... 7-32
- Figure 7.20: Simplified schematic of the cathodic and anodic half reactions that can occur on a carbon steel surface in (a) non-irradiated water, and (b) water subjected to γ -radiation. Note that the anodic reaction can also lead to oxide film formation..... 7-37

- Figure 7.15: The UV-Visible spectra of irradiated $[\text{Fe}^{2+}]_0 = 5 \times 10^{-4} \text{ mol} \cdot \text{dm}^{-3}$ deaerated solutions at pH 6.0 and a dose rate of $1.4 \text{ Gy} \cdot \text{s}^{-1}$ with the absorption contribution of the hydrated ferric ion removed. (a) Ferrous solutions irradiated in the absence of a coupon and (b) ferrous solutions irradiated in contact with a stainless steel coupon. 7-26
- Figure 7.16: The UV-Visible spectra collected for pH 6.0 deaerated (a) water ($[\text{Fe}^{2+}]_0 = 0 \text{ mol} \cdot \text{dm}^{-3}$), and (b) ferrous solution ($[\text{Fe}^{2+}]_0 = 5 \times 10^{-4} \text{ mol} \cdot \text{dm}^{-3}$), that were irradiated in contact with a carbon steel coupon at a dose rate of $1.4 \text{ Gy} \cdot \text{s}^{-1}$. The absorption contribution of the hydrated ferric ion was removed..... 7-27
- Figure 7.17: Optical images of 1st trial test solutions following 136 h of (a) irradiation at a dose rate of $1.4 \text{ Gy} \cdot \text{s}^{-1}$, or (b) no irradiation, with a carbon steel coupon (left), a stainless steel coupon (middle) and no coupon (right), where $[\text{Fe}^{2+}]_0 = 5 \times 10^{-4} \text{ mol} \cdot \text{dm}^{-3}$ 7-29
- Figure 7.18: The concentrations of H_2 (solid lines) and O_2 (dashed lines) measured in the gas phase for 1st trial test vials containing carbon steel, stainless steel, or no coupon in contact with a $5 \times 10^{-4} \text{ mol} \cdot \text{dm}^{-3}$ ferrous solution as a function of (a) irradiation time (at a dose rate of $1.4 \text{ Gy} \cdot \text{s}^{-1}$), or (b) contact time outside of a radiation field. 7-31
- Figure 7.19: The relative concentrations of Fe^{2+} (grey) and Fe^{3+} (purple) species measured in the aqueous phase for test vials containing carbon steel (CS), stainless steel (SS), or no coupon (NC) in contact with a $5 \times 10^{-4} \text{ mol} \cdot \text{dm}^{-3}$ ferrous solution as a function of irradiation time (at a dose rate of $1.4 \text{ Gy} \cdot \text{s}^{-1}$). From left to right, the sets of bars represent times of 21, 41, 64, 138, and 183 h. ... 7-32
- Figure 7.20: Simplified schematic of the cathodic and anodic half reactions that can occur on a carbon steel surface in (a) non-irradiated water, and (b) water subjected to γ -radiation. Note that the anodic reaction can also lead to oxide film formation..... 7-37

CHAPTER 1 INTRODUCTION

1.1 THESIS OBJECTIVES AND METHODS

Accurate understanding of the effects of ionizing radiation on aqueous chemistry and materials performance is important for the assessment of various operational and maintenance requirements of nuclear power plants. Of particular concern is the chemistry driven by the radiolysis of water. Deposition of ionizing radiation into water leads to the formation of both radicals and molecular species, termed the primary radiolysis products, as given in reaction 1.1 [1].



The primary radiolysis products differ considerably in their chemical reactivity and redox properties. They can participate in electrochemical reactions leading to corrosion, and understanding their production rates and subsequent reactions can provide the basis for selecting materials and water chemistry control agents to mitigate corrosion.

For most situations of practical interest, radiation fields are present on a continuous basis, or at least over time scales that are long compared to the time scale for primary radiolysis species production. Most corrosion processes (oxidation/dissolution), or other processes involving interfacial reactions and transport have high activation energies and only occur substantially over long periods of time. It follows, then, that the water chemistry influencing the corrosion of reactor structural materials will be controlled by steady-state radiolysis kinetics. Despite this, studies of long-term water radiolysis behaviour are sparse.

The main objective of this research program was to develop a mechanistic understanding of the effect of dissolved impurities and interfacial reactions on the long-term chemical kinetics of irradiated aqueous systems by employing a combined experimental and modeling approach. As an initial benchmark, these experiments were performed at room temperature, far removed from the operating conditions of nuclear reactor systems. This temperature facilitated the experimental analysis of radiolytically-generated species whose experimental concentration profiles were used to validate a

chemical kinetics model. At higher temperatures, thermal decomposition of hydrogen peroxide, a primary radiolysis product, would reduce the number of stable chemical species that can be measured for comparison with model simulations. Furthermore, significant uncertainties in the model calculations could arise if the temperature dependences of the rate constants are not properly defined, particularly as the reaction set becomes more complex.

The aqueous systems studied were chosen to constitute a small but representative cross-section of chemical additives, impurities, and interfacial reactions that can impact long-term coolant water chemistry in nuclear reactors. The parameters studied, each described in individual chapters, are outlined below in the order in which they appear in this thesis:

- The effect of varied headspace volume on the mass transport of volatile water radiolysis products was examined as a function of pH, and related to the steady-state concentrations of water radiolysis products in the aqueous phase. Irradiation products were monitored by gas chromatographic and spectrophotometric techniques, and the trends in their concentrations were simulated by incorporating mass transfer parameters into the collected reaction model.
- The steady-state radiolysis behavior of water containing initially dissolved oxygen was studied to validate the basic reaction set, and to confirm that the mass-transport parameters determined previously can accurately describe the kinetic system. Experimental measurements of water radiolysis products were compared with model simulation results. Model simulations were used to describe differences in the mechanism of reaction at early times that cannot be characterized experimentally.
- The steady-state radiation chemistry of nitrate and nitrite solutions was investigated as a function of pH. The water radiolysis product concentrations, as well as the nitrogen speciation, were monitored with time by chromatographic and spectrophotometric methods. The kinetic modeling results were used to aid in the mechanistic understanding of the reaction pathway.

- The production of uniformly sized iron oxyhydroxide colloids was observed during irradiation of ferrous sulfate solutions. The bulk particles were characterized by spectroscopic methods, while the local structure and composition were obtained by transmission electron microscopy and electron diffraction. Water radiolysis products were also monitored as a function of time.
- The influence of long-term irradiation on the corrosion behavior of carbon steel and stainless steel coupons in slightly acidic ferrous solutions was studied. Aqueous solutions were spectrophotometrically examined for water radiolysis products and ferric/ferrous ion speciation. Hydrogen and oxygen concentrations in the gas phase were also monitored with time. Coupon surfaces were imaged with scanning electron microscopy.

1.2 RADIATION CHEMISTRY

1.2.1 Radiation-Matter Interaction

Radiation chemistry describes the field of study focused on the chemical effects induced in matter exposed to high energy ionizing radiation. The radiation types considered include energetic charged particles (fast electrons/beta(β) particles, protons, alpha(α) and other heavy particles) as well as high energy photons (x- and γ -rays) that can cause ionization (along with some excitation) of molecules in a medium. Ionizing radiation can be generated by the acceleration of charged particles or the decay of radioactive nuclei (naturally occurring or generated from the fission of nuclear materials).

Radiation chemistry is a separate field of study from that of photochemistry; solutions exposed to ionizing radiation experience chemistry that differs significantly from solutions exposed to much lower-energy radiation, such as infrared (IR) and ultraviolet (UV) photons. The latter are typically considered to be non-ionizing. The difference in observed chemistry is related to the fundamental difference in how the radiation energy is absorbed into the matter. The low energy radiation from IR and UV sources often corresponds to bond vibrational energies or molecular electronic energy level differences, and hence tends to cause molecular vibrations or electronic excitations in the target molecules. These types of interactions are performed in a one-to-one

manner, in which a single photon can interact with only one molecule. They also tend to be highly specific; the frequency of the radiation can be tuned to interact with a selected molecular group. Due to the high specificity and singular interaction involved, photochemistry can be described as a solute-oriented process in which the bulk solution is largely unaffected by the presence of the radiation.

In contrast, the energy absorption mechanisms in radiation chemistry are largely insensitive to molecular structure, and are instead almost entirely dependent on atomic composition. The energy of ionizing radiation lies in the keV-MeV range, as compared to energies of only a few eV in the case of photochemistry. As a result, radiation-induced chemical reactions mainly occur through the formation of intermediate ion pairs. Due to their high energy, each fast electron (β -particle or an electron generated by Compton scattering of a γ -photon) undergoes many collisions, primarily with the electrons in matter, until it loses sufficient energy to eventually become “thermalized”. These interactions are not selective, and depend only on the relative abundance of electrons in the matter. Since the electron density of an atom is nearly proportional to its mass, the energy transfer from the ionizing radiation to matter is nearly the same per unit mass for all types of matter. The amount of energy absorbed by an interacting medium is expressed in units of Gray (Gy), where $1 \text{ Gy} = 1 \text{ J}\cdot\text{kg}^{-1}$. Therefore, the probability of an incident electron or photon interacting with solutes in a dilute aqueous system is very small compared to the probability of the electron interacting with the bulk matter in that system. For this reason, the radiation chemistry of dilute systems is often referred to as a solvent-oriented process.

1.2.1.1 The Linear Energy Transfer Rate

As described above, ionizing radiation transfers its energy mainly through collisions with electrons in the medium. The linear energy transfer (LET) rate of an incident radiation particle or photon traversing a medium is defined as the amount of total energy lost per unit length travelled [2]. The LET rate decreases, while the penetration depth increases, for a given medium from α -particles to β -particles to γ -photons; in liquid water at room temperature, the penetration depths are $< 50 \mu\text{m}$ for α -particles, 0.5-1.0 cm for β -particles, and tens of cm for γ -rays (the distance in which there is a $\frac{1}{2}$ reduction in

their intensity) [1]. The LET rate is dependent on the radiation type (charge, mass and energy).

Alpha-particles (the nuclei of helium atoms) and β -particles (high energy electrons) both interact with a medium primarily through inelastic collisions with electrons located along the radiation path. Due to their large mass in comparison with the electrons they perturb, α -particles lose only small amounts of their energy with each collision and are not easily deflected from their straight paths [1]. However, α -particles have a large collision cross section with electrons, which prevents these particles from penetrating deeply into a medium. As a result, a very dense collection of excited and ionized particles lies along a short radiation track (Figure 1.1a). In contrast, β -particles share the same mass with the electrons with which they interact; they can lose up to half of their energy with each collision and be deflected through a large angle [1]. Beta-particles can interact with multiple electrons with their remaining energy as they move along a near linear track, but with reduced efficiency through each cascade. The ejected electrons following a collision typically have much lower energy than the incident electron, but they can have sufficient energy to further propagate the electron ejection process and create local ionization 'spurs'. Therefore, these particles create a low-density collection of ions or excited molecules along their radiation tracks (Figure 1.1b).

Gamma rays are electromagnetic radiation with energies in the range of 40 keV to 4 MeV and have the largest penetration depth of the ionizing radiation types [1]. A given gamma radiation source emits γ -rays of specific energies; for example, γ -rays from the decay of Co-60 have an energy of either 1.17 MeV or 1.33 MeV, whereas those from Cs-137 have an energy of 0.66 MeV. Gamma-rays transfer most of their energy by Compton scattering if their energy exceeds 0.01 MeV [3]. Compton scattering is a phenomenon in which the photon interaction with matter causes electron ejection from the molecule and the resulting γ -ray photon is re-emitted with a reduced energy. Each ejected electron from a high-energy collision acts similarly to a β -particle and produces a characteristic ionization cascade. Due to the lower probability of an inelastic Compton scattering event compared to an electron collision, the penetration depth of γ -radiation is large relative to other radiation forms (Figure 1.1c). The LET of a radiation type can

influence the initial distribution of species created by radiolysis. This effect will be discussed further in Section 1.2.2.1.

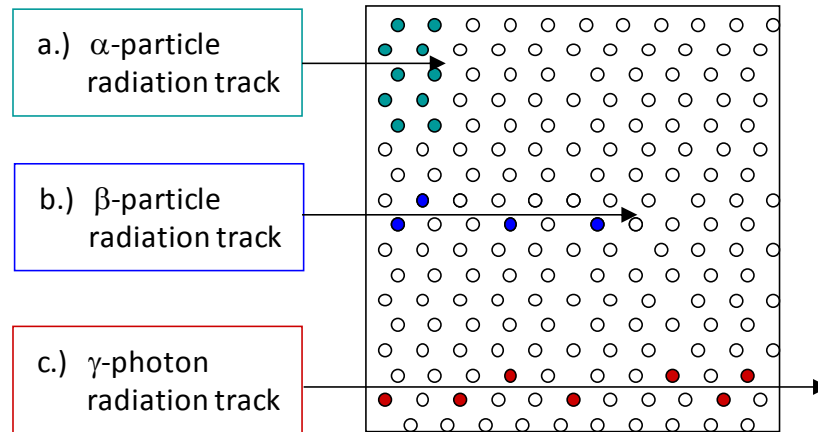


Figure 1.1: Schematic representation of the clusters of ions and excited molecules along the radiation track for different types of ionizing radiation [1].

1.2.2 Water Radiolysis by Low LET Radiation

1.2.2.1 Primary Radiolysis Processes

As described in Section 1.2.1, the initial interaction of ionizing radiation with matter involves a series of collisions between the incident radiation and the electrons in the medium. In nuclear power reactors, the radiation sources are fission products that are trapped in the ceramic fuel and leak-tight fuel sheath. Low-penetrating, high LET α -radiation cannot escape the fuel sheath and contributes no dose to aqueous reactor systems such as the coolant system, the moderator system, or the end shield cooling system. The radiation chemistry of these water systems will be controlled by more penetrating β - and γ -radiation. Neutron radiation is also a significant contributor to the total radiation flux in a nuclear reactor core (and associated water systems), but the effects of neutrons on matter are initiated through collisions with atomic nuclei as opposed to electrons, and these effects are outside the scope of this work. The following discussion will focus mainly on the early events of water radiolysis initiated by low LET radiation sources, with comparison to high LET radiation processes where appropriate.

When passing through liquid water, energetic electrons will undergo collisions with water molecules, with each collision transferring < 100 eV of energy, and the

average energy transferred per collision ranging from 30-40 eV [1,4]. The initial consequence of such a collision is the ionization or excitation of the water molecule. This creates ion pairs ($\text{H}_2\text{O}^{\bullet+}$ and e^-_{hot}) or electronically excited water molecules (H_2O^*) along the radiation track. The energetic or “hot” electron (e^-_{hot}) produced in such an ion pair may have sufficient energy to collide with a neighbouring solvent molecule to produce either a secondary ion pair or another excited water molecule. Because the energy of the ‘hot’ electron is much lower than that of the incident radiation, the secondary ionization will be located in close proximity to the main ionization track and result in a cluster of 2-3 groups of ionized or excited species. This cluster is referred to as a “spur” along the ionizing track, and is represented schematically in Figure 1.2 for a low LET radiation source [1]. As described in Section 1.2.1.1, the spurs may be sparsely or densely distributed along the radiation track according to the radiation type and LET.

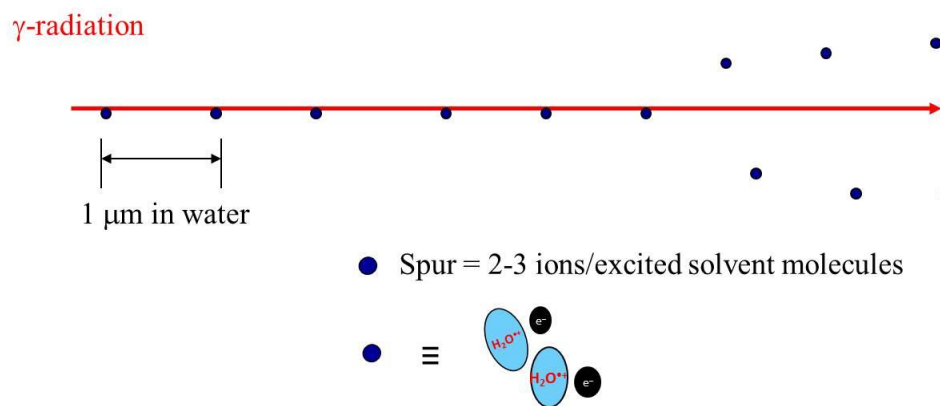


Figure 1.2: A representation of the spur distribution in water along the radiation track for γ -radiation [1].

Following ion-pair formation, the electrons can have sufficient kinetic energy to move away from the water counter cations that were simultaneously formed in the spur. As the spurs expand, the cations and excited molecules undergo various intra- and intermolecular energy transfers including energy relaxation to vibrational and rotational motions, bond dissociations to form radical and ion pairs (such as $\text{H} + \text{OH}$ and $\text{H}_3\text{O}^+ + \text{OH}$), and ion-molecule and ion-ion recombination reactions [1]. The recombination of

ion pairs due to the Coulombic interaction between the charged counter ions is referred to as geminate recombination. Radical pairs can also experience geminate recombination, but this is not driven by electrostatic attraction. The probability of escaping geminate recombination has a significant effect on the chemical yields from irradiation as determined at later times, and depends on how fast these species diffuse away from each other or become solvated. For a given radiation type, the dielectric constant of the medium and the distance between the counter ions of a pair dictates the probability of the ion pair escaping geminate recombination; the probability of escape (the free ion yield) increases with an increase in the dielectric constant of the solvent [4].

The Coulombic force between the counter ions diminishes as the spur expands and the counter ions are no longer distinguishable from the other ions formed in different spurs. This homogeneous out-of-spur distribution of water decomposition products is obtained approximately 100 ns after the incident radiation interaction in liquid water at 25 °C, as shown in Figure 1.3. This time scale is short compared to the time scale for subsequent bulk phase chemical reaction kinetics. The chemical species present at the end of this homogeneous distribution stage are often referred to as the ‘primary’ radiolysis products, and the chemical yields, termed the primary radiolysis yields, are expressed in G-values. Despite the label of ‘primary’ products, they are not the first species formed in a radiation track (in the first few ps of an electron-molecule interaction), but are the set of ‘stable’ species which can subsequently participate in bulk chemical reaction processes on the time scale normally associated with reactions in solution.

For a specific type of radiation and a given absorbing medium, the primary radiolysis yields depend mainly on the amount of energy absorbed by the medium, hence the G-values are expressed per unit of absorbed energy, with the traditional units of molecules formed per 100 eV or SI units of $\mu\text{mol}\cdot\text{J}^{-1}$. The G-values strongly depend on the type of radiation and the solvent properties of the absorbing medium (such as dielectric constant) since those properties influence the spur density and the rates of geminate recombination reactions. With respect to water radiolysis, radiation sources with high LET values characteristically generate a higher proportion of molecular products, while sources with low LET values yield a much lower level of molecular

products [1,3]. High-LET radiation such as α -radiation, creates an elevated local concentration of highly reactive radicals and excited species since collision events occur very close together and this can result in significant spur overlap (Figure 1.1a). The proximity of these reactive species to one another allows some of them to recombine quickly to form molecular species of much lower reactivity. In contrast, for low LET radiation (like x-rays or γ -rays) in liquid water at 25°C, the excited species are spread out along the track due to the relatively large distance between adjacent spurs (Figure 1.2). The low local concentrations allow the reactive molecules to more easily diffuse away from the radiation track and escape recombination to molecular products. This cycle of production and diffusion of radical species results in a much higher proportion of radical species to molecular species being formed with low LET radiation [1,3]. These mechanistic differences in the early radiolysis processes for α - and γ -radiation can be observed in the respective G-values for the two radiation types, as shown in Table 1.1.

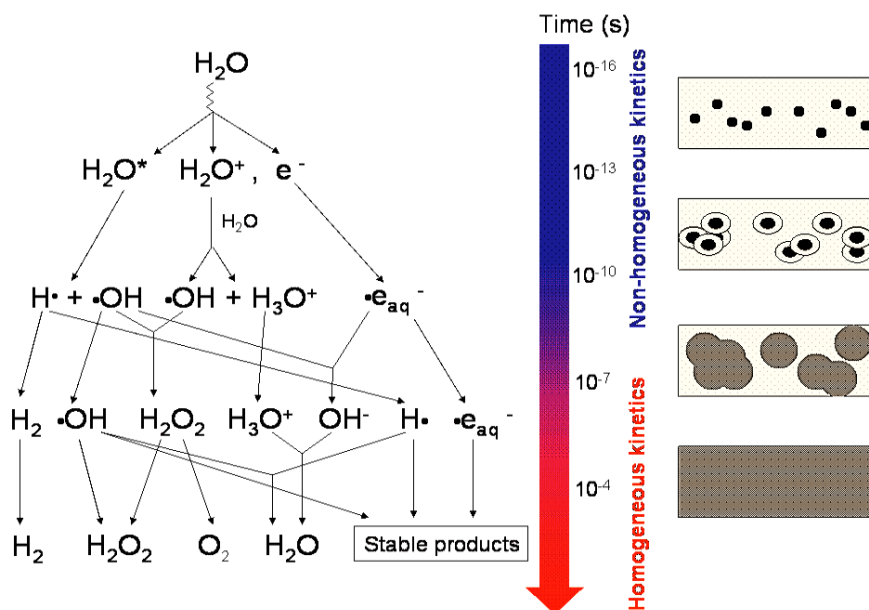


Figure 1.3: Schematic of water radiolysis events as a function of time following absorption of radiation energy. The right hand panel shows the expansion of spurs with time [5].

Table 1.1: The primary α - and γ -radiolysis yields (G-values, $\mu\text{mol}\cdot\text{J}^{-1}$) at 25 °C for liquid water [1].

Radiation	H ₂ O	$\bullet\text{e}_{\text{aq}}^-$	H ⁺	$\bullet\text{OH}$	$\bullet\text{H}$	HO ₂ \bullet	H ₂	H ₂ O ₂
α , 12 MeV	-0.30	0.04	0.04	0.06	0.03	0.01	0.12	0.11
γ , 0.1-20 MeV	-0.43	0.28	0.28	0.28	0.06	0	0.045	0.07

1.2.2.2 Bulk Phase Chemistry and the Steady State

The G-values represent the yields of radiolytically generated species that are present, following a single fast pulse of radiation, once the system has reached homogeneity in the bulk phase following spur diffusion. The concentrations of the species present at this stage can be taken as the initial reactant concentrations for bulk phase reactions. While these yields of the primary water radiolysis products show a distinct dependence on radiation type (LET) (Table 1.1), the kinetics of their subsequent reactions are independent of the radiation type. As such, the chemical processes of the system after this stage can be described by traditional homogeneous kinetics. For a system exposed to a continuous radiation flux, the radiolytic production rates are described by the product of the G-values and the radiation dose rate. The rates of removal of the primary radiolysis products are determined by the product of reactant concentrations and their respective reaction rate constants. Pulse radiolysis, a technique where a short (typically < 1 μs duration) and intense radiation pulse is delivered to the aqueous chemical system can be used to probe the kinetics of individual radiolytic reactions. In this technique, a fixed quantity of primary radiolysis products is formed and the reactions of radiolytically-formed transient species can be followed using time-resolved spectroscopic methods [6-22].

While pulse radiolysis is a very powerful technique, the distributions of chemical species attained from short term radiation exposures should not be used to predict the redox condition in solutions exposed to a continuous flux of radiation for longer times. In a continuously irradiated system, radiolysis products are generated at a constant rate and will initially accumulate in the system (according to their radiolytic yield, or G-value). However with increased irradiation time, the removal of these species via

reactions with other radiolysis products and chemical species present will accelerate. Eventually, the loss rates of individual species will equal their respective radiolytic production rates, and the aqueous system will reach a pseudo-steady state in which the concentrations of dissolved species remain approximately constant with time. Due to the large number of fast removal and regeneration reactions for the radiolytic species, their concentrations are highly interdependent and solving such a kinetic system manually is not practical. Commercially available software can be used to solve the collection of coupled, stiff differential rate equations that constitute a chemical kinetics description of the system. The capabilities of the kinetic modeling software will be described further in Section 2.3.

Although a pseudo-steady-state concentration of primary and secondary radiolysis products can be attained fairly quickly, the concentrations of these species will continually and slowly change over time as slower reactions begin to take place. Hence, the term pseudo-steady-state is used to describe the distribution of species concentrations during this period. The effect of long-term continuous irradiation on slow processes such as interfacial reactions (including mass transfer, liquid-liquid interfacial reactions, and corrosion) are determined by the pseudo-steady-state concentrations of reactive species [23-27]. Most industrial irradiation applications (such as electron beam accelerators) involve time scales exceeding μs , and can be considered continuously irradiated systems [27-43]. Such systems include food and medical equipment sterilization systems, and polymer processing methods. In the nuclear industry, such conditions arise in the water systems around a nuclear reactor core and also in the liquid phases encountered in nuclear fuel waste management or reprocessing technologies.

1.3 IRRADIATED AQUEOUS SYSTEMS IN A NUCLEAR REACTOR

This thesis is focused on the influence of chemical impurities and interfacial reactions of importance for nuclear power plant operation in continuously irradiated aqueous systems. There are currently three principal water-cooled reactor designs in operation worldwide: the boiling water reactor (BWR), the pressurized light water reactor (PWR), and the pressurized heavy water reactor (PHWR) [44-47]. BWRs are a direct cycle light water reactor system. The heating of the primary coolant produces steam that

then goes on to drive the steam turbines directly. For PWR reactor designs, the coolant and steam generator systems are separated, but the primary coolant also functions as the neutron moderator. In PHWR designs, the coolant, moderator and steam generator systems are all separated. While there are differences in the specific purity requirements of the irradiated aqueous systems present in each design, most radiation chemistry considerations are common to all water-cooled reactor types [48-50]. A brief overview of the radiation chemistry of selected aqueous reactor systems is provided below. In Canada, the nuclear power generating stations are equipped with CANada Deuterium Uranium (CANDU) reactors, which are of the PHWR type. The following discussion will focus mainly on this design. A schematic of the overall CANDU layout is shown in Figure 1.4.

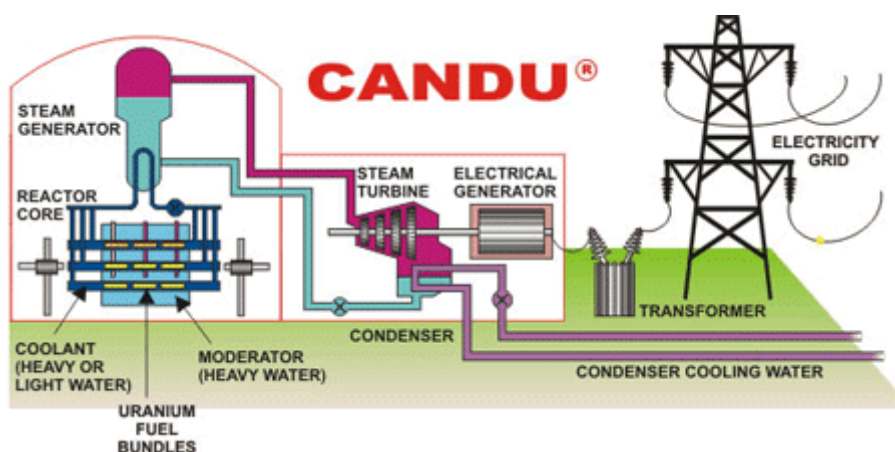


Figure 1.4: Overview of the layout of a CANDU pressurized heavy water reactor.

1.3.1 Heat Transport System

1.3.1.1 Corrosion and Activity Transport

In a CANDU reactor, the heat transport system (HTS) is composed of an array of zirconium alloy pressure tubes in the reactor core that are connected to carbon steel feeder pipes outside of the core. Heavy water (D_2O) coolant, maintained at an alkaline

$\text{pH}_a(25^\circ\text{C})^1$ of 10.2-10.4 [50,51], circulates through the reactor core, where it absorbs the heat released by the fissioning of the UO_2 fuel, and carries the heat to the steam generators. From the inlet to the outlet of the reactor core, the coolant temperature increases from approximately 250 to 300 °C [44].

Minimizing the corrosion of reactor materials is important to optimize reactor performance and lifetime. In all reactor designs, the heat transport system, or reactor coolant system, is operated with strict chemistry control to ensure low corrosion rates. Limits for impurity concentrations, pH ranges, and oxygen concentrations are all defined in operational guidelines [48-50] and are dependent on the materials present in the system. For example, CANDU systems operate at alkaline pH, where the solubilities of iron species reach a minimum, to promote the formation of compact and protective magnetite oxide on the carbon steel feeder tubes [50,52,53]. In PWR and BWR reactors, stainless steel and Ni-based alloys are more frequently used, and these materials display good corrosion resistance at near-neutral pH in high temperature water due to the formation of Cr and Ni-containing passive oxide films [54-57].

Radiolytically-generated oxygen and hydrogen peroxide are effective oxidants, and can impact the corrosion rates of reactor structural materials in contact with irradiated aqueous systems. Since corrosion involves the oxidation of metal species coupled with the reduction of aqueous species, its rate depends on the potential at the metal-water interface, the electrochemical corrosion potential (ECP). Due to mass and charge balance, the net rate of oxidation and reduction must be equal on a corroding surface, and hence, an increase in oxidant concentration in the aqueous phase will increase the rate of the reduction half reaction. This is compensated by a corresponding increase in the metal oxidation rate, and leads to an increase in the ECP. Therefore, the ECP quantifies the oxidizing power of a solution in contact with a metal surface. The ECP of stainless steel and carbon steel electrodes in alkaline and argon-purged borate solutions have been shown to increase when subjected to γ -irradiation [24,58]. In the case of carbon steel, the ECP increase can be reproduced in the absence of radiation by

¹ These pH values represent the experimental readings obtained for D_2O coolant at 25°C using a pH meter that was calibrated in H_2O . The pD values can be calculated from the relationship $\text{pD} = \text{pH}_a + 0.41$.

the addition of hydrogen peroxide to the solution. Numerous studies on stainless steel materials used in BWR and PWR reactor vessels have also shown that high oxidant concentrations (O_2 and H_2O_2) correlate with more positive ECP values at which there is a greater tendency for stress corrosion cracking (SCC) to occur [48,59-62]. Consequently, most operating reactors employ chemistry control strategies to reduce the radiolytic production rate of oxidizing species in the coolant.

Corrosion processes can release dissolved metal ions (typically transition metal ions) into the reactor coolant system, and these can impact the system in a variety of ways. The temperature gradients within the HTS can lead to changes in solubility for the dissolved metal species and may result in the deposition of species in locations where solubilities are low (generally lower temperature regions). A buildup of corrosion product deposits in the HTS piping can lead to decreased heat transfer efficiency (in steam generators). Metal species deposited in the reactor core may absorb a neutron; if the resulting isotope is radioactive, this is termed neutron activation. For example, the gamma-emitting isotope ^{60}Co is generated by the neutron activation of stable ^{59}Co . The subsequent circulation of such radioactive species through the HTS is called activity transport and is a radiological safety concern. Resuspension of activated products followed by redeposition on piping surfaces located outside the reactor core increases the radioactivity level in less radiation shielded areas and can provide higher than anticipated radiation doses to maintenance workers during reactor outages. Radiolytic effects of corrosion products on the coolant chemistry are also a concern. Dissolved transition metals can react with redox active species in the coolant (such as radiolysis products) to change oxidation state. In doing so, the steady-state concentrations of radiolysis products could be perturbed away from their usual condition, and the overall redox state of the water may change. These changes in the balance of reducing and oxidizing species in the coolant can then influence corrosion of downstream materials. This synergistic relationship between corrosion and radiolysis is represented for iron in Figure 1.5.

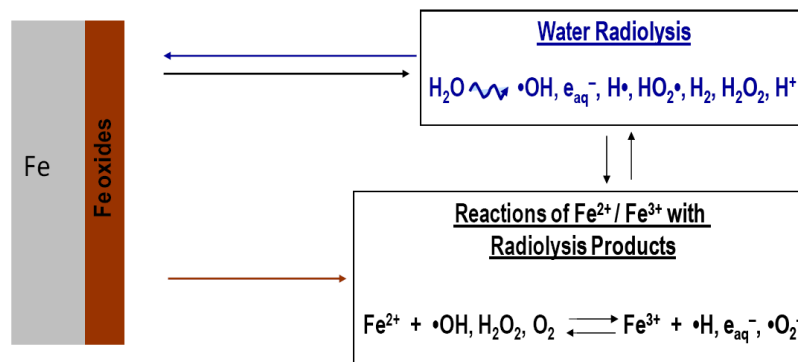
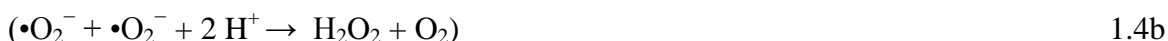


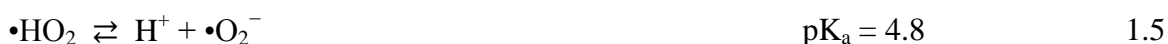
Figure 1.5: The feedback relationship of corrosion and radiolysis for an irradiated aqueous system in contact with iron.

1.3.1.2 Chemistry Control

The main radiolytically-produced oxidants of concern for the corrosion of heat transport system components are the stable molecular products O_2 and H_2O_2 since their concentrations can persist once the coolant has exited the high radiation flux region of the reactor core. Hydrogen peroxide is a primary water radiolysis product (reaction 1.1) and is generated by recombination reactions in a spur. Oxygen, however, is produced only as a secondary radiolysis product; the mechanism for this is initiated by the reaction of hydrogen peroxide with the hydroxyl radical:



where



As described in Section 1.3.1.1, most reactor designs employ chemistry control strategies to reduce the concentrations of these oxidizing molecular species in the coolant and minimize corrosion rates. The most common radiolytic suppression strategy involves hydrogen addition to the coolant, and this chemistry control regime is generally referred

to as hydrogen water chemistry (HWC). While radiolysis will continue by reaction 1.1 as long as an aqueous system is exposed to a radiation source, the addition of sufficient quantities of hydrogen will promote reaction pathways that result in the removal of oxidizing species [2,63-68]:



where



This chain reaction clearly demonstrates the destruction of the primary radiolysis product H_2O_2 , while oxygen is prevented from forming due to the inhibition of reaction 1.2. The net result of this chain reaction is radiolytic suppression:



To ensure that an aqueous system (in the absence of other chemical impurities) operates in radiolytic suppression (reaction 1.9) as opposed to net radiolysis (reaction 1.1), the hydrogen concentration must be sufficiently high to ensure that reaction 1.6 proceeds more rapidly than reaction 1.2. For this reason, the production rate of hydrogen by reaction 1.1 (in the absence of other chemical impurities) is not sufficient to allow H_2 to outcompete H_2O_2 for reaction with $\bullet\text{OH}$. The minimum hydrogen concentration required to achieve radiolytic suppression is termed the critical hydrogen concentration (CHC). For CANDU reactors, which operate with a heavy water coolant, the current specification for dissolved deuterium (D_2) is 3-10 mL/kg D_2O , where the lower specification limit is determined by the CHC [51,66].

1.3.2 Moderator System

The neutrons released by nuclear fission have very high speeds. The moderator is a material in the reactor core that serves to slow down these neutrons by inelastic scattering so that they can be more efficiently absorbed to continue the fission chain

reaction. For PWR and BWR systems, the light water coolant also functions as the moderator, and the radiation chemistry considerations of the moderator are those outlined in Section 1.3.1. CANDU reactors utilize heavy water as the neutron moderator due to its lower neutron absorption cross section, and the HTS and moderator systems in CANDU reactors are separated (as shown in Figure 1.6) and maintained with different chemistry.

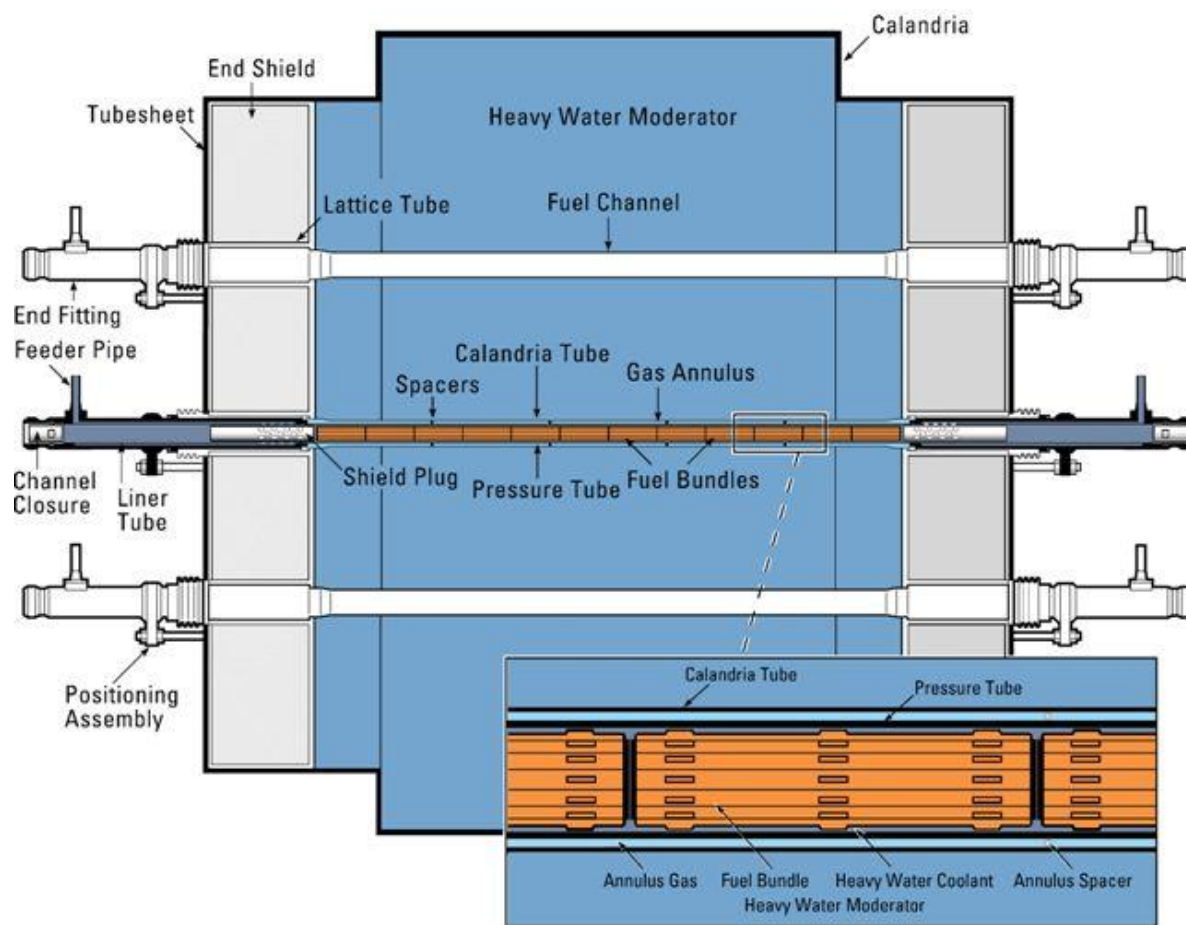


Figure 1.6: Simplified overview of the separated coolant system, moderator system and end shield cooling system in a CANDU nuclear reactor.

Unlike the HTS, the moderator system operates at near-neutral pH and much lower temperatures (between 50 and 70 °C), and is blanketed by a He cover gas [66]. Net radiolysis can occur to form stable products (D_2 , D_2O_2 and O_2), and the volatile products can transfer from the aqueous phase into the cover gas. In this design, it is not possible to

maintain a critical hydrogen (deuterium) concentration to prevent this process. As a result, the moderator cover gas is continuously circulated through a hydrogen recombination unit (to regenerate D₂O from the radiolytically generated deuterium and oxygen gases). This ensures that the level of deuterium is kept well below the flammability limit.

1.3.3 End Shield Cooling System

In CANDU systems, the end shield cooling (ESC) system is a large volume, low pressure, light water system operated at low temperatures (~ 50 °C). It consists of the calandria vault which surrounds the reactor core and two end shields for the reactor (filled with carbon steel balls) located at the fuel channel exits from the core (see Figure 1.6). The calandria vault has a nitrogen cover gas. One purpose of the end shields is to provide shielding for personnel approaching the reactor core (when the reactor is not operating). The neutron and gamma dose rates drop significantly with distance from the core within the end shield, but radiolysis can occur [69,70]. In order to minimize potential carbon steel corrosion, an alkaline pH (9.0-10.5) is maintained in the end shield water (light water). The large surface area of the carbon steel balls is thought to react with the low concentrations of radiolytic oxidants to generate an excess hydrogen concentration that can suppress radiolysis according to reaction 1.9.

1.3.4 Radiation Chemistry Considerations under other Conditions

1.3.4.1 Radiolysis of Chemical Impurities

Occasionally, undesired chemicals can be introduced into an irradiated aqueous system. Such situations can arise from pump leaks (introducing organic oils) or degradation of ion exchange water purification resins (introducing nitrogen-containing species). The introduction of species that can hold many different oxidation states, such as nitrogen and carbon, can introduce complex radiolytic reaction schemes and dramatically alter the net redox condition of the aqueous system.

When organics are added to an irradiated aqueous system, the radiolytic mechanisms that ensue are largely determined by the phase in which the organic species is located. When soluble organic species are added to an aqueous phase in dilute

quantities, the radiation chemistry of the solution will remain dominated by water radiolysis since the majority of the radiation energy will be deposited into the water solvent. The predominant organic-water interaction is the degradation of the soluble organic species to CO_2 and H_2 by reaction with water radiolysis products. When the organic and aqueous phases remain separated (typically the case for long-chain, high molecular weight organics such as pump oils), the overall radiation chemistry can become more complex, as each solvent phase can undergo separate radiolytic reactions, followed by the interaction of the respective radiolysis products at the water-organic interface. In the organic phase, the deposition of radiation energy can lead to fragmentation and overall breakdown of the organic material as well as cross-linking and polymerization reactions. Small fragmentation products with increased mobility may enter the aqueous phase with time and can react with water radiolysis products as dissolved dilute impurities [27].

The introduction of dissolved inorganic impurities such as transition metals and nitrogen-containing ionic species is the focus of several chapters of this thesis. These interactions will be discussed in detail in subsequent chapters.

1.3.4.2 Air Radiolysis in Humid Environments

In nuclear reactor systems, the draining of aqueous systems during maintenance outages can generate moist air environments, which, when irradiated, can lead to the formation of nitric acid [71-74]. Since N_2 is relatively an inert molecule, dissolved N_2 does not react with water radiolysis products directly. Instead, the radiation chemistry mechanism is driven by direct energy deposition from the ionizing radiation source to the N_2 molecule. Dissociation of molecular nitrogen leads to the formation of reactive $\bullet\text{N}$ atoms which can subsequently react with water and water radiolysis products [75-78]. Due to the low solubility of nitrogen in water, the probability of a direct energy deposition event occurring is greater in the gas phase where the concentration of nitrogen is several orders of magnitude larger than it is in the liquid phase. As a result, the gas phase G-value for nitrate formation in biphasic air-water systems is in the range of 1-3 molecules/ 100 eV, while the liquid phase G-value can be considered negligible.

Once formed, any dissolved ionic nitrogen species can participate in further redox reactions with water radiolysis products or impact reactions on material surfaces. The acidification resulting from the radiolysis of humid air has been linked to the corrosion of the J-rod annulus in the AECL NRU (National Research Universal) research reactor [79,80]. The influence of humid air radiolysis must be carefully considered when irradiated aqueous systems are exposed to cover gas volumes with air ingress (such as during outages where systems must be temporarily drained).

1.4 REFERENCES

- [1] Spinks, J.W.T., Woods, R.J. *An Introduction to Radiation Chemistry*, 3rd ed., Wiley-Interscience: New York, 1990.
- [2] Allen, A.O. *The Radiation Chemistry of Water and Aqueous Solutions*, Van Nostrand Company, Inc.: New York, 1961.
- [3] Draganic, I.G., Draganic, Z.D. *The Radiation Chemistry of Water*, Academic Press, Inc.: New York, 1971.
- [4] *Radiation Chemistry: Principles and Applications*, Farhataziz, Rodgers, A.J., Eds., VCH Publishers, Inc.: New York, 1987.
- [5] *Radiation Chemistry: From Basics to Applications in Material and Life Sciences*, Belloni, J., Douki, T., Mostafavi, M., Spothem-Maurizot, M., Eds., EDP Sciences: Paris, 2008.
- [6] Alam, M.S., Kelm, M., Rao, B.S.M., Janata, E., "Reaction of H with H₂O₂ as observed by optical absorption of perhydroxyl radicals or aliphatic alcohol radicals and of OH with H₂O₂. A pulse radiolysis study", *Radiat. Phys. Chem.*, **2004**, *71*, 1087-1093.
- [7] Baldacchino, G., De Waele, V., Monard, H., Sorgues, S., Gobert, F., Larbre, J.P., Vigneron, G., Marignier, J.L., Pommeret, S., Mostafavi, M., "Hydrated electron decay measurements with picosecond pulse radiolysis at elevated temperatures up to 350°C", *Chem. Phys. Lett.*, **2006**, *424*, 77-81.
- [8] Christensen, H., Sehested, K., "Reaction of hydroxyl radicals with hydrogen at elevated temperatures. Determination of the activation energy", *J. Phys. Chem.*, **1983**, *87*, 118-120.
- [9] Ershov, B.G., Gordeev, A.V., Kelm, M., Janata, E., "Rate constant for the reaction of the H atom with H₂O₂ in aqueous solution", *Radiat. Phys. Chem.*, **2003**, *67*, 613-616.
- [10] Goel, N.K., Joshi, R., Bhardwaj, Y.K., Varshney, L., "Role of radiolytically generated species in polymerization of [2-(acryloyloxy)ethyl]trimethylammonium chloride (AETC) in aqueous medium: Steady state and pulse radiolysis study", *Radiat. Phys. Chem.*, **2013**, *92*, 66-70.
- [11] Janata, E., Schuler, R.H., "Rate constant for scavenging e_{aq}⁻ in nitrous oxide-saturated solutions", *J. Phys. Chem.*, **1982**, *86*, 2078-2084.
- [12] Lin, M., Katsumura, Y., Muroya, Y., He, H., Miyazaki, T., Hiroishi, D., "Pulse radiolysis of sodium formate aqueous solution up to 400°C: Absorption spectra,

- kinetics and yield of carboxyl radical CO_2^- ", *Radiat. Phys. Chem.*, **2008**, *77*, 1208-1212.
- [13] Lundström, T., Christensen, H., Sehested, K., "The reaction of OH with H at elevated temperatures", *Radiat. Phys. Chem.*, **2002**, *64*, 29-33.
- [14] Lundström, T., Christensen, H., Sehested, K., "Reactions of the HO_2 radical with OH, H, Fe^{2+} and Cu^{2+} at elevated temperatures", *Radiat. Phys. Chem.*, **2004**, *69*, 211-216.
- [15] Pálfi, T., Wojnárovits, L., Takács, E., "Calculated and measured transient product yields in pulse radiolysis of aqueous solutions: Concentration dependence", *Radiat. Phys. Chem.*, **2010**, *79*, 1154-1158.
- [16] Schmidt, K.H., Bartels, D.M., "Lack of ionic strength effect in the recombination of hydrated electrons: $(e^-)_{\text{aq}} + (e^-)_{\text{aq}} \rightarrow 2(\text{OH}^-) + \text{H}_2$ ", *Chem. Phys.*, **1995**, *190*, 145-152.
- [17] Stanisky, C.M., Bartels, D.M., Takahashi, K., "Rate constants for the reaction of hydronium ions with hydrated electrons up to 350°C ", *Radiat. Phys. Chem.*, **2010**, *79*, 64-65.
- [18] Sweet, J.P., Thomas, J.K., "Absolute rate constants for H atom reactions in aqueous solutions", *J. Phys. Chem.*, **1964**, *68*, 1363-1368.
- [19] Takahashi, K., Sato, T., Katsumura, Y., Yang, J., Kondoh, T., Yoshida, Y., Katoh, R., "Reactions of solvated electrons with imidazolium cations in ionic liquids", *Radiat. Phys. Chem.*, **2008**, *77*, 1239-1243.
- [20] Thomas, J.K., "Rates of reaction of the hydroxyl radical", *Transactions of the Faraday Society*, **1965**, *61*, 702-707.
- [21] Wu, G., Katsumura, Y., Muroya, Y., Li, X., Terada, Y., "Pulse radiolysis of high temperature and supercritical water: experimental setup and e_{aq}^- observation", *Radiat. Phys. Chem.*, **2001**, *60*, 395-398.
- [22] Yang, J., Kondoh, T., Norizawa, K., Nagaishi, R., Taguchi, M., Takahashi, K., Katoh, R., Anishchik, S.V., Yoshida, Y., Tagawa, S., "Picosecond pulse radiolysis: Dynamics of solvated electrons in ionic liquid and geminate ion recombination in liquid alkanes", *Radiat. Phys. Chem.*, **2008**, *77*, 1233-1238.
- [23] Wren, J.C. In *ACS Symposium Series: Nuclear Energy and the Environment*, Chien, W., Mincher, B., Eds., American Chemical Society: Washington, D.C., 2010, p 271-295.
- [24] Daub, K., Zhang, X., Noël, J.J., Wren, J.C., "Effects of γ -radiation versus H_2O_2 on carbon steel corrosion", *Electrochim. Acta*, **2010**, *55*, 2767-2776.
- [25] Glass, R.S., Overturf, G.E., Van Konynenburg, R.A., McCright, R.D., "Gamma radiation effects on corrosion—I. Electrochemical mechanisms for the aqueous corrosion processes of austenitic stainless steels relevant to nuclear waste disposal in tuff", *Corros. Sci.*, **1986**, *26*, 577-590.
- [26] Behazin, M., Noël, J.J., Wren, J.C., "Combined effects of pH and γ -irradiation on the corrosion of Co-Cr alloy stellite-6", *Electrochim. Acta*, **2014**, *134*, 399-410.
- [27] Howett, S.E., Joseph, J.M., Noël, J.J., Wren, J.C., "Effect of gamma irradiation on gas-ionic liquid and water-ionic liquid interfacial stability", *J. Colloid Interface Sci.*, **2011**, *361*, 338-350.
- [28] Drobny, J.G. In *Ionizing Radiation and Polymers*, Drobny, J.G., Ed., William Andrew Publishing: 2013, p 149-212.

- [29] Chmielewski, A.G., Haji-Saeid, M., Ahmed, S., "Progress in radiation processing of polymers", *Nucl. Instr. and Meth. in Phys. Res. B*, **2005**, 236, 44-54.
- [30] Cleland, M.R., Parks, L.A., Cheng, S., "Applications for radiation processing of materials", *Nucl. Instr. and Meth. in Phys. Res. B*, **2003**, 208, 66-73.
- [31] McKeen, L. In *The Effect of Sterilization on Plastics and Elastomers (Third Edition)*, McKeen, L., Ed., William Andrew Publishing: Boston, 2012, p 1-40.
- [32] Iqbal, S.Z., Bhatti, I.A., Asi, M.R., Zuber, M., Shahid, M., Parveen, I., "Effect of γ irradiation on fungal load and aflatoxins reduction in red chillies", *Radiat. Phys. Chem.*, **2013**, 82, 80-84.
- [33] Braghini, R., Pozzi, C.R., Aquino, S., Rocha, L.O., Corrêa, B., "Effects of γ -radiation on the fungus *Alternaria alternata* in artificially inoculated cereal samples", *Appl. Radiat. Isot.*, **2009**, 67, 1622-1628.
- [34] Jalili, M., Jinap, S., Noranizan, M.A., "Aflatoxins and ochratoxin a reduction in black and white pepper by gamma radiation", *Radiat. Phys. Chem.*, **2012**, 81, 1786-1788.
- [35] Jha, P.K., Kudachikar, V.B., Kumar, S., "Lipase inactivation in wheat germ by gamma irradiation", *Radiat. Phys. Chem.*, **2013**, 86, 136-139.
- [36] Supriya, P., Sridhar, K.R., Ganesh, S., "Fungal decontamination and enhancement of shelf life of edible split beans of wild legume *Canavalia maritima* by the electron beam irradiation", *Radiat. Phys. Chem.*, **2014**, 96, 5-11.
- [37] Roberts, P.B., "Food irradiation is safe: Half a century of studies", *Radiat. Phys. Chem.*, **2014**, 105, 78-82.
- [38] Kume, T., Furuta, M., Todoriki, S., Uenoyama, N., Kobayashi, Y., "Status of food irradiation in the world", *Radiat. Phys. Chem.*, **2009**, 78, 222-226.
- [39] Ramanujam, A. In *Encyclopedia of Materials: Science and Technology*, 2nd ed., Buschow, K.H.J., Cahn, R.W., Flemings, M.C., Ilshner, B., Kramer, E.J., Mahajan, S., Veyssi re, P., Eds., Elsevier: Oxford, 2001, p 7918-7924.
- [40] Mincher, B.J., Modolo, G., Mezyk, S.P., "Review article: The effects of radiation chemistry on solvent extraction: 1. Conditions in acidic solution and a review of TBP radiolysis", *Solvent Extr. Ion Exch.*, **2009**, 27, 1-25.
- [41] Mezyk, S.P., Mincher, B.J., Ekberg, C., Skarnemark, G., "Alpha and gamma radiolysis of nuclear solvent extraction ligands used for An(III) and Ln(III) separations", *J. Radioanal. Nucl. Chem.*, **2013**, 296, 711-715.
- [42] Shoesmith, D.W., King, F., *The Effects of Gamma Radiation on the Corrosion of Candidate Materials for the Fabrication of Nuclear Waste Packages*, Atomic Energy of Canada Limited Report, AECL-11999, July 1999.
- [43] Sunder, S., Shoesmith, D.W., Miller, N.H., "Oxidation and dissolution of nuclear fuel (UO₂) by the products of the alpha radiolysis of water", *J. Nucl. Mater.*, **1997**, 244, 66-74.
- [44] Harms, A.A. *An Introduction to the CANDU Nuclear Energy Conversion System*, McMaster University: Hamilton, ON, 1975.
- [45] *CANDU 6 Technical Summary*, Atomic Energy of Canada Limited, May 2005.
- [46] *BWR-6 General Description of a Boiling Water Reactor*, General Electric Nuclear Energy Group: San Jose, 1980.
- [47] *Nuclear Reactor Concepts Manual - Rev 0200*, United States Nuclear Regulatory Commission: USNRC Technical Training Center.

- [48] *BWR Water Chemistry Guidelines - 2008 Revision*, EPRI, Palo Alto, CA, Report 1016579, October 2008.
- [49] *Pressurized Water Reactor Primary Water Chemistry Guidelines: Revision 7*, EPRI, Palo Alto, CA, Report 3002000505, April 2014.
- [50] Turner, C.W., Guzonas, D., Burton, G.R., Deaconescu, R., Wei, X., Angell, P., *Chemistry Control Design Guide for Pressurized Heavy Water CANDU Reactors*, Atomic Energy of Canada Limited Report, 95-03081-DM-001, November 2004.
- [51] Stuart, C.R., Reid, V., Turner, C.W. "Optimization of Chemistry Control in the Primary Heat Transport System of CANDU Reactors" In *Proceedings of the International Conference on Water Chemistry of Nuclear Reactor Systems Jeju Island, Korea*, 2006.
- [52] Cook, W.G., Olive, R.P., "Pourbaix diagrams for the iron–water system extended to high-subcritical and low-supercritical conditions", *Corros. Sci.*, **2012**, *55*, 326-331.
- [53] Tremaine, P.R., LeBlanc, J.C., "The solubility of magnetite and the hydrolysis and oxidation of Fe^{2+} in water to 300°C", *J. Solution Chem.*, **1980**, *9*, 415-442.
- [54] Machet, A., Galtayries, A., Zanna, S., Klein, L., Maurice, V., Jolivet, P., Foucault, M., Combrade, P., Scott, P., Marcus, P., "XPS and STM study of the growth and structure of passive films in high temperature water on a nickel-base alloy", *Electrochim. Acta*, **2004**, *49*, 3957-3964.
- [55] Cook, W.G., Olive, R.P., "Pourbaix diagrams for the nickel-water system extended to high-subcritical and low-supercritical conditions", *Corros. Sci.*, **2012**, *58*, 284-290.
- [56] Maurice, V., Yang, W.P., Marcus, P., "X-ray photoelectron spectroscopy and scanning tunneling microscopy study of passive films formed on (100) Fe-18Cr-13Ni single-crystal surfaces", *J. Electrochem. Soc.*, **1998**, *145*, 909-920.
- [57] Massoud, T., Maurice, V., Klein, L.H., Seyeux, A., Marcus, P., "Nanostructure and local properties of oxide layers grown on stainless steel in simulated pressurized water reactor environment", *Corros. Sci.*, **2014**, *84*, 198-203.
- [58] Knapp, Q.W., Wren, J.C., "Film formation on type-316L stainless steel as a function of potential: Probing the role of gamma-radiation", *Electrochim. Acta*, **2012**, *80*, 90-99.
- [59] *Corrosion Potential (ECP) Measurement Sourcebook*, EPRI, Palo Alto, CA, Report NP-7142, January 1991.
- [60] Indig, M.E., Nelson, J.L., "Electrochemical measurements and modeling predictions in boiling water reactors under various operating conditions", *Corrosion*, **1991**, *47*, 202-209.
- [61] Cowan, R.L., Indig, M.E., Kass, J.N., Law, R.J., Sundberg, L.L. "Experience with hydrogen water chemistry in boiling water reactors", Fourth International Conference on Water Chemistry of Nuclear Systems, Bournemouth, U.K., 1986.
- [62] Molander, A., Pein, K., Tarkpea, P., Takagi, J., Karlberg, G., Gott, K. "Comparison of the corrosion potential for stainless steel measured in-plant and in laboratory during BWR normal water chemistry conditions", JAIF international conference on water chemistry in nuclear power plants, Kashiwazaki, Japan, 1998, p 412-418.

- [63] Bartels, D.M., Henshaw, J., Sims, H.E., "Modeling the critical hydrogen concentration in the AECL test reactor", *Radiat. Phys. Chem.*, **2013**, 82, 16-24.
- [64] Kanjana, K., Haygarth, K.S., Wu, W., Bartels, D.M., "Laboratory studies in search of the critical hydrogen concentration", *Radiat. Phys. Chem.*, **2013**, 82, 25-34.
- [65] Pastina, B., Isabey, J., Hickel, B., "The influence of water chemistry on the radiolysis of the primary coolant water in pressurized water reactors", *J. Nucl. Mater.*, **1999**, 264, 309-318.
- [66] Stuart, C.R., *Radiation Chemistry Manual - Revision 2*, CANDU Owners Group Inc. Report, COG-02-4022 R1, 153-127160-COG-007, October 2010.
- [67] McCracken, D.R., Rasewych, J.B., Shorter, W.R., *Studies of Coolant Radiolysis and Boiling in the NRU Reactor*, CANDU Owners Group Inc. Report, Atomic Energy of Canada Limited, COG-89-046 September 1989.
- [68] Allen, A.O., Hochanadel, C.J., Ghormley, J.A., Davis, T.W., "Decomposition of water and aqueous solutions under mixed fast neutron and γ -radiation", *J. Phys. Chem.*, **1952**, 56, 575-586.
- [69] Glowa, G.A., Stuart, C.R., *A Radiolysis Model to Investigate the Production of Hydrogen in the End Shield Cooling System*, CANDU Owners Group Inc. Technical Note, TN-04-4010, January 2005.
- [70] Stuart, C.R., Li, H., Glowa, G.A., Searle, H., Webb, D.G., *Hydrogen Production in the End Shield Cooling System*, CANDU Owners Group Inc. Report, COG-05-4002, September 2005.
- [71] Wright, J., Linacre, J.K., Marsh, W.R., Bates, T.H. "Effect of Radiation on Heterogeneous Systems of Air or Nitrogen and Water" In *Proceedings of the International Conference on the Peaceful Uses of Atomic Energy*, United Nations: Geneva, 1955, Vol. 7, p 560-563.
- [72] Jones, A.R., "Radiation-induced reactions in the N_2 - O_2 - H_2O system", *Radiat. Res.*, **1959**, 10, 655-663.
- [73] Linacre, J.K., Marsh, W.R., *The Radiation Chemistry of Heterogeneous and Homogeneous Nitrogen and Water Systems*, Atomic Energy Research Establishment Harwell Report, AERE-R-10027, June 1981.
- [74] Gray, W.J., McVay, G.L., "Nitric acid formation during gamma irradiation of air/water mixtures", *Radiation Effects*, **1985**, 89, 257-262.
- [75] Christensen, H., *The Radiolysis of Aqueous Solutions of Ammonia and Nitrogen: A Literature Review*, Studsvik Technical Report, Studsvik, STUDSVIK-E2-79-23, 1979.
- [76] Etoh, Y., Karasawa, H., Ibe, E., Sakagami, M., Yasuda, T., "Radiolysis of N_2 - H_2O systems", *J. Nucl. Sci. Technol.*, **1987**, 24, 672-674.
- [77] Ibe, E., Karasawa, H., Nagase, M., Utamura, M., Uchida, S., "Behaviour of nitrogen compounds in radiation field and nuclear reactor system", *J. Nucl. Sci. Technol.*, **1989**, 26, 760-769.
- [78] Karasawa, H., Ibe, E., Uchida, S., Etoh, Y., Yasuda, T., "Radiation induced decomposition of nitrogen", *Radiat. Phys. Chem.*, **1991**, 37, 193-197.
- [79] Stuart, C.R., Wright, M.D., Mancey, D.S. "Corrosion Control for the NRU Reactor Vessel", Nuclear Plant Chemistry Conference (International Conference on Water Chemistry of Nuclear Reactor Systems), Quebec City, 2010, p 929.

- [80] Wilkin, B.G., "NRU Reactor Vessel Repair", Technical Session 3: Research Reactor Modifications, Knoxville, TN. http://neutrons.ornl.gov/conf/TRTR_IGORR/TechnicalSessions/5_Tech%20Session%203_Research%20Reactor%20Mods/Wilkin_NRU%20Repair.pdf, Sept. 19-23, 2010.

CHAPTER 2 EXPERIMENTAL PRINCIPLES AND DETAILS

The following chapter summarizes the analytical techniques and imaging methods that were used for the work presented in this thesis. General experimental procedures common to all research chapters are also described. Any deviations or extensions of these techniques are outlined in the experimental sections of later research chapters as necessary.

2.1 ANALYTICAL AND IMAGING METHODS

2.1.1 UV-Visible (UV-Vis) Spectrophotometry

UV-Visible (UV-Vis) spectrophotometry was used to determine the aqueous concentrations of radiolysis products (e.g., H_2O_2 , NO_2^- , NO_3^- , Fe^{2+} , Fe^{3+}). In this technique, electrons in the target molecule are electronically excited by the absorption of light, and the wavelength of light absorbed corresponds to the energy difference of the transition [1,2]. The amount of light absorbed by a sample solution at a given wavelength is related linearly to the concentration of the target molecule in the sample solution by the Beer-Lambert law (Equation E2.1):

$$A = \log \frac{I_0}{I} = \epsilon lc \quad \text{E2.1}$$

where, ϵ is the molar absorption coefficient for the target molecule at a given wavelength and in a given solvent, l is the path length of the light through the absorbing solution, and c is the concentration of the target molecule in the solution.

A quartz cuvette, which does not absorb light in the visible, ultraviolet or near infrared regions, is filled with a sample of the aqueous solution and placed into the spectrophotometer. The spectrophotometer generates an absorbance spectrum by measuring the light intensity after the beam has passed through the absorbing solution (I) in comparison to the incident intensity of the beam (I_0) as the wavelength of the light is changed (typically from 300-2500 nm). The incident beam intensity is obtained by scanning a reference solution (a solution of identical solvent and matrix composition, but absent the target molecule) under the same conditions. The light intensity is often

measured by a photomultiplier tube, particularly when a scanning mode is used for absorption measurements.

While some chemical species may have distinctive UV-Vis absorption spectra that can be followed directly (e.g., dissolved Fe^{3+}), others require the target molecule to be chemically modified (either by formation of a chemical complex or by a chemical reaction to form a different UV-Vis active species) in order to observe strong absorption in the UV-Visible region.

2.1.2 Gas Chromatography

Gas chromatography (GC) is an analytical technique that can be used to separate and quantify the chemical components of a gaseous mixture [2]. Following injection of a sample into the gas chromatograph inlet, the vaporized sample is introduced to a capillary column that is coated with a thin layer of adsorbent material (stationary phase). The flow of an inert carrier gas (mobile phase) transports the gas sample through the column, where the volatile components become separated by their differential partitioning between the mobile and stationary phases. For a given set of operational parameters (e.g., column temperature, carrier gas flow rate), the separated gaseous components will be eluted off the column at defined times. Hence, the quantity of a particular gaseous species in a sample mixture can be determined from the magnitude of the signal detected at the characteristic elution time for that species.

While many different detectors can be used in combination with GC separation techniques, the selection of a detector is often influenced by the gaseous species that are of interest in the experiment and the carrier gas of the system. For example, a thermal conductivity detector (TCD) is non-selective and functions by observing changes in the rate of heat loss across a filament as it is exposed to the column effluent. However, to induce a noticeable change in the rate of heat loss, an eluted analyte gas must have a different thermal conductivity than that of the reference carrier gas. As a result, a GC system equipped with a TCD detector and using a nitrogen carrier gas can effectively detect H_2 , but is less reliable for O_2 (the thermal conductivities for N_2 , H_2 , and O_2 are 26.0, 186.6, and 26.5 $\text{mW}\cdot\text{m}^{-1}\cdot\text{K}^{-1}$ at 300 K [3]). Instead, the high electron affinity of oxygen facilitates its measurement by an electron capture detector (ECD). For the

radiolysis experiments described in this thesis, hydrogen and oxygen are the primary volatile species produced, and a GC with both a TCD and a ECD was used.

2.1.3 Transmission Electron Microscopy (TEM)

Transmission electron microscopy (TEM) is an imaging technique that uses a high energy electron beam to study the microstructure of a sample [4]. Since TEM uses electrons instead of light to probe the sample material, very thin samples (typically 20-200 nm) must be used and the analysis must be performed under vacuum to allow a sufficient flux of electrons through the sample for detection. For specimens with sufficiently small dimensions (e.g., nanoparticles), TEM samples can be prepared by depositing a dilute solution of the specimen onto TEM support grids. These grids can be loaded onto a stage and placed into the focus of the microscope for analysis.

Within the microscope, an electron source (cathode) emits electrons that are subsequently accelerated until their kinetic energy is sufficiently high to pass through the thin sample. Most TEM instruments operate at electron energies of 100-300 keV. The electron beam focus and magnification is adjusted with two condenser lenses while the alignment of the beam is controlled by magnetic coils. Similar to light microscopes where image resolution is limited by the wavelength of the source photons, TEM resolution is limited by the de Broglie wavelength of the electrons. Hence, in comparison to light microscopes, much higher resolution images can be obtained by TEM owing to the small de Broglie wavelength of electrons.

Bright field imaging is the most common operation mode for TEM. In this mode, the aperture is placed so that the direct electron beam can pass through it, and the contrast of the image is determined by the level of interaction of incident electrons with different areas of the sample. Thicker regions of the sample or regions enriched with higher atomic number elements will obstruct the beam more and appear darker, while regions with no sample present, where the sample is thinner, or where the sample is comprised of lower atomic number constituents will allow for higher electron flux and appear brighter in the image.

2.1.4 Selected Area Electron Diffraction (SAED)

While the conventional TEM bright field imaging mode provides detailed information regarding the morphology and microstructure of a given sample, the operation of a TEM in selected area electron diffraction (SAED) mode can provide crystal structure and composition information. The wave nature of electrons allows for interference patterns to be produced as electrons are scattered due to interactions with a sample material. If the material has a crystalline and periodic structure, the scattering occurs in a predictable manner, and yields a diffraction pattern that is characteristic of the material. Single crystals can produce highly resolved spot patterns, while amorphous crystallites usually produce ring patterns due to variations in their orientations.

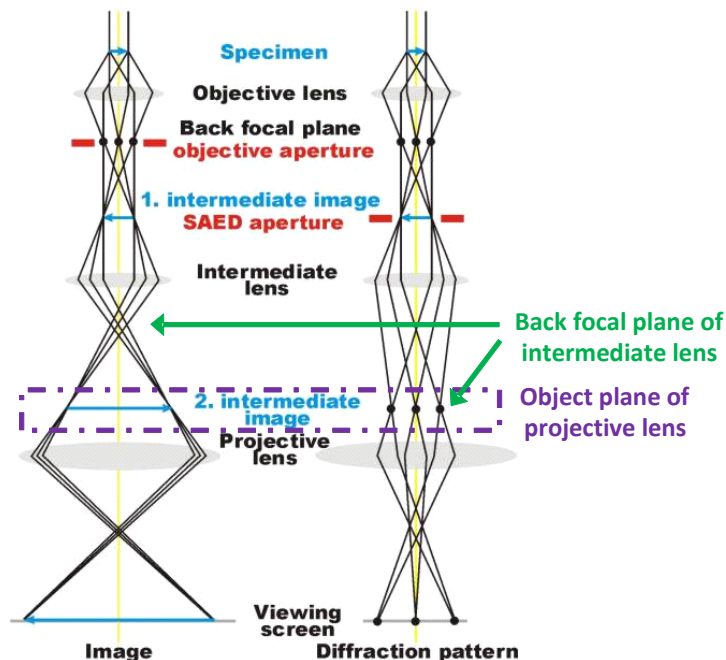


Figure 2.1: Differences in the imaging (left) and electron diffraction (right) modes for a transmission electron microscope.

In bright field mode, the intermediate image is displayed in the object plane of the projective lens, and hence an image of the sample is projected to the viewing screen (left image of Figure 2.1) [4,5]. To view the electron diffraction pattern arising from a TEM

sample, the imaging system lenses are adjusted. The intermediate lens is weakened (its focal length is made larger) such that its back focal plane coincides with the object plane of the projective lens, and the diffraction pattern is displayed on the viewing screen (Figure 2.1, right). SAED patterns can be obtained from localized regions of the sample by inserting a selected area diffraction aperture into the object plane of the intermediate lens. Hence, local structural information can be obtained for different regions of the sample.

2.1.5 Scanning Electron Microscopy (SEM)

Scanning electron microscopy (SEM) is a surface analysis technique used to investigate topography. A high resolution electron beam is directed onto the sample surface and the scattered electrons are detected [2,4]. Similar to TEM, the system is operated under vacuum to allow the electrons (both incident and secondary) to pass from the source to the sample and from the sample to the detector without excess loss due to interactions with gaseous molecules. The system includes an electron source and one or two condenser lenses to focus the beam to a small focal spot (< 10 nm in diameter). Typically, the incident electrons are accelerated to energies between 1 and 40 keV. Two pairs of deflector plates or scanning coils are then used to deflect the beam and complete a raster scan of a rectangular area of the sample surface; one pair deflects the electron beam in the x-direction across the sample, and the other deflects the beam in the y-direction. Hence, the entire selected region can be irradiated by electrons by rapidly moving the beam.

Atoms on or near the surface of the sample can interact with the incident electrons. This can result in electrons being ejected from the sample and the emission of X-rays characteristic to the elemental species from which they originate. The electron ejection process is exploited by SEM. These electrons are termed secondary electrons and are lower in energy than those of the incident beam. Only electrons ejected from the top few nanometers of the sample surface will have sufficient energy to escape the sample matrix and reach the detector. Similarly, secondary electrons originating from higher topographical points on the sample surface (which are closer to the detector) are more likely to be detected than electrons from lower topographical regions. The

differences in electron flux arising from the topographical morphology of the sample lead to contrast formation in the image and provide depth perspective in the micrograph image.

2.1.6 Energy Dispersive X-ray (EDX) Spectroscopy

Energy dispersive X-ray spectroscopy (EDX) is frequently coupled with SEM as an elemental analysis technique and takes advantage of the X-ray emission that can occur when samples interact with a high energy electron beam. As described above, when a sample material is exposed to the electron beam, atoms at the near-surface can become ionized. When an inner shell electron is ejected, an electron from a higher energy outer shell can fill the electron hole. This can result in the emission of an X-ray photon with an energy equal to the potential energy difference between the two electron shells. Hence, each elemental species has characteristic X-ray emission energies. Furthermore the energies of the electron shells can be influenced by the chemical environment of an atom (e.g., its oxide structure). EDX can provide compositional information of the near-surface on the micrometer scale (the primary electron beam can penetrate to depths of $> 1\mu\text{m}$ in the sample, depending on the incident electron energy and the atomic nature of the sample material) [2].

2.1.7 X-Ray Photoelectron Spectroscopy (XPS)

X-ray photoelectron spectroscopy (XPS) is a quantitative spectroscopic technique that can provide the elemental composition, and chemical and electronic state information that exist within the outer surface layers (first 10 nm) of a material [2]. With the exception of hydrogen and helium, all elements in the periodic table can be detected by this technique. An XPS spectrum is obtained by irradiating a material with X-rays and measuring the number of photoelectrons that are ejected and their kinetic energies. The absorption of an X-ray (of known energy, $h\nu$) by an atom on the material surface leads to the ejection of a single electron from a core or valence shell. The kinetic energy (KE) of the emitted photoelectron is measured by the spectrometer. The binding energy of the photoelectron (BE), which is characteristic of the atom and orbital from which the electron originates, can then be calculated by means of the equation [2]:

$$KE = h\nu - BE - \Phi$$

E2.2

where Φ is the work function of the spectrometer.

A typical XPS spectrum is a plot of the measured photoelectron intensity as a function of the binding energy of the detected electrons. Each element produces a set of XPS peaks at characteristic binding energy values. For a given element (e.g., iron), the varying binding energies can be useful in determining the oxidation states and bonding environments present. The areas of the peaks can be related to the amount of a particular element within the sample volume that is irradiated.

2.1.8 Fourier Transform Infrared (FTIR) Spectroscopy

Fourier transform infrared (FTIR) spectroscopy is an effective analytical tool to probe the bulk molecular (or crystal) structures in a sample. An infrared spectrum of a sample is made by passing a beam of infrared light through a sample (or reflecting off of the surface of the sample) and measuring the observed transmittance of light that occurs at each excitational wavelength. Compared to a typical dispersive spectrometer design that measures absorption intensities while scanning only a narrow range of excitation wavelengths at a time, FTIR spectrometers expose the sample to a wide range of IR frequencies simultaneously. The broadband light source is split by the interferometer which is comprised of a stationary mirror and a moving mirror. As the mirror configuration is changed, the intensities of the different wavelengths of light change at different times due to wave interference [2,6]. Hence, the beam exiting the interferometer has a different spectral distribution with each change in configuration. The intensity information over all the mirror configurations is collected as an interferogram, and a Fourier transform mathematical process is required to convert the data into a recognizable spectrum.

This absorption spectroscopic technique utilizes light in the mid-IR region (400-4000 cm^{-1} , 25000-2500 nm). These IR photons have frequencies of comparable magnitude to the vibrational frequencies that occur in molecules, such as stretching and bending vibrations between bonded atoms. Hence, for a given chemical bond, the

frequency (energy) of the IR photon that it absorbs will match the frequency of the vibration of that bond [2,6]. However, for a vibrational mode in a molecule to be IR active, it must induce a change in the dipole moment of the molecule. The vibrational frequency depends on the bond strength and the masses of the atoms participating in the vibration, and can be further modulated by the extended chemical environment [6]. As a result, peaks present in an IR spectrum for a molecule can be correlated to the specific bonds and functional groups that it contains. The typical fingerprinting region for bond vibrational frequencies in IR spectra spans $500\text{-}1500\text{ cm}^{-1}$.

2.1.9 Raman Spectroscopy

Similar to FTIR spectroscopy, Raman spectroscopy provides information about the vibrational modes of molecules, and hence can qualitatively describe the chemical composition of materials. However, there are several differences between the techniques. Raman spectroscopy is a scattering technique that detects changes in the polarizability of the electron cloud surrounding a molecule following an interaction with light [2,7]. An intense monochromatic light source is used to excite electrons into a virtual energy state. As the molecule relaxes back to a lower energy state, a photon is released. This excitation and decay process can result in both elastically and inelastically scattered photons. The majority of interactions will be elastic scattering, termed Rayleigh scattering, where the molecule quickly relaxes to its initial vibrational state and the scattered photon has the same energy as the incident photon. However, a small fraction of the interactions between the incident light and the molecule will result in a net change in the vibrational state of the molecule. In this inelastic process the scattered photon has a different energy than the incident photon, with the energy difference corresponding to the energy of the net vibrational state transition in the molecule. The low probability of inelastic scattering in comparison to elastic scattering requires the use of a high intensity light source, such as a laser, to improve the signal strength of scattered photons [2,7].

The difference in energy between the incident and scattered light leads to a shift in the frequency of the scattered light (ν') away from the excitation frequency (ν''). The relationship is given by Equation E2.3 [2,7]:

$$h\nu'' = h\nu' \pm \Delta E_{\text{vibration}} \quad \text{E2.3}$$

where h is Planck's constant and $\Delta E_{\text{vibration}}$ is the energy gap between the initial and final vibrational states. For excited molecules that relax from their virtual energy state to a vibrational level that is higher than their initial vibrational state (net vibrational excitation), the scattered photon has less energy than the incident particle. This inelastic process is referred to as Stokes scattering. Conversely, if the molecule was initially in a high vibrational energy state prior to excitation and is then returned to a lower energy vibrational state, the scattered photon has more energy than the incident light, and this is referred to as Anti-Stokes scattering. The ratio of Stokes to Anti-Stokes scattering is proportional to temperature, as regulated by the Boltzmann distribution that defines the equilibrium populations of the target molecules in different vibrational states. Furthermore, the probability of a molecule encountering a change in its vibrational state of more than one unit ($\Delta v > 1$) is low. As a result, a Raman spectrum for a sample measured at room temperature is dominated by Stokes scattering of the vibrational state transition $v = 0$ to $v = 1$ [2,7].

2.2 GENERAL EXPERIMENTAL DESIGN AND SET-UP

2.2.1 Solution Preparation and Degassing

All experimental solutions were prepared daily using purified water with a measured resistivity of 18.2 M Ω ·cm from a NANOpure Diamond UV ultrapure water system (Barnstead International). The pH was adjusted to either pH 6.0 or pH 10.6 using sulfuric acid or sodium hydroxide. Experiments at pH 6.0 were performed without the addition of any buffer, and those at pH 10.6 used a phosphate buffer (1×10^{-3} mol·dm $^{-3}$). The pH of the solution was measured prior to and at the end of the irradiation period using a pH meter (Accumet).

Deoxygenated solutions were prepared by purging a bulk solution with ultra high purity argon (impurity < 0.001%) for more than 1 h. The solution was then transferred into an Ar-purged glove box, where the atmospheric oxygen concentration was maintained below 1000 ppm. The desired sample volume of the deoxygenated solution

was then transferred into 20 mL glass vials, and the vials were sealed with aluminum crimp caps with PTFE silicone septa (Agilent Technologies) that provided a vacuum seal to prevent loss of gaseous species during irradiation. For aerated solutions, a bulk solution was saturated with hydrocarbon free air (Praxair) for more than 1 h. Each individual vial was then pre-capped and saturated for 10 min with the hydrocarbon free air before the saturated solution was transferred into the 20 mL vial with a syringe. Pressure increase in the vial was avoided by removing the displaced gas with the transfer syringe.

2.2.2 Irradiation Technique

All irradiations were carried out in a ^{60}Co gamma cell (MDS Nordion, Model 220), Figure 2.2b, which contains aluminum-encapsulated ^{60}Co pencils ($\gamma = 1.17$, 1.33 MeV) that are aligned in a cylindrical array. Lead shielding surrounds the exterior of the irradiation chamber to reduce the dose rate to personnel. The loading chamber (visible at the top of Figure 2.2b) descends into the irradiation chamber by a vertical lift. A digital timer is programmed to terminate the radiation exposure by returning the loading chamber to its raised position after the time setpoint has been reached.

For the experiments presented in this thesis, the sample vials were placed in a custom designed sample holder such that each vial was located equidistant from the cylindrical edge of the irradiation chamber, Figure 2.2a. This ensured a uniform absorption dose rate for all samples throughout the irradiation period. Individual vials were removed from the irradiation chamber at regular time intervals to allow for gas and liquid phase analysis.

Over time, the source strength of the ^{60}Co pencils decreases (^{60}Co $t_{1/2} = 5.27$ years) and the absorption dose rate to the irradiated solutions also decreases with time. Over the time frame of the experiments documented in this thesis, the dose rate varied from 2.5 to 1.3 $\text{Gy}\cdot\text{s}^{-1}$, as determined by Fricke Dosimetry [8,9].

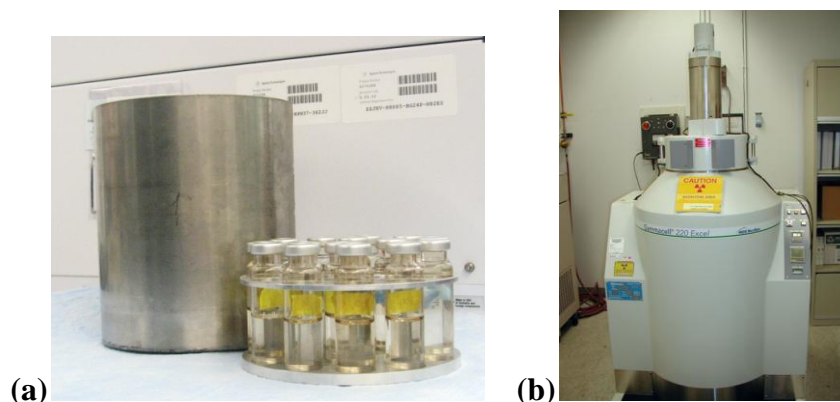


Figure 2.2: The sample vial holder (a) custom designed to fit into the irradiation chamber of the MDS Nordion 220 Gamma Cell (b).

2.2.3 Solution Analysis

The aqueous phase of each sample was analyzed by UV spectrophotometric methods. In all experiments, the concentration of the molecular radiolysis product hydrogen peroxide was measured. All spectrophotometric measurements were performed using a diode array UV spectrophotometer (BioLogic Science Instruments). The concentration of hydrogen peroxide was determined by the Ghormley tri-iodide method in which I^- is oxidized to I_3^- by H_2O_2 in the presence of an ammonium molybdate catalyst [10,11]. The I_3^- concentration was measured using UV spectrophotometry of the I_3^- absorption peak at 350 nm with a molar extinction coefficient of $25500 \text{ M}^{-1}\cdot\text{cm}^{-1}$ [12]. Using this method, the detection limit for $[H_2O_2]$ was $3 \times 10^{-6} \text{ mol}\cdot\text{dm}^{-3}$ and the uncertainties in the measurement arising from sampling and instrumental errors were estimated to be $\pm 0.2\%$ at the lower end of the measured concentration range and $\pm 0.05\%$ at the higher end of the measured range. The H_2O_2 analysis was performed immediately after removal of a vial from the gamma-irradiation cell to minimize any thermal decomposition of H_2O_2 in the sample vials.

Additional UV spectrophotometric methods used to analyze solutions from radiolysis experiments with chemical additives are described in individual chapters focused on each specific additive.

2.2.4 Gas Composition Analysis

Gas sampling was carried out by extracting a gas sample from the test vial headspace using a gas-tight syringe with a Luer lock valve (Agilent Technologies). For test solutions that were irradiated with no headspace volume, an additional preparation step was required. Half (10 mL) of the test solution was removed from the test vial. This vial was aggressively shaken and left standing for 5 minutes prior to gas sampling to allow any dissolved gases to equilibrate between the aqueous and gas phases.

Gas samples were injected through a septum into the sample loop of a Gas Chromatography (GC) system equipped with a 60 m GS-GASPRO column of 0.32 μm diameter (6580, Agilent Technologies). The column was connected to three detectors: a thermal conductivity detector (TCD), μ -electron capture detector (ECD), and a mass selective detector (MSD) (not used for analysis here) [13]. Quantification of the amount of hydrogen and oxygen in the cover gas of irradiated sample solutions was performed using the TCD and ECD detectors, respectively. Nitrogen was used as the carrier gas at a flow rate of 4.6 mL/min, and the detectors were calibrated biweekly by injecting certified gas mixtures with concentrations ranging from 0.1 to 5% v/v H_2 and 1 to 35% O_2 (Praxair). The corresponding aqueous H_2 concentration was calculated from the measured gas phase concentration using the known aqueous-gas partition coefficient for H_2 , $[\text{C}_{\text{aq}}]/[\text{C}_{\text{g}}] = 0.019$ at 25°C, a variation of the Henry's constant value of 7.8×10^{-4} [14,15].

While the analysis of oxygen was performed for all experiments, minimizing the introduction of atmospheric oxygen during sampling proved extremely difficult. As a result, accurate quantification of low concentrations of oxygen was not possible. Instead, only qualitative trends in oxygen production were used to support other collected data.

2.3 THE RADIOLYSIS KINETIC MODEL

Computer modeling of chemical systems is a tool that can be used to aid in the understanding of mechanistic processes, as well as to guide further experimental research. Kinetic analysis, when used in combination with experimental results, can provide a means of deducing key reaction pathways in a chemical system and interpreting experimentally observed trends. Once validated under a large range of conditions, a

kinetic model can also be used to predict system behavior with time as a function of different parameters, such as pH, aeration condition, or initial speciation. In essence, experimental and modeling results are inherently complementary; experimental data is required to validate the accuracy and comprehensiveness of the kinetic model, while the model is required to interpret the experimental data. As a result, assembling a robust kinetic model that can reproduce experimental trends over a wide range of conditions provides a measure of the overall mechanistic understanding of the chemical system.

As described in Chapter 1, the concentrations of water radiolysis products are highly interdependent due to the large number of reactions available for each chemical species and the links between species. To model the long-term radiolysis kinetics (the changes in radiolysis product concentrations with time), the assembled reaction set must include all relevant reactions and their respective rate constants. The basic room temperature water radiolysis kinetic model, previously compiled and reported in References [16] and [13], consists of ~ 40 elementary homogeneous reactions. These include the primary production of water radiolysis products, subsequent aqueous phase reactions of the radiolysis products with each other, hydrolysis reactions and related acid-base equilibria (Table 2.1). (Note that some reactions previously considered in Chapter 1 have been renumbered in Table 2.1 for consistency.

In the basic water radiolysis model, the rate of production of species i (in units of $\text{mol}\cdot\text{dm}^{-3}\cdot\text{s}^{-1}$) by radiolysis is modeled as a zeroth order process using the homogeneous primary radiolysis yields (G-values) and the rate of radiation energy deposition:

$$\left[\frac{d[i]}{dt}\right]_{\text{Primary Production}} = D_R \cdot (1.036 \times 10^{-7} \cdot G_i) \cdot \rho \quad \text{E2.4}$$

where D_R is the absorbed radiation dose rate in the water in units of $\text{Gy}\cdot\text{s}^{-1}$ (or $\text{J}\cdot\text{kg}^{-1}\cdot\text{s}^{-1}$), G_i is the G-value for species i in units of molecules/100 eV, ρ is the density of the water in units of $\text{kg}\cdot\text{dm}^{-3}$, and the constant 1.036×10^{-7} provides for the conversion of units. (Note that for room temperature irradiations, the density of the aqueous phase will be approximately $1 \text{ kg}\cdot\text{dm}^{-3}$.) The early radiolysis processes that occur $< 100 \text{ ns}$ from the initial interaction of a radiation particle with a water molecule are not modeled here.

Instead, the homogeneous out-of-spur distribution of primary water radiolysis products is assumed to be the instantaneous result of irradiation.

As demonstrated in Table 2.1, the primary radiolysis species are chemically reactive, and each species can undergo numerous chemical reactions with other species in the aqueous phase. The overall rate of removal of species i from the aqueous phase by reaction can then be described by the sum of the classical chemical rate equations for the bimolecular reaction of species i with species j :

$$\left[\frac{d[i]}{dt}\right]_{Removal} = - \sum_j k_{ij} \cdot [i] \cdot [j] \quad \text{E2.5}$$

where k_{ij} is the 2nd order rate constant for the reaction of species i and j in units of $\text{mol}^{-1} \cdot \text{dm}^3 \cdot \text{s}^{-1}$. Similarly, species i may be produced in the aqueous phase due to the reaction of species l and m , where k_{lm} is the 2nd order rate constant:

$$\left[\frac{d[i]}{dt}\right]_{Production} = \sum_{l,m} k_{lm} \cdot [l] \cdot [m] \quad \text{E2.6}$$

The net change in the concentration of species i with time in an irradiated system can then be described as the overall sum of its production rates and its removal rates, and is given by Equation E2.7. However, for primary radiolysis products, the radiation production rate (E2.4) will far exceed the rate of production arising from subsequent chemical reactions in the aqueous phase (E2.6).

$$\frac{d[i]}{dt} = [D_R \cdot (1.036 \times 10^{-7} \cdot G_i) \cdot \rho] + \sum_{l,m} k_{lm} \cdot [l] \cdot [m] - \sum_j k_{ij} \cdot [i] \cdot [j] \quad \text{E2.7}$$

To follow the time-dependent concentration profiles for each radiolysis product, the overall rate equation (E2.7) must be constructed and solved for each individual species. Due to the size of the basic water radiolysis model reaction set, solving such a kinetic system manually is not practical. As well, the system of differential equations that comprises the model is termed a set of stiff differential equations which cannot be solved analytically. Instead, the commercially available software package, FACSIMILE,

was used to solve the set of stiff differential rate equations comprising the radiolysis model presented in this thesis by a numerical integration method [17].

The basic radiolysis model presented here does not contain any reactions associated with the radiolysis of water vapour (that would be present in a headspace for some test vials). The density of water molecules in the gas phase at room temperature is very low compared to the density of liquid water which justifies this simplification. This decision would need to be reconsidered for test conditions at much higher temperatures (where saturated water vapour pressures are much higher) or when the volume of the gas phase exposed to radiation is much greater than the volume of the aqueous phase. Neither circumstance is approached in the tests described here.

Although the reactions comprising the basic water radiolysis model are presented in detail in Table 2.1, relevant equations are restated in subsequent chapters for simplicity, and are renumbered in accordance with their appearance in those chapters.

Table 2.1: The G-values, reactions and rate constants, and equilibria that form the basic water radiolysis kinetic model.

γ-Radiation G-values (units of molecules/100 eV)				
<i>Radiolytic production reaction</i>			<i>G-value</i>	<i>Reaction</i>
H ₂ O	→	•e _{aq} ⁻	2.6	2.1a
H ₂ O	→	H ⁺	2.6	2.1b
H ₂ O	→	•H	0.6	2.1c
H ₂ O	→	•OH	2.7	2.1d
H ₂ O	→	H ₂	0.45	2.1e
H ₂ O	→	H ₂ O ₂	0.7	2.1f
Reactions and Rate Constants (mol⁻¹·dm³·s⁻¹ or s⁻¹)				
<i>Chemical reaction</i>			<i>Rate constant (25 °C)</i>	
•e _{aq} ⁻ + •e _{aq} ⁻ + 2H ₂ O	→	H ₂ + 2OH ⁻	5.5 × 10 ⁹	2.2
•e _{aq} ⁻ + •H + H ₂ O	→	H ₂ + OH ⁻	2.5 × 10 ¹⁰	2.3
•e _{aq} ⁻ + •OH	→	OH ⁻	3.0 × 10 ¹⁰	2.4
•e _{aq} ⁻ + O ₂	→	•O ₂ ⁻	2.22 × 10 ¹⁰	2.5
•e _{aq} ⁻ + H ₂ O ₂	→	OH ⁻ + •OH	1.6 × 10 ¹⁰	2.6
•e _{aq} ⁻ + HO ₂ •	→	HO ₂ ⁻	1.3 × 10 ¹⁰	2.7
•e _{aq} ⁻ + HO ₂ ⁻	→	•O ⁻ + OH ⁻	3.5 × 10 ⁹	2.8
•e _{aq} ⁻ + •O ⁻ + H ₂ O	→	OH ⁻ + OH ⁻	2.2 × 10 ¹⁰	2.9
•H + •OH	→	H ₂ O	7 × 10 ⁹	2.10
•H + •H	→	H ₂	7.75 × 10 ⁹	2.11
•H + O ₂	→	HO ₂ •	2.1 × 10 ¹⁰	2.12

$\bullet\text{H} + \text{HO}_2\bullet$	\rightarrow	H_2O_2	1.0×10^{10}	2.13
$\bullet\text{H} + \text{H}_2\text{O}_2$	\rightarrow	$\bullet\text{OH} + \text{H}_2\text{O}$	9.0×10^7	2.14
$\bullet\text{H} + \bullet\text{O}_2^-$	\rightarrow	HO_2^-	2.0×10^{10}	2.15
$\bullet\text{H} + \text{H}_2\text{O}$	\rightarrow	$\text{H}_2 + \bullet\text{OH}$	$1.1 \times 10^{11}[\text{H}_2\text{O}]$	2.16
$\bullet\text{OH} + \bullet\text{OH}$	\rightarrow	H_2O_2	5.5×10^9	2.17
$\bullet\text{OH} + \text{H}_2\text{O}_2$	\rightarrow	$\text{HO}_2\bullet + \text{H}_2\text{O}$	2.7×10^7	2.18
$\bullet\text{OH} + \text{H}_2$	\rightarrow	$\text{H}\bullet + \text{H}_2\text{O}$	4.2×10^7	2.19
$\bullet\text{OH} + \bullet\text{O}_2^-$	\rightarrow	$\text{OH}^- + \text{O}_2$	8×10^9	2.20
$\bullet\text{OH} + \text{HO}_2\bullet$	\rightarrow	$\text{H}_2\text{O} + \text{O}_2$	6×10^9	2.21
$\bullet\text{OH} + \text{HO}_2^-$	\rightarrow	$\text{HO}_2\bullet + \text{OH}^-$	7.5×10^9	2.22
$\bullet\text{OH} + \bullet\text{O}^-$	\rightarrow	HO_2^-	2.0×10^{10}	2.23
$\bullet\text{O}^- + \text{H}_2\text{O}_2$	\rightarrow	$\bullet\text{O}_2^- + \text{H}_2\text{O}$	2×10^8	2.24
$\bullet\text{O}^- + \text{H}_2$	\rightarrow	$\text{H}\bullet + \text{OH}^-$	8.0×10^7	2.25
$\bullet\text{O}^- + \text{HO}_2^-$	\rightarrow	$\bullet\text{O}_2^- + \text{OH}^-$	4.0×10^8	2.26
$\bullet\text{O}^- + \bullet\text{O}_2^-$	\rightarrow	$2\text{OH}^- + \text{O}_2$	6.0×10^8	2.27
$\bullet\text{O}^- + \text{O}_2$	\rightarrow	$\bullet\text{O}_3^-$	3.8×10^9	2.28
$\bullet\text{O}_3^-$	\rightarrow	$\text{O}_2 + \bullet\text{O}^-$	3.0×10^2	2.29
$\bullet\text{O}_3^- + \text{H}_2\text{O}_2$	\rightarrow	$\bullet\text{O}_2^- + \text{O}_2 + (\text{H}_2\text{O})$	1.6×10^6	2.30
$\bullet\text{O}_3^- + \text{HO}_2^-$	\rightarrow	$\bullet\text{O}_2^- + \text{O}_2 + \text{OH}^-$	8.9×10^5	2.31
$\bullet\text{O}_3^- + \text{H}_2$	\rightarrow	$\text{O}_2 + \text{H}\bullet + \text{OH}^-$	2.5×10^5	2.32
$\text{HO}_2\bullet + \bullet\text{O}_2^-$	\rightarrow	$\text{HO}_2^- + \text{O}_2$	8.9×10^7	2.33
$\text{HO}_2\bullet + \text{HO}_2\bullet$	\rightarrow	$\text{H}_2\text{O}_2 + \text{O}_2$	2.0×10^6	2.34
H_2O_2	\rightarrow	$\bullet\text{OH} + \bullet\text{OH}$	2.3×10^{-7}	2.35

Related Equilibria and their Equilibrium Constants				
<i>Equilibria</i>			K_{eq}	
$H^+ + OH^-$	\rightleftharpoons	H_2O	1.78×10^{-16}	2.36
$H^+ + HO_2^-$	\rightleftharpoons	H_2O_2	1.6×10^{-12}	2.37
$H^+ + \bullet O_2^-$	\rightleftharpoons	$HO_2\bullet$	1.5×10^{-5}	2.38
$H^+ + \bullet O^-$	\rightleftharpoons	$\bullet OH$	1.6×10^{-12}	2.39
$H^+ + \bullet e_{aq}^-$	\rightleftharpoons	$\bullet H$	$k_{2.40f} = 2.25 \times 10^{10}$ $k_{2.40b} = 0.63 \times 10^1$	2.40

2.4 REFERENCES

- [1] Faust, C.B. *Modern Chemical Techniques*, 3rd ed., Royal Society of Chemistry: London, 1997.
- [2] Skoog, D.A., Holler, F.J., Crouch, S.R. *Principles of Instrumental Analysis*, 6th ed., Thomson Brooks/Cole: Belmont, CA, 2007.
- [3] *CRC Handbook of Chemistry and Physics*; 94th ed., Haynes, W.M., Bruno, T.J., Lide, D.R., Eds., CRC Press, Inc.: Boca Raton, FL., 2013.
- [4] Egerton, R.F. *Physical Principles of Electron Microscopy: An Introduction to TEM, SEM, and AEM*, Springer: New York, 2005.
- [5] Williams, D.B., Carter, C.B. *Transmission Electron Microscopy: A Textbook for Materials Science*, Plenum Press: New York, 1996.
- [6] Smith, A.L. *Applied Infrared Spectroscopy: Fundamentals, Techniques, and Analytical Problem-Solving*, Wiley-Interscience: New York, 1979.
- [7] Smith, E., Dent, G. *Modern Raman Spectroscopy - A Practical Approach*, John Wiley & Sons: West Sussex, England, 2005.
- [8] Spinks, J.W.T., Woods, R.J. *An Introduction to Radiation Chemistry*, 3rd ed., Wiley-Interscience: New York, 1990.
- [9] Upadhyay, S.N., Ray, N.K., Goel, H.C., "Dose distribution inside Gamma Cell 5000", *Indian J. Nucl. Med.*, **2002**, 17, 35-41.
- [10] Hochanadel, C.J., "Effects of cobalt γ -radiation on water and aqueous solutions", *J. Phys. Chem.*, **1952**, 56, 587-594.
- [11] Allen, A.O., Davis, T.W., Elmore, G., Ghormley, J.A., Haines, B.M., Hochanadel, C.J., Oak Ridge National Laboratory Report, Oak Ridge National Laboratory, ORNL-130, 1949.
- [12] Stefanic, I., LaVerne, J.A., "Temperature dependence of the hydrogen peroxide production in the gamma-radiolysis of water", *J. Phys. Chem. A*, **2002**, 106, 447-452.

- [13] Joseph, J.M., Choi, B.S., Yakabuskie, P.A., Wren, J.C., "A combined experimental and model analysis on the effect of pH and O₂(aq) on γ -radiolytically produced H₂ and H₂O₂", *Radiat. Phys. Chem.*, **2008**, 77, 1009-1020.
- [14] Gevantman, L.H. In *CRC Handbook of Chemistry and Physics*, 94th ed., Haynes, W.M., Bruno, T.J., Lide, D.R., Eds., CRC Press, Inc.: Boca Raton, FL., 2013.
- [15] Sander, R., "Compilation of Henry's Law Constants for Inorganic and Organic Species of Potential Importance in Environmental Chemistry", Rev. 3, [Online], <http://www.henrys-law.org/henry.pdf>, April 8, 1999.
- [16] Wren, J.C., Ball, J.M., "LIRIC 3.2 an updated model for iodine behaviour in the presence of organic impurities", *Radiat. Phys. Chem.*, **2001**, 60, 577-596.
- [17] *FACSIMILE Kinetic Modelling Software*, MCPA Software Ltd., 2003.

CHAPTER 3 THE EFFECT OF INTERFACIAL MASS TRANSPORT ON STEADY-STATE WATER RADIOLYSIS*

3.1 INTRODUCTION

Accurate understanding of the effects of ionizing radiation on nuclear reactor system chemistry and materials performance is important for assessment of various operational and maintenance requirements of nuclear power plants. Of particular concern is the chemistry driven by the radiolysis of water. Deposition of ionizing radiation into water leads to the formation of primary water radiolysis products as given in reaction 3.1:



The primary water radiolysis products differ considerably in their chemical reactivity and redox properties. The elementary reactions of the primary radiolysis products with each other and with other water-derived species have been studied extensively [1-4]. Pulse radiolysis studies have been extremely useful for establishing the primary radiolysis yields and the rates of fast free radical and ion reactions [5]. With a constant (or slowly changing) radiation source, radiation energy deposition is continuous, and the solution chemistry evolves towards a steady state in which the concentrations of radiolysis products differ substantially from the concentrations associated with the primary radiolysis yields. As described previously in Chapter 2, the long-term kinetics of radiolysis products can be described using classical chemical reaction rate and transport equations, where the concentration of a given species is determined by a balance between its radiolytic production and its removal by reactions with other species in the aqueous phase. It follows that the bulk phase chemical reaction rates (removal rates) are very sensitive to changes in the aqueous environment such as pH, temperature and chemical additives that can participate in acid-base equilibrium and redox reactions. Thus, while changes in aqueous environment, such as pH or the

* Reproduced in part with permission from Elsevier:

Yakabuskie, P.A., Joseph, J.M., Wren, J.C., "The effect of interfacial mass transfer on steady-state water radiolysis", *Radiat. Phys. Chem.*, **2010**, 79, 777-785.

presence of chemical additives at low concentrations, will not significantly affect the primary radiolysis yields, they can significantly influence the subsequent chemical reactions and alter the eventual steady-state species concentrations. For example, the concentrations of H_2 and H_2O_2 are more than two orders of magnitude greater in water with a pH of 10.6 compared to water with a pH of 6.0 following an extended period of γ -radiolysis, yet the primary yields for these species remain constant over this same pH range [6].

For most situations of practical interest, radiation fields are present on a continuous basis. Most corrosion processes, or other processes involving interfacial transport, have high activation energies and only occur substantially over long time periods. Hence, constant radiation fields will drive water radiolysis chemistry that can influence the corrosion of reactor structural materials over those time scales. To assess the impact of long-term radiolysis on corrosion requires that we understand and can predict the speciation and concentrations in water under steady-state conditions.

Water radiolysis produces two volatile species, H_2 and O_2 . In the presence of a headspace or cover gas volume, these species can transfer to the gas phase until equilibrium is established. Similarly, gases may transfer from the gas phase to the liquid phase when introduced into the blanketing cover gas. The impact of this aqueous-gas interfacial mass transfer on radiolysis driven chemistry has not been studied systematically. This is important because it can impact predictions of hydrogen gas generation, particularly if the headspace communicates with other gas volumes. Volumes of hydrogen in the gas phase are important because they represent a potential combustion hazard. Interfacial transfer of volatile species can also alter the aqueous phase concentrations, and because of the complex chemistry, affect the steady-state concentrations of the reactive species that are most important in controlling corrosion rates. Quantitative understanding of interfacial mass transfer and its connection to the aqueous state has another important application. Measurement of the amount of H_2 and O_2 in a gas sample is much simpler and more accurate than measurement of the quantities of these species dissolved in water. Under many extreme experimental conditions, as with online in-plant system chemistry monitoring, cover-gas analysis may be the only practical measurement that can be carried out.

This study examines the effect of interfacial transfer of the volatile radiolysis products H_2 and O_2 on steady-state water radiolysis chemistry by performing experiments using different gas-to-liquid volume ratios at various solution pH and cover gas compositions. The concentrations of the molecular water radiolysis products $H_2(g)$ and $H_2O_2(aq)$ were monitored as a function of irradiation time, and the experimental results were compared with computer simulations using a water radiolysis chemical kinetic model that includes the aqueous-gas phase transfer kinetics of the volatile species.

3.2 EXPERIMENTAL PROCEDURE

Aerated and deaerated solutions were prepared as described in detail in Section 2.2.1. To test the effects of mass transfer of radiolytically-produced gases, the experiments were performed with different ratios of gas volume to aqueous volume, V_g/V_{aq} , in the test vials, with the aqueous-gas interfacial area maintained constant at 3.14 cm^2 (the cross-sectional area of the vials).

Irradiations were carried out at an absorption dose rate of $2.5 \text{ Gy}\cdot\text{s}^{-1}$ over a total time period of 5 h. At regular time intervals, individual test vials were removed from the ^{60}Co gamma cell and analyzed for stable molecular water radiolysis products H_2O_2 , H_2 , and O_2 by UV-Visible spectrophotometry and gas chromatography, as described in Sections 2.2.3 and 2.2.4.

3.3 INTERFACIAL MASS TRANSFER IN THE RADIOLYSIS MODEL

3.3.1 Aqueous-Gas Interfacial Transfer

To address the interfacial transfer of H_2 and O_2 , two phase equilibria were added to the standard radiolysis model described previously in Section 2.3:



where $H_2(g)$ and $O_2(g)$ represent H_2 and O_2 in the gas phase. The designation of (aq) and (g) is used only for H_2 and O_2 in the following kinetics discussion because all other species associated with pure water radiolysis have negligible volatility and will remain in the aqueous phase throughout the experiments.

The interfacial mass transfer kinetics is modeled based on the assumption that the transfer rate depends on a driving force (a concentration differential from that at equilibrium) and a resistance represented by an overall interfacial transfer coefficient, v_{int}^i , of species i :

$$\frac{dC_{aq}^i(t)}{dt} = -\frac{V_g}{V_{aq}} \frac{dC_g^i(t)}{dt} = -v_{int}^i \frac{A_{int}}{V_{aq}} \left(1 - K_p^i \frac{C_g^i(t)}{C_{aq}^i(t)} \right) C_{aq}^i(t) \quad \text{E3.1}$$

where $C_{aq}^i(t)$ and $C_g^i(t)$ are the aqueous and gas phase concentrations of species i at time t , A_{int} the aqueous-gas phase interfacial area, and V_{aq} and V_g are the aqueous and gas phase volumes, respectively. The partition coefficient, K_p^i , is one form of Henry's constant and is defined as

$$K_p^i = \frac{C_{aq}^i(eq)}{C_g^i(eq)} \quad \text{E3.2}$$

where $C_{aq}^i(eq)$ and $C_g^i(eq)$ are the aqueous and gas phase concentrations, respectively, at phase equilibrium. The interfacial mass transfer equation can be rewritten in the form of a first order reaction as

$$\frac{dC_{aq}^i(t)}{dt} = -\frac{V_g}{V_{aq}} \frac{dC_g^i(t)}{dt} = -k_{app}^i(t) C_{aq}^i(t) \quad \text{E3.3}$$

by defining a net mass transfer coefficient that is time dependent, $k_{app}^i(t)$

$$k_{app}^i(t) = v_{int}^i \frac{A_{int}}{V_{aq}} \left(1 - K_p^i \cdot \frac{C_g^i(t)}{C_{aq}^i(t)} \right) \quad \text{E3.4}$$

These transport rate equations are incorporated in our basic radiolysis reaction model.

The overall interfacial transfer coefficient, v_{int}^i , is further modeled using the stagnant two-film model [7,8] and is defined as the sum of resistances through the stagnant films on each side of the interface [9]:

$$\frac{1}{v_{int}^i} = \frac{1}{v_{aq}} + \frac{K_p^i}{v_g} \quad \text{E3.5}$$

In the stagnant two-film model, the resistance to diffusion in each phase is represented in terms of molecular diffusion through a stagnant (un-mixed) boundary layer or film where a concentration gradient of the species under consideration exists. Resistance to transfer at the interface itself is considered to be negligible. From Fick's first law of diffusion, the individual resistances in each phase can be described by the diffusivity of the species through the medium and the thickness of the boundary layer [9]:

$$v_{aq} = \frac{D_{aq}}{\delta_{aq}} \quad \text{and} \quad v_g = \frac{D_g}{\delta_g} \quad \text{E3.6}$$

where D_{aq} and D_g are the species diffusivities and δ_{aq} and δ_g are the thicknesses of the boundary layer in the aqueous and gas phases, respectively. The diffusivities of H_2 and O_2 in liquid water are $5.11 \times 10^{-9} \text{ m}^2 \cdot \text{s}^{-1}$ and $2.42 \times 10^{-9} \text{ m}^2 \cdot \text{s}^{-1}$, and in air they are $7.56 \times 10^{-5} \text{ m}^2 \cdot \text{s}^{-1}$ and $2.02 \times 10^{-5} \text{ m}^2 \cdot \text{s}^{-1}$, respectively at 25 °C [10]. Implicit in E3.6 is an assumption that the boundary layer thickness is independent of species. The thickness of the boundary layer depends on bulk-flow dynamic conditions in the different phases (such as fluid or gas mixing and temperature gradient driven convection). Since the diffusivities for a variety of compounds at a given temperature vary by only a factor of 5 in air and even less, by only a factor of 2, in the aqueous phase [10], a much greater uncertainty in v_{aq} and v_g will arise from uncertainties in defining the hydrodynamic conditions present and because the effects of very fast chemical reactions on mass transfer are not well understood [11]. Thus, although there is an assumed relationship between δ and bulk hydrodynamic conditions, the thickness of the boundary layer under a given flow dynamic condition is often experimentally determined by monitoring evolutions of gaseous and aqueous concentrations. It can be noted that in the relatively small vials used in our tests, the liquid and gas volumes are too small to support large convection cells, or other bulk hydrodynamic features, and flow conditions near the boundary layers should be modest. In the present study, δ_{aq} and δ_g values were not measured values, but were treated as adjustable model parameters. The best fit values, which reproduced the experimental data obtained under a wide range of pH and cover gas

conditions, were found to be $\delta_{aq} = 5.1 \times 10^{-4}$ m and $\delta_g = 7.6 \times 10^{-2}$ m. These values were used in all the radiolysis model analysis results presented in this thesis.

3.4 RESULTS AND DISCUSSION

3.4.1 General Observations

The concentrations of H_2 in the headspace, $H_2(g)$, observed at pH 6.0 and at pH 10.6 under aerated and deaerated conditions are compared in Figure 3.1. For these experiments, the gas-to-aqueous volume ratio, V_g/V_{aq} , was 1:1. Also included in the figure are the model predictions as lines. Under all conditions, $H_2(g)$ increases linearly with time except at early times. Since the only source of $H_2(g)$ is the aqueous to gas phase transfer of $H_2(aq)$ that is radiolytically produced, the linear increase in $[H_2(g)]$ with time suggests that $[H_2(aq)]$ quickly reaches a steady state. The different slopes then imply that different steady-state concentrations of $H_2(aq)$ are reached under different pH and aeration conditions. A previous experimental and model simulation study on γ -radiolysis has shown that in the absence of headspace, the steady state $H_2(aq)$ concentration, $[H_2(aq)]_{ss}$, varies from 1.8×10^{-6} mol·dm⁻³ (below detection limit) to 2.0×10^{-5} (2.6×10^{-5}), 4.1×10^{-4} (2.0×10^{-4}), and 5.3×10^{-4} (1.9×10^{-4}) mol·dm⁻³ as the conditions change from pH 6.0 deaerated to pH 6.0 aerated, pH 10.6 deaerated, and pH 10.6 aerated. The values are model predictions and experimentally measured concentrations are given in brackets [6].

The effect of aqueous-gas phase partitioning on water radiolysis chemistry was studied in detail under pH 6.0 aerated and pH 10.6 deaerated conditions by varying the gas-to-aqueous volume ratio from 4:1 to 1:4. The time-dependent concentrations of H_2 in the headspace, $[H_2(g)]$, and the concentrations of H_2O_2 in the aqueous phase, $[H_2O_2]$, observed as a function of V_g/V_{aq} , are presented in Figure 3.2 for aerated water at pH 6.0 and in Figure 3.3 for deaerated water at pH 10.6. The model predictions are again shown as lines. For aerated water at pH 6.0, after a short delay, $[H_2(g)]$ increases linearly with irradiation time and the rate of the increase is inversely proportional to V_g , while H_2O_2 quickly reaches a steady-state concentration, $[H_2O_2]_{ss}$, that is nearly independent of V_g or V_{aq} . For deaerated water at pH 10.6, a similar trend is observed for $[H_2(g)]$, but the time-dependent behaviour of $[H_2O_2]$ is different. The $[H_2O_2]$ continuously increases with

time and does not reach a steady-state level within the 5 h experimental period. Also, the rate of increase in $[\text{H}_2\text{O}_2]$ is progressively slower with increasing V_g/V_{aq} ratio. These observations indicate that $[\text{H}_2(\text{g})]$ does not have a simple dependence on $[\text{H}_2\text{O}_2]$ or possibly the concentrations of other radiolytically produced species. One important implication of this observation is that measurement of $[\text{H}_2(\text{g})]$ alone is not sufficient to determine the state of the chemistry in irradiated water.

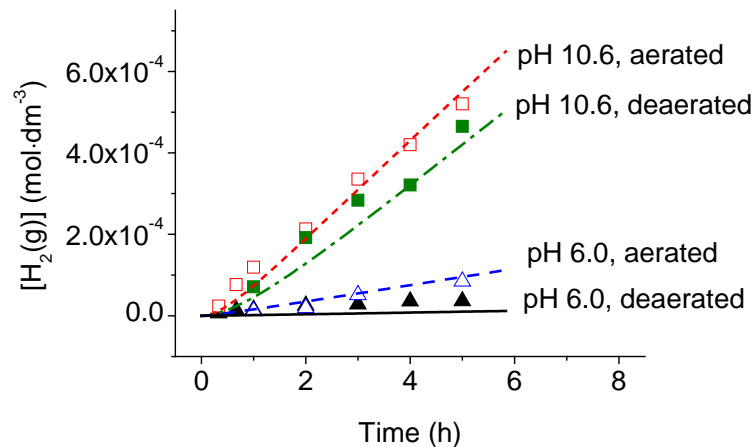


Figure 3.1: $\text{H}_2(\text{g})$ concentration in the headspace as a function of irradiation time for a volume ratio ($V_g:V_{aq}$) of 1:1 and a dose rate of $2.5 \text{ Gy}\cdot\text{s}^{-1}$.

The symbols represent the experimental data and the lines the radiolysis model results for pH 6.0 under aerated (Δ , ---) and deaerated (\blacktriangle , —) conditions and pH 10.6 under aerated (\square , -.-) and deaerated (\blacksquare , -.-) conditions.

The model described in Section 2.3 reproduces the experimental results for both $[\text{H}_2(\text{g})]$ and $[\text{H}_2\text{O}_2]$ within experimental uncertainties. In a previous study, it was shown that the same radiolysis kinetics model reproduces the radiolysis behaviour of pure water without a cover gas under a wider range of conditions [6]. The ability of the model with interfacial transport kinetics included to match our experimental observations further confirms that the kinetics model includes all of the necessary elementary reactions for prediction of continuous radiolysis of water.

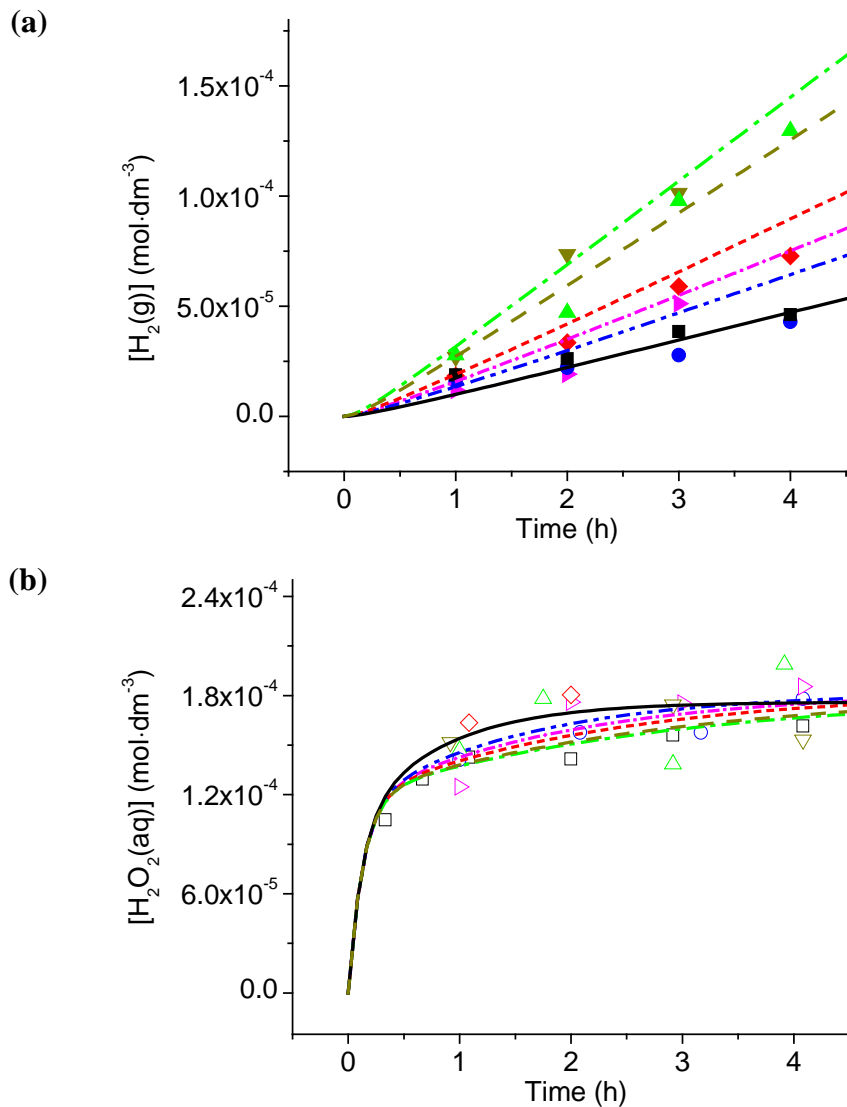


Figure 3.2: H_2 concentrations in the headspace (a) and H_2O_2 concentrations in the aqueous phase (b) as a function of irradiation time for aerated water at pH 6.0 at $2.5 \text{ Gy}\cdot\text{s}^{-1}$. The symbols represent the experimental data and the lines the radiolysis model results.

The H_2 data are shown with solid symbols and H_2O_2 with open symbols for different $V_g:V_{aq}$ ratios; 4:1 ($\blacksquare, \square, \text{—}$), 3:2 ($\bullet, \circ, \text{---}$), 1:1 ($\blacktriangleright, \triangleright, \text{-}\cdot\text{-}$), 2:3 ($\blacklozenge, \lozenge, \text{-}\cdot\text{-}$), 1:3 ($\blacktriangledown, \triangledown, \text{---}$) and 1:4 ($\blacktriangle, \triangle, \text{-}\cdot\text{-}$) respectively.

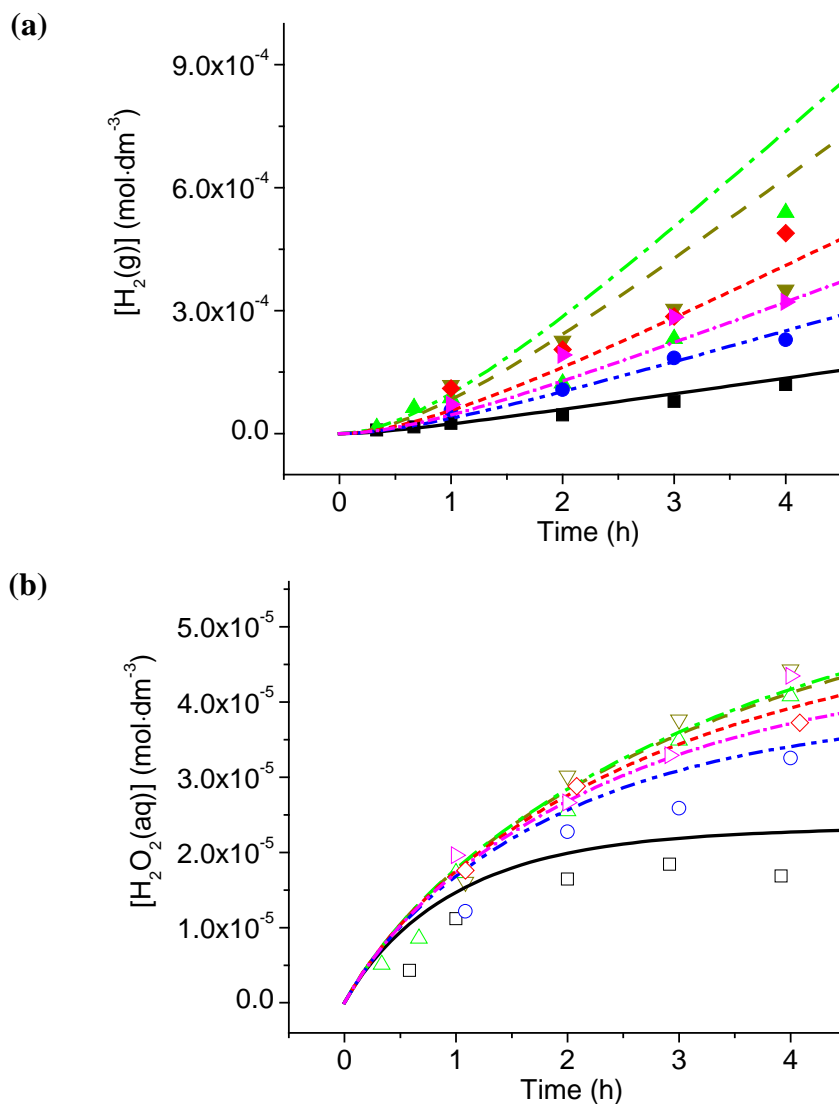


Figure 3.3: H_2 concentrations in the headspace (a) and H_2O_2 concentrations in the aqueous phase (b) as a function of irradiation time for deaerated water at pH 10.6 at $2.5 \text{ Gy}\cdot\text{s}^{-1}$. The symbols represent the experimental data and the lines the radiolysis model results.

The H_2 data are shown with solid symbols and H_2O_2 with open symbols for different $V_g:V_{aq}$ ratios; 4:1 ($\blacksquare, \square, \text{—}$), 3:2 ($\circ, \bullet, \text{---}$), 1:1 ($\blacktriangleright, \blacktriangleleft, \text{-.-}$), 2:3 ($\blacklozenge, \blacklozenge, \text{-.-}$), 1:3 ($\blacktriangledown, \blacktriangledown, \text{---}$) and 1:4 ($\blacktriangle, \triangle, \text{-.-}$) respectively.

3.4.2 Radiolytic Production of Hydrogen in the Cover Gas

The source of H₂ in the cover gas is the aqueous-to-gas phase transfer of hydrogen produced in the aqueous phase, H₂(aq), by radiolytic decomposition of liquid water



where the net interfacial transfer rate constant, $k_{app}^{\text{H}_2}(t)$, defined in E3.4, decreases with time as the system approaches the equilibrium concentrations of H₂ in the two phases. At phase equilibrium, $k_{app}^{\text{H}_2}(t)$ is zero, and the gas- and aqueous-phase concentrations of H₂ are determined by the phase equilibrium partition coefficient, see E3.2. The partition coefficient of H₂, $K_p^{\text{H}_2}$, as defined in E3.2, is 0.019 at 25 °C and smaller at higher temperatures. In a constant radiation field there will be continuous radiolytic production of H₂. For a highly volatile gas like H₂, if its initial concentration in the gas phase is negligible, the system will remain far away from phase equilibrium even over a long period of irradiation. During the early time after the start of irradiation, $t \ll t^{eq}$, it can be assumed that

$$k_{app}^{\text{H}_2}(t) \approx k_{app}^{\text{H}_2}(t = 0) = v_{int}^{\text{H}_2} \frac{A_{int}}{V_{aq}} \quad \text{E3.7}$$

From E 3-3, the rate of change in the concentration of H₂(g) is then

$$\frac{d}{dt} [\text{H}_2(\text{g})]_t^{\text{HS}} \approx v_{int}^{\text{H}_2} \frac{A_{int}}{V_g} \cdot [\text{H}_2(\text{aq})]_t^{\text{HS}} \quad \text{E3.8}$$

This equation predicts that for an interfacial geometry defined by V_{aq} , V_g , and A_{int} , the rate of H₂(g) production is proportional to $[\text{H}_2(\text{aq})]_t^{\text{HS}}$. Thus, if the concentration of H₂(aq) does not change significantly with time, i.e. if the aqueous system reaches (pseudo-) steady state relatively quickly, $[\text{H}_2(\text{g})]_t^{\text{HS}}$ will increase linearly with irradiation time:

$$[\text{H}_2(\text{g})]_t^{HS} \approx v_{int}^{H_2} \frac{A_{int}}{V_g} [\text{H}_2(\text{aq})]_{SS}^{HS} (t - t_{SS}) + [\text{H}_2(\text{g})]_{t_0}^{HS} \quad \text{E3.9}$$

where $[\text{H}_2(\text{aq})]_{SS}^{HS}$ represents the steady-state concentration of $\text{H}_2(\text{aq})$, t_{SS} the time to establish steady state in the aqueous system, and $[\text{H}_2(\text{g})]_{t_0}^{HS}$ the concentration of $\text{H}_2(\text{g})$ in the gas phase at t_0 . This linear increase in $[\text{H}_2(\text{g})]_t^{HS}$ is observed at both pHs as shown in Figure 3.2a and Figure 3.3a. The linear increase region is established more slowly at pH 10.6 than at pH 6.0 and this is attributed to the longer time required for $[\text{H}_2(\text{aq})]$ to reach steady state at pH 10.6, see further discussion below.

The most important aspect of E3.8 is that it predicts the rate of increase in the gaseous concentration of $\text{H}_2(\text{g})$ in the gas phase, which is proportional to $[\text{H}_2(\text{aq})]_t^{HS}$ with a proportionality constant of $v_{int}^{H_2} \frac{A_{int}}{V_g}$. This relationship is difficult to confirm experimentally because it is difficult to measure the aqueous concentration of hydrogen with a reasonable accuracy. Measurements of $[\text{H}_2(\text{aq})]_t^{Full}$ in tests without headspace cannot be used to determine $[\text{H}_2(\text{aq})]_t^{HS}$ because the transfer of H_2 to the gas phase can influence $[\text{H}_2(\text{aq})]_t^{HS}$.

Figure 3.4 shows the calculated $[\text{H}_2(\text{aq})]_t^{HS}$ for the different ratios of gas and liquid volumes (V_g/V_{aq}), and the measured and calculated aqueous H_2 concentrations for test samples without cover gas. The model calculations predict that the presence or absence of headspace on $[\text{H}_2(\text{aq})]_t^{HS}$ is negligible at pH 6.0. However, at pH 10.6 it is no longer negligible and $[\text{H}_2(\text{aq})]_t^{HS}$ depends on the available gas volume. The model predictions for $[\text{H}_2\text{O}_2]_t^{HS}$ that are presented in Figure 3.2b and Figure 3.3b show excellent agreement with the data within experimental uncertainties. The model calculation results are replotted and compared with the measured and calculated $[\text{H}_2\text{O}_2]_t^{Full}$ for samples without headspace in Figure 3.5. While we could not measure $[\text{H}_2(\text{aq})]_t^{HS}$ accurately in our experiments, we could effectively measure $[\text{H}_2\text{O}_2]_t^{HS}$. Comparison of Figure 3.4 and Figure 3.5 shows that the behaviour of $[\text{H}_2\text{O}_2]_t^{HS}$ exhibits similar pH dependence to that of $[\text{H}_2(\text{aq})]_t^{HS}$, indicating that the behaviour of other radiolysis products in the aqueous phase can be inferred from that of H_2O_2 . The small difference in the influence of headspace on $[\text{H}_2(\text{aq})]_t^{HS}$ versus $[\text{H}_2\text{O}_2]_t^{HS}$ arises from the fact that $[\text{H}_2(\text{aq})]_t^{HS}$ is affected

by the interfacial transfer of H_2 alone while $[H_2O_2]_t^{HS}$ is affected by the transfer of O_2 as well as H_2 .

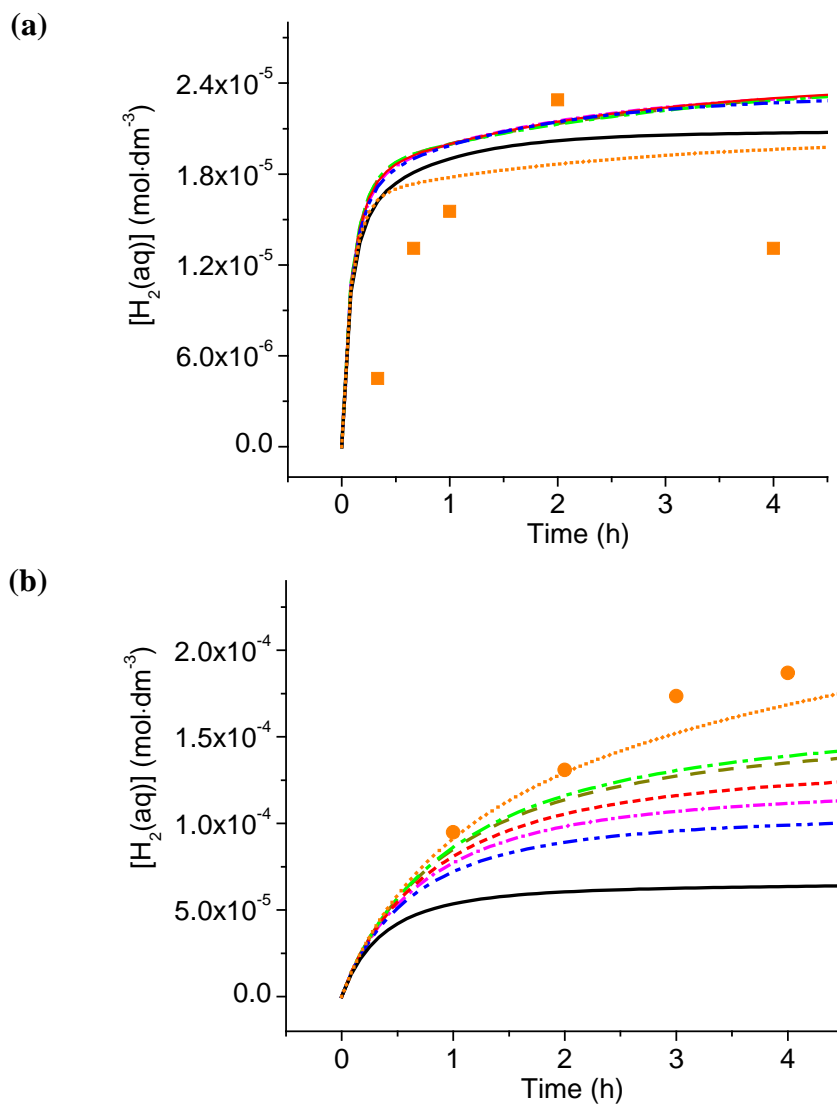


Figure 3.4: H_2 concentrations in the aqueous phase as a function of irradiation time for aerated water at pH 6.0 (a) and deaerated water at pH 10.6 (b) at $2.5 \text{ Gy} \cdot \text{s}^{-1}$.

The solid symbols (\blacksquare, \bullet) are the experimentally measured $[H_2(aq)]$ from tests with no cover gas headspace and the lines are the radiolysis model results for different $V_g:V_{aq}$ ratios: 4:1 (—), 3:2 (-·-·-), 1:1 (-·-·-), 2:3 (-·-·-), 1:3 (-·-·-), 1:4 (-·-·-) and no headspace (·····) respectively.

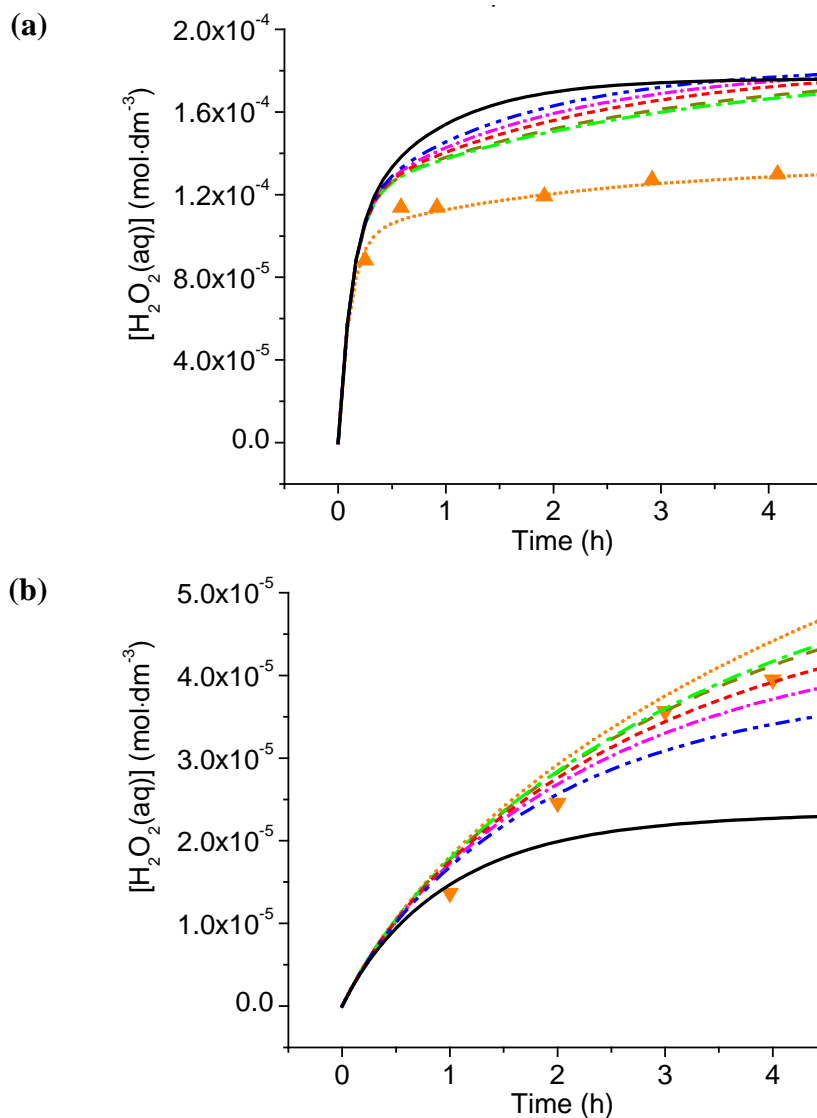


Figure 3.5: H_2O_2 concentrations in the aqueous phase as a function of irradiation time for aerated water at pH 6.0 (a) and deaerated water at pH 10.6 (b) at $2.5 \text{ Gy}\cdot\text{s}^{-1}$. The solid symbols (\blacktriangle , \blacktriangledown) are the experimentally measured $[\text{H}_2\text{O}_2(\text{aq})]$ from tests with no cover gas headspace and the lines are the radiolysis model results for different $V_g:V_{\text{aq}}$ ratios: 4:1 (—), 3:2 (···), 1:1 (---), 2:3 (---), 1:3 (---), 1:4 (---) and no headspace (···) respectively.

To analyze the data, we rearrange E3.8 as:

$$\log \left(V_g \frac{d[\text{H}_2(\text{g})]_t^{\text{HS}}}{dt} \right) \approx \log(v_{\text{int}}^{\text{H}_2} A_{\text{int}}) + \log[\text{H}_2(\text{aq})]_t^{\text{HS}} \quad \text{E3.10}$$

In Figure 3.6, the $d[\text{H}_2(\text{g})]_t^{\text{HS}}/dt$ values, obtained from the slopes of the linear regions of the $[\text{H}_2(\text{g})]_t^{\text{HS}}$ versus t plots in Figure 3.2a and Figure 3.3a, and multiplied by the cover gas volume, are plotted against the calculated (pseudo) steady-state concentrations, $[\text{H}_2(\text{aq})]_{\text{SS}}^{\text{HS}}$, in Figure 3.4. The data are shown in a log-log plot due to the large span in $[\text{H}_2(\text{aq})]_{\text{SS}}^{\text{HS}}$. A linear fit to the log-log data in Figure 3.6 has a slope of 1.000 and an intercept, $\log(v_{\text{int}}^{\text{H}_2} A_{\text{int}})$ of -2, confirming that equations E3.8 and E3.10 hold under all conditions. This result confirms that the concentration of H_2 in the liquid water phase during irradiation can be derived from the more easily measurable mass of $\text{H}_2(\text{g})$ ($= V_g[\text{H}_2(\text{g})]$) in the headspace, irrespective of conditions of the irradiation.

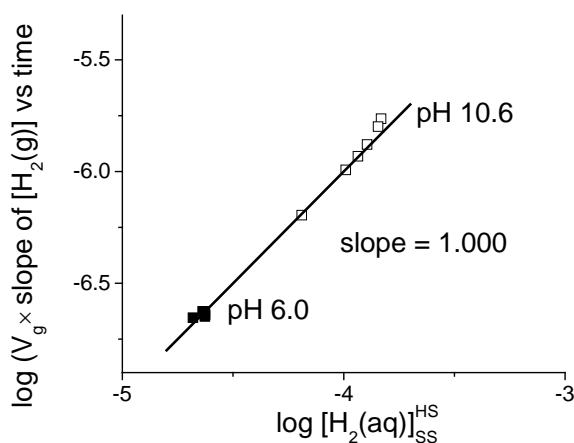


Figure 3.6: The log of ($V_g \times$ slope of $[\text{H}_2(\text{g})]$ vs time) is shown as a function of $\log[\text{H}_2(\text{aq})]_{\text{SS}}^{\text{HS}}$ for aerated water at pH 6.0 and deaerated water at pH 10.6.

3.4.3 Effect of Interfacial Transfer of Volatile Species on Aqueous Products

The results of this work, as shown in Figure 3.2 and Figure 3.3, demonstrate that the presence of headspace will have an impact on the concentrations of radiolytically produced aqueous species, and this influence depends on pH. The work reported here has been conducted at only two pH values because these are sufficient to sample two

different regions for water radiolysis chemistry. A previous study by our group on water radiolysis in the absence of headspace has established that the kinetic behaviour of the water decomposition products and their consequential steady-state concentrations can vary considerably over the pH range of $8 < \text{pH} < 11$, whereas outside this range they are nearly independent of pH [6]. This is shown in Figure 3.7, which is reproduced from Reference [6] (for initially deaerated samples).

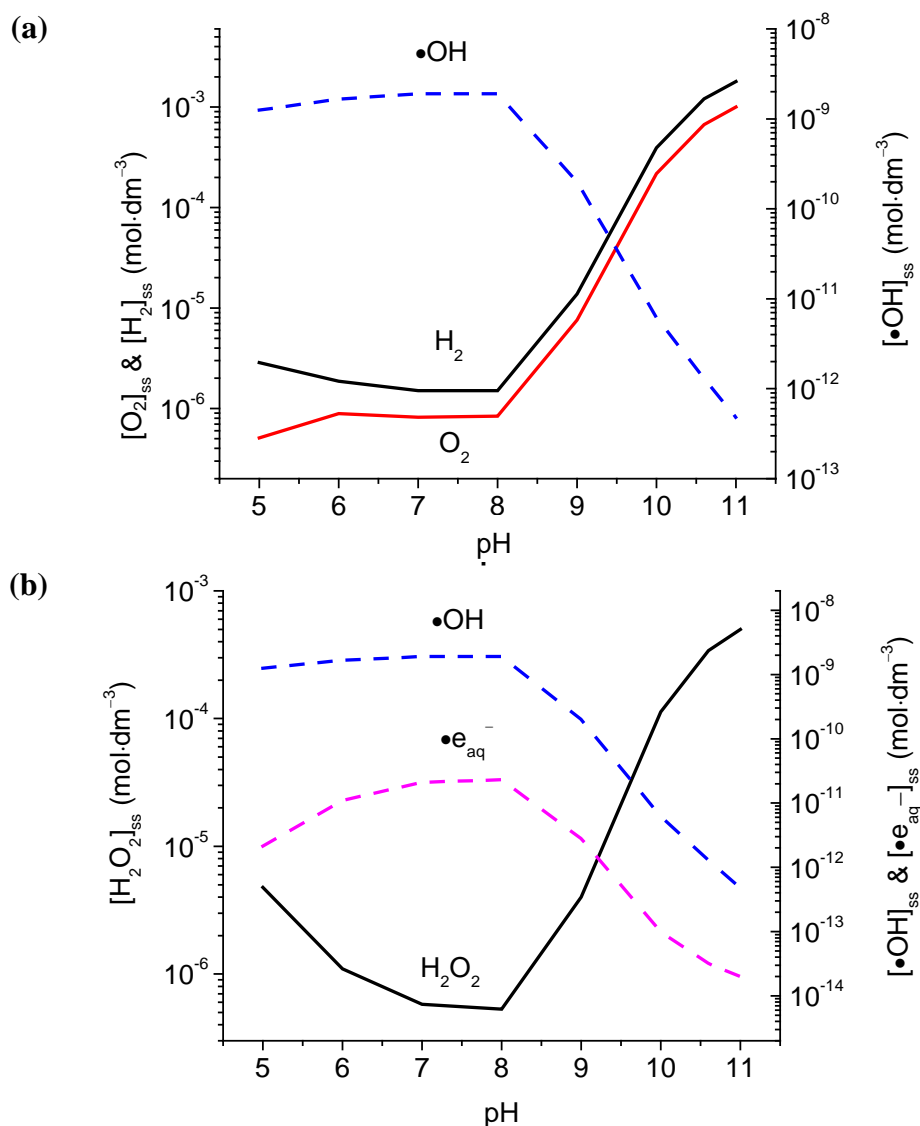


Figure 3.7: Full model predictions for the steady-state concentrations of H_2 and O_2 along with $[\bullet\text{OH}]_{\text{ss}}$ (a) and H_2O_2 along with $[\bullet\text{OH}]_{\text{ss}}$ and $[\bullet\text{e}_{\text{aq}}^-]_{\text{ss}}$ (b), as a function of pH for deaerated water.

This pH dependence was attributed to the change in the net rate of the reaction of $\bullet e_{aq}^-$ with H^+ [12,13].



The slow net forward rate of this reaction at $pH > pK_a$ of $\bullet H$ leads to a slow but considerable radiolytic production of O_2 and secondary and tertiary oxygen products such as $\bullet O_2^-$ and $\bullet O_3^-$. The presence of these oxygen products can significantly alter the concentrations of other radiolysis products. The influence of oxygen on the time-dependent radiolysis product concentrations is discussed in detail in Chapter 4.

3.4.3.1 pH 6.0

At $pH \leq 8$ and in the absence of a headspace, the key reactions that determine the behaviour of H_2 during steady-state radiolysis include its primary radiolysis production, reaction 3.1a, and its removal via the reaction with $\bullet OH$, reaction 3.5.



The concentration of $H_2(aq)$ in the absence of headspace, $[H_2(aq)]_t^{Full}$, can be derived from the following expression:

$$[H_2(aq)]_t^{Full} \approx \frac{k_{Rad}^{H_2}}{k_{R3.5}[\bullet OH]_t^{Full}} \quad k_{Rad}^{H_2} \approx C_R G_{H_2} D_R \quad E3.11$$

where C_R is a unit conversion constant (1.036×10^{-7}), G_{H_2} is the G-value for H_2 production (0.45 molecules/100 eV at 25 °C), D_R is the gamma-radiation dose rate in units of $Gy \cdot s^{-1}$ (2.5 in this work), and $k_{R3.5}$ represents the rate constant for reaction 3.5. For irradiation at a constant dose rate, $C_R G_{H_2} D_R$ is equivalent to a zeroth-order rate constant, $k_{Rad}^{H_2}$.

In the presence of a headspace, the aqueous-gas phase transfer, reaction 3.2, may become an important additional removal path for hydrogen from the aqueous phase, and the $H_2(aq)$ concentration then follows the expression:

$$[H_2(aq)]_t^{HS} \approx \frac{k_{Rad}^{H_2}}{k_{R3.5}[\bullet OH]_t^{HS} + k_{app}^{H_2}(t)} \quad E3.12$$

where $k_{app}^{H_2}(t)$ can be further approximated as shown in E3.7. Note that the aqueous concentrations of $\bullet OH$ in the absence and the presence of headspace, $[\bullet OH]_t^{Full}$ and $[\bullet OH]_t^{HS}$ in Equations E3.11 and E3.12, are not necessarily the same. However, at $pH \leq 8$, $[\bullet OH]_t^{Full}$ is relatively large ($> 10^{-8} \text{ mol}\cdot\text{dm}^{-3}$ for deaerated solutions and $> 10^{-10} \text{ mol}\cdot\text{dm}^{-3}$ for aerated solutions) [6]. Thus, with the small A_{int}/V_{aq} used in this study, $k_{R3.5}[\bullet OH]_{SS}^{HS} > v_{int}^{H_2} \cdot A_{int}/V_{aq}$ ($= 4.2 \times 10^{-3} > 3.14 \times 10^{-4} \text{ s}^{-1}$). Under these conditions, E3.12 can be further approximated to

$$[H_2(aq)]_t^{HS} \approx \frac{k_{Rad}^{H_2}}{k_{R3.5}[\bullet OH]_t^{HS}} \quad E3.13$$

This is equivalent to the relationship given in Equation E3.11, and illustrates that the concentration of H_2 is mainly determined by that of $\bullet OH$ for $pH \leq 8$. Hence, in evaluating the effect of headspace, not only the interfacial transfer of $H_2(aq)$, but also the behaviour of $\bullet OH$ must be considered.

For reactive $\bullet OH$, there are additional removal paths available besides reaction 3.5. At $pH \leq 8$, the reactions that control the concentration of $\bullet OH$ are primary radiolysis production (3.1b), and removal by reactions 3.5, 3.6, and 3.7 (under aerated conditions).



where $\bullet\text{O}_2^-$ is produced by



(Note that the values for reaction rate constants here and elsewhere are for 25 °C.)

The aqueous-to-gas phase transfer of volatile species, H_2 and O_2 , can affect the concentration of $\bullet\text{OH}$ if the transfer to the gas phase significantly reduces $[\text{H}_2(\text{aq})]$ and $[\text{O}_2(\text{aq})]$. Under the pH 6.0 aerated conditions used in this study, the effect of transfer of H_2 to the gas phase on $\text{H}_2(\text{aq})$ is small, as discussed above. Furthermore, at this pH, the $[\text{O}_2(\text{aq})]$ produced radiolytically is small. Since the aqueous and gas phases were initially saturated in air, there would be negligible net interfacial transfer of O_2 . Hence, under these conditions, the presence of headspace would have no significant impact on the concentrations of radicals, $\bullet\text{OH}$, $\bullet\text{e}_{\text{aq}}^-$, or $\bullet\text{O}_2^-$. The effect of headspace on the radical concentration was examined by model analysis and the results presented in Figure 3.8 confirm that the interfacial transfer of volatile species has a negligible effect on radical concentrations evolved at pH 6.0.

The observation that $[\text{H}_2\text{O}_2]$ does not depend on V_g/V_{aq} , Figure 3.2b, further supports the conclusion that the effect of headspace on radical concentrations is small at $\text{pH} \leq 8$. The key reactions determining $[\text{H}_2\text{O}_2]_t^{\text{Full}}$ are production by primary radiolysis (reaction 3.1c) and decomposition via reactions with $\bullet\text{OH}$ and $\bullet\text{e}_{\text{aq}}^-$, reactions 3.6 and 3.9 respectively.



In fully aerated solutions, reaction 3.10 also becomes important for production of hydrogen peroxide, and the steady-state concentration of H_2O_2 can then be described by Equation E3.14.



$$[H_2O_2]_t^{Full} \approx \frac{k_{Rad}^{H_2O_2} + k_{R3.10} [\bullet HO_2]_t^{Full} [\bullet O_2^-]_t^{Full}}{k_{R3.6} [\bullet OH]_t^{Full} + k_{R3.9} [\bullet e_{aq}^-]_t^{Full}} \quad k_{Rad}^{H_2O_2} \approx C_R G_{H_2O_2} D_R \quad E3.14$$

Unlike H_2 , H_2O_2 is non-volatile, and hence, the presence of headspace does not provide an additional removal pathway for it. Therefore, the expression for $[H_2O_2]_t^{HS}$ in the presence of headspace is equivalent to E3.14, except that the radical concentrations are those seen when a headspace is present.

$$[H_2O_2]_t^{HS} \approx \frac{k_{Rad}^{H_2O_2} + k_{R3.10} [\bullet HO_2]_t^{HS} [\bullet O_2^-]_t^{HS}}{k_{R3.6} [\bullet OH]_t^{HS} + k_{R3.9} [\bullet e_{aq}^-]_t^{HS}} \quad E3.15$$

Hence, any effect of headspace on $[H_2O_2]$ will occur via the impact of a gas phase on solution radical concentrations. A previous study established that in aerated solutions, the concentrations of $\bullet OH$ and $\bullet e_{aq}^-$ can be approximated [6]:

$$[\bullet OH]_t^{Full} \approx \frac{k_{Rad}^{\bullet OH}}{k_{R3.7} [\bullet O_2^-]_t^{Full}} \quad E3.16$$

$$[\bullet e_{aq}^-]_t^{Full} \approx \frac{k_{Rad}^{\bullet e_{aq}^-}}{k_{R3.8} [O_2(aq)]_t^{Full}} \quad E3.17$$

while the concentrations of $\bullet O_2^-$ and $\bullet HO_2$ depend on approximately the square root of $[O_2(aq)]$.

For aerated water at pH 6.0, the $[H_2O_2]_t^{HS}$ observed in the presence of a headspace is slightly higher than the $[H_2O_2]_t^{Full}$ observed in the absence of headspace, Figure 3.5a. Although the net interfacial transfer of O_2 is small under these conditions, it

does have a small impact on $[\text{H}_2\text{O}_2]$ (while negligible impact on $[\text{H}_2(\text{aq})]$), because of a strong influence of $[\text{O}_2(\text{aq})]$ on $[\bullet\text{HO}_2]$ or $[\bullet\text{O}_2^-]$, $[\bullet\text{OH}]$ and $[\bullet\text{e}_{\text{aq}}^-]$.

The $[\text{H}_2\text{O}_2]$ strongly depends on the initially dissolved oxygen concentration. As a result, for deaerated water at pH 6.0, the concentrations of H_2O_2 are below the detection limit for samples with and without headspace, as expected.

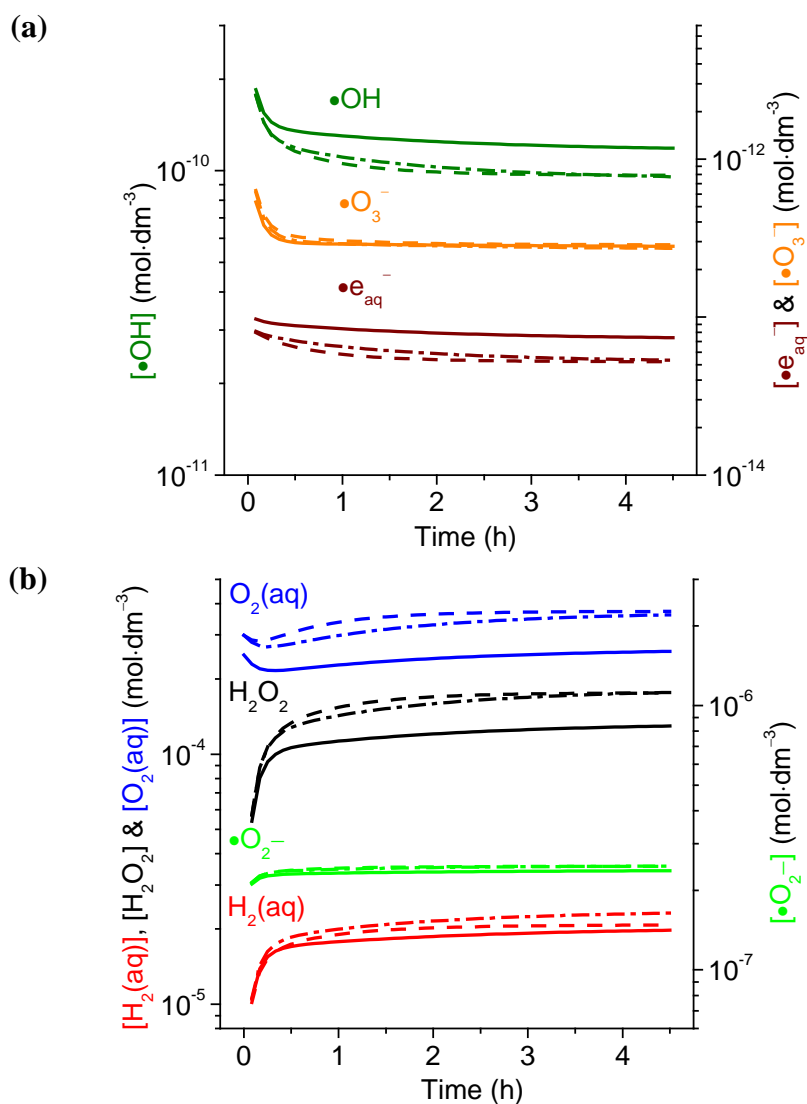


Figure 3.8: Model predictions for the steady-state concentrations of $\bullet\text{OH}$, $\bullet\text{e}_{\text{aq}}^-$ and $\bullet\text{O}_3^-$ (a) and $\text{H}_2(\text{aq})$, H_2O_2 , $\text{O}_2(\text{aq})$ and $\bullet\text{O}_2^-$ (b) for aerated water at pH 6.0 as a function of time at 2.5 Gy·s⁻¹. The radiolysis model results are shown for $V_g:V_{\text{aq}}$ ratios of 4:1 (—) and 1:1 (---) and for water with no headspace ($V_g = 0$) (—).

3.4.3.2 pH 10.6

At pHs higher than 9.6 (the pK_a of $\bullet H$), the radiolytic production of $O_2(aq)$ is significant, and its presence reduces the concentrations of primary radiolysis radicals such as $\bullet OH$ and $\bullet e_{aq}^-$ (see E3.16 and E3.17). Being a secondary product, $[O_2(aq)]$ takes a long time to reach steady state. This, combined with increased rates of the reactions of O_2 with other radiolysis products, results in slowing the approach to steady-state concentrations for all of the other radiolysis products. This slow accumulation of radiolytically produced O_2 also significantly increases the concentrations of the tertiary oxygen products, $\bullet O_3^-$ and $\bullet O^-$, and the secondary oxygen product, $\bullet O_2^-$. Thus, at high pHs, the reactions of the tertiary oxygen products also become important in determining water radiolysis behaviour. Reaction 3.11 becomes important for removal of H_2 :



As a result, the concentration of $H_2(aq)$ for test vials without a headspace can be expressed as

$$[H_2(aq)]_t^{Full} \approx \frac{k_{Rad}^{H_2}}{k_{R3.5} \cdot [\bullet OH]_t^{Full} + k_{R3.11} \cdot [\bullet O_3^-]_t^{Full}} \quad E3.18$$

Similarly, the reaction of $\bullet O_3^-$ with H_2O_2 also contributes to H_2O_2 removal and the concentration of H_2O_2 is determined by



$$[H_2O_2]_t^{Full} \approx \frac{k_{Rad}^{H_2O_2} + k_{R3.10} [\bullet HO_2]_t^{Full} [\bullet O_2^-]_t^{Full}}{k_{R3.6} [\bullet OH]_t^{Full} + k_{R3.9} [\bullet e_{aq}^-]_t^{Full} + k_{R3.12} [\bullet O_3^-]_t^{Full}} \quad E3.19$$

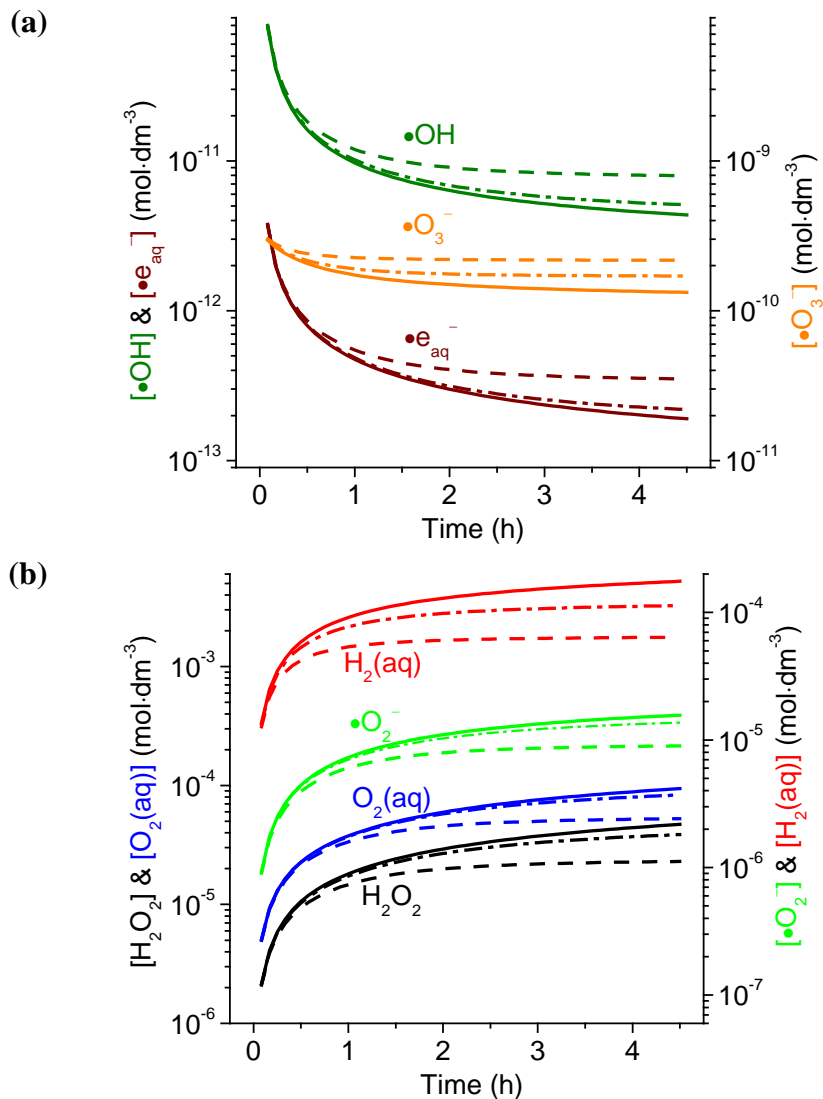


Figure 3.9: Model predictions for the steady-state concentrations of $\bullet\text{OH}$, $\bullet\text{e}_{\text{aq}}^-$ and $\bullet\text{O}_3^-$ (a) and $\text{H}_2(\text{aq})$, H_2O_2 , $\text{O}_2(\text{aq})$ and $\bullet\text{O}_2^-$ (b) for deaerated water at pH 10.6 as a function of time at 2.5 Gy·s⁻¹. The radiolysis model results are shown for $V_g:V_{\text{aq}}$ ratios of 4:1 (---) and 1:1 (- - -) and for water with no headspace ($V_g = 0$) (—).

In the presence of a headspace, $[\text{H}_2(\text{aq})]_t^{HS}$ can be described by Equation E3.20, while $[\text{H}_2\text{O}_2]_t^{HS}$ has the same form as E3.19 but with the radical concentrations corresponding to those found in the presence of headspace.

$$[\text{H}_2(\text{aq})]_t^{HS} \approx \frac{k_{Rad}^{H_2}}{k_{R3.5}[\bullet\text{OH}]_t^{HS} + k_{R3.11}[\bullet\text{O}_3^-]_t^{HS} + v_{int}^{H_2} \frac{A_{int}}{V_{aq}}} \quad \text{E3.20}$$

At $\text{pH} \geq 8$, the production of volatile species H_2 and O_2 is considerable while radical production is reduced (for $\bullet\text{OH}$ and $\bullet\text{e}_{aq}^-$) (Figure 3.9). The H_2 interfacial transfer term in the denominator of E3.20 is not negligible. In addition, due to the role of oxygen species in determining the concentrations of other radiolysis products (E3.16 and E3.17), the aqueous-to-gas phase transfer of O_2 becomes important



where

$$k_{app}^{O_2}(t) \approx k_{app}^{O_2}(t=0) = v_{int}^{O_2} \frac{A_{int}}{V_{aq}} \quad \text{E3.21}$$

Transfer of O_2 to the gas phase decreases $[\bullet\text{O}_2^-]$, while increasing $[\bullet\text{OH}]$, $[\bullet\text{e}_{aq}^-]$, and $[\bullet\text{O}_3^-]$. These changes occur in addition to the increase in $[\bullet\text{OH}]$ arising from the loss of $\text{H}_2(\text{aq})$. Equations E3.20 and E3.21 indicate that the effect of interfacial transfer of H_2 and O_2 on the concentrations of aqueous species becomes more important with increasing A_{int}/V_{aq} , as one might expect; a large surface area to liquid volume ratio allows for faster loss of volatile gases from the liquid phase. Our model successfully matches this effect of headspace on the radical concentrations for deaerated water at pH 10.6, as shown in Figure 3.9.

3.5 CONCLUSIONS

In many real environments where radiolysis of water can occur, a connecting gas volume is present. This study has examined the impact of such a cover gas on the water

chemistry driven by radiolysis. The effect of the aqueous-gas phase interfacial transfer of volatile species, H_2 and O_2 , on steady-state radiolysis chemistry was studied. At $pH \leq 8$ (lower than the pK_a of $\bullet H$ of 9.6), the effect of aqueous-to-gas phase transfer of these volatile species on the concentrations of the other aqueous species generated by radiolysis is negligible. The experimental results confirm the capability of the basic water radiolysis chemical kinetics model, which predicts these results. For low pH, the gaseous concentration of H_2 in a cover gas volume increases linearly with time during steady-state irradiation and the rate of increase is proportional to $1/V_g$, while the aqueous concentrations of $H_2(aq)$ and H_2O_2 are effectively independent of A_{int}/V_{aq} .

At higher pH (≥ 8), radiolytic production of $O_2(aq)$ is slow but considerable. This results in significant increases in the steady-state concentrations of $H_2(aq)$ and H_2O_2 compared to those achieved for irradiation of water at a lower pH. Thus, in the presence of a headspace, the interfacial transfer of both H_2 and O_2 becomes significant, decreasing the aqueous concentrations of the volatile species and influencing the concentrations of radical species. As a result, the aqueous concentration of $H_2(aq)$ is no longer independent of A_{int}/V_{aq} . Irrespective of the pH dependence that a headspace imparts on system chemistry, the accumulated mass of $H_2(g)$ in the headspace ($V_g[H_2(g)]$) is proportional to the aqueous concentration of H_2 :

$$V_g \cdot [H_2(g)]_t^{HS} \approx v_{int}^{H_2} A_{int} [H_2(aq)]_{SS}^{HS} t \quad E3.22$$

Thus, the measurement of the gaseous concentration of H_2 in the headspace can be used to infer the aqueous concentration, $H_2(aq)$.

3.6 REFERENCES

- [1] Allen, A.O. *The Radiation Chemistry of Water and Aqueous Solutions*, Van Nostrand Company, Inc.: New York, 1961.
- [2] Draganic, I.G., Draganic, Z.D. *The Radiation Chemistry of Water*, Academic Press, Inc.: New York, 1971.
- [3] *Radiation Chemistry: Principles and Applications*, Farhataziz, Rodgers, A.J., Eds., VCH Publishers, Inc.: New York, 1987.
- [4] Spinks, J.W.T., Woods, R.J. *An Introduction to Radiation Chemistry*, 3rd ed., Wiley-Interscience: New York, 1990.

- [5] Buxton, G.V., Greenstock, C.L., Helman, W.P., Ross, A.B., "Critical-review of rate constants for reactions of hydrated electrons, hydrogen atoms and hydroxyl radicals (OH/O⁻) in aqueous solution", *J. Phys. Chem. Ref. Data*, **1988**, 17, 513-886.
- [6] Joseph, J.M., Choi, B.S., Yakabuskie, P.A., Wren, J.C., "A combined experimental and model analysis on the effect of pH and O₂(aq) on γ -radiolytically produced H₂ and H₂O₂", *Radiat. Phys. Chem.*, **2008**, 77, 1009-1020.
- [7] Whitman, W.G., "The two-film theory of gas absorption", *Chem. Met. Eng.*, **1923**, 29, 146-148.
- [8] Lewis, W.K., Whitman, W.G., "Principles of gas absorption", *Ind. Eng. Chem.*, **1924**, 16, 1215-1220.
- [9] Treybal, R.E. *Mass Transfer Operations*, McGraw-Hill Book Company: New York, 1955.
- [10] *CRC Handbook of Chemistry and Physics*; 94th ed., Haynes, W.M., Bruno, T.J., Lide, D.R., Eds., CRC Press, Inc.: Boca Raton, FL., 2013.
- [11] Evans, G.J., Ling, J.R., "Enhancement of the interfacial transfer of iodine by chemical reaction", *Can. J. Chem. Eng.*, **2000**, 78, 221-225.
- [12] Hart, E.J., Gordon, S., Fielden, E.M., "Reaction of the hydrated electron with water", *J. Phys. Chem.*, **1966**, 70, 150-156.
- [13] Shiraishi, H., Sunaryo, G.R., Ishigure, K., "Temperature dependence of equilibrium and rate constants of reactions inducing conversion between hydrated electron and atomic hydrogen", *J. Phys. Chem.*, **1994**, 98, 5164-5173.

CHAPTER 4 THE EFFECT OF INITIALLY ADDED OXYGEN ON STEADY-STATE WATER RADIOLYSIS KINETICS

4.1 INTRODUCTION

A quantitative understanding of the chemical or redox environments generated in water by ionizing radiation is important for material selection, maintenance program improvement, and safety assessments for water-cooled nuclear power reactors. The long-term effects of water radiolysis are particularly important to develop a clear understanding of the influence of radiolysis products on the material degradation process. Since water radiolysis products include both highly oxidizing ($\bullet\text{OH}$, H_2O_2 , O_2) and highly reducing ($\bullet\text{e}_{\text{aq}}^-$, $\bullet\text{H}$, H_2) species, the relative balance of the steady-state concentrations of these species will determine the overall aqueous redox state of the water and influence the aqueous corrosion kinetics of metallic surfaces in radiation-exposed systems [1-5]. The presence of dissolved impurities or additives (e.g., O_2 which could be introduced due to air ingress) can impose changes to the coolant water chemistry by altering the steady-state concentrations of the water radiolysis products attained under continuous irradiation. In particular, the concentrations of oxidizing molecular products generated via radiolysis, mainly H_2O_2 and O_2 , play a key role in the corrosion of reactor components. Compared to radical species with shorter lifetimes, the molecular products are more stable and can diffuse to the surface and influence corrosion reactions. Corrosion potential measurements performed by Daub et al. have shown that H_2O_2 is one of the main radiolysis species responsible for the corrosion of carbon steel [6,7]. The change in the corrosion potential of carbon steel when subjected to gamma radiation was effectively simulated in a non-radiation field by adding H_2O_2 [8]. Similar results have been observed with stainless steel [9].

The development of a comprehensive chemical kinetics model that can satisfactorily replicate the temporal trends in radiolysis product behavior for a wide range of dissolved solutes is a primary goal of this thesis. However, due to the large and interdependent set of reactions that exist for pure water alone, the most basic reaction set must first be validated experimentally prior to expanding the reaction set to include other (non-water radiolysis product) dissolved solutes that can impact the radiation chemistry. As a result, the radiolysis of pure water must be examined by perturbing the system with

methods other than chemical impurity additions, and measuring the concentrations of stable radiolysis products. Perturbations that can be performed include changing the available cover gas volume, the pH of the solution, or the concentrations of initially dissolved water radiolysis decomposition products. In Chapter 3, the basic water radiolysis reaction set with the addition of mass transfer terms was shown to reproduce the experimental data for the stable molecular water radiolysis products at different pH while the cover gas and liquid volume ratios were varied. Additionally, the build-up of the secondary water radiolysis product O_2 was shown to induce changes in the time-dependent behavior of the radical and molecular species [10]. Hence, monitoring changes to the concentrations of molecular products, H_2 and H_2O_2 , while varying the concentration of initially dissolved O_2 provides supplementary data to evaluate the mechanisms that determine the long-term chemistry. In this Chapter, the experimental and modeling studies provide further proof of the capabilities of the basic reaction model and mass transfer parameters to replicate experimental trends.

This chapter describes the impact of initially dissolved O_2 on the steady-state γ -radiolysis of water as a function of pH. The radiolysis kinetic model was used to examine the radiolysis behaviour at short time scales, infer the radical concentrations that cannot be followed experimentally, and confirm the experimental molecular product concentrations observed at longer times. Experimentally, this work was completed prior to the mass transfer data set presented in Chapter 3. However, in order to accurately model the effect of a gaseous impurity such as oxygen on the steady-state radiolysis behavior, it was determined that the aqueous-gas partitioning of volatile species should first be included in the radiolysis model. As a result, the kinetic modeling for this data set was only performed after the effects of aqueous-gas phase mass transfer were evaluated and added to the basic water radiolysis model previously described in Section 2.3.

4.2 EXPERIMENTAL PROCEDURE

Oxygenated solutions were prepared as described in detail in Section 2.2.1 with saturating gases of 10, 20, or 35% v/v ultra high purity oxygen with an argon balance (Praxair, impurity 0.001%). In all vials, the gas volume to aqueous volume, V_g/V_{aq} , in

the vials was maintained constant at 1:1, and the aqueous-gas interfacial area was equal to the cross-sectional area of the vials (3.14 cm²).

Irradiations were carried out at an absorption dose rate of 2.5 Gy·s⁻¹ over a total time period of 5 h. At hourly intervals, individual test vials were removed from the ⁶⁰Co gamma cell and analyzed for the stable molecular water radiolysis products H₂O₂, H₂, and O₂ by UV-Visible spectrophotometry and gas chromatography as described in Section 2.2.

4.3 THE WATER RADIOLYSIS MODEL

The water radiolysis reaction set and additional mass transfer parameters that comprise the basic chemical kinetics model have been described previously in Section 2.3 and in Chapter 3. The kinetics of the coupled reaction set (termed the model) were solved using a commercially available software package, FACSIMILE [11]. In the current study, the model has been used to identify the key reactions that control the radiolysis product concentrations and to interpret the experimental data.

4.4 RESULTS AND DISCUSSION

4.4.1 Time-Dependent Behaviour of Water Radiolysis Products

The radiolytic decomposition of water generates the primary radiolysis products (reaction 4.1) that quickly react with one another to generate additional reactive species such as O₂ and •O₂⁻ [12-16].



Figure 4.1 shows the model prediction for the time-dependent behaviour of the primary and secondary water radiolysis products under deaerated conditions at pH 6.0 (a) and 10.6 (b). Note that the concentration and time axes are both plotted on a log scale to accommodate the large changes in concentration that are observed over a time scale that spans many orders of magnitude. At both pHs, the concentrations of the radical and molecular radiolysis products show distinct behaviour at different times. At very early irradiation times (< 10⁻⁵ s), the concentrations of the primary radiolysis products increase linearly. The increase is observed to be identical at pH 6.0 and 10.6. At intermediate

times ($10^{-5} > t < 1$ s), the secondary radiolysis products (O_2 , $\bullet O_2^-$ and HO_2) are produced in the water at fast rates as the radical primary product concentrations plateau to a steady state. However, the concentrations of the molecular primary products, H_2 and H_2O_2 , continue to increase at a similar rate as that seen at shorter times. At longer time scales (> 1 s), the concentrations of the primary radical species ($\bullet e_{aq}^-$, $\bullet H$, $\bullet OH$) are lower than those of the molecular products (H_2 , O_2 and H_2O_2). This effect is more pronounced at pH 10.6. Additionally, at pH 6.0 the concentrations of all the radiolysis products approach steady state much faster than at the higher pH, as observed in Figure 4.1.

Figure 4.2 shows the changes in the behaviour of the radiolysis products for solutions with initially added O_2 ($2.3 \times 10^{-4} \text{ mol}\cdot\text{dm}^{-3}$) at pH 6.0 (a) and 10.6 (b). Similar to results from tests under deaerated conditions, the primary radiolysis product concentrations increase linearly at very early times. However for both pHs, on the time scale of about 10^{-6} s, the concentrations of $\bullet e_{aq}^-$ and $\bullet H$ plateau and remain low compared to the other radiolysis products. The secondary radiolysis products $\bullet O_2^-$ and HO_2 are formed almost immediately upon irradiation (as compared to after $\sim 10^{-3}$ s in deaerated water). Comparison of Figure 4.1a and Figure 4.2a shows that the molecular product concentrations in pH 6.0 solutions reach much higher values when dissolved oxygen is initially present. At pH 10.6, the steady-state concentrations of the molecular products are attained more quickly in oxygenated compared to deaerated solutions. By examination of Figure 4.2, the concentration profiles of the primary radical and molecular water radiolysis products show little dependence on pH in initially oxygenated solutions.

The radiolysis product concentration profiles presented in Figure 4.1 and Figure 4.2 reveal a distinct conversion in speciation behaviour from short to long time scales. More specifically, for times $< 10^{-5}$ s, the kinetic model shows that the product concentrations attained for a given species are independent of pH (and virtually independent of the presence of any additional dissolved species). In contrast, at times > 1 s, differences in the radiolysis speciation are observed as the pH is changed, and the speciation that occurs is sensitive to the presence of initially dissolved solutes. These long-term effects can be better understood by identifying the key reactions that control the molecular and radical species levels at steady state.

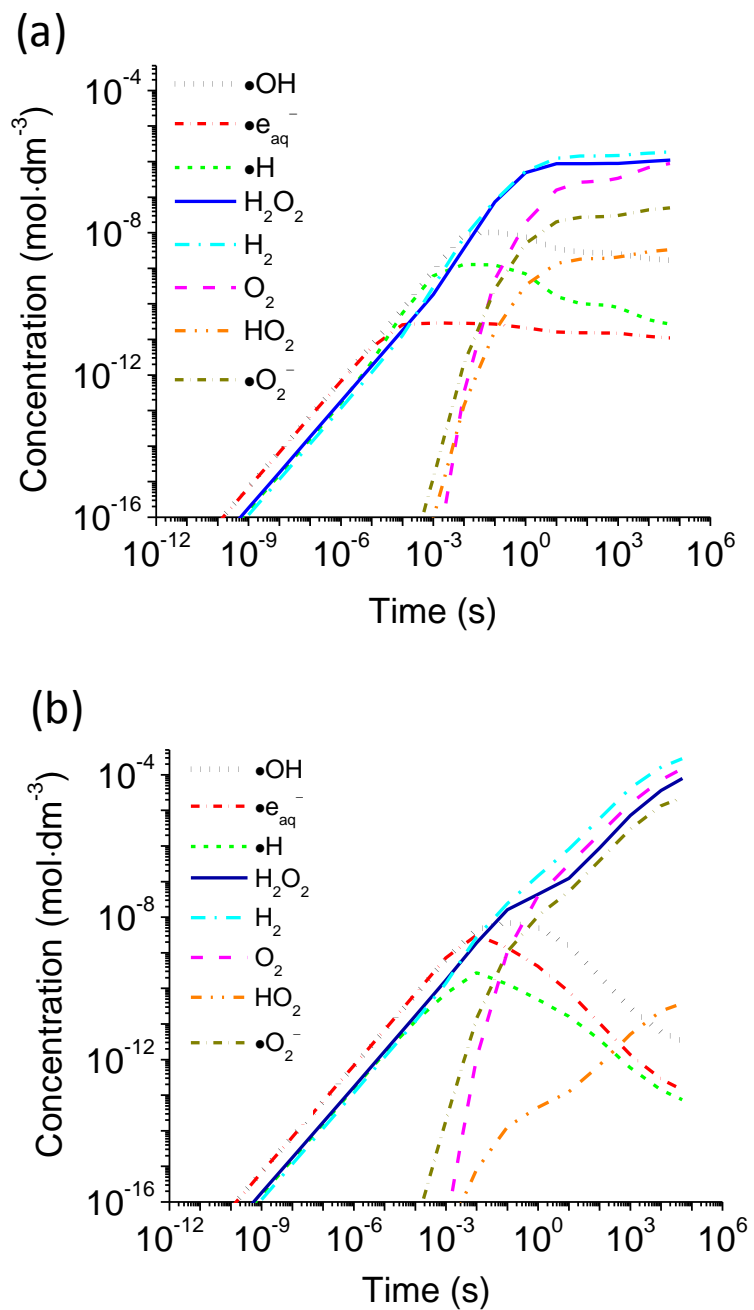


Figure 4.1: Model predictions of water radiolysis product behaviour at pH 6.0 (a) and pH 10.6 (b) for deaerated water as a function of time at 2.5 Gy·s⁻¹.

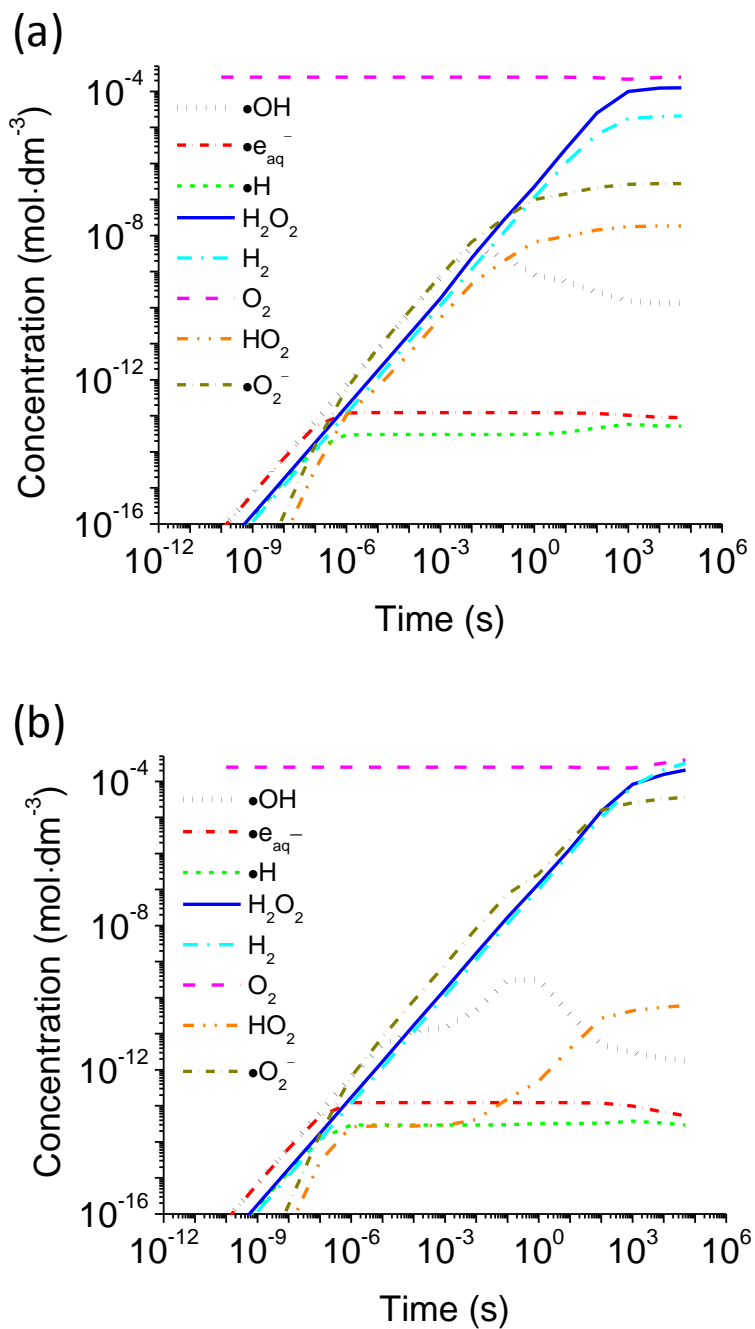


Figure 4.2: Model predictions of water radiolysis product behaviour at pH 6.0 (a) and pH 10.6 (b) for water with $2.3 \times 10^{-4} \text{ mol}\cdot\text{dm}^{-3}$ of initially dissolved O_2 as a function of time at $2.5 \text{ Gy}\cdot\text{s}^{-1}$.

The radiolysis of pure water under long-term irradiation conditions has been studied for full vials [17] and vials with a headspace gas [10]. These studies included both experiments and model simulations to understand the complex radiolysis kinetics and focused on identifying key reactions that determine the concentrations of molecular water radiolysis products H_2 and H_2O_2 in different pH regions.

4.4.1.1 Time-Dependent Behaviour in Initially Deaerated Water

For initially deaerated water at a low pH with an available headspace, hydrogen is produced by radiolysis, and it is removed by its reaction with radiolytically-produced $\bullet OH$ and its transfer to the gas phase:



where $k_{app}^{H_2}(t)$ is the apparent rate constant for the mass transfer of hydrogen from the aqueous to the gas phase, as defined in Chapter 3. Similarly, the primary production and removal reactions for non-volatile H_2O_2 in deaerated water were established previously:



Except at short time scales (< 1 s), the net changes in the concentrations of H_2 and H_2O_2 are relatively small with time, as demonstrated in Figure 4.1a. A steady-state approximation can thus be applied using only the main reactions listed above to obtain analytical solutions for the rate equations, given in Equations E4.1 and E4.2. The analytical solutions define the concentrations for the molecular species as a function of the radical species:

$$[\text{H}_2(\text{aq})]_t^{HS} \approx \frac{k_{Rad}^{H_2}}{k_{R4.2}[\bullet\text{OH}]_t^{HS} + k_{app}^{H_2}(t)} \quad k_{Rad}^{H_2} \approx C_R G_{H_2} D_R \quad \text{E4.1}$$

$$[\text{H}_2\text{O}_2]_t^{HS} \approx \frac{k_{Rad}^{H_2O_2}}{k_{R4.4}[\bullet\text{OH}]_t^{HS} + k_{R4.5}[\bullet e_{aq}^-]_t^{HS}} \quad k_{Rad}^{H_2O_2} \approx C_R G_{H_2O_2} D_R \quad \text{E4.2}$$

where $k_{R4.2}$, $k_{R4.4}$, and $k_{R4.5}$ are bimolecular rate constants, C_R is a unit conversion constant (1.036×10^{-7}), G_x is the G-value for production of species x at 25 °C, and D_R is the gamma-radiation dose rate in units of $\text{Gy}\cdot\text{s}^{-1}$ (2.5 in this work). For irradiation at a constant dose rate, $C_R G_x D_R$ is equivalent to a zeroth-order rate constant, k_{Rad}^x .

As stated in Chapter 3, the effect of interfacial transfer on $[\text{H}_2(\text{aq})]$ is small for the experimental conditions used, and Equation E4.1 can be reduced to:

$$[\text{H}_2(\text{aq})]_t^{HS} \approx \frac{k_{Rad}^{H_2}}{k_{R4.2}[\bullet\text{OH}]_t^{HS}} \quad \text{E4.3}$$

These analytical equations state that the concentrations of $\text{H}_2(\text{aq})$ and H_2O_2 are inversely proportional to the concentrations of $\bullet e_{aq}^-$ and $\bullet\text{OH}$. Since the molecular radiolysis product behaviour is strongly influenced by changes in the radical species concentrations, it is important to examine the behaviour of these key radical products as well. Primary radiolysis (reaction 4.1) remains the main production pathway for the radicals, but they can be removed through other reaction pathways in addition to those discussed above:

For $\bullet\text{OH}$:



And for $\bullet e_{aq}^-$:



Figure 4.1 shows that even under deaerated conditions, interaction between the molecular and radical radiolysis products leads to the generation of the secondary radiolysis product O_2 that can establish a pseudo-catalytic reaction cycle with the radical species by reactions 4.8 and 4.6. As water radiolysis progresses, the accumulation of O_2 changes the relative contributions of different radical removal pathways. Reactions 4.8 and 4.6 become more important as the concentration of O_2 builds up, leading to lower concentrations of $\bullet e_{aq}^-$ and $\bullet OH$ in the system. As a result the removal rates of H_2 and H_2O_2 via reactions with $\bullet OH$ and $\bullet e_{aq}^-$ decrease (E4.2 and E4.3) and this leads to higher molecular product concentrations. Hence, at longer irradiation times (> 1 s), the concentrations of the primary radical species are lower than those of the molecular products.

Also observed in Figure 4.1 is that the molecular product concentrations reached at steady state are about three orders of magnitude larger in deaerated water at pH 10.6 than in deaerated water at pH 6.0. These dramatic changes in concentration occur in the pH range 9 to 11 [17]. At pH 10.6, the solution pH is higher than the pK_a of $\bullet H$ (9.6). This causes reaction 4.7 (the forward reaction as shown) to be very slow. The reaction of $\bullet e_{aq}^-$ with the secondary radiolysis product, O_2 (reaction 4.8) then becomes an important removal path for $\bullet e_{aq}^-$. However, the resulting product, $\bullet O_2^-$, reacts with $\bullet OH$ to reform O_2 (reaction 4.6). Once this pseudo-catalytic cycle is established, the secondary radiolysis product O_2 can continuously remove the radicals from the aqueous phase. Consequently, at high pH, reactions 4.8 and 4.6 become the dominant removal pathways for the radical species. This leads to a reduction of the loss rates of the molecular products, thus increasing their concentrations.

A consequence of this pH dependence is that, for $pH > 9$, the concentrations of O_2 and H_2O_2 must reach higher levels before the rate of removal of $\bullet e_{aq}^-$ matches its rate of radiolytic production. While O_2 is generated by reaction 4.6, H_2O_2 can also be radiolytically produced by reaction 4.9 in this pH region:



The accumulation of molecular products, however, is fairly slow, and attainment of steady state is delayed at high pH compared to a lower pH (Figure 4.1). Furthermore, considerable net production of O₂ leads to the generation of secondary and tertiary oxygen products, such as •O₂⁻ and •O₃⁻, and these oxygen products can significantly alter the behaviour of the molecular radiolysis products [10,16,17]



Thus, at pH 10.6, more complex relationships are required to describe the steady-state concentrations of the molecular products:

$$[\text{H}_2(\text{aq})]_t^{\text{HS}} \approx \frac{k_{\text{Rad}}^{\text{H}_2}}{k_{\text{R4.2}}[\bullet\text{OH}]_t^{\text{HS}} + k_{\text{R4.11}}[\bullet\text{O}_3^-]_t^{\text{HS}}} \quad \text{E4.4}$$

$$[\text{H}_2\text{O}_2]_t^{\text{HS}} \approx \frac{k_{\text{Rad}}^{\text{H}_2\text{O}_2} + k_{\text{R4.9}}[\bullet\text{HO}_2]_t^{\text{HS}}[\bullet\text{O}_2^-]_t^{\text{HS}}}{k_{\text{R4.4}}[\bullet\text{OH}]_t^{\text{HS}} + k_{\text{R4.5}}[\bullet\text{e}_{\text{aq}}^-]_t^{\text{HS}} + k_{\text{R4.12}}[\bullet\text{O}_3^-]_t^{\text{HS}}} \quad \text{E4.5}$$

Although the molecular and radical products are produced continuously by water radiolysis at different rates and have different removal paths, their steady-state concentrations are still inversely related.

4.4.1.2 Time-Dependent Behaviour in Initially Oxygenated Water

With initially added O₂ (2.3 × 10⁻⁴ mol·dm⁻³) (Figure 4.2) the behaviour of the radical and molecular products was similar to that seen in deaerated pH 10.6 water (Figure 4.1b), with the molecular radiolysis products reaching similar steady-state concentrations in the oxygenated solutions and in the alkaline deaerated solution. However, the steady state is reached much faster when O₂ is initially present than under deaerated conditions at high pH where O₂ is generated slowly. For oxygenated solutions, reactions 4.8 and 4.6 are the dominant removal paths for •e_{aq}⁻ and •OH, regardless of pH,

thereby increasing the steady-state concentrations of H_2 and H_2O_2 by slowing the molecular products' removal by reactions 4.2, 4.4 and 4.5.

4.4.2 Effect of Initially Dissolved O_2 on Steady-State Radiolysis Behaviour

Irradiation experiments were performed with aqueous solutions saturated with oxygen concentrations of 0%, 10%, 23% and 35% v/v. The concentrations of H_2 in the gas phase and H_2O_2 in the aqueous phase were measured as a function of irradiation time and the experimental values were compared to the model simulations. The chemical kinetics model was also used to infer the behaviour of the radical species (which cannot be measured directly in our experimental design) to explain the changes observed in the molecular radiolysis product concentrations.

4.4.2.1 Hydrogen Behaviour as a Function of pH

Figure 4.3 shows the concentration profiles of radiolytically-generated $H_2(g)$ in the headspace and $H_2(aq)$ in the aqueous phase for pH 6.0 solutions with various concentrations of initially dissolved O_2 . The time-dependent $[H_2(g)]$ and $[H_2(aq)]$ produced in pH 10.6 solutions under different oxygenation conditions are shown in Figure 4.4. The symbols are the experimental data and the lines are the model predictions. For both pHs there is a good agreement between the experimental and the model predicted concentrations. From Figure 4.3b and Figure 4.4b it is observed that $H_2(aq)$ reaches steady state after approximately 1 h, whereas the concentration of $H_2(g)$ increases continuously (due to the ongoing transfer of H_2 from the aqueous phase) and does not reach a steady state even after 5 h of irradiation.

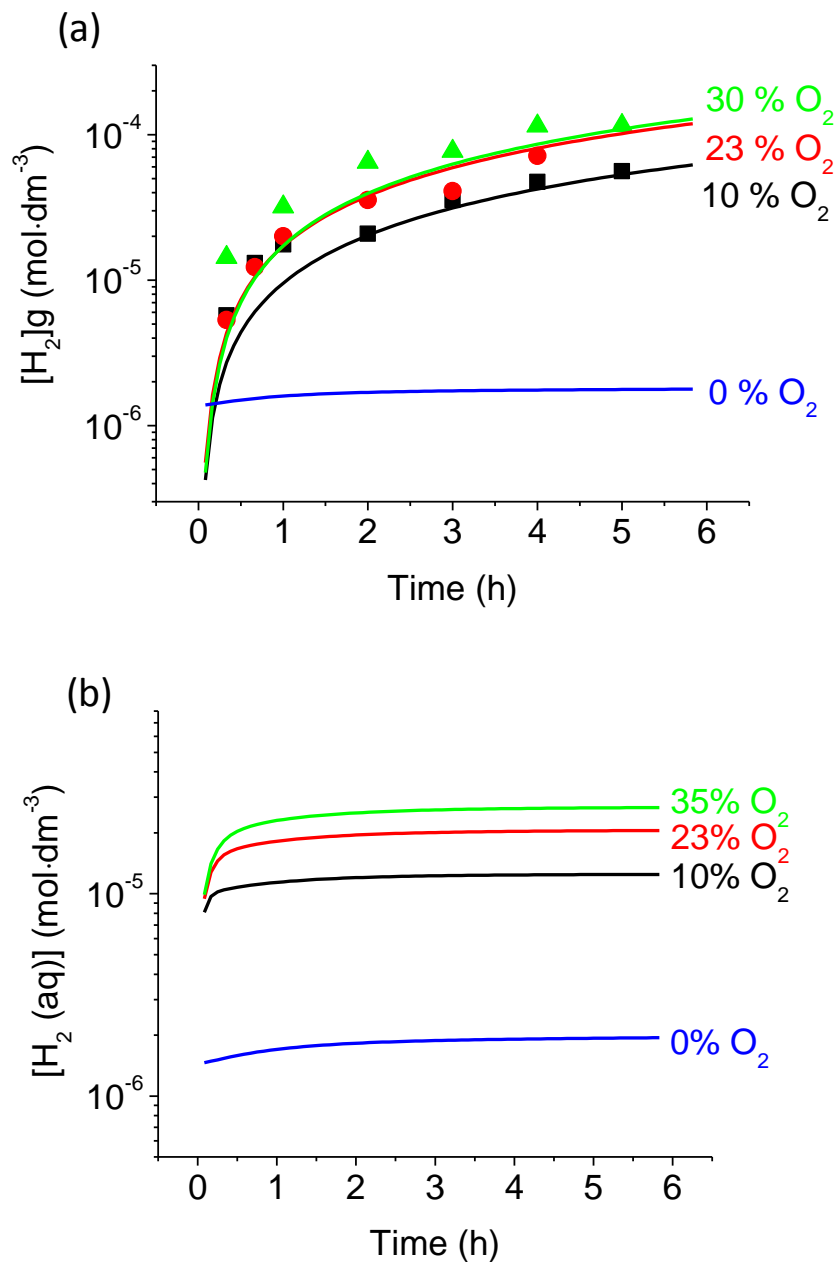


Figure 4.3: The [H₂(g)] (a) and [H₂(aq)] (b) concentrations shown as a function of irradiation time for headspace samples at pH 6.0 at a dose rate of 2.5 Gy·s⁻¹.

The solid symbols represent the experimental data and the lines show the radiolysis model results for different initial O₂ concentrations: 35% O₂ (▲,—), 23% O₂ (●,—), 10% O₂ (■,—) and 0% O₂ (Ar purged) (—).

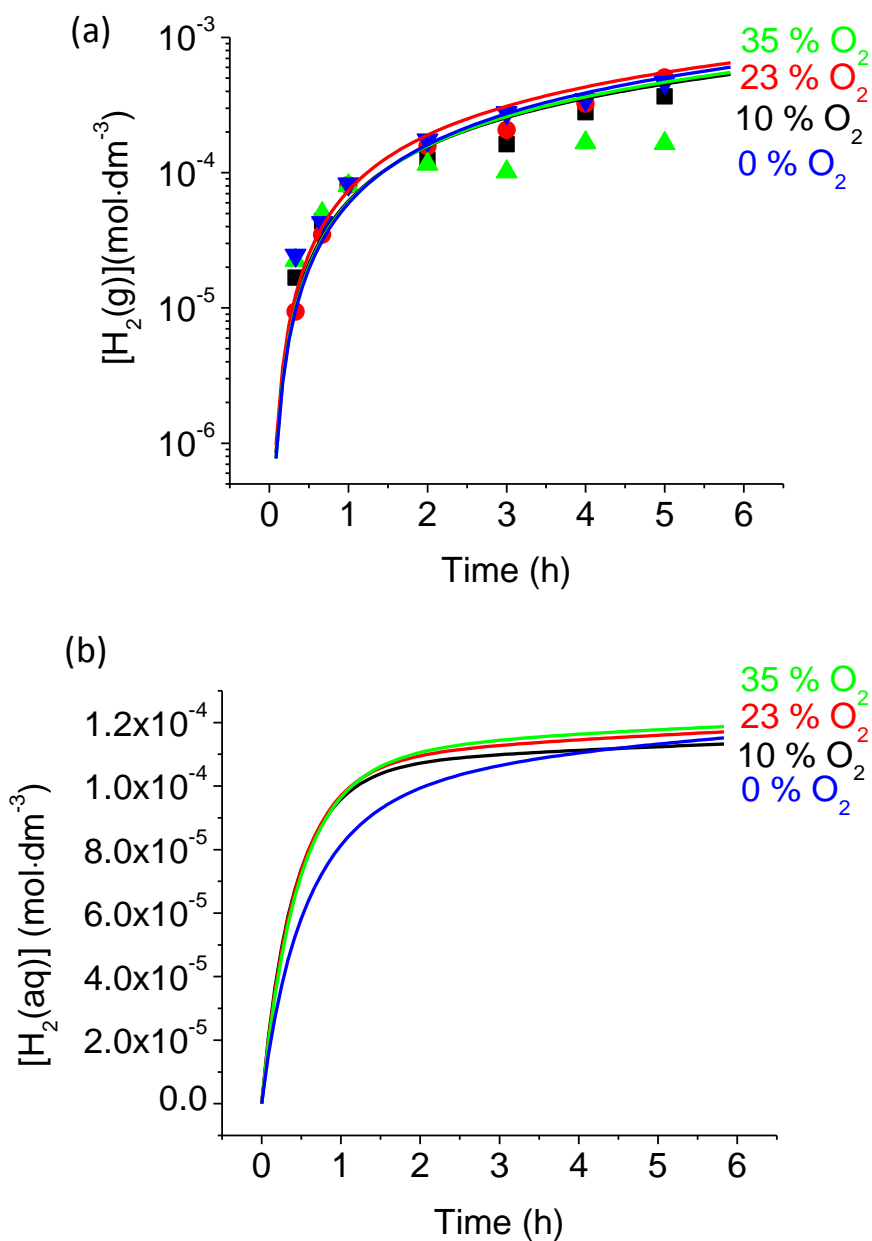


Figure 4.4: The $[H_2(g)]$ (a) and $[H_2(aq)]$ (b) concentrations shown as a function of irradiation time for headspace samples at pH 10.6 at a dose rate of 2.5 Gy·s⁻¹.

The solid symbols represent the experimental data and the lines show the radiolysis model results for different initial O₂ concentrations: 35% O₂ (▲,—), 23% O₂ (●,—), 10% O₂ (■,—) and 0% O₂ (Ar purged) (—).

Considering the radiolytic production of H_2 , Figure 4.3 and Figure 4.4 show that the initial presence of dissolved O_2 induces a greater change in the system at pH 6.0 than at pH 10.6 when compared to the results observed for the irradiation of deaerated water samples. At pH 6.0, the steady-state hydrogen concentration in the gas phase is below the detection limit for initially deaerated water, but increases to $\sim 10^{-4} \text{ mol}\cdot\text{dm}^{-3}$ for 35% oxygenated water. For solutions at pH 10.6, only a moderate change in the hydrogen concentration was measured as the oxygenation level increased, with all test solutions (0-35% O_2) showing $[H_2(g)]$ in the range $1-3 \times 10^{-4} \text{ mol}\cdot\text{dm}^{-3}$. This pH dependence can be explained by the relative change in the steady-state concentrations of the radical species that occurs at each pH when oxygen is introduced. The model-predicted concentration profiles of $\bullet e_{aq}^-$ and $\bullet OH$ in solutions with different concentrations of initially dissolved O_2 are shown for pH 6.0 and 10.6 in Figure 4.5 and Figure 4.6, respectively.

For deaerated water, $[\bullet OH]_{ss}$ is higher at pH 6.0 than at pH 10.6. Because of this, the removal of H_2 described by E4.3 (or E4.4) proceeds more quickly at a lower pH. This kinetic behaviour was observed experimentally where $[H_2(g)]$ was below detection at pH 6.0 but measurable at pH 10.6. For initially oxygenated solutions, the scavenging of $\bullet e_{aq}^-$ by O_2 to generate $\bullet O_2^-$ (reaction 4.8) becomes more effective. The increasing $[\bullet O_2^-]$ subsequently increases the rate of removal of $\bullet OH$ by reaction 4.6. This removal of $\bullet OH$ from the chemical system slows the decomposition of H_2 allowing it to accumulate with time. As higher levels of O_2 are initially dissolved into the water, the resultant $[\bullet e_{aq}^-]_{ss}$ and $[\bullet OH]_{ss}$ will be decreased to a greater extent as observed in Figure 4.5 and Figure 4.6.

Since the steady-state concentrations of both $\bullet OH$ and $\bullet e_{aq}^-$ are (for deaerated water) much higher at a lower pH, reactions 4.8 and 4.6 will proceed more quickly in low pH solutions upon the addition of O_2 . This means there is a greater margin to reduce the radical concentrations at pH 6.0 than at pH 10.6. At pH 10.6, the radical concentrations are already very low (Figure 4.6), so their reactions through the O_2 pathway do not significantly alter their resulting steady states. Thus, at high pH, the decomposition rate of H_2 remains relatively stable over the range of all dissolved O_2 concentrations (Figure 4.4).

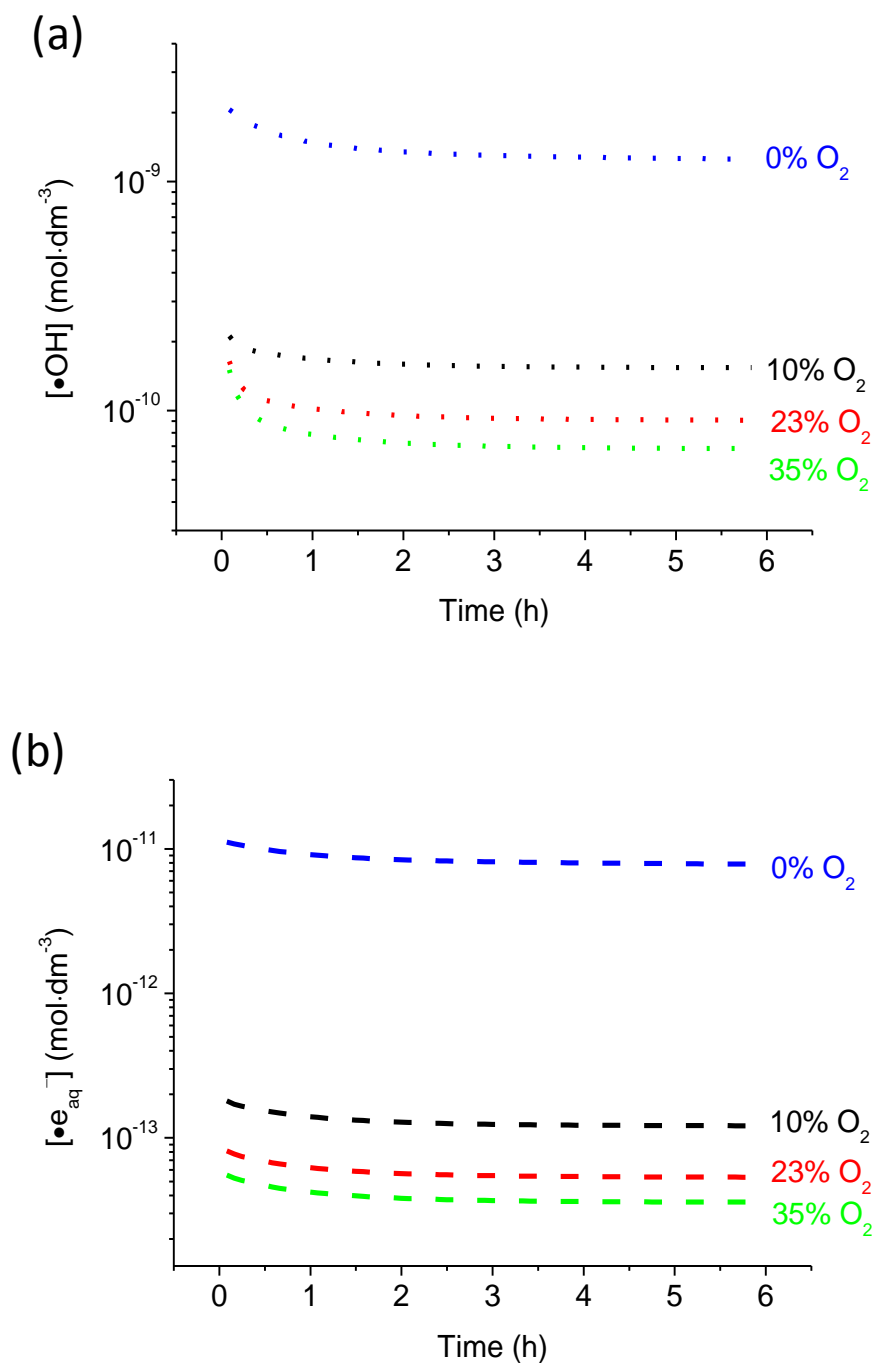


Figure 4.5: Radiolysis model predictions for the concentrations of $\bullet\text{OH}$ (a) and $\bullet\text{e}_{\text{aq}}^-$ (b) as a function of irradiation time for headspace samples at pH 6.0 at a dose rate of $2.5 \text{ Gy}\cdot\text{s}^{-1}$ for different initial O_2 concentrations: 35% O_2 (\cdots , $- -$), 23% O_2 (\cdots , $- -$), 10% O_2 (\cdots , $- -$) and 0% O_2 (Ar purged) (\cdots , $- -$).

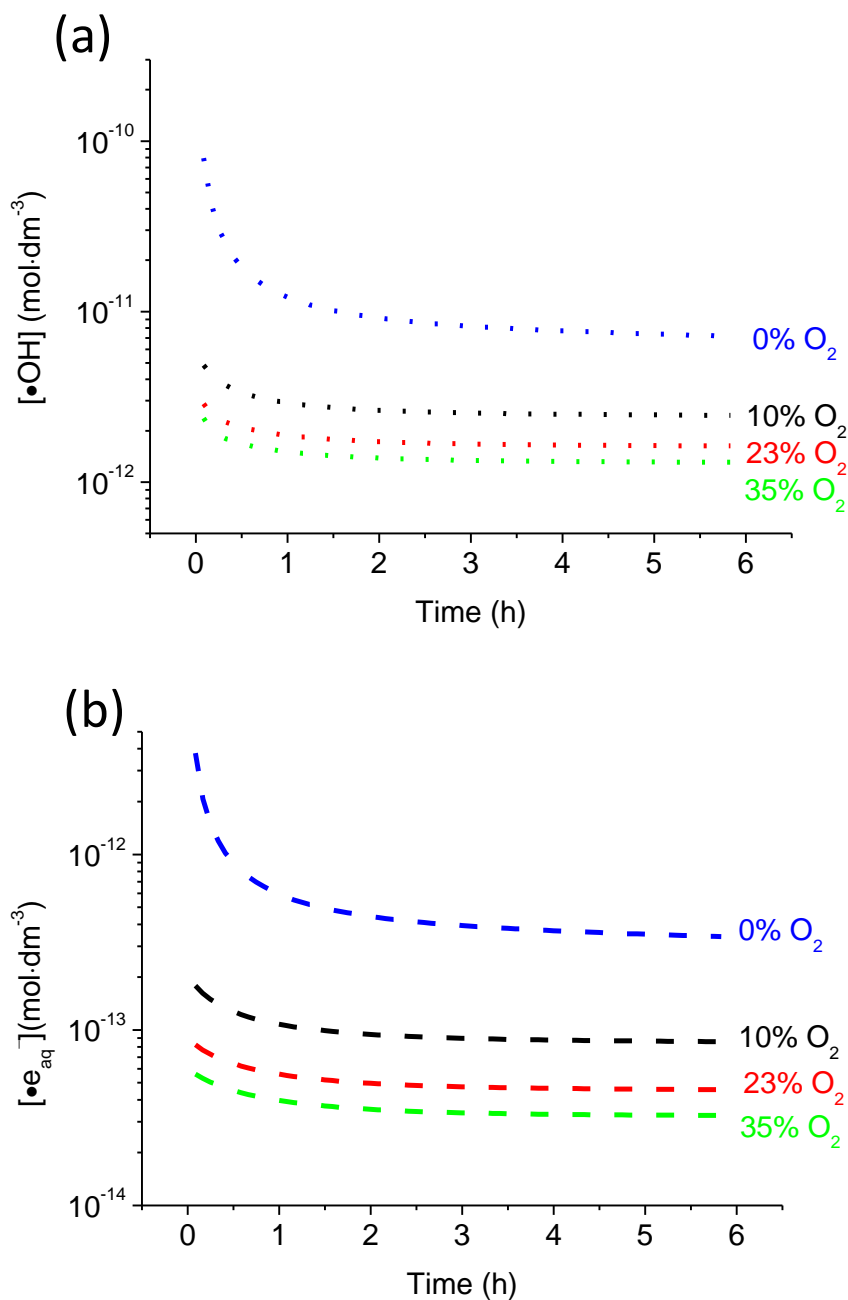


Figure 4.6: Radiolysis model predictions for the concentrations of $\bullet\text{OH}$ (a) and $\bullet\text{e}_{\text{aq}}^-$ (b) as a function of irradiation time for headspace samples at pH 10.6 at a dose rate of $2.5 \text{ Gy}\cdot\text{s}^{-1}$ for different initial O_2 concentrations: 35% O_2 (····, — —), 23% O_2 (····, — —), 10% O_2 (····, — —) and 0% O_2 (Ar purged) (····, — —).

4.4.2.2 Hydrogen Peroxide Behaviour as a Function of pH

The time-dependent concentrations of H_2O_2 generated during water radiolysis for various initial dissolved O_2 concentrations are shown for pH 6.0 (Figure 4.7a) and pH 10.6 (Figure 4.7b). The experimental data is represented by the data points and the kinetic modeling results are shown as solid lines.

Hydrogen peroxide is mainly removed by reaction with $\bullet\text{OH}$ and $\bullet\text{e}_{\text{aq}}^-$ in deaerated water. The presence of O_2 provides $\bullet\text{e}_{\text{aq}}^-$ with an alternative reaction pathway which leads to the production of $\bullet\text{O}_2^-$, and the subsequent removal of $\bullet\text{OH}$. As a result, the presence of initially dissolved oxygen decreases the concentrations of both $\bullet\text{e}_{\text{aq}}^-$ and $\bullet\text{OH}$. Since these radicals impact on the removal rate of H_2O_2 , the resulting steady-state concentration of H_2O_2 , $[\text{H}_2\text{O}_2]_{\text{SS}}$, increases as the amount of dissolved O_2 increases. Although an increase in $[\text{H}_2\text{O}_2]_{\text{SS}}$ is observed with O_2 addition at both pHs studied, the effect is more pronounced at pH 6.0 than pH 10.6. Additionally, the relative increase in $[\text{H}_2\text{O}_2]_{\text{SS}}$ slows as the concentration of the oxygen saturation gas increases beyond 10%. Figure 4.7a shows that the measured $[\text{H}_2\text{O}_2]_{\text{SS}}$ increases from below the detection limit (of $3 \times 10^{-6} \text{ mol}\cdot\text{dm}^{-3}$) for deaerated solutions at pH 6.0 to $6 \times 10^{-5} \text{ mol}\cdot\text{dm}^{-3}$ for solutions with a 10% O_2 saturation. This represents more than a 20-fold increase in concentration. At pH 10.6, an increase in the range of 2 to 4-fold is observed over the same O_2 saturation range. The reduced impact of initially added O_2 on the radiolytic production of hydrogen peroxide at high pH can be easily explained by the radical species behaviour. As previously described for H_2 behaviour, the steady-state radical concentrations are, in general, orders of magnitude smaller at higher pH than at low pH. Hence, when a radical scavenging species, such as O_2 , is added to an alkaline medium, the net change in the radical concentrations will be minimal and the resulting change in molecular species concentrations will be smaller. For example, $[\bullet\text{e}_{\text{aq}}^-]$ drops 80-fold from $8 \times 10^{-12} \text{ mol}\cdot\text{dm}^{-3}$ to $1 \times 10^{-13} \text{ mol}\cdot\text{dm}^{-3}$ moving from 0 to 10% O_2 in pH 6.0 solutions (Figure 4.5b). At pH 10.6, the same change in O_2 saturation results in only a 4-fold decrease ($4 \times 10^{-13} \text{ mol}\cdot\text{dm}^{-3}$ to $9 \times 10^{-14} \text{ mol}\cdot\text{dm}^{-3}$). A similar trend is observed in $\bullet\text{OH}$ as a function of pH.

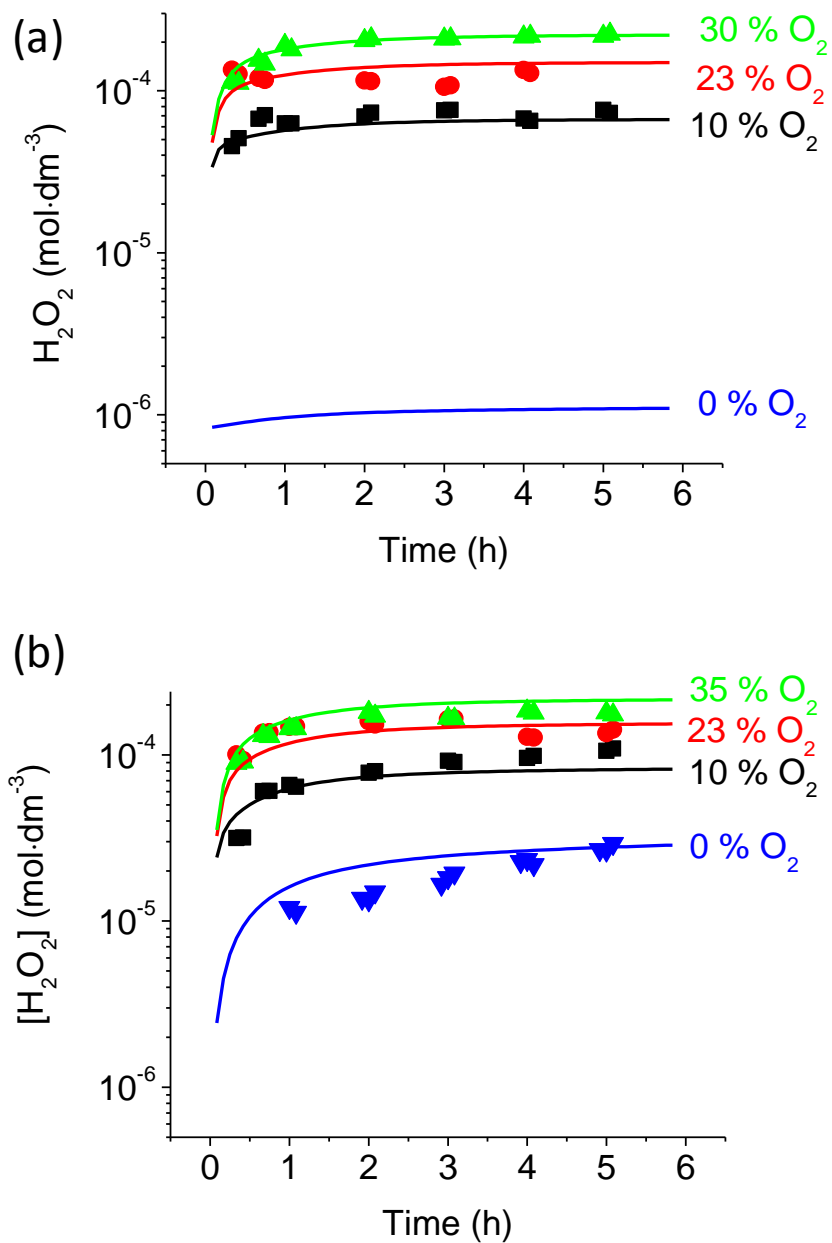


Figure 4.7: The H_2O_2 concentrations shown as a function of irradiation time for headspace samples at pH 6.0 (a) and pH 10.6 (b) at a dose rate of $2.5 \text{ Gy}\cdot\text{s}^{-1}$. The solid symbols represent the experimental data and the lines show the radiolysis model results for different initial O_2 concentrations: 35% O_2 (\blacktriangle ,—), 23% O_2 (\bullet ,—), 10% O_2 (\blacksquare ,—) and 0% O_2 (Ar purged) (\blacktriangledown ,—).

An additional observation from this study is that dissolved O_2 appears to have a greater impact on $[H_2O_2]$ than on $[H_2]$. Both $[H_2O_2]_{SS}$ and $[H_2]_{SS}$ will be determined by the relative rates of the main decomposition reactions; for H_2O_2 by reactions with $\bullet OH$ and $\bullet e_{aq}^-$, and for H_2 by reaction with $\bullet OH$. Dissolved O_2 reacts directly with $\bullet e_{aq}^-$ to alter its eventual steady-state concentration, however the effect of oxygen on $\bullet OH$ is indirect, proceeding through the reactive intermediate $\bullet O_2^-$. As a result, the effect of O_2 is most noticeable for water radiolysis products whose decompositions are directly related to $[\bullet e_{aq}^-]$, as is the case for H_2O_2 .

4.4.2.3 *Effect of Dissolved Oxygen for Samples with No Headspace*

A subset of experiments on oxygenated solutions in tests with no gas headspace were performed at pH 6.0 and pH 10.6. The results for the measured aqueous hydrogen and hydrogen peroxide concentrations are presented in Figures 4.8 and 4.9, respectively. Once more the model calculated concentration profiles show good agreement with the experimental data

By comparison with Figures 4.3b, 4.4b, and 4.7, the $[H_2(aq)]$ and $[H_2O_2]$ measured for full test vials are very similar to the concentrations of these species found in tests with a headspace. This is as expected since the interfacial transfer of oxygen and hydrogen do not cause significant changes in the aqueous phase concentrations under the experimental conditions studied. As described previously in Chapter 3, oxygen is already at equilibrium between the gas and liquid phases due to the initial saturation of the solution with a high concentration of oxygen. Furthermore, due to the geometry of our test vial, the interfacial transfer of hydrogen will be insufficient to dramatically alter the aqueous concentration of $\bullet OH$. As a result, neither the interfacial transfer of oxygen or hydrogen are likely to impact the aqueous concentrations of radicals like $\bullet OH$, $\bullet e_{aq}^-$, or $\bullet O_2^-$ and affect their subsequent aqueous phase reaction kinetics. This explains the similarity in concentration profiles for molecular products in the aqueous phase for tests both with and without a gas headspace.

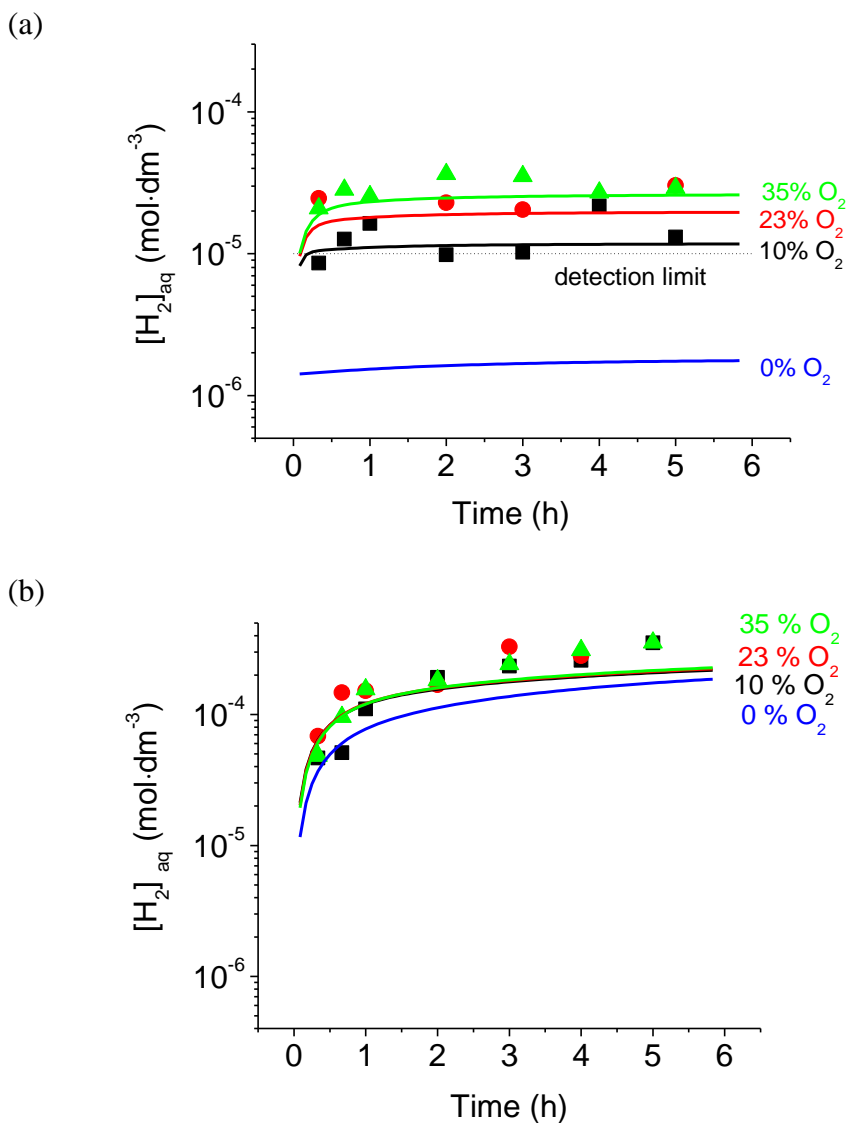


Figure 4.8: The $\text{H}_2(\text{aq})$ concentrations shown as a function of irradiation time for full samples at pH 6.0 (a) and pH 10.6 (b) at a dose rate of $2.5 \text{ Gy}\cdot\text{s}^{-1}$. The solid symbols represent the experimental data and the lines show the radiolysis model results for different initial O_2 concentrations: 35% O_2 (\blacktriangle ,—), 23% O_2 (\bullet ,—), 10% O_2 (\blacksquare ,—) and 0% O_2 (Ar purged) (—).

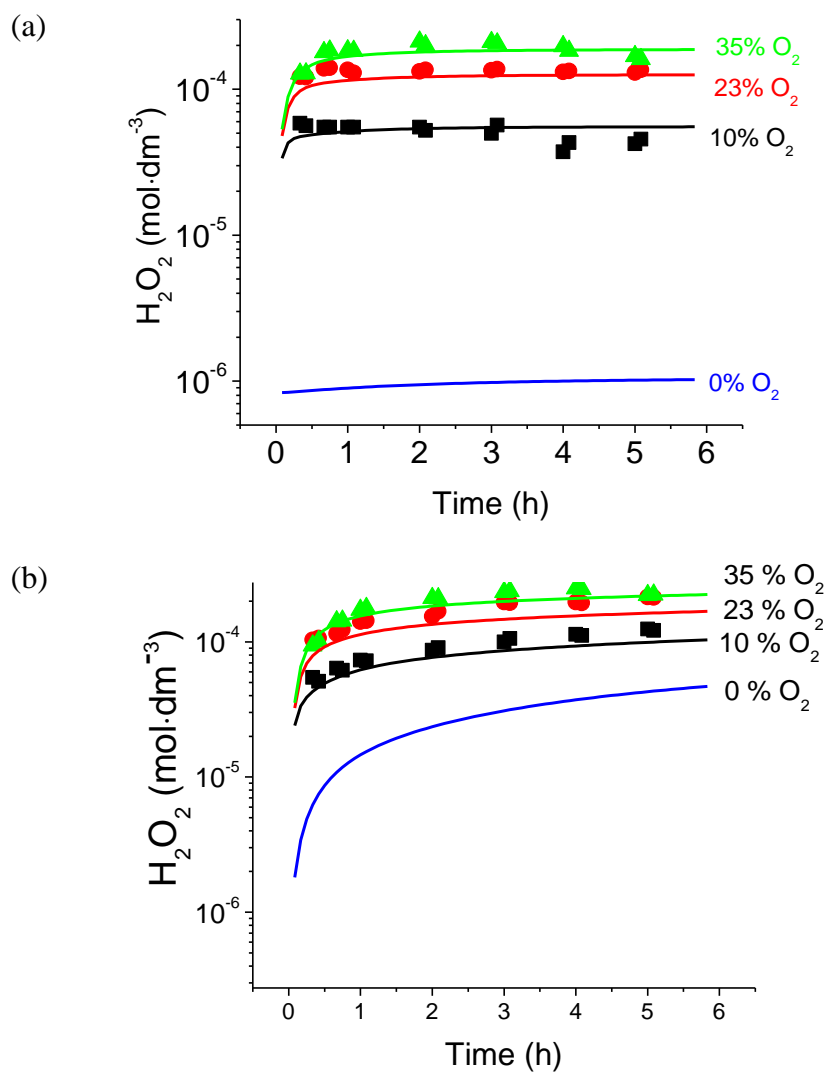


Figure 4.9: The H_2O_2 concentrations shown as a function of irradiation time for full samples at pH 6.0 (a) and pH 10.6 (b) at a dose rate of $2.5 \text{ Gy}\cdot\text{s}^{-1}$. The solid symbols represent the experimental data and the lines show the radiolysis model results for different initial O_2 concentrations: 35% O_2 (\blacktriangle , —), 23% O_2 (\bullet , —), 10% O_2 (\blacksquare , —) and 0% O_2 (Ar purged) (—).

4.5 CONCLUSIONS

This time-dependent kinetic study has shown that the long-term behaviour of water radiolysis products with a continuous radiation flux is very different from the behaviour observed at short time scales. While the concentrations of radical and molecular primary radiolysis products are on the same order of magnitude at early times, prolonged irradiation allows the build-up in the concentration of the secondary radiolysis product O_2 to establish a pseudo-catalytic reaction cycle with radical species. This results in lower radical and higher molecular product concentrations at long times.

The pH study of systems containing the dissolved molecular radiolysis product O_2 has shown that the presence of O_2 indirectly alters the steady-state concentrations of the measurable molecular radiolysis products H_2O_2 and H_2 that arise in a system. The dissolved O_2 initiates the scavenging of the radical species that drive the removal of those molecular products. In particular, dissolved O_2 reacts directly to reduce $[e_{aq}^-]$ and produce a reactive intermediate ($\bullet O_2$) that reduces $[\bullet OH]$. This results in a net increase in the molecular product concentrations as the removal rates of H_2 (by reaction with $\bullet OH$) and H_2O_2 (by reaction with $\bullet OH$ and e_{aq}^-) are decreased.

The impact of oxygen addition on the steady-state concentrations of H_2O_2 and H_2 was consistently more pronounced for low pH solutions. At $pH < 8$, the steady-state radical concentrations are relatively high, and the net result of scavenging is a very large drop in $[e_{aq}^-]_{SS}$ and $[\bullet OH]_{SS}$ in the presence of dissolved O_2 . At a higher pH, the effect of dissolved O_2 is smaller because the radical concentrations are already low and a further decrease in their steady-state concentrations has less impact.

Dissolved O_2 was also found to have a greater effect on $[H_2O_2]$ than on $[H_2]$. In oxygenated solutions, the concentration of e_{aq}^- is directly diminished by reaction with O_2 , while $\bullet OH$ is only indirectly affected as it is removed by reaction with the $\bullet O_2^-$ intermediate. Hence, the H_2 removal pathway via reaction with $\bullet OH$ is only indirectly related to the presence of dissolved oxygen. In contrast, since H_2O_2 reacts with both $\bullet OH$ and e_{aq}^- , its removal is more directly impacted by the presence of additional oxygen.

These results show that solution pH and dissolved reactive species can have a major impact on the steady-state concentrations of the molecular species important to redox chemistry that arise as a result of exposure to a radiation field.

The assembled chemical kinetics model for water radiolysis chemistry has effectively reproduced the experimentally measured data observed over the wide range of experimental conditions outlined in this Chapter and in the previous Chapter 3. This demonstrates that the chemical reactions and transport equations that comprise the basic radiolysis model are correct and sufficiently comprehensive. Furthermore, it gives us confidence that the chemical kinetics model can be used to evaluate changes in radical concentrations (which cannot be measured experimentally) and improve our mechanistic understanding of solute effects on aqueous irradiated systems.

4.6 REFERENCES

- [1] Pastina, B., Isabey, J., Hickel, B., "The influence of water chemistry on the radiolysis of the primary coolant water in pressurized water reactors", *J. Nucl. Mater.*, **1999**, 264, 309-318.
- [2] Stefanic, I., LaVerne, J.A., "Temperature dependence of the hydrogen peroxide production in the gamma-radiolysis of water", *J. Phys. Chem. A*, **2002**, 106, 447-452.
- [3] Cowan, R.L., Indig, M.E., Kass, J.N., Law, R.J., Sundberg, L.L. "Experience with hydrogen water chemistry in boiling water reactors", Fourth International Conference on Water Chemistry of Nuclear Systems, Bournemouth, U.K., 1986.
- [4] Pastina, B., LaVerne, J.A., "Effect of molecular hydrogen on hydrogen peroxide in water radiolysis", *J. Phys. Chem. A*, **2001**, 105, 9316-9322.
- [5] Ishigure, K., Fujita, N., Tamura, T., Oshima, K., "Effect of gamma radiation on the release of corrosion products from carbon steel and stainless steel in high temperature water", *Nucl. Technol.*, **1980**, 50, 169-177.
- [6] Daub, K., Zhang, X., Noël, J.J., Wren, J.C., "Gamma-radiation-induced corrosion of carbon steel in neutral and mildly basic water at 150°C", *Corros. Sci.*, **2011**, 53, 11-16.
- [7] Daub, K., Zhang, X., Noël, J.J., Wren, J.C., "Gamma radiation-induced carbon steel corrosion", *ECS Trans.*, **2011**, 33, 15-24.
- [8] Daub, K., Zhang, X., Noël, J.J., Wren, J.C., "Effects of γ -radiation versus H₂O₂ on carbon steel corrosion", *Electrochim. Acta*, **2010**, 55, 2767-2776.
- [9] Knapp, Q.W., Wren, J.C., "Film formation on type-316L stainless steel as a function of potential: Probing the role of gamma-radiation", *Electrochim. Acta*, **2012**, 80, 90-99.
- [10] Yakabuskie, P.A., Joseph, J.M., Wren, J.C., "The effect of interfacial mass transfer on steady-state water radiolysis", *Radiat. Phys. Chem.*, **2010**, 79, 777-785.
- [11] *FACSIMILE Kinetic Modelling Software*, MCPA Software Ltd., 2003.
- [12] Spinks, J.W.T., Woods, R.J. *An Introduction to Radiation Chemistry*, 3rd ed., Wiley-Interscience: New York, 1990.
- [13] Draganic, I.G., Draganic, Z.D. *The Radiation Chemistry of Water*, Academic Press, Inc.: New York, 1971.

- [14] Allen, A.O. *The Radiation Chemistry of Water and Aqueous Solutions*, Van Nostrand Company, Inc.: New York, 1961.
- [15] *Radiation Chemistry: Principles and Applications*, Farhataziz, Rodgers, A.J., Eds., VCH Publishers, Inc.: New York, 1987.
- [16] Wren, J.C. In *ACS Symposium Series: Nuclear Energy and the Environment*, Chien, W., Mincher, B., Eds., American Chemical Society: Washington, D.C., 2010, p 271-295.
- [17] Joseph, J.M., Choi, B.S., Yakabuskie, P.A., Wren, J.C., "A combined experimental and model analysis on the effect of pH and O₂(aq) on γ -radiolytically produced H₂ and H₂O₂", *Radiat. Phys. Chem.*, **2008**, 77, 1009-1020.

CHAPTER 5 LONG TERM γ -RADIOLYSIS KINETICS OF NO_3^- AND NO_2^- SOLUTIONS*

5.1 INTRODUCTION

Many of the current operational and safety issues associated with nuclear power plants are related to materials degradation. An ability to accurately monitor and control the redox state of the coolant could support strategies to reduce corrosion rates and increase the lifetime of the piping. Chapter 4 showed that higher initial dissolved oxygen concentrations in irradiated water lead to increased production of hydrogen peroxide, which has been shown to be one of the main redox active species responsible for the corrosion of carbon steel [1,2]. Careful control of the redox conditions of the coolant during plant outages and start-up to remove oxidants prior to raising the coolant temperature to above 150°C has been shown to minimize the risk of degradation of system materials [3,4]. Similarly, during operation, many BWR and PWR nuclear plants have adopted hydrogen water chemistry to control the radiolytic production of oxidants and reduce the risk of SCC for in-core materials [5-8].

Optimizing aqueous chemistry in environments where ionizing radiation fields are present requires a detailed understanding of the chemistry driven by water radiolysis during long duration irradiation. Over longer time frames, slower reactions and interfacial mass transport processes, such as corrosion of piping surfaces or colloid formation from dissolved metal species, become important. The rates of these processes are hence determined by the (pseudo) steady-state concentrations of the aqueous chemical species established at times well beyond the sub-microsecond time scale typically employed in pulse radiolysis [2,9-11]. As a consequence, the changes in the radiation chemistry that occur when solutes are initially present in the water must be evaluated over longer irradiation times to fully understand the effect they may have on the steady state and subsequent corrosion processes.

* Reproduced in part with permission from the American Chemical Society:

Yakabuskie, P.A., Joseph, J.M., Stuart, C.R., Wren, J.C., "Long-term γ -radiolysis kinetics of NO_3^- and NO_2^- solutions", *J. Phys. Chem. A*, **2011**, *115*, 4270-4278.

The previous two chapters demonstrated that the basic water radiolysis reaction set is robust to a variety of variables, including pH, headspace volume, and oxygenation conditions. As a result, expansion of the basic model by the addition of supplementary reaction sets (to include interactions of water radiolysis products with other chemical solutes) was deemed appropriate. While several types of impurities can be present in the irradiated aqueous nuclear systems, nitrogen-containing species are among the most common. Nitric acid is used in spent reactor fuel processing and waste treatment, while hydrazine and ammonia are used as corrosion inhibitors or radiolytic oxidant suppressants in nuclear facilities [4,12-14]. Degradation of ion exchange resins used for water purification in coolant systems or unintended air ingress (leading to nitric acid production) may also inadvertently introduce nitrogen compounds into the coolant.

A key result from Chapter 3 and Chapter 4 was that the steady-state concentrations that develop during continuous γ -irradiation are strongly affected by pH and the presence of dilute dissolved species if the dissolved species can react readily with water radiolysis products, and particularly if the reactions of the dissolved solute can proceed in a cyclic manner. Due to the many potential oxidation states of N, ranging from -3 in $\text{NH}_3/\text{NH}_4^+$ to $+5$ in NO_3^- under ambient conditions, nitrogen-containing compounds have the potential to interact cyclically with water radiolysis products. For example, dissolved NO_3^- can react with reducing species (such as $\bullet e_{\text{aq}}^-$, $\bullet\text{H}$, and $\bullet\text{O}_2^-$) to form NO_2^- and the NO_2^- can then react with oxidizing species (such as $\bullet\text{OH}$ and H_2O_2) to regenerate the NO_3^- . Such a series of reactions can affect the balance of the redox-active species in solution and result in significant changes in their steady-state concentrations.

Our understanding of the radiolysis of nitrate and nitrite in water in a continuous radiation flux is not clear, even after several years of investigation [15-19]. Better knowledge of the radiation-induced decomposition of nitrate and nitrite is important because this process occurs not only in nuclear systems, but in a wide range of fields such as atmospheric chemistry, UV-disinfection, and high temperature combustion [20-22]. In particular, studies of high-flux, continuous radiolysis behaviour are very rare. The focus of this work is to identify the set of reactions that control the nitrogen and water radiolysis product speciation during long-term irradiation and to determine how the speciation is affected by the initial solution pH.

This chapter describes the room temperature γ -radiolysis kinetics observed for NO_3^- and NO_2^- solutions. Air- or argon-saturated nitrate or nitrite solutions at pH 6.0 and 10.6 were irradiated and the aqueous concentrations of molecular water decomposition products, H_2 and H_2O_2 , and the variation in the concentrations of NO_3^- and NO_2^- were measured as a function of irradiation time. The experimental data were compared with computer simulations using a comprehensive radiolysis kinetic model to aid in interpretation of the experimental results.

5.2 EXPERIMENTAL PROCEDURE

High-purity sodium nitrate and sodium nitrite were obtained from Sigma-Aldrich (purity $\geq 99\%$) and used without further purification. Deaerated and aerated solutions containing $10^{-3} \text{ mol}\cdot\text{dm}^{-3}$ nitrate or nitrite were prepared using the techniques described in Section 2.2.1. The 20 mL pyrex vials were completely filled with solution and capped with PTFE silicone septa, leaving no cover gas above the solution. Irradiations of the test vials were performed at a dose rate of $2.1 \text{ Gy}\cdot\text{s}^{-1}$ for maximum durations of 5 hours with the technique described in Section 2.2.2.

Water radiolysis product concentrations were measured by gas chromatography and UV-Visible spectrophotometry as described in Section 2.2. To minimize any potential interference caused by nitrite species, the H_2O_2 analysis for samples containing NO_2^- was performed using a reagent where the concentration of the KI was reduced from $0.40 \text{ mol}\cdot\text{dm}^{-3}$ to $0.078 \text{ mol}\cdot\text{dm}^{-3}$ as described in literature [23].

The concentration of dissolved nitrite was determined spectrophotometrically by the Griess method [24,25]. A solution aliquot was treated in an acidic medium with sulfanilamide, a diazotizing reagent, to form an intermediate diazonium salt. The diazonium salt then reacts with the coupling reagent N-(1-Naphthyl)-ethylenediamine to form a stable azo compound with a maximum UV absorption peak at 540 nm with a molar extinction coefficient of $4.0 \times 10^4 \text{ dm}^3\cdot\text{mol}^{-1}\cdot\text{cm}^{-1}$ [25]. Calibration with solutions of known nitrite concentration yielded a detection limit for $[\text{NO}_2^-]$ of $3 \times 10^{-6} \text{ mol}\cdot\text{dm}^{-3}$.

The concentration of nitrate in the irradiated solution was determined by reducing the nitrate to nitrite by exposing the test solution to copper-coated cadmium pellets [25,26]. The total nitrite concentration following the reduction step was then

measured as described above by the Griess method. The nitrate concentration originally present in the test solution was then calculated as the difference between the nitrite concentration determined following the reduction step ($\text{NO}_3^- + \text{NO}_2^-$) and the nitrite concentration determined prior to the reduction step.

5.3 WATER RADIOLYSIS MODEL

The radiolysis kinetic model used in this study incorporates a comprehensive reaction set for γ -radiolysis of pure water that has been reported previously in Chapter 2. This model has been shown to reproduce the steady-state radiolysis data of liquid water over a wide range of conditions [27,28].

The effects of dissolved nitrate and nitrite on the steady-state concentrations of radiolysis products have been modeled by incorporating an additional simplified reaction set to the existing model framework. Included in the nitrogen subset are reactions of nitrate and nitrite species with radiolysis products and associated equilibria. The nitrogen reaction subset is provided in Table 5.1. The rate constants for these reactions were taken from literature [29-38].

Table 5.1: The reactions and rate constants that comprise the simplified nitrogen reaction set of the radiolysis kinetic model.

Reactions and Rate Constants ($\text{mol}^{-1}\cdot\text{dm}^3\cdot\text{s}^{-1}$ or s^{-1})			
<i>Chemical Reaction</i>		<i>Rate Constant (25 °C)</i>	<i>Reaction #</i>
$\bullet\text{e}_{\text{aq}}^- + \text{NO}_3^-$	$\rightarrow \text{NO}_3^{2-}$	9.7×10^9	5.1
$\text{NO}_3^{2-} + \text{H}_2\text{O}$	$\rightarrow \bullet\text{NO}_2 + 2\text{OH}^-$	5.5×10^4	5.2
$\bullet\text{e}_{\text{aq}}^- + \text{NO}_2^-$	$\rightarrow \text{NO}_2^{2-}$	3.5×10^9	5.3
$\text{NO}_2^{2-} + \text{H}_2\text{O}$	$\rightarrow \bullet\text{NO} + 2\text{OH}^-$	4.3×10^4	5.4
$\bullet\text{OH} + \text{NO}_2^-$	$\rightarrow \bullet\text{NO}_2 + \text{OH}^-$	5.0×10^9	5.5
$\bullet\text{O}_2^- + \text{NO}_3^-$	$\rightarrow \text{NO}_3^{2-} + \text{O}_2$	$1.0 \times 10^6{}^a$	5.6

$2 \bullet\text{NO}_2 + \text{H}_2\text{O} \rightarrow \text{NO}_3^- + \text{NO}_2^- + 2\text{H}^+$	6.5×10^7	5.7
$\bullet\text{e}_{\text{aq}}^- + \bullet\text{NO}_2 \rightarrow \text{NO}_2^-$	$1.0 \times 10^{10}{}^b$	5.8
$\bullet\text{O}_2^- + \bullet\text{NO}_2 \rightarrow \text{NO}_2^- + \text{O}_2$	2.0×10^8	5.9
$\bullet\text{O}_2^- + \text{NO}_2^- \rightarrow \text{NO}_2^{2-} + \text{O}_2$	5.0×10^6	5.10
$\bullet\text{OH} + \bullet\text{NO} \rightarrow \text{HNO}_2$	1.0×10^{10}	5.11
$\bullet\text{O}_2^- + \bullet\text{NO} \rightarrow \text{ONOO}^-$	6.7×10^9	5.12
$\bullet\text{e}_{\text{aq}}^- + \bullet\text{NO} \rightarrow \text{NO}^-$	2.3×10^{10}	5.13
Related Equilibria and their pK_a Values		
<i>Equilibrium</i>	<i>pK_a</i>	
$\text{H}^+ + \text{NO}_3^- \rightleftharpoons \text{HNO}_3$	-1.6	5.14
$\text{H}^+ + \text{NO}_2^- \rightleftharpoons \text{HNO}_2$	3.4	5.15
$\text{H}^+ + \text{NO}_3^{2-} \rightleftharpoons \text{HNO}_3^-$	7.5	5.16
$\text{H}^+ + \text{NO}_2^{2-} \rightleftharpoons \text{HNO}_2^-$	7.7	5.17
$\text{H}^+ + \text{ONOO}^- \rightleftharpoons \text{ONOOH}$	6.8	5.18

^a This reaction rate constant was not available in literature and was estimated to be on the order of 10^6 based on other available rate constants for reactions of $\bullet\text{O}_2^-$ with other molecular ionic species (e.g., reaction 5.10) or other molecular complexes [39,40].

^b This reaction rate constant was not available in literature and was estimated to be on the order of 10^{10} based on other available rate constants for reactions of $\bullet\text{e}_{\text{aq}}^-$ with radical species (e.g., reaction 5.13).

The nitrogen reaction subset included in the model spans nitrogen oxidation states from +5 (NO_3^-) to +1 (NO^-). The reactions of NO^- and further reactions that are associated with forming nitrogen species with an oxidation state lower than +2 are not included in the reaction set. These reactions occur at much longer time scales than the durations of the experimental study, and, hence, will not significantly influence the radiolysis kinetics observed in our experiments. Omission of these reactions is supported

by our ability to measure a mass balance of stable nitrogen species (nitrate and nitrite) at nearly 100% without including the lower oxidation state nitrogen species. The evolution of these coupled reactions was solved using the software package FACSIMILE [41].

5.4 EXPERIMENTAL RESULTS

The concentrations of the molecular products (H_2 and H_2O_2) of radiolytic decomposition of water, and the nitrogen species (NO_3^- and NO_2^-) as a function of irradiation time were measured in aqueous solutions initially containing $1 \times 10^{-3} \text{ mol}\cdot\text{dm}^{-3} \text{NO}_3^-$ or $1 \times 10^{-3} \text{ mol}\cdot\text{dm}^{-3} \text{NO}_2^-$. The results are shown for deaerated water at pH 6.0 (Figure 5.1) and at pH 10.6 (Figure 5.2). For comparison, the molecular product concentrations arising from the irradiation of water free of dissolved nitrate and nitrite are shown in Figure 5.3. Also shown in these figures are the results of computer simulations performed using the radiolysis kinetics model described above. For pH 6.0 deaerated water absent dissolved nitrogen species, the concentrations of H_2O_2 and H_2 were below the detection limit. Therefore only the model predictions are shown in the figure. The pHs of the sample solutions were measured before and after irradiation. Following the 5 hour irradiation period, the change in pH was less than half a pH unit for all samples.

For all of the conditions studied, the addition of NO_3^- or NO_2^- increases the radiolytic production of both reducing (H_2) and oxidizing (H_2O_2 and O_2) molecular products relative to that seen in water without nitrogen additives. The addition of nitrate ions increases the H_2O_2 production more than the addition of nitrite ions does, while the addition of nitrite increases the H_2 production more than the addition of nitrate does. However, the differences between the molecular product concentrations in nitrite and nitrate solutions are small, less than a factor of two for all of the tested conditions. For solutions containing a given ionic nitrogen impurity, the concentrations of H_2 and H_2O_2 reached at longer times are nearly independent of pH. This is in contrast to the observed molecular product behaviour in pure water, where the molecular product concentrations show a strong dependence on pH [10,27,28]. (For the purposes of this thesis, the term 'pure water' is intended to describe water that does not contain any intentionally added redox active solutes. It is acknowledged that modifying the pH inherently introduces

ionic impurities such as Na^+/OH^- or $\text{H}^+/\text{SO}_4^{2-}$ into the water. However, Na^+ and SO_4^{2-} are stable during irradiation and act as spectator ions in the aqueous solution, and the reactions of the counter ions OH^- and H^+ are already included in the radiolysis model.)

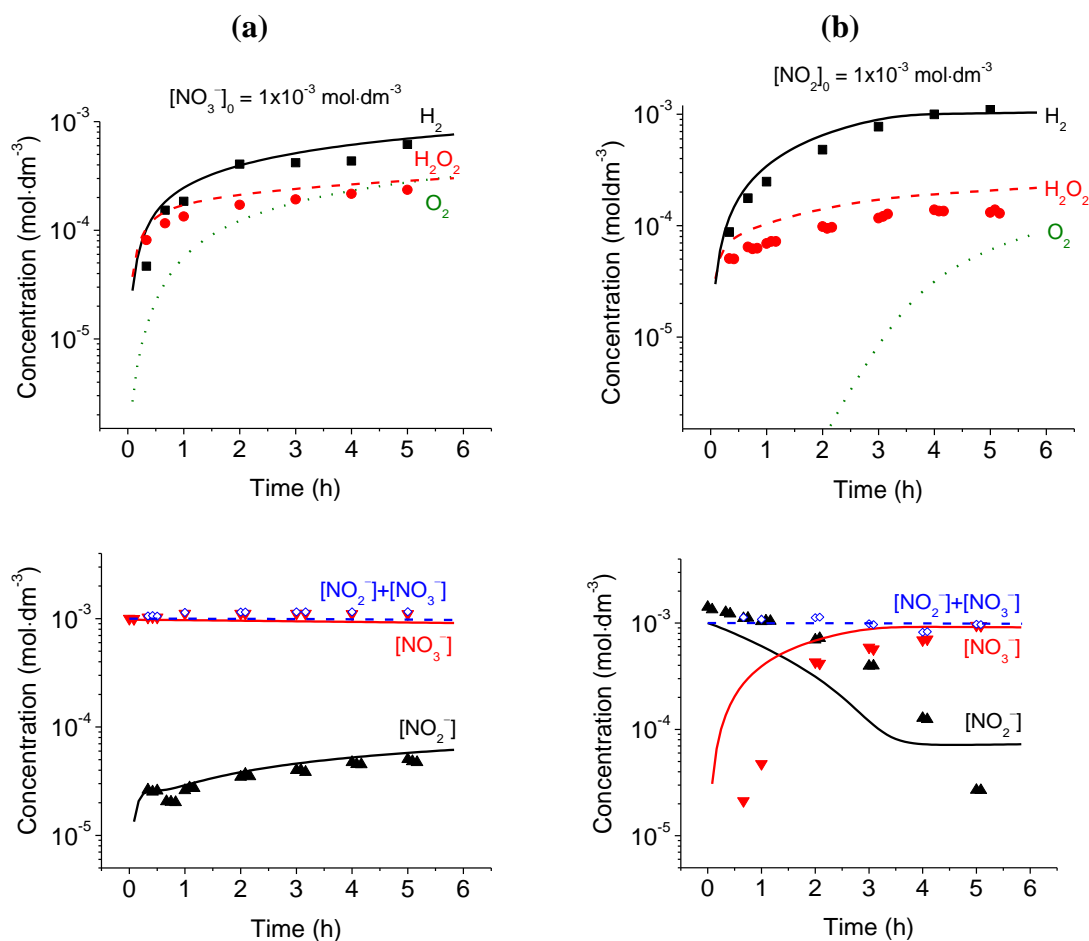


Figure 5.1: The time-dependent concentrations of H_2 (■, —), H_2O_2 (●, ---) and O_2 (⋯) (top) and the time-dependent speciation of NO_3^- (▼, —) and NO_2^- (▲, —), along with the overall mass balance of nitrogen species (◇, ---) (bottom) for deaerated pH 6.0 water containing (a) $1 \times 10^{-3} \text{ mol-dm}^{-3} [\text{NO}_3^-]_0$ and (b) $1 \times 10^{-3} \text{ mol-dm}^{-3} [\text{NO}_2^-]_0$. Data points represent the experimental data for irradiations at $2.1 \text{ Gy}\cdot\text{s}^{-1}$ and the lines are the model simulation results.

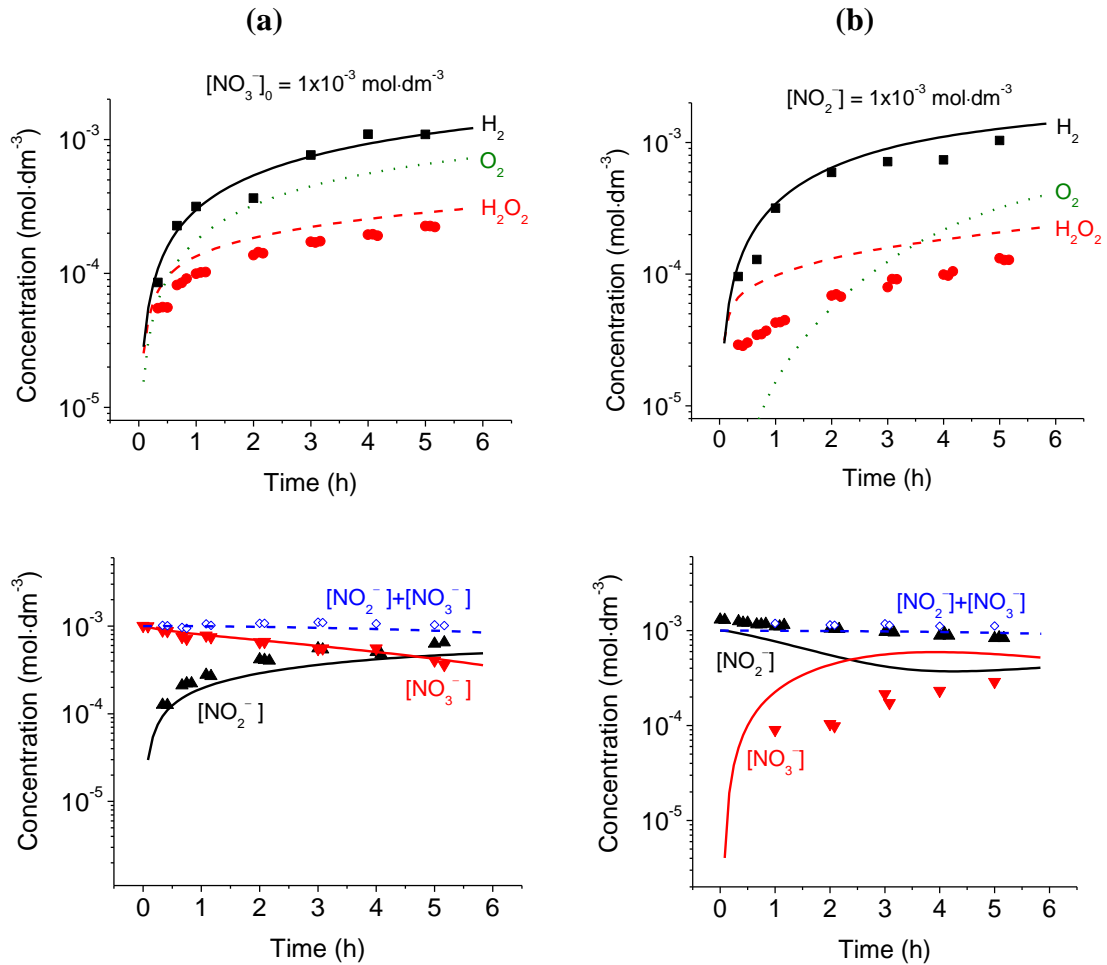


Figure 5.2: The time-dependent concentrations of H₂ (■, —), H₂O₂ (●, ---) and O₂ (⋯) (top) and the time-dependent speciation of NO₃⁻ (▼, —) and NO₂⁻ (▲, —), along with the overall mass balance of nitrogen species (◇, ---) (bottom) for deaerated pH 10.6 water containing (a) $1 \times 10^{-3} \text{ mol}\cdot\text{dm}^{-3} [\text{NO}_3^-]_0$ and (b) $1 \times 10^{-3} \text{ mol}\cdot\text{dm}^{-3} [\text{NO}_2^-]_0$. Data points represent the experimental data for irradiations at $2.1 \text{ Gy}\cdot\text{s}^{-1}$ and the lines are the model simulation results.

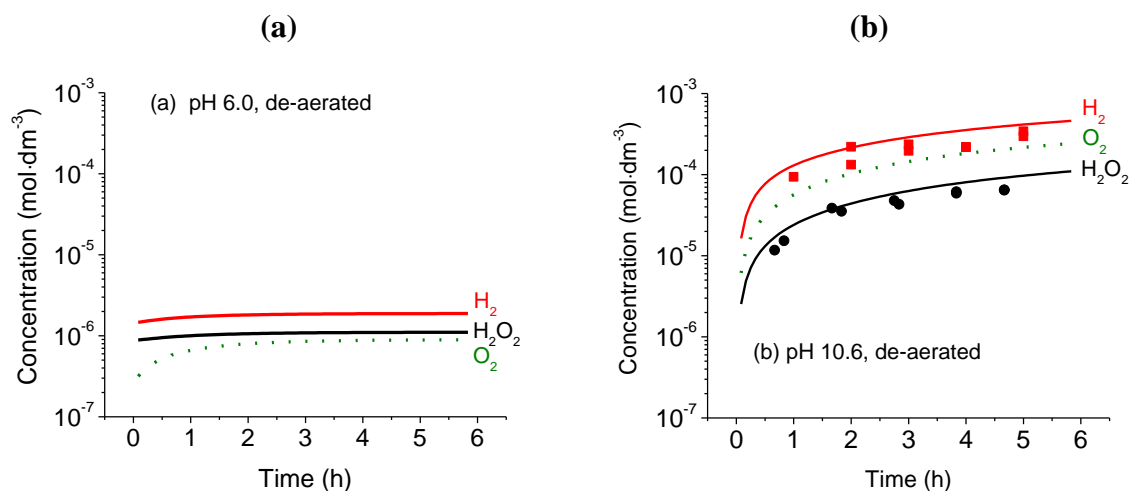


Figure 5.3: The time-dependent concentrations of H_2 (■, —), H_2O_2 (●, ---) and O_2 (····) for de-aerated water at (a) pH 6.0 and (b) pH 10.6. Data points represent the experimental data for irradiations at $2.1 \text{ Gy}\cdot\text{s}^{-1}$ and the lines are the model simulation results. At pH 6.0 the measured concentrations of H_2 and H_2O_2 were below the detection limits of $1 \times 10^{-5} \text{ mol}\cdot\text{dm}^{-3}$ and $3 \times 10^{-6} \text{ mol}\cdot\text{dm}^{-3}$, respectively.

Comparison of Figure 5.1 and Figure 5.2 shows that the kinetic behaviour of the nitrogen speciation is very different depending on whether the initially dissolved nitrogen species is NO_3^- or NO_2^- . Nevertheless, the nitrate and nitrite concentrations attained at longer times are nearly independent of the initial nitrogen species, but strongly dependent upon the solution pH.

5.5 MODEL SIMULATION RESULTS

The main objective of the model simulation is to follow the kinetics and concentrations of radical species that are difficult (practically impossible) to monitor directly. The results of model simulations are used in interpreting the overall radiolysis kinetics.

The computer simulation results are in good agreement with the experimental data over a wide range of conditions; the model predictions are within a factor of two of the observed data for both the time to reach steady state and the steady-state concentrations. Such agreement is remarkable considering that the radiolysis kinetic model consists of

such a large number of different reactions and we have limited confidence in the rate constants for some of the reactions of nitrogen species. This is particularly true for those slower reactions of nitrogen species with the more 'stable' radicals in the system such as $\bullet\text{O}_2^-$.

Furthermore, the slight discrepancies between the model-predicted concentrations and the experimentally measured values (particularly concerning the nitrite fitting results) could be attributed to the assumptions made during the modeling process. First, the model fits were performed using a simplified reaction set. The most reduced nitrogen species assumed to form in this model is NO^- . Although a near 100% nitrogen mass balance was measured for most experiments, which validates the use of a simplified reaction set, it is possible that even small contributions from additional reactions involving species with lower nitrogen oxidation states may change the rate of achieving steady state and affect the model fits. Secondly, the modeling calculations were performed by holding the pH of the solution constant throughout the irradiation period. This was deemed to be an appropriate assumption based on the consistency of the experimentally measured pH values (± 0.5 pH unit) before and after irradiation. However, some variations between the model simulations and the experimental data may be partially attributable to the neglect of the slight pH changes during the modeling.

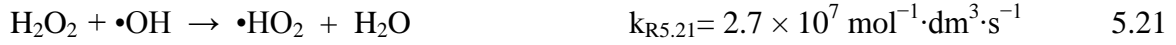
5.6 DISCUSSION OF RESULTS

5.6.1 Water Radiolysis in the Absence of Dissolved Nitrate and Nitrite

Previous studies have established the key reactions that determine the concentrations of the molecular water radiolysis products, H_2 and H_2O_2 in pure water systems, and this topic has been discussed in detail in the previous two Chapters [27,28]. Among the ~ 40 elementary reactions that occur in pure water upon irradiation, the main production pathway for the molecular products is primary radiolysis (reaction 5.19), while the main removal pathways for these species are by reaction with $\bullet\text{OH}$ and $\bullet\text{e}_{\text{aq}}^-$ in the aqueous phase (reactions 5.20, 5.21, and 5.22).



where G_{H_2} and $G_{\text{H}_2\text{O}_2}$ are 0.45 and 0.70 molecules/100 eV, respectively.



Since the changes in the concentrations of the molecular and radical radiolysis products are relatively slow (except at very short time scales ($< \text{ms}$)), a steady-state approximation can be applied to the respective rate equations for reactions 5.19 to 5.22. The concentrations of the molecular products can then be described as a function of the key radical species:

$$[\text{H}_2(\text{aq})]_t \approx \frac{k_{\text{Rad}}^{\text{H}_2}}{k_{\text{R}5.20}[\cdot\text{OH}]_t} \quad k_{\text{Rad}}^{\text{H}_2} \approx C_R G_{\text{H}_2} D_R \quad \text{E5.1}$$

$$[\text{H}_2\text{O}_2]_t \approx \frac{k_{\text{Rad}}^{\text{H}_2\text{O}_2}}{k_{\text{R}5.21}[\cdot\text{OH}]_t + k_{\text{R}5.22}[\cdot\text{e}_{\text{aq}}^-]_t} \quad k_{\text{Rad}}^{\text{H}_2\text{O}_2} \approx C_R G_{\text{H}_2\text{O}_2} D_R \quad \text{E5.2}$$

where k_{Rad}^x represents a zeroth-order radiolytic production rate that is determined by the G-value for species x at 25 °C (G_x) multiplied by the gamma-radiation dose rate (D_R) in units of $\text{Gy} \cdot \text{s}^{-1}$ (2.1 in this work) and the unit conversion constant (C_R) (1.036×10^{-7}). The other rate constants, $k_{\text{R}5.20}$, $k_{\text{R}5.21}$, and $k_{\text{R}5.22}$ are second order rate constants.

The results of the previous Chapters have supported the validity of the inverse relationships shown in Equations E5.1 and E5.2.

For the radical radiolysis products $\cdot\text{OH}$ and $\cdot\text{e}_{\text{aq}}^-$, primary radiolysis (reaction 5.19) is also the main production pathway but the main removal paths are reactions with molecular species:

For $\bullet\text{OH}$:



And for $\bullet\text{e}_{\text{aq}}^-$:



Note that although the reaction of $\bullet\text{OH}$ with H_2 (reaction 5.20) is an important removal path for H_2 , it is only important for the removal of $\bullet\text{OH}$ if H_2 is present at a high concentration prior to the build-up of H_2O_2 and $\bullet\text{O}_2^-$.

When present in water, some chemical species can establish pseudo-catalytic reaction cycles with the radical species. This changes the relative contributions of different reactions to the net removal of the radical species as water radiolysis progresses. Since the molecular radiolysis product concentrations are also a function of the radical concentrations in the solution, it is difficult to predict the net effect of cyclic reactions on radiolysis at longer times based on the rates of elementary reactions alone.

The concept of cycling reactions was first introduced in this thesis in Chapter 3, where differences in the kinetics of O_2 production lead to a pH effect on radiolysis behaviour. This was further explored in Chapter 4, where O_2 was added as an initially dissolved solute. In initially deaerated solutions, changes in the kinetics of the $\bullet\text{H}/\bullet\text{e}_{\text{aq}}^-$ equilibrium (reaction 5.24) with pH leads to a shift in the relative contributions of the $\bullet\text{e}_{\text{aq}}^-$ removal reactions. While the reaction of $\bullet\text{e}_{\text{aq}}^-$ and H^+ (reaction 5.24) is very slow at $\text{pH} > \text{pK}_a$ of $\bullet\text{H}$ (9.6), the reaction with the secondary radiolysis product O_2 (reaction 5.25) becomes an important removal path for $\bullet\text{e}_{\text{aq}}^-$ at these pH conditions. The product of this reaction, $\bullet\text{O}_2^-$, can then react with $\bullet\text{OH}$ (reaction 5.23) to regenerate O_2 . Once this pseudo-catalytic cycle is established, oxygen can build up to high levels in the system and the radical species can be effectively scavenged from the aqueous phase. This results in a reduction of the removal rates of the associated molecular products, thus, increasing the observed concentrations of H_2 and H_2O_2 (E5.1 and E5.2). Hence, solutions

containing higher concentrations of dissolved oxygen, arising from either a change in pH (Chapter 3) or initial saturation with O₂ (Chapter 4), yield higher concentrations of the molecular radiolysis products H₂ and H₂O₂ upon irradiation.

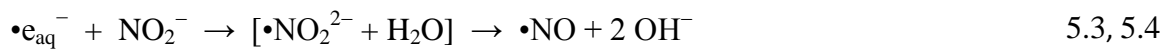
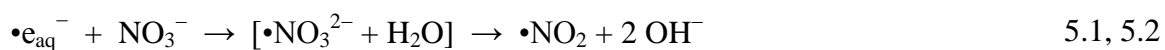
The pH effect described above is easily observed for deaerated water in Figure 5.3. At pH 6.0, the molecular products could not be measured experimentally, and the model simulations predict concentrations below the detection limits of $1 \times 10^{-5} \text{ mol} \cdot \text{dm}^{-3}$ and $3 \times 10^{-6} \text{ mol} \cdot \text{dm}^{-3}$ for H₂ and H₂O₂ respectively (Figure 5.3a). The molecular concentrations remain low for pH 8.5 solution (results not shown). However, for solutions at pH 10.6 (> 9.6, the pK_a of •H), the molecular product concentrations are measurable, demonstrating an increase of 2-3 orders of magnitude in comparison to the model predicted concentrations at pH 6.0 (Figure 5.3b).

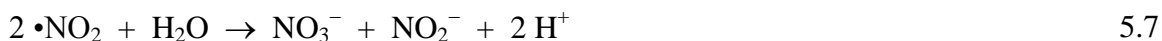
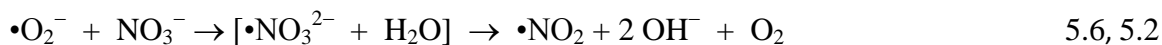
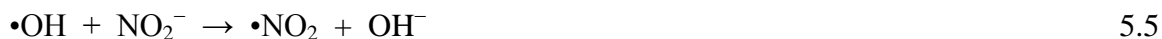
The introduction of other chemical species that can react with the radical species can upset the system chemistry by providing additional removal pathways for those radicals. If the added species can be partially regenerated by back reactions such that they can establish a (semi) pseudo-catalytic cycle with the radical species before they are totally consumed, their influence on radiolysis product concentrations can be significant and last for a long time. Aqueous phase reactions of a chemical additive with the molecular water radiolysis products are typically too slow to be important. However, dissolved additives can affect the molecular product concentrations indirectly, via their interactions with radical species.

5.6.2 Radiolysis of Aqueous Solutions Initially Containing Nitrate or Nitrite

5.6.2.1 Production of H₂ and H₂O₂

Under all conditions studied, both NO₃⁻ and NO₂⁻ increase the radiolytic production of H₂ and H₂O₂ compared to that seen for pure water (Figure 5.1 to Figure 5.3). Dissolved nitrogen species can provide several additional reaction pathways for radical radiolysis products, with the key reactions being:





Nitrate and nitrite ion reactions (5.1 to 5.5) can compete with reactions 5.21 and 5.23 for $\bullet\text{OH}$ and with reactions 5.22, 5.24, and 5.25 for $\bullet\text{e}_{\text{aq}}^-$. At sufficiently high concentrations, reactions with nitrate or nitrite ions can become the dominant removal paths for these radicals. The presence of nitrate/nitrite in the irradiated water will lower the concentrations of $\bullet\text{e}_{\text{aq}}^-$ and $\bullet\text{OH}$, thereby reducing the rate of removal of H_2 by reaction 5.20 and the decomposition rate of H_2O_2 by reactions 5.21 and 5.22. This can be clearly seen in Figure 5.4, where the model predicted concentrations of $\bullet\text{OH}$, $\bullet\text{e}_{\text{aq}}^-$ and $\bullet\text{O}_2^-$ in pure water are compared to their predicted concentrations in solutions with initially dissolved NO_3^- or NO_2^- . At a given pH, the concentrations of all three radicals are modeled to be substantially lower in nitrate or nitrite solutions than in pure water. The lowered radical concentrations lead to reduced removal rates for molecular water radiolysis products, and cause the observed increase in the net radiolytic production of H_2 and H_2O_2 in the presence of nitrogen species.

The increases in $[\text{H}_2]$ and $[\text{H}_2\text{O}_2]$ due to the addition of nitrate or nitrite, compared to pure water, are larger for pH 6.0 than pH 10.6 solutions. This is analogous to what was observed in Chapter 4 for O_2 saturated solutions. For oxygenated solutions, the pH effect was associated with the lower radical concentrations that are attained at higher pH than at lower pH for pure water (Figure 5.5, reproduced from Chapter 4). For pH > 9.6, the reaction of $\bullet\text{e}_{\text{aq}}^-$ with H^+ (5.24) is significantly restricted and no longer a main loss path for $\bullet\text{e}_{\text{aq}}^-$. Hence, the pseudo-catalytic cycle of reactions 5.25 and 5.23, as described earlier in Section 5.6.1, is established even for initially deaerated water. This substantially increases not only $[\text{O}_2]$ but also $[\text{H}_2]$ and $[\text{H}_2\text{O}_2]$ for pure alkaline water at longer times while decreasing the concentrations of $\bullet\text{OH}$ and $\bullet\text{e}_{\text{aq}}^-$. As a result, any additional radical scavenging that arises from higher initial oxygen concentrations has a lesser effect on higher pH solutions.

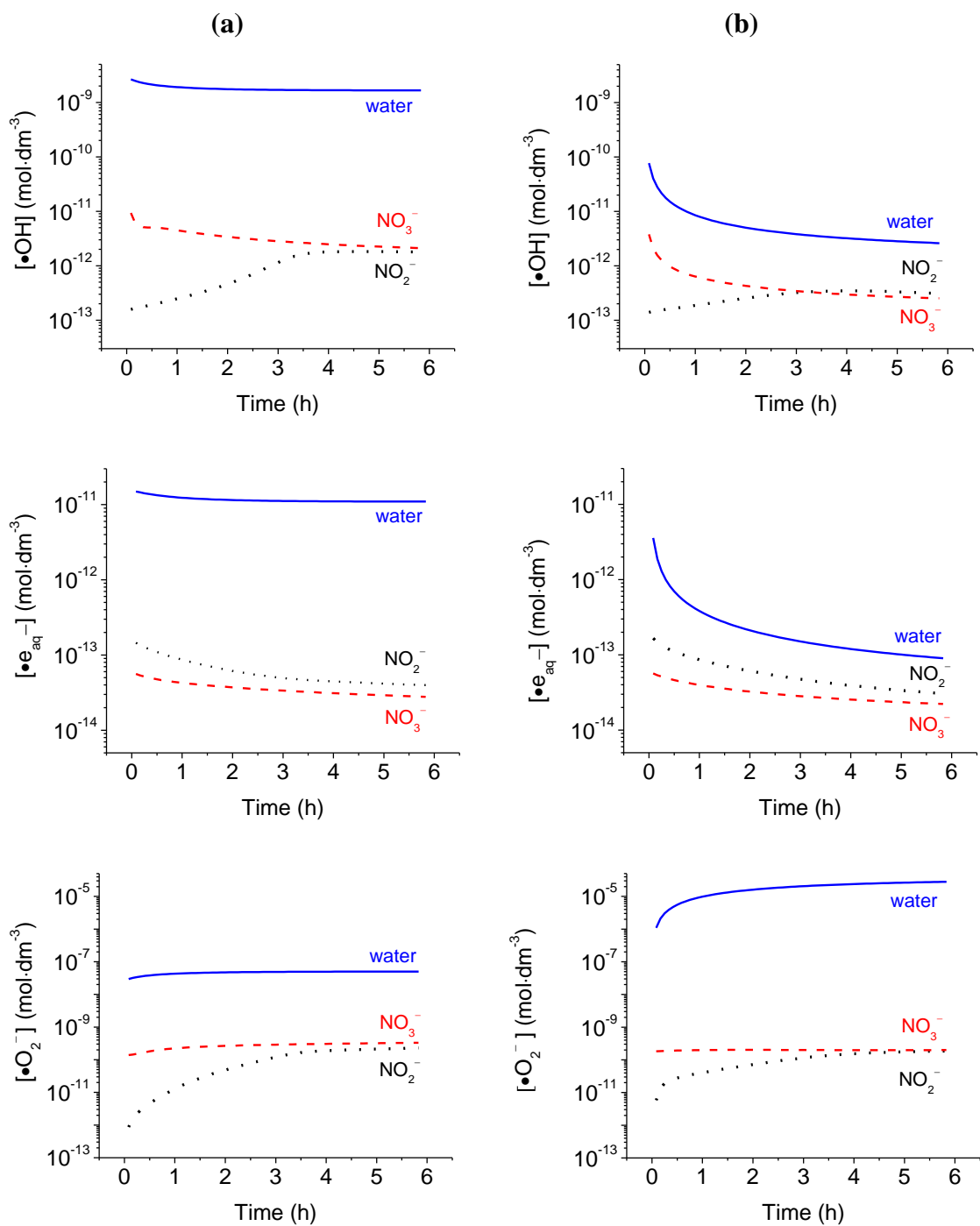


Figure 5.4: The model simulation results for the time-dependent concentrations of $\bullet\text{OH}$, $\bullet\text{e}_{\text{aq}}^-$, and $\bullet\text{O}_2^-$ achieved in the radiolysis of deaerated solutions of pure water (—), $[\text{NO}_3^-]_0 = 1 \times 10^{-3} \text{ M}$ (---), and $[\text{NO}_2^-]_0 = 1 \times 10^{-3} \text{ M}$ (...), at pH 6.0 (a) and pH 10.6 (b).

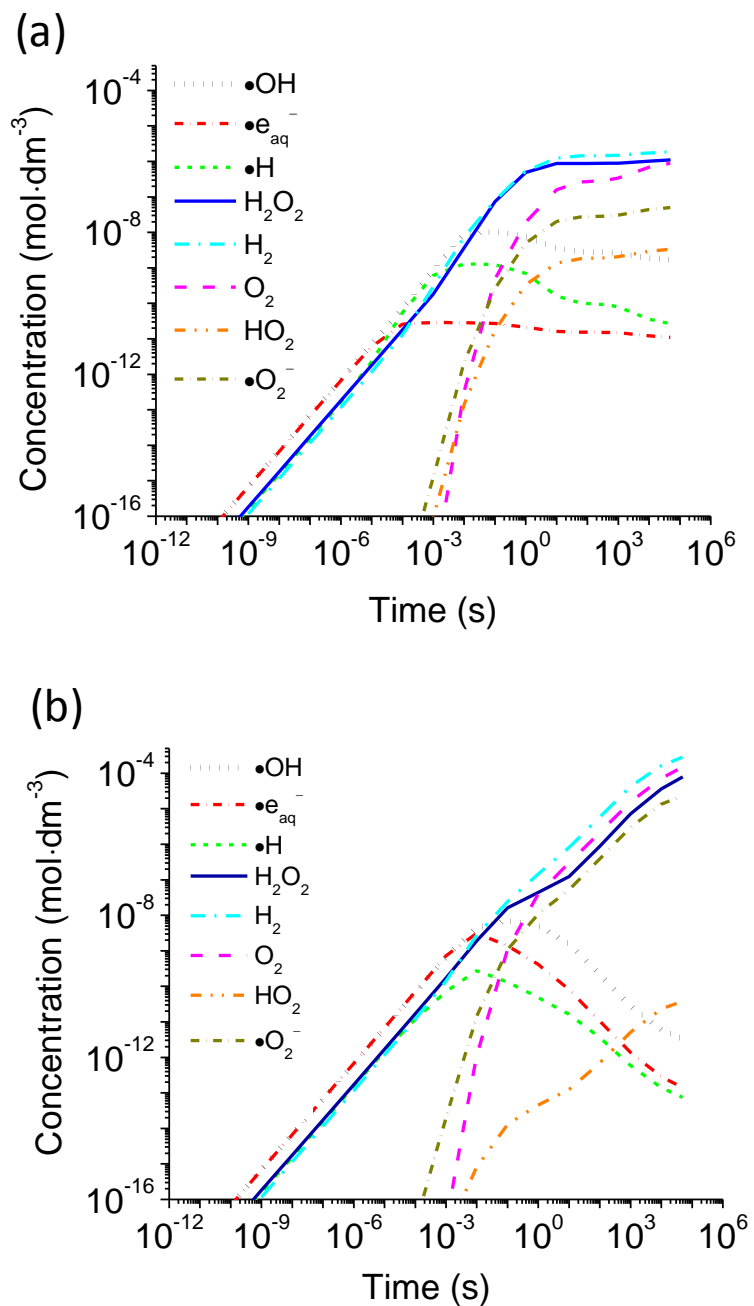


Figure 5.5: The behaviour of water radiolysis products at pH 6.0 (a) and pH 10.6 (b) shown for deaerated water as a function of time.

When nitrate or nitrite are initially dissolved in the water, they compete with ionic and molecular water radiolysis products for reaction with the radicals, mainly with H^+ at $pH < 9.6$ (for $\bullet e_{aq}^-$, reaction 5.24), and with the molecular radiolysis products O_2 , H_2 , and H_2O_2 at $pH > 9.6$ (for $\bullet e_{aq}^-$ and $\bullet OH$, 5.25, 5.22 and 5.21). As described above, the significant net radiolytic production of the molecular species in pure water at the higher pH (Figure 5.5b) leads to the radical concentrations being depressed relative to their concentrations at lower pH. Consequently, there is less margin for added nitrate or nitrite to impact the radical concentrations ($\bullet e_{aq}^-$ and $\bullet OH$) in alkaline water (Figure 5.4), and greater increases in $[H_2]$ and $[H_2O_2]$ are observed for nitrate/nitrite solutions (relative to pure water) at lower pH.

Furthermore, in pure water, the loss paths for the radicals change as the pH changes around the pKa of $\bullet H$. However, in dilute nitrate/nitrite solutions, the radicals are mainly removed by their reactions with nitrate and nitrite ions, and their removal paths don't change with pH. Figure 5.6 demonstrates that the model simulated concentration profiles of the water radiolysis products are almost identical at pH 6.0 and 10.6 for a dilute nitrate solution. Hence, the net water radiolysis molecular product concentrations do not vary significantly with pH in the presence of nitrogen-containing species. This was observed experimentally, as shown in Figure 5.1 and Figure 5.2.

At a given pH, the addition of nitrate ions increased H_2O_2 production more than the addition of nitrite ions, while the addition of nitrite increased the H_2 production more than the addition of nitrate. These differences can be partially attributed to the different rate constants of the reactions of NO_3^- and NO_2^- with the radical water radiolysis products, reactions 5.1 to 5.5. The reaction of NO_3^- with $\bullet e_{aq}^-$ (5.1) has a larger rate constant than the reaction of NO_2^- with $\bullet e_{aq}^-$ (5.3), and a larger increase in $[H_2O_2]$ is expected for the radiolysis of nitrate solutions than nitrite solutions. Similarly, nitrite solutions are expected to yield a higher $[H_2]$ than nitrate solutions since NO_2^- is a good scavenger for $\bullet OH$ (5.5), whereas no reaction of $\bullet OH$ with NO_3^- has been observed [15]. The computer model indeed predicts initially two orders of magnitude higher $[\bullet OH]$ and a factor of two lower $[\bullet e_{aq}^-]$ in nitrate solution than those in nitrite solution at both pHs.

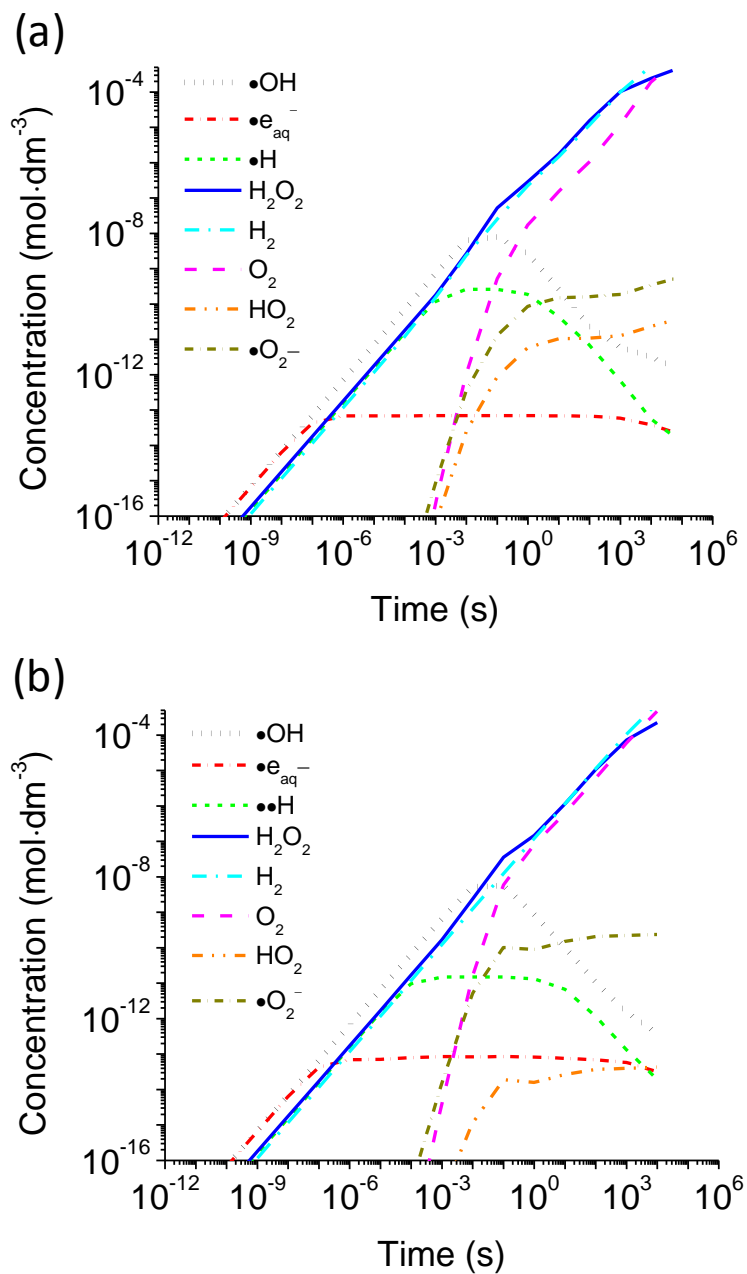


Figure 5.6: The behaviour of water radiolysis products at pH 6.0 (a) and pH 10.6 (b) shown as a function of time for a deaerated $1 \times 10^{-3} \text{ mol}\cdot\text{dm}^{-3} \text{ NO}_3^-$ solution.

While the initial trends in H_2 and H_2O_2 behaviour with dissolved nitrate/nitrite present can be explained by the elementary reaction rate constants, the effect of the initial nitrogen species on the net radiolytic production of H_2 and H_2O_2 diminishes with irradiation time. As a result, the pseudo-steady-state concentrations of H_2 and H_2O_2 attained do not show a strong dependence on the initial nitrogen speciation. This behaviour can be explained by the radiolytically-induced interconversion between nitrate and nitrite in the water. Nitrate and nitrite ions can participate in a series of redox reactions with reducing (e.g., $\bullet e_{aq}^-$, $\bullet O_2^-$) and oxidizing (e.g., $\bullet OH$, $HO_2\bullet$) species. More importantly, one of their intermediate products, $NO_2\bullet$, disproportionates to form NO_3^- and NO_2^- (reaction 5.7). This series of reactions establishes a pseudo-catalytic cycle between NO_3^- and NO_2^- . Under continuous irradiation, this will result in a slow net conversion between nitrate and nitrite. Even when there is very little net conversion of NO_3^- to NO_2^- in the solution, the net radiolytic production of H_2 , H_2O_2 and O_2 is significant, Figure 5.1a and Figure 5.2a.

The competitiveness of nitrate and nitrite for the radicals under a given set of conditions determines the interconversion rate towards a steady state. The concentrations of $\bullet OH$ and $\bullet O_2^-$ increase with time in the nitrite solution while the concentration of $\bullet OH$ decreases and the concentration of $\bullet O_2^-$ is nearly constant with time in the nitrate solution. This results in nearly the same steady-state concentrations of the radicals and correspondingly the molecular radiolysis products for nitrate and nitrite solutions, independent of the initial nitrogen speciation at a given pH. The observed nitrogen speciation at steady state, where the relative changes in concentrations are small, is thus also nearly independent of whether the initial nitrogen species is NO_3^- or NO_2^- .

5.6.2.2 Nitrogen speciation, $[NO_3^-]$ and $[NO_2^-]$

The pseudo-catalytic reactions of the nitrogen compounds with the radicals and their competition with the reactions between radical and molecular water radiolysis products are responsible for the net production of H_2 and H_2O_2 observed under different experimental conditions. Although the nitrogen speciation reached at longer times is nearly independent of the initially dissolved nitrogen species, it is strongly dependent on pH.

Nitrate will initially react with reducing radical species ($\bullet e_{aq}^-$ and $\bullet O_2^-$) to form NO_2^- , but NO_2^- will quickly react with the oxidizing radical species ($\bullet OH$) to reform NO_3^- resulting in a slow evolution towards a steady-state speciation. Applying a steady-state approximation yields an approximate analytical solution for the ratio of NO_2^- and NO_3^- that can be compared with the computer predictions:

$$\frac{[NO_2^-]_t}{[NO_3^-]_t} \approx \frac{k_{R5.1}[\bullet e_{aq}^-]_t + k_{R5.6}[\bullet O_2^-]_t}{k_{R5.5}[\bullet OH]_t} \quad E5.3$$

The ratio of NO_2^- to NO_3^- is a function of the concentrations of three radical species, $\bullet e_{aq}^-$, $\bullet O_2^-$, and $\bullet OH$ (E5.3) and the pH dependence of the ratio arises from the dependence of the radical concentrations on pH. From Figure 5.4 it is seen that the steady-state concentrations of $\bullet e_{aq}^-$ and $\bullet O_2^-$ do not change when the pH is changed from 6.0 to 10.6. However, the concentration of $\bullet OH$ is about 10 times lower at pH 10.6 than at pH 6.0. This causes the change in the ratio of NO_2^- to NO_3^- observed as a function of pH. Solving the right hand side of Equation E5.3 for both pHs studied using the steady-state concentrations of the radicals observed in Figure 5.4 yields nitrite/nitrate ratios similar to those observed experimentally in Figure 5.1 and Figure 5.2

The combination of E5.1, E5.2, and E5.3 suggests that approximate concentrations of the radical species in solution can be determined indirectly from measurements of H_2 , H_2O_2 and the steady-state ratio of $[NO_2^-]$ and $[NO_3^-]$ in solution. This can provide a complete picture of water radiolysis product distribution in a given irradiated system. This is a valuable tool for monitoring water chemistry since radical concentrations cannot be measured directly, but measurement of a combination of the concentrations of the molecular species can give us an indirect measurement.

5.6.2.3 Assessment of Nuclear Reactor Data

The ultimate objective of studying the chemistry of water systems in a radiation field is to be able to predict chemical behaviour and to use this knowledge to develop an effective means to mitigate the damaging consequences of corrosion. To further validate our understanding of the chemistry of nitrogen compounds in irradiated water, we can

compare model predictions for nitrogen speciation with data from operating nuclear power reactors. Nitrogen compounds can be present in nuclear reactor water systems as a result of inadvertent ingress (e.g., air ingress during maintenance or degradation of purification resins) or deliberate addition (e.g., added for chemistry control regimes). Some CANDU plants experience periodic, inadvertent air ingress into the end shield cooling system (a low temperature, light water system). The water in this system (which is maintained at pH 10) is exposed to high fluxes of γ -radiation during reactor operation. Measured nitrate and nitrite concentrations in end shield water at the Point Lepreau Generating Station are shown for a 2 month period in Figure 5.7. The data show that the speciation of nitrogen compounds in the system favours nitrite over nitrate. This finding is in agreement with the results of our work which predict the same trend in speciation, as shown in Figure 5.2. The radiolytic production of hydrogen with air ingress (data not shown) is also elevated in this system, in further agreement with the predictions of our model. We expect that further improvements in our knowledge of the radiation chemistry of nitrogen compounds will support analysis of real reactor chemistry conditions and understanding of the consequences and mitigation of abnormal reactor chemical conditions in the future.

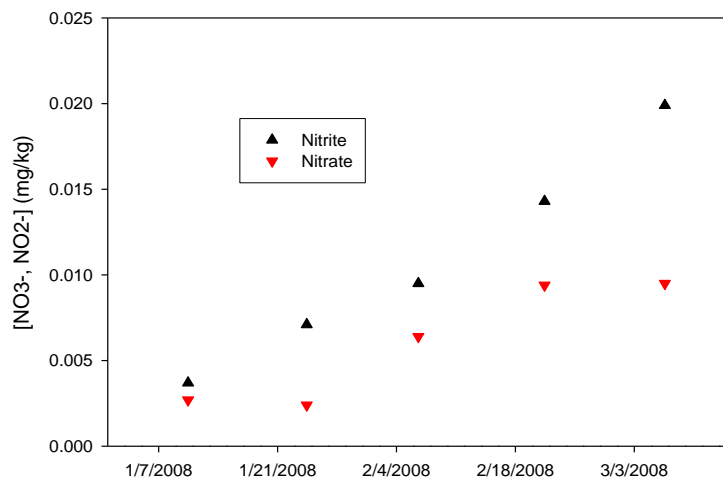


Figure 5.7: The speciation of NO_3^- (▼) and NO_2^- (▲), in the end shield cooling system (pH 10) at Point Lepreau Generating Station.

5.7 CONCLUSIONS

The kinetics of nitrate/nitrite solution radiolysis was followed by monitoring the concentrations of molecular water radiolysis products, H_2 and H_2O_2 , as well as NO_2^- and NO_3^- , as a function of irradiation time. The temporal evolution of the concentrations is described well by reactions of nitrogen species with the radicals generated by the ionizing radiation. The complete reaction kinetics model for radiolysis of nitrate/nitrite solutions was reduced to include only those reactions with highly reducing ($\bullet e_{aq}^-$ and $\bullet O_2^-$) and highly oxidizing ($\bullet OH$) radicals, and the disproportionation reaction of $\bullet NO_2$. Analysis using this reduced reaction set demonstrated that it was sufficient to match the observed system chemistry well. Using this reaction set, the ratio of steady-state concentrations of NO_2^- and NO_3^- can be expressed as a simple function of the concentrations of the key water radicals.

This study, which combines experiments and kinetic model analysis, has established a reaction mechanism for the steady-state radiolysis of nitrate and nitrite solutions that can satisfactorily explain data from a nuclear power reactor station as well as laboratory scale experiments. For water systems containing nitrate or nitrite, the concentrations of the redox radical species arising during water radiolysis can be determined from measurements of H_2 , H_2O_2 and the ratio of NO_2^- and NO_3^- in solution. The ratio of NO_2^- to NO_3^- at steady state is shown to be independent of the initial nitrogen species, but a strong function of pH; at pHs < 9.6 (the pK_a of $\bullet H$), nitrate is the dominant species at steady state whereas nitrite is dominant at higher pHs.

5.8 ACKNOWLEDGEMENTS

The work described herein has been published, and is included as Reference [42]. NB Power (New Brunswick Power) staff are acknowledged for providing reactor data for the end shield cooling system.

This work was funded under the NSERC/AECL (Natural Science and Engineering Research Council of Canada/Atomic Energy of Canada Limited) Industrial Research Chair in Radiation Induced Processes. Support from the Canada Foundation for Innovation New Opportunity grant is also greatly acknowledged for the purchase of the Gamma-cell, GC-MSD/TCD, and UV-Vis absorption spectrophotometer.

5.9 REFERENCES

- [1] Daub, K., Zhang, X., Noël, J.J., Wren, J.C., "Gamma-radiation-induced corrosion of carbon steel in neutral and mildly basic water at 150°C", *Corros. Sci.*, **2011**, 53, 11-16.
- [2] Daub, K., Zhang, X., Noël, J.J., Wren, J.C., "Gamma radiation-induced carbon steel corrosion", *ECS Trans.*, **2011**, 33, 15-24.
- [3] Stuart, C.R., Reid, V., Turner, C.W. "Optimization of Chemistry Control in the Primary Heat Transport System of CANDU Reactors" In *Proceedings of the International Conference on Water Chemistry of Nuclear Reactor Systems Jeju Island, Korea*, 2006.
- [4] *BWRVIP-201: BWR Vessel and Internals Project, Technical Basis for Plant-Specific Safety Evaluation for Hydrazine Injection for Startup ECP Reduction in BWRs*, EPRI, Palo Alto, CA, Report 1016581, December 2008.
- [5] Cowan, R.L., Indig, M.E., Kass, J.N., Law, R.J., Sundberg, L.L. "Experience with hydrogen water chemistry in boiling water reactors", Fourth International Conference on Water Chemistry of Nuclear Systems, Bournemouth, U.K., 1986.
- [6] Indig, M.E., Nelson, J.L., "Electrochemical measurements and modeling predictions in boiling water reactors under various operating conditions", *Corrosion*, **1991**, 47, 202-209.
- [7] *Pressurized Water Reactor Primary Water Chemistry Guidelines: Revision 7*, EPRI, Palo Alto, CA, Report 3002000505, April 2014.
- [8] *BWR Water Chemistry Guidelines - 2008 Revision*, EPRI, Palo Alto, CA, Report 1016579, October 2008.
- [9] Daub, K., Zhang, X., Noël, J.J., Wren, J.C., "Effects of γ -radiation versus H₂O₂ on carbon steel corrosion", *Electrochim. Acta*, **2010**, 55, 2767-2776.
- [10] Wren, J.C. In *ACS Symposium Series: Nuclear Energy and the Environment*, Chien, W., Mincher, B., Eds., American Chemical Society: Washington, D.C., 2010, p 271-295.
- [11] Yakabuskie, P.A., Joseph, J.M., Keech, P., Botton, G.A., Guzonas, D., Wren, J.C., "Iron oxyhydroxide colloid formation by gamma-radiolysis", *Phys. Chem. Chem. Phys.*, **2011**, 13, 7198-7206.
- [12] Kysela, J., Zmítko, M., Yurmanov, V.A., Tiapkov, V.F., "Primary coolant chemistry in VVER units", *Nucl. Eng. Des.*, **1996**, 160, 185-192.
- [13] Simpson, M.F., Law, J.D., *Nuclear Fuel Reprocessing*, Idaho National Laboratory, Idaho Falls, Idaho, Report INL/EXT-10-17753, February 2010.
- [14] Ramanujam, A. In *Encyclopedia of Materials: Science and Technology*, 2nd ed., Buschow, K.H.J., Cahn, R.W., Flemings, M.C., Ilshner, B., Kramer, E.J., Mahajan, S., Veyssièrè, P., Eds., Elsevier: Oxford, 2001, p 7918-7924.
- [15] Mezyk, S.P., Bartels, D.M., "Temperature dependence of hydrogen atom reaction with nitrate and nitrite species in aqueous solution", *J. Phys. Chem. A*, **1997**, 101, 6233-6237.
- [16] Buxton, G.V., Stuart, C.R., "Radiation chemistry of aqueous solutions of hydrazine at elevated temperatures. Part 1. Oxygen-free solutions", *J. Chem. Soc., Faraday Trans.*, **1996**, 92, 1519-1525.
- [17] Buxton, G.V., Lynch, D.A., Stuart, C.R. "Radiation chemistry of aqueous solutions of hydrazine and ammonia up to 200°C" In *Water Chemistry of Nuclear*

- Reactor Systems 7: Proceedings of the British Nuclear Energy Society Conference*, Thomas Telford Publishing: Bournemouth, United Kingdom, 1996, p 150-152.
- [18] Buxton, G.V., Stuart, C.R., "Radiation chemistry of aqueous solutions of hydrazine at elevated temperatures Part 2. Solutions containing oxygen", *J. Chem. Soc., Faraday Trans.*, **1997**, 93, 1535-1538.
- [19] Buxton, G.V., Lynch, D.A., "Investigation of the NH_2 radical in aqueous solution up to 200 °C by pulse radiolysis", *J. Chem. Soc., Faraday Trans.*, **1998**, 94, 3271-3274.
- [20] Wayne, R.P., Barnes, I., Biggs, P., Burrows, J.P., Canosa-Mas, C.E., Hjorth, J., Le Bras, G., Moortgat, G.K., Perner, D., Poulet, G., Restelli, G., Sidebottom, H., "The nitrate radical: Physics, chemistry, and the atmosphere", *Atmospheric Environment. Part A. General Topics*, **1991**, 25, 1-203.
- [21] Keen, O.S., Love, N.G., Linden, K.G., "The role of effluent nitrate in trace organic chemical oxidation during UV disinfection", *Water Res.*, **2012**, 46, 5224-5234.
- [22] Tsang, W., Herron, J.T., "Chemical kinetic database for propellant combustion I. Reactions involving NO, NO₂, HNO, HNO₂, HCN and N₂O", *J. Phys. Chem. Ref. Data*, **1991**, 20, 609-663.
- [23] Schwarz, H.A., Salzman, A.J., "The radiation chemistry of aqueous nitrite solutions: The hydrogen peroxide yield", *Radiat. Res.*, **1958**, 9, 502-508.
- [24] Slack, P.T. *Analytical Methods Manual*, 2nd ed., Leatherhead Food R.A.: London, 1987.
- [25] Sun, J., Zhang, X., Broderick, M., Fein, H., "Measurement of nitric oxide production in biological systems by using Griess reaction assay", *Sensors*, **2003**, 3, 276-284.
- [26] Cortas, N.K., Wakid, N.W., "Determination of inorganic nitrate in serum and urine by a kinetic cadmium-reduction method", *Clin. Chem.*, **1990**, 36, 1440-1443.
- [27] Joseph, J.M., Choi, B.S., Yakabuskie, P.A., Wren, J.C., "A combined experimental and model analysis on the effect of pH and O₂(aq) on γ -radiolytically produced H₂ and H₂O₂", *Radiat. Phys. Chem.*, **2008**, 77, 1009-1020.
- [28] Yakabuskie, P.A., Joseph, J.M., Wren, J.C., "The effect of interfacial mass transfer on steady-state water radiolysis", *Radiat. Phys. Chem.*, **2010**, 79, 777-785.
- [29] Bielski, B.H., Cabelli, D.E., Arudi, R.L., "Reactivity of HO₂/O₂⁻ radicals in aqueous solution", *J. Phys. Chem. Ref. Data*, **1985**, 14, 1041-1100.
- [30] Buxton, G.V., Greenstock, C.L., Helman, W.P., Ross, A.B., "Critical-review of rate constants for reactions of hydrated electrons, hydrogen atoms and hydroxyl radicals (OH/O⁻) in aqueous solution", *J. Phys. Chem. Ref. Data*, **1988**, 17, 513-886.
- [31] Cook, A.R., Dimitrijevic, N., Dreyfus, B.W., Meisel, D., Curtiss, L.A., Camaioni, D.M., "Reducing radicals in nitrate solutions. The NO₃²⁻ system revisited", *J. Phys. Chem. A*, **2001**, 105, 3658-3666.

- [32] Goldstein, S., Czapski, G., "The reaction of $\text{NO}\cdot$ with $\text{O}_2^{\cdot-}$ and $\text{HO}_2^{\cdot-}$: A pulse radiolysis study", *Free Radical Biol. Med.*, **1995**, *19*, 505-510.
- [33] Goldstein, S., Czapski, G., "Formation of peroxyxynitrite from the nitrosation of hydrogen peroxide by an oxygenated nitric oxide solution", *Inorg. Chem.*, **1996**, *35*, 5935-5940.
- [34] Goldstein, S., Lind, J., Merényi, G., "Chemistry of peroxyxynitrites as compared to peroxyxynitrates", *Chem. Rev.*, **2005**, *105*, 2457-2470.
- [35] Logager, T., Sehested, K., "Formation and decay of peroxyxynitrous acid: a pulse radiolysis study", *J. Phys. Chem.*, **1993**, *97*, 6664-6669.
- [36] Lymar, S.V., Schwarz, H.A., Czapski, G., "Reactions of the dihydroxylamine ($\text{HNO}_2\cdot$) and hydronitrite ($\text{NO}_2^{2-\cdot}$) radical ions", *J. Phys. Chem. A*, **2002**, *106*, 7245-7250.
- [37] Seddon, W.A., Young, M.J., "Pulse radiolysis of nitric oxide in aqueous solution", *Can. J. Chem.*, **1970**, *48*, 393-394.
- [38] Tret'yakov, V.P., Min'ko, L.A., Rudakov, E.S., Alekhina, T.A., "Mechanism of the oxidation of cyclohexane by peroxyxynitrous acid in media with and without oxygen", *Theor. Exp. Chem.*, **2003**, *39*, 36-40.
- [39] Lauricella, R.P., Bouteiller, J.-C.H., Tuccio, B.N., "Evidence of overestimation of rate constants for the superoxide trapping by nitrones in aqueous media", *Phys. Chem. Chem. Phys.*, **2005**, *7*, 399-404.
- [40] Buettner, G.R., Doherty, T.P., Patterson, L.K., "The kinetics of the reaction of superoxide radical with Fe(III) complexes of EDTA, DETAPAC and HEDTA", *FEBS Lett.*, **1983**, *158*, 143-146.
- [41] *FACSIMILE Kinetic Modelling Software*, MCPA Software Ltd., 2003.
- [42] Yakabuskie, P.A., Joseph, J.M., Stuart, C.R., Wren, J.C., "Long-term γ -radiolysis kinetics of NO_3^- and NO_2^- solutions", *J. Phys. Chem. A*, **2011**, *115*, 4270.

CHAPTER 6 IRON OXY-HYDROXIDE COLLOID FORMATION BY γ -RADIOLYSIS*

6.1 INTRODUCTION

The previous chapters have shown that dissolved gases and salts, as well as the presence of an available headspace volume, can significantly impact water radiolysis kinetics. Dissolved solutes can scavenge key water radiolysis radicals that control the removal rates of stable molecular radiolysis products such as hydrogen and hydrogen peroxide, while the presence of a headspace provides supplemental loss pathways for gaseous radiolysis products such as H₂ and O₂ from the aqueous phase. As a result, the steady-state concentrations of the molecular water radiolysis products, and hence the aqueous redox condition of the irradiated water, can be significantly affected by the initial cover gas volume and composition and the presence of initially dissolved salts.

So far, the solutes studied have encompassed a small subsection of those that may be encountered in a nuclear reactor system, either by inadvertent addition or as byproducts of intentionally added chemistry control agents. The practical objective of assembling a radiation chemistry kinetic model capable of addressing such a wide variety of conditions is to provide a means of understanding the eventual redox condition that will be achieved in a real system. This measure of the general oxidizing ability of the solvent can then be used to understand how impurities can affect the corrosion rates of reactor materials.

Minimizing the release of metal ions into the reactor coolant (due to corrosion of materials or wear of in-core surfaces) is a primary goal of nuclear power plants for a variety of safety and operational reasons. These metallic species can take the form of dissolved ions or suspended particulates that may avoid capture by filtration systems. These species can subsequently be transported throughout the heat transport system and into the reactor core where they are subjected to high intensity radiation fields. Neutron activation of some metallic species can generate radioactive isotopes that can recirculate

* Reproduced in part with permission from PCCP Owner Societies:

Yakabuskie, P.A., Joseph, J.M., Keech, P., Botton, G.A., Guzonas, D., Wren, J.C., "Iron oxyhydroxide colloid formation by gamma-radiolysis", *Phys. Chem. Chem. Phys.*, **2011**, *13*, 7198-7206.

with the coolant (activity transport) creating a potential source of radiation exposure to plant workers. In addition, the corrosion products can deposit on thin-walled heat exchanger piping surfaces, decreasing heat transfer efficiencies.

Any released corrosion products (dissolved transition metals) can themselves be considered as dissolved impurities in the coolant water. When exposed to the intense γ -radiation fields of the reactor core, these metallic species can influence, and be influenced by, the radiolytic water chemistry of the coolant, which can then feedback on further corrosion processes.

Many studies have examined the influence of γ -radiation on the surface oxides and corrosion rates of iron-based materials such as carbon steel in aqueous systems [1-4], but little research has focused on the chemistry of dissolved metal ions in irradiated aqueous systems. Some radiation chemistry studies to determine the rate constants of reactions between water radiolysis products and dissolved transition metal species have been performed [5-11]. While the data from these studies can provide a starting point for the development of kinetic models, such information (obtained from short irradiation exposures) cannot be used to predict the behaviour of systems exposed to long-term, continuous radiation sources where back reactions and redox-cycling are important. For example, a series of studies performed in highly acidic ferrous sulfate solutions demonstrated that, while the initial oxidation rate to ferric ions remains fairly reproducible in these solutions with small changes in pH or oxygen concentration, there is great variation in the net oxidation rate observed in these systems at longer irradiation times [10,12,13].

Aqueous phase speciation is not the only concern when considering the radiation chemistry of metallic species. The generation of solid corrosion product deposits in reactor systems, often referred to as crud, is well documented [14-17], yet a detailed understanding of the radiolytic formation mechanism of this material is lacking. Radiation-induced nanoparticle formation from dissolved metal ions in aqueous solutions has been investigated previously, but most work has been limited to noble metals [18-21]. These studies primarily examined the ability of hydrated electrons ($\bullet e_{aq}^-$) and hydrogen atoms ($\bullet H$) from the radiolytic decomposition of water to reduce dissolved noble metal ions to a zero-valence state, leading to their condensation to form insoluble metallic

particles. Silver nanoclusters with very uniform and narrow size distributions have been formed by irradiation of aqueous solutions containing Ag^+ in electron accelerators and gamma irradiation cells [18]. The formation of nanoclusters of bi-metallic species under γ -irradiation and the formation of gold nanoparticles in a room temperature ionic liquid (RTIL) have been also observed [20,21]. These noble metal studies have demonstrated that the size of the clusters formed can be 'tuned' by manipulating the radiation dose rate. The simplicity of this radiation-induced particle formation gives it an advantage over other synthetic processes that require chemical additives and stabilizers since those species can lead to undesired changes to the nanoparticle structure and chemistry.

The syntheses of metal oxides by radiolysis have also been reported [22-25]. The metal-oxide nanoparticles were again formed by a radiolytic reduction mechanism; the metal species were reduced from a higher oxidation state to a lower oxidation state, generally using a short-duration radiation pulse and chemical scavengers to optimize the reducing radical concentrations in solution. Under continuous steady-state irradiation conditions (as would be present in reactor systems), the presence of scavengers changes the distribution of radical and molecular water radiolysis products attained on longer time scales, and cannot be used to elucidate the mechanism of colloid formation in "pure" aqueous systems. We are not aware of any reported studies on the formation of iron oxide nanoparticles utilizing the oxidizing radiolytic products of water formed during long-term γ -irradiation in aqueous solutions in the absence of chemical scavengers.

In this study we report on the *oxidative* formation of uniform-sized colloidal particles of γ -FeOOH by gamma-irradiation of deaerated aqueous solutions of FeSO_4 in slightly acidic (pH 5.5) water. Analyses of dissolved ferric and ferrous species as well as molecular water radiolysis products (H_2 , O_2 and H_2O_2) were performed as a function of irradiation time. The Fe^{3+} -containing colloidal particles were characterized using transmission electron microscopy (TEM), selected area electron diffraction (SAED), Fourier transform infrared (FTIR) spectroscopy, and UV-Vis absorption spectroscopy.

6.2 EXPERIMENTAL PROCEDURE

High-purity iron (II) sulfate was obtained from Sigma-Aldrich (purity $\geq 99\%$) and used without further purification. Deaerated solutions containing dissolved Fe^{2+} in the

concentration range 1×10^{-4} to 5×10^{-4} mol·dm⁻³ were prepared inside a glove box. The pH of the solution was adjusted to 5.5 using sulphuric acid, as measured with a Mettler Toledo pH meter. The solutions were then transferred into 20-ml pyrex vials (Agilent Technologies), leaving no gas headspace, and sealed with PTFE silicon septa. The test vials were irradiated as described in Section 2.2.2 for a maximum duration of 5 hours. The gamma cell provided a uniform absorption dose rate of 1.9 Gy·s⁻¹ to the ferrous solution.

Following irradiation, the concentrations of aqueous and gas phase water radiolysis products were analyzed as described in Sections 2.2.3 and 2.2.4 by UV-Visible spectrophotometry and gas chromatography. The concentrations of ferrous and ferric species were also analyzed spectrophotometrically. The concentration of Fe²⁺ in solution was determined using the ferrozine method. A solution containing ferrozine is mixed with a sample of a test solution. The ferrozine reacts with Fe²⁺ to form a coloured complex that absorbs light at 563 nm with a molar extinction coefficient of 27900 dm³·mol⁻¹·cm⁻¹ [26,27]. Additional solution aliquots were treated with hydroxylamine hydrochloride (1.4 mol·dm⁻³ in concentration) to reduce all Fe³⁺ species to Fe²⁺. This allowed for the total iron concentration in solution to be measured by the ferrozine method. The Fe³⁺ concentration originally present in the test solution was then calculated as the difference between the measured Fe²⁺ concentration following the reduction (equating to the total iron concentration) and the Fe²⁺ concentration measured in the test solution without a reduction step. The Fe³⁺ concentration determined by this method may include contributions from completely solvated Fe³⁺ as well as Fe^{III} oxides or hydroxides in colloidal particles that were transferred by the sampling syringe and underwent reduction to Fe²⁺ by hydroxylamine hydrochloride. Interference tests were performed to show that the presence of the molecular water radiolysis product H₂O₂, which remains in the post-irradiated solutions, did not interfere with the Fe²⁺ and Fe³⁺ measurements. Similarly, it was confirmed that dissolved Fe²⁺ and Fe³⁺, when present at the concentrations observed at steady state, did not interfere with the H₂O₂ analysis separately performed by the Ghormley tri-iodide method [28].

UV-Visible spectrophotometry was also used to monitor the change in the absorbance properties of the irradiated solution as a function of irradiation time. All of

the spectrophotometric measurements were carried out using a diode array detector (BioLogic Science Instruments).

The diameter and shape of the iron nanoparticle clusters formed in the irradiated solutions were directly measured using transmission electron microscopy (TEM) with the electron microscope operated at 80 keV. The TEM samples were prepared by dipping a carbon-coated copper grid into the test solution and then drying the sample grid in flowing air. Selected area electron diffraction (SAED) patterns for the iron colloids were collected at various loci on the high resolution TEM sample grids using an acceleration voltage of 200 kV.

Fourier transform infrared (FTIR) spectroscopy measurements of the iron nanoparticles were performed using a Bruker IR spectrophotometer with Fourier transformation in the 4000 to 400 cm^{-1} frequency range. An aliquot of solution from an irradiated test vial was centrifuged and the particles thus collected were transferred to a glass plate and air dried. The dried sample was incorporated into a KBr pellet for the FTIR measurement. Spectra of standard samples of different oxides of iron were also measured using the same method for references.

6.3 EXPERIMENTAL RESULTS

The optical images of the irradiated solutions and TEM images of the colloidal particles formed are shown in Figure 6.1. These results were obtained by irradiating deaerated solutions initially containing $5 \times 10^{-4} \text{ mol}\cdot\text{dm}^{-3} \text{ FeSO}_4$ at pH 5.5 at a dose rate of $1.9 \text{ Gy}\cdot\text{s}^{-1}$. Over the irradiation period, the appearance of the solution changed from colorless to increasingly yellow in colour while remaining clear (Figure 6.1a). The TEM images at short irradiation times (20 min) show spherical particles with a uniform size on the order of 10 nm. Larger particles, approximately 60 nm in size, started to appear at longer irradiation times (≥ 60 min). These larger particles showed a dendritic structure. Further irradiation up to 5 hours did not lead to an additional increase in the final size of the particles formed or the size distribution, but did result in an increase in the number of larger particles formed.

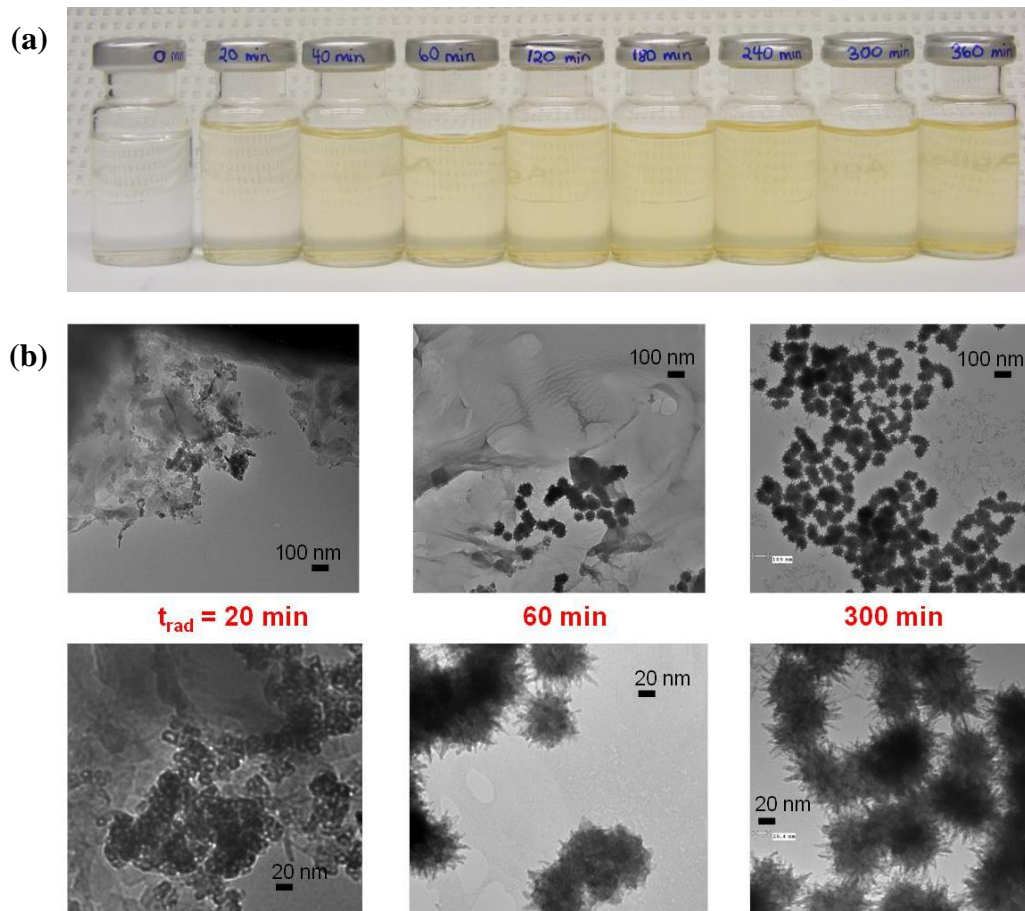


Figure 6.1: (a) Optical images of the test solutions arranged in order of irradiation duration and (b) TEM images showing the size and morphology of iron nanoparticles formed by the irradiation of $[\text{Fe}^{2+}]_0 = 5 \times 10^{-4} \text{ mol}\cdot\text{dm}^{-3}$ deaerated solution at pH 5.5 and a dose rate of $1.9 \text{ Gy}\cdot\text{s}^{-1}$ shown as a function of irradiation time.

Figure 6.2 shows TEM images of particles formed during irradiation of a lower concentration iron sulphate solution ($1 \times 10^{-4} \text{ mol}\cdot\text{dm}^{-3} \text{ FeSO}_4$, pH 5.5) as a function of irradiation time. In this solution the particles grew to their final size faster (in less than 20 min) and were smaller (on the order of 20 nm) than the particles formed in a more concentrated iron solution. The particles formed at the lower iron concentration were spherical and did not display a dendritic structure. Similar results were observed for the

lowest iron concentration studied ($5 \times 10^{-5} \text{ mol}\cdot\text{dm}^{-3}$) (not shown) and the particles formed here were even smaller than those measured for the $1 \times 10^{-4} \text{ mol}\cdot\text{dm}^{-3}$ solution.

The ferrous and ferric concentrations of the irradiated solutions initially containing $[\text{Fe}^{2+}]_0 = 5 \times 10^{-4} \text{ mol}\cdot\text{dm}^{-3}$ are presented in Figure 6.3b. The conversion of Fe^{2+} to Fe^{3+} species was already significant after 20 min, the time of the first measurement. The concentrations of both redox states then changed more slowly, with the concentrations reaching a steady state after approximately 3 h of irradiation. At a lower initial Fe^{2+} concentration ($1 \times 10^{-4} \text{ mol}\cdot\text{dm}^{-3}$) (Figure 6.3a), the same trend was observed, but the steady state was achieved earlier, after about 2 h. It must be noted that the mass balance for iron in the irradiated solutions was poor; only 90% of the initially dissolved iron was detected in the solution at steady state, see Figure 6.3. We assume that the ‘missing’ iron was located in particulates at the bottom of the test vial (gravitational settling) and, hence, escaped the aqueous ferrozine analysis.

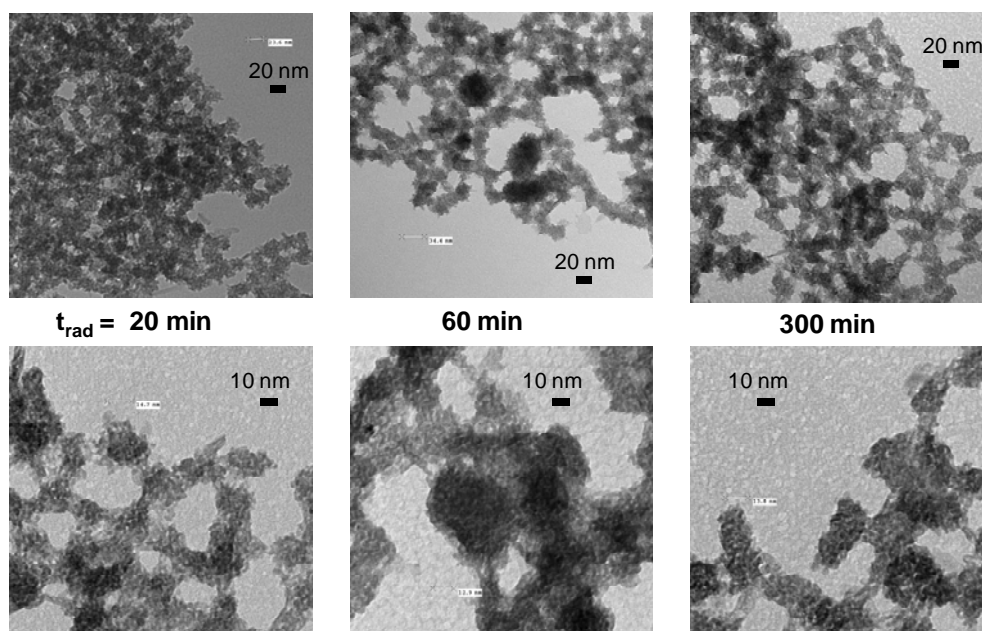


Figure 6.2: TEM images showing the size and morphology of iron nanoparticles formed by the irradiation of a $[\text{Fe}^{2+}]_0 = 1 \times 10^{-4} \text{ mol}\cdot\text{dm}^{-3}$ deaerated solution at pH 5.5 and a dose rate of $1.9 \text{ Gy}\cdot\text{s}^{-1}$, shown as a function of irradiation time.

The concentrations of the stable water radiolysis products, H₂ and O₂, and H₂O₂, were monitored as a function of irradiation time using gas chromatography and UV-Vis spectrophotometry, respectively. In the absence of any dissolved iron, the concentration of H₂ was below the experimental detection limit at irradiation times up to 6 h, Figure 6.4. This is as expected for a low pH solution (see Chapter 3 and 4). The presence of initially dissolved iron raised the concentration of dissolved H₂ to measurable values within 20 min. Inspection of Figure 6.4 shows that the time profile for H₂ was nearly independent of the initial dissolved iron concentration in the range studied. An initial rapid rise in H₂ concentration was followed by a slower increase. It is difficult to discern from Figure 6.4 whether the [H₂] has reached a steady state after 5 h, like the iron ion concentrations, because of the scatter in the data. In contrast, the concentration of radiolytically produced H₂O₂ remained below the detection limit of $3 \times 10^{-6} \text{ mol}\cdot\text{dm}^{-3}$ and the O₂ concentration did not increase as a function of irradiation time for all iron concentrations studied (data not shown). Since mass balance for radiolytic decomposition of water dictates that the total number of hydrogen atoms available must be twice that of the oxygen atoms, these results suggest that the oxygen from water decomposition was preferentially consumed to form solid iron oxide/oxy-hydroxide species instead of O₂.

To determine the chemical composition and phase of the nanoparticles formed, the FTIR spectra of the colloidal particles were compared with the FTIR spectra of standard powder samples of various mineral iron oxides and oxy-hydroxides. In Figure 6.5, only two standard spectra are shown, for simplicity, along with the spectrum obtained from a colloid sample. The colloidal particle spectrum matches that of γ -FeOOH well, except for three additional peaks located between 1000–1300 cm⁻¹. These peaks are characteristic of S-O stretches and are attributed to terminal SO₄²⁻ groups that adsorbed onto the γ -FeOOH nanoparticle surface during the spectroscopy sample preparatory drying stage [29].

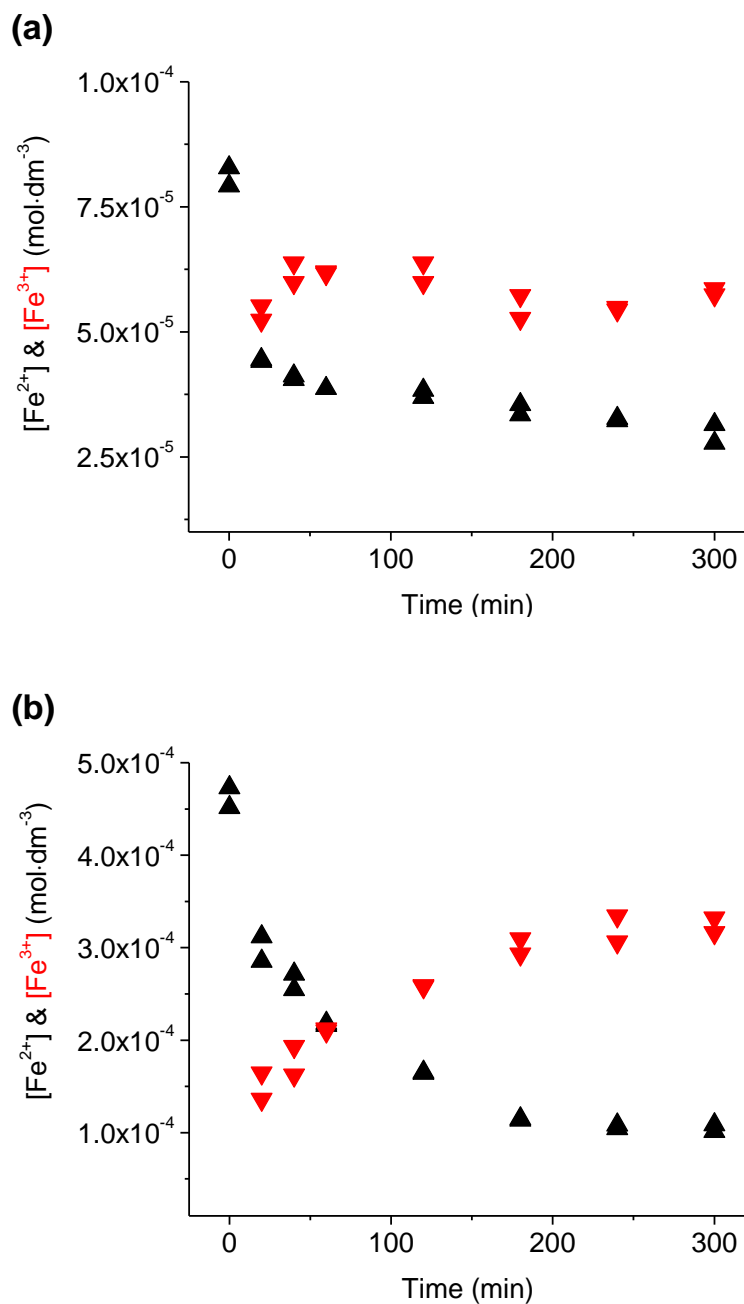


Figure 6.3: The concentration profiles of Fe^{2+} (\blacktriangle) and Fe^{3+} (\blacktriangledown) in pH 5.5 deaerated solutions of (a) $[\text{Fe}^{2+}]_0 = 1 \times 10^{-4} \text{ mol}\cdot\text{dm}^{-3}$, and (b) $[\text{Fe}^{2+}]_0 = 5 \times 10^{-4} \text{ mol}\cdot\text{dm}^{-3}$ at a dose rate of $1.9 \text{ Gy}\cdot\text{s}^{-1}$ as a function of irradiation time.

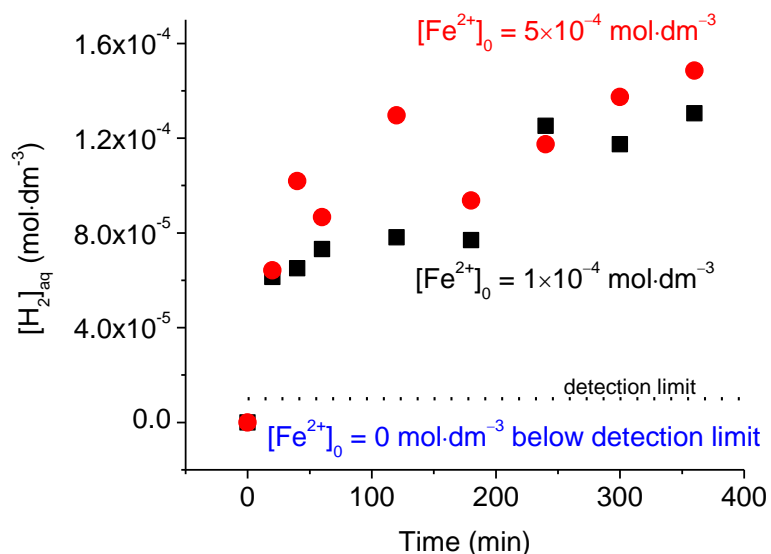


Figure 6.4: The dissolved H₂ concentration measured as a function of irradiation time for deaerated solutions initially containing $1 \times 10^{-4} \text{ mol}\cdot\text{dm}^{-3}$ (■); and $5 \times 10^{-4} \text{ mol}\cdot\text{dm}^{-3}$ (●) at pH 5.5 and a dose rate of 1.9 Gys^{-1} .

The SAED patterns of the colloidal particles collected following 5 h of irradiation were also compared to electron diffraction reference spectra of various iron oxide/oxyhydroxides. Figure 6.6 shows a characteristic ring pattern measured for the colloidal samples along with a corresponding reference intensities profile. The small size of the crystallites caused broadening of the observed reflections in the diffraction pattern. However, intense reflections at 2.53 \AA and 1.53 \AA , and a weak reflection at 2.1 \AA are consistent with the $\gamma\text{-FeOOH}$ reference structure (ICSD file 108876). The colloid sample diffraction patterns were found to match the referenced line pattern for $\gamma\text{-FeOOH}$ at all locations analyzed, confirming that the composition of the nanoparticles is homogeneous and single phase $\gamma\text{-FeOOH}$. In addition, the TEM images and SAED patterns obtained for colloidal particles formed in the same initial ferrous solution but irradiated for a much longer time (20 h) were the same.

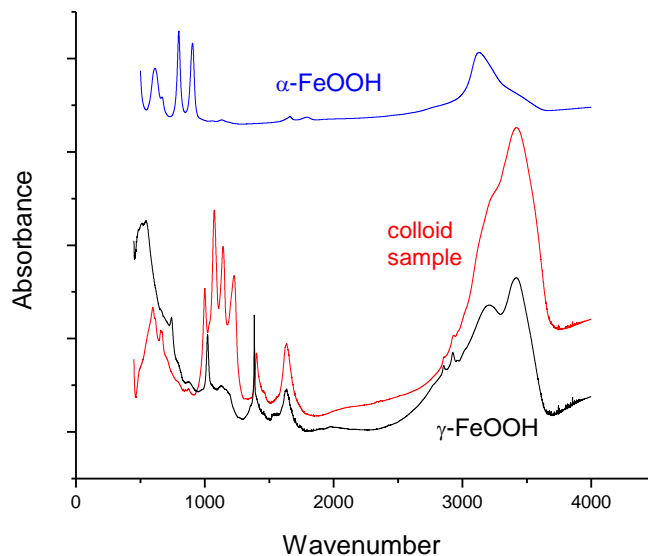


Figure 6.5: The FTIR spectrum obtained for iron nanoparticles formed by the radiolysis of a $[\text{Fe}^{2+}]_0 = 5 \times 10^{-4} \text{ mol}\cdot\text{dm}^{-3}$ deaerated solution at pH 5.5, at a dose rate of $1.9 \text{ Gy}\cdot\text{s}^{-1}$. The reference spectrum of $\alpha\text{-FeOOH}$ is displayed upwards for easier viewing.

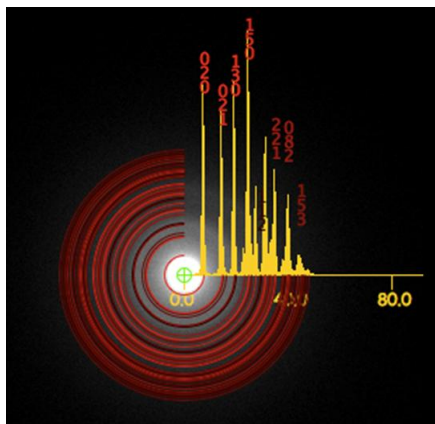


Figure 6.6: The SAED ring pattern and the associated diffraction spectrum (inset) of iron nanoparticles formed by the radiolysis of a $[\text{Fe}^{2+}]_0 = 5 \times 10^{-4} \text{ mol}\cdot\text{dm}^{-3}$ deaerated solution at pH 5.5, at a dose rate of $1.9 \text{ Gy}\cdot\text{s}^{-1}$ for 5 hours.

The UV-Vis absorption spectra of the irradiated solutions were also compared with those obtained from standard solutions containing Fe^{2+} (prepared with FeSO_4) and Fe^{3+} (prepared with $\text{Fe}(\text{NO}_3)_3$), Figure 6.7a. The spectra of irradiated solutions show a UV-Vis absorption band centered at ~ 304 nm that is associated with the presence of hydrated Fe^{3+} species (from comparison with the $\text{Fe}(\text{NO}_3)_3$ and an additional band at ~ 370 nm. The contribution to the absorption by hydrated Fe^{3+} species was subtracted from the UV-Vis spectra (by matching the peak intensities at 304 nm), and the resulting ‘hydrated- Fe^{3+} subtracted’ spectra show a well-defined absorption band at ~ 370 nm, Figure 6.7b. This peak is tentatively attributed to absorption (and/or scattering) by the colloidal particles formed by gamma irradiation. At a given $[\text{Fe}^{2+}]_0$, the peak position and width of the absorption band at 370 nm did not change significantly, but the absorbance intensity increased with irradiation time. This is consistent with an increase in concentration, but not size, of the γ -FeOOH nanoparticles as a function of irradiation time, as was also observed in the TEM images (Figure 6.1b).

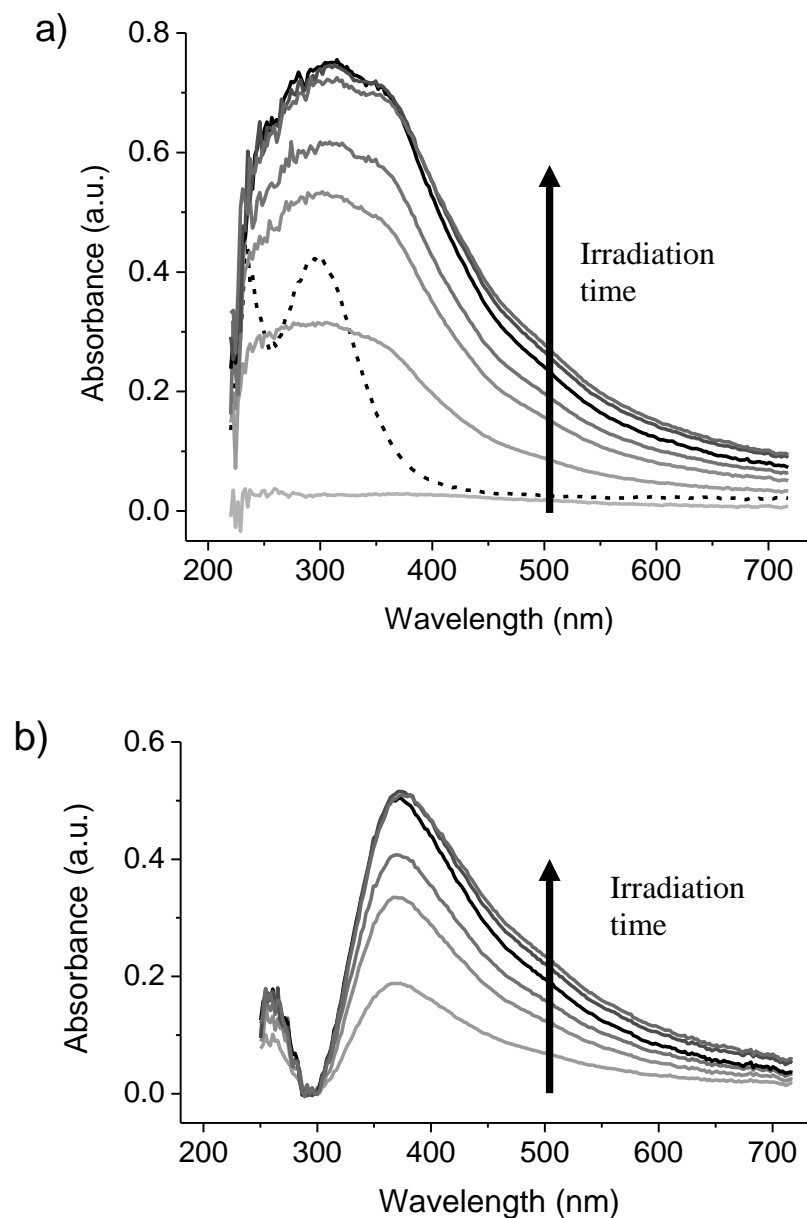


Figure 6.7: UV-Vis spectra of irradiated $[\text{Fe}^{2+}]_0 = 5 \times 10^{-4} \text{ mol} \cdot \text{dm}^{-3}$ deaerated solutions at pH 5.5 and a dose rate of $1.9 \text{ Gy} \cdot \text{s}^{-1}$. (a) Spectra of irradiated ferrous sulphate solutions (solid lines, irradiation times from bottom to top are 0, 20, 40, 60, 120, 240 and 300 minutes) along with the spectrum for an unirradiated ferric nitrate solution (dashed line). (b) Spectra of the irradiated ferrous sulphate solutions with the absorption contribution of the hydrated ferric ion removed (irradiation times from bottom to top are 20, 40, 60, 120, 240 and 300 minutes).

6.4 DISCUSSION OF RESULTS

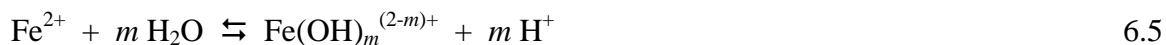
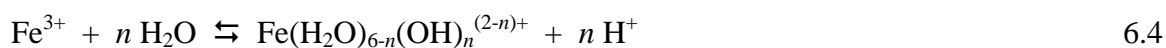
Under γ -irradiation the concentrations of water radiolysis products (reaction 6.1) reach pseudo-equilibrium (or steady state) very quickly at pH values < 9 [30-32].



In the presence of dissolved species at low concentrations ($< 10^{-2} \text{ mol}\cdot\text{dm}^{-3}$), the steady-state concentrations of radiolysis products dictate the bulk aqueous chemistry of the dissolved species. For dissolved metal ion redox reactions, the key radiolytic products of water are the $\bullet\text{OH}$ and $\bullet\text{e}_{\text{aq}}^-$ radicals due to their high oxidizing and reducing powers. The elementary reactions of ferric and ferrous ions with these water radiolysis products have been studied and their rate constants are established [6,9,11]:



The ferric and ferrous ions in these reactions are also in fast hydrolysis equilibria:



where n and m are integers from 1 to 4 and from 1 to 3 for reactions 6.4 and 6.5, respectively. The rate constants listed above, $k_{\text{R6.2}}$ and $k_{\text{R6.3}}$, are the net rate constants including the contributions of all of the iron species involved in the hydrolysis equilibria 6.4 and 6.5. Due to the fast hydrolysis equilibria, all the hydrated ferric or ferrous species combined will be, hereafter, referred to as $\text{Fe}^{3+}(\text{aq})$ or $\text{Fe}^{2+}(\text{aq})$ respectively.

Reactions 6.2 and 6.3 are expected to be fast due to the relatively high concentrations of $\bullet\text{OH}$ and $\bullet\text{e}_{\text{aq}}^-$ generated during radiolysis, and the dynamic system is predicted to reach an initial steady state very quickly. The conversion from ferrous to ferric ion was, indeed, observed to be initially very fast, with more than 30 to 50% conversion seen after only 20 min. However, this change was followed by a period of

progressively slower increase in the ferric iron concentration which is not predicted by a homogeneous aqueous reaction kinetic model [30]. At longer times (> 120 min) the relative concentrations of ferrous and ferric ions do not change, but only 90% of the initially dissolved iron was detected in the irradiated solutions. The ferrozine method used to detect iron in solution can reduce suspended Fe^{III} colloidal particles and thereby detect this undissolved iron, but the water sampling method would not collect any gravitationally-settled particles. This may account for the apparent loss of iron as a function of time.

To explain the observed three stage ferrous to ferric conversion behaviour, we propose a series of processes that are schematically shown in Figure 6.8. The first stage ($t < 20$ min) is the nucleation and primary particle formation stage. Since the reactions of $\bullet e_{aq}^-$ and $\bullet OH$ with other radiolytic products of water, as well as with ferrous and ferric ions, are very fast, the concentrations of the radicals reach a pseudo-steady state very quickly (within ms) under continuous irradiation. This type of behaviour was previously seen and modeled correctly for solutions containing dissolved O₂ or NO₃⁻ (see Chapter 4 and Chapter 5). Thus, the irradiation of ferrous solutions should result in a fast pseudo equilibrium between [Fe²⁺(aq)] and [Fe³⁺(aq)], with the equilibrium concentrations determined by:

$$\frac{[Fe^{3+}(aq)]_t}{[Fe^{2+}(aq)]_t} = \frac{[Fe^{3+}(aq)]_t}{[Fe^{2+}(aq)]_0 - [Fe^{3+}(aq)]_t} \approx \frac{k_{R6.2} \cdot [\bullet OH^-]_t}{k_{R6.3} \cdot [\bullet e_{aq}^-]_t} \quad E6.1$$

At the pH studied this ratio is greater than 1 because the steady-state concentration of $\bullet OH$ is 2-3 orders of magnitude higher than that of $\bullet e_{aq}^-$ [31]. This leads to supersaturation of Fe³⁺(aq) in the solution.

The solubility of ferric hydroxide species is several orders of magnitude lower than that of ferrous hydroxide species at pH < 8.5; for example, at pH 5.5, the solubilities of Fe(OH)₃ and Fe(OH)₂ are on the order of 10⁻⁸ mol·dm⁻³ and 10⁻¹ mol·dm⁻³, respectively [33]. Thus, radiolysis of a solution containing Fe²⁺ at a concentration far below its solubility limit produces Fe³⁺(aq) at a concentration that is well above the ferric ion solubility limit. (Note that since the aqueous chemistry in the presence of ionizing

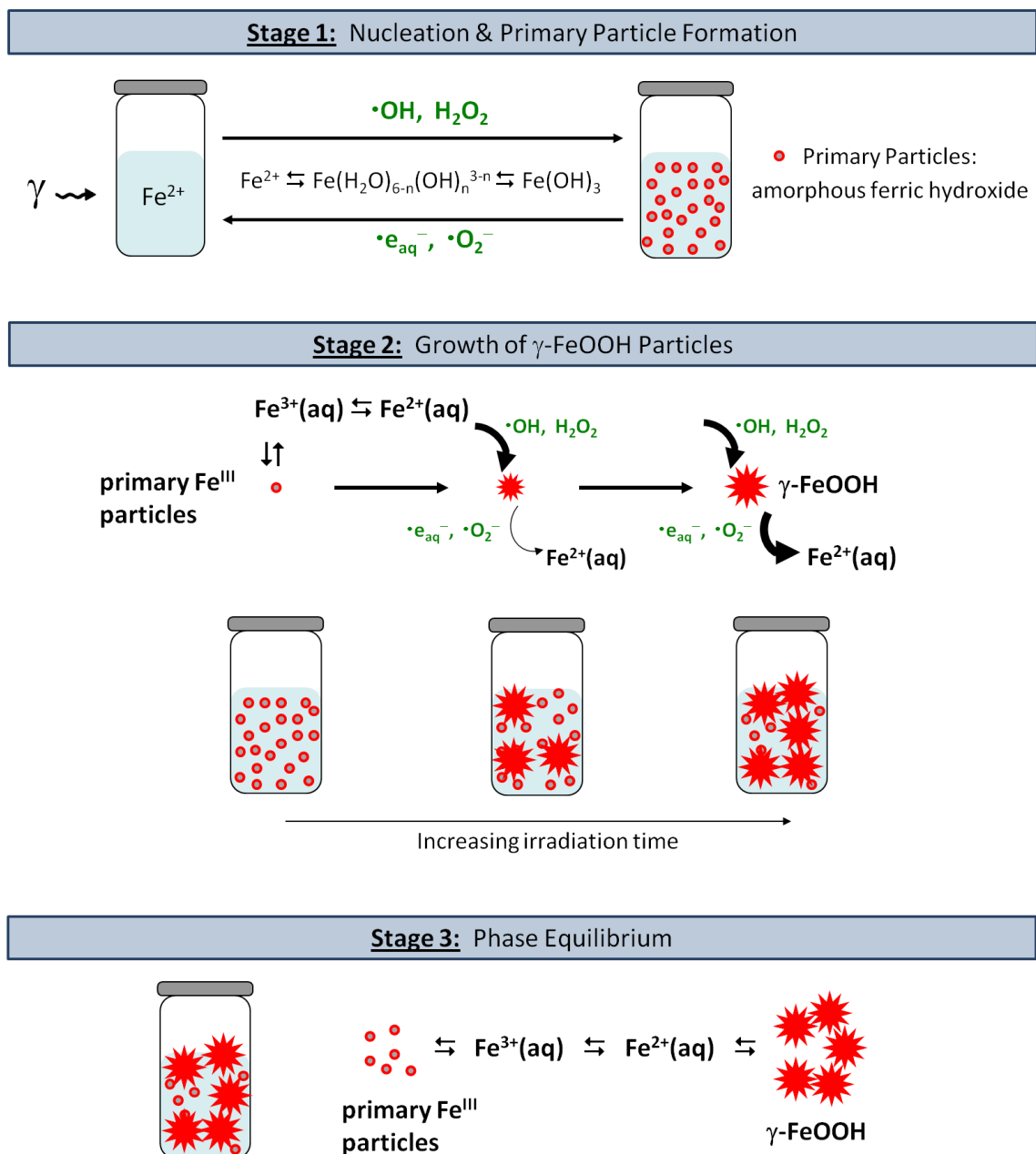


Figure 6.8: Proposed three stage growth mechanism of γ -FeOOH particles induced by the γ -irradiation of deaerated FeSO_4 solutions at pH 5.5.

radiation is not at thermal equilibrium, the solubilities of iron species under irradiation conditions could be somewhat different than their solubilities at thermal equilibrium.) This supersaturation drives condensation/dehydration of hydrated ferric species to form initial (or primary) particles composed of $\text{Fe}(\text{OH})_3(\text{s})$:



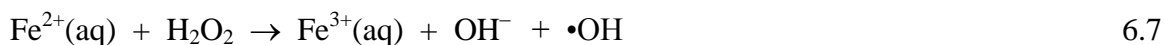
The condensed ferric hydroxide could be partially hydrated (at least on the surface), but hereafter, $\text{Fe}(\text{OH})_3(\text{s})$ will be used to represent the condensed ferric hydroxide.

This primary particle formation occurs rapidly because of the rapid homogeneous generation of supersaturated $\text{Fe}^{3+}(\text{aq})$ throughout the solution. Compared to this radiolytic process, chemical syntheses of iron oxy-hydroxide nanoparticles by other processes are slower. For example, in forced hydrolysis methods, in which the generation of primary particles is also based on the condensation and dehydration of ferric ions, the starting iron species are soluble ferric species and the condensation/dehydration of the ferric species is achieved by changing temperature to shift the hydrolysis equilibria of the ferric species [34]. The rapid production of powerful redox radicals by ionizing radiation shortens the time required for production of the primary particles contributing to the uniform size distribution of the resulting particles.

The concentration of radiolytically-produced H_2 is inversely proportional to the concentration of $\cdot\text{OH}$ [30-32]. The increase in the net radiolytic production of H_2 (relative to pure water) in the presence of ferrous iron can be attributed to the competitive reaction kinetics of $\cdot\text{OH}$ with $\text{Fe}^{2+}(\text{aq})$, H_2 and H_2O_2 . An initial steady-state balance is achieved between ferric species in aqueous and solid forms, reaction 6.6. Depending on the concentration of iron initially dissolved in the system, a greater proportion of the radiolytically-formed Fe^{3+} may enter the solid phase. This would result in the fraction of iron remaining as dissolved in the aqueous phase (and undergoing cycling between Fe^{2+} and Fe^{3+}) to be about the same at early irradiation times. As a result, the ratio of $\text{Fe}^{2+}(\text{aq})$ to $\text{Fe}^{3+}(\text{aq})$ in the first stage (< 20 min) is not sensitive to the initial ferrous concentration. Consequently, the removal rate of OH due to ongoing scavenging by reaction with

$\text{Fe}^{2+}(\text{aq})$, and the corresponding increase in $[\text{H}_2]$, is also nearly independent of the initially dissolved ferrous concentration.

Unlike the case with radical scavengers studied in Chapter 4 and Chapter 5, the H_2O_2 and O_2 concentrations did not increase along with H_2 for irradiated ferrous solutions. Reactions with the hydrated electron can remove both H_2O_2 and O_2 . However, removal of H_2O_2 can also occur by the Fenton reaction:



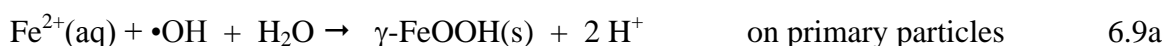
Combined with the net removal of $\bullet\text{OH}$ that can arise from $\text{Fe}^{2+}/\text{Fe}^{3+}$ cycling, the rate of formation of the secondary radiolysis product O_2 , which is due to the reaction of hydrogen peroxide with the hydroxyl radical, can also be reduced. As a result, a net consumption of oxygen-containing species occurs during the formation of $\text{Fe}^{3+}(\text{aq})$ and $\text{Fe}(\text{OH})_3(\text{s})$ from $\text{Fe}^{2+}(\text{aq})$.

In the second stage, the conversion from ferrous to ferric species still occurs, but at a slower rate compared to that occurring in stage 1, Figure 6.3. The duration of this stage depends on the initial ferrous ion concentration at the studied pH; it lasts approximately 20 min for the lower concentration case and up to 200 min at the higher concentrations tested. During this stage the particles grow and establish a specific oxide or oxyhydroxide phase. The chemical composition, phase and size of the nanoparticles eventually formed depend on pH, temperature, ionic strength, aqueous redox conditions and initial ferrous ion concentration since these parameters will affect the free energy of formation of the solid phase, particle surface reactivity and charge, and, hence, the solid-water interfacial partitioning of ferric species [35-37]. In the second stage, the redox reactions 6.2 and 6.3 can continue on the surface of the particles as well as in the aqueous phase. The increasing importance of heterogeneous reactions on the particle surface explains the slowing in the rate of conversion of ferrous to ferric ion. Molecular products from water radiolysis, such as H_2O_2 , and the secondary radiolysis products such as O_2 and $\bullet\text{O}_2^-$, can accumulate to substantial concentrations and, hence, can participate in the redox reactions (see further discussion below).

Under the conditions of this study, the final nanoparticles formed are composed of γ -FeOOH, as identified by FTIR, SAED and UV-Vis, Figure 6.5 to Figure 6.7. The formation of γ -FeOOH from the primary $\text{Fe}(\text{OH})_3(\text{s})$ particles requires either dehydration of $\text{Fe}(\text{OH})_3(\text{s})$:



or oxidation of ferrous ions by $\bullet\text{OH}$ or H_2O_2 on the surface of the primary particles:

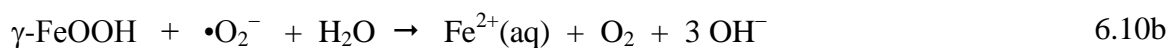
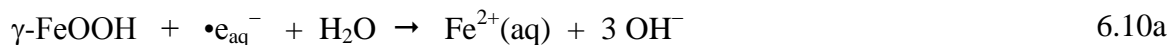


At room temperature with radiation present, the phase conversion from solid ferric hydroxide to lepidocrocite, reaction 6.8, is very slow relative to the formation of γ -FeOOH by reaction of dissolved ferrous ion with water radiolysis products $\bullet\text{OH}$ and H_2O_2 , and, hence, reaction 6.9 is the preferable path for γ -FeOOH growth. Reaction 6.9 is also an electrochemical redox reaction and should occur at a faster rate on a more conducting surface. Compared with insulating $\text{Fe}(\text{OH})_3$, γ -FeOOH is a better electrical conductor, as it exhibits semi-conductive properties and has been known to support the reduction or oxidation of adsorbed species such as H_2O_2 [38,39]. The growth of γ -FeOOH is accelerated as the more conducting γ -FeOOH layer thickens and this could explain the observed particle size growth behaviour.

The TEM images (Figure 6.1b) show that the particles formed following 60 min of irradiation have only two sizes, ~ 20 nm, the size of the primary particles, and ~ 60 nm, the final size of the γ -FeOOH nanoparticles, and that longer irradiation does not affect the final particle size, but only increases the number of the final-sized particles. These results suggest that once a distinct layer of γ -FeOOH is formed on the surface of a primary particle, further iron oxidation by water radiolysis products occurs at a faster rate on the γ -FeOOH surface layer than on the $\text{Fe}(\text{OH})_3$ surface layer. This preferential oxidation of ferrous to ferric species on the γ -FeOOH layer over the primary $\text{Fe}(\text{OH})_3$

particles results in the γ -FeOOH nanoparticles growing to the final size one at a time. This explains the absence of intermediate-sized particles in the TEM images.

The final size is reached when the rate of reduction of γ -FeOOH to $\text{Fe}^{2+}(\text{aq})$ by reducing water radiolysis products, such as $\bullet\text{e}_{\text{aq}}^-$ or $\bullet\text{O}_2^-$, reaction 6.10, becomes equal to the rate of the γ -FeOOH formation, reaction 6.9:



At the early stage of γ -FeOOH growth in stage 2, the ferrous oxidation (reaction 6.9) on the surface of the particles is faster than the ferric reduction (reaction 6.10). However, as the γ -FeOOH particles grow in a dendritic shape, their surface areas increase relative to the primary particles that have near spherical shape and the rate of ferric reduction (reaction 6.10) increases. The γ -FeOOH particles reach their final size when the ferric reduction rate equals the ferrous oxidation rate. Note that the concentrations of molecular water radiolysis products such as H_2O_2 and H_2 and the secondary radiolysis products such as O_2 and $\bullet\text{O}_2^-$ can also reach relatively high concentrations at longer times [30-32]. Thus, not only the redox reactions of radical products but also those of the molecular products need to be taken into account in the chemistry occurring on surfaces.

In stage 2, the concentrations of water radiolysis products, $\bullet\text{OH}$, H_2O_2 , $\bullet\text{e}_{\text{aq}}^-$ and $\bullet\text{O}_2^-$, are at (pseudo-) steady state, and reactions 6.2 and 6.3 continually occur in the aqueous phase. In addition, $\text{Fe}^{3+}(\text{aq})$ is in aqueous-solid phase equilibrium with ferric hydroxide via reaction 6.6. These (pseudo-) equilibrium reactions maintain the ratio of the aqueous ferric and ferrous concentrations at a stable level with time, see equation E6.1. Thus, although most of the initially added $\text{Fe}^{2+}(\text{aq})$ has been oxidized to $\text{Fe}^{3+}(\text{aq})$ and then quickly converted to the primary $\text{Fe}(\text{OH})_3$ particles in stage 1, these primary particles can dissolve back into solution to continuously provide $\text{Fe}^{2+}(\text{aq})$ for incorporation into the solid phase γ -FeOOH on other particles by reaction 6.9 in stage 2. Once the particles reach a critical size their growth rate accelerates as the growth progresses. The net result is the slow conversion of the primary particles to mature

γ -FeOOH nanoparticles. The conversion of the primary particles to the final particles occurs via radiolytically-induced oxidation and reduction reactions and, hence, the final particles do not appear to grow by the aggregation of the primary particles.

The dendritic structure observed for the nanoparticles produced after long irradiation times is also consistent with solid-state growth of the γ -FeOOH crystals rather than homogeneous aggregation of smaller particles. Similar formation of dendrites has been observed in γ -FeOOH deposited chemically as a thin film on glass and in γ -FeOOH formed electrochemically on carbon steel [34,40].

The surface redox reaction rates eventually reach steady state (via reactions 6.9 and 6.10), regulating the further growth of the particles and the particles do not grow beyond a certain size. Stage 3 is reached when the aqueous ferric and ferrous ion concentrations, and the γ -FeOOH nanoparticle size, reach steady state.

6.5 CONCLUSIONS

Uniform-sized colloidal particles of γ -FeOOH are formed by gamma-irradiation of deaerated aqueous solutions containing soluble Fe^{2+} species (as FeSO_4) at pH 5.5. At short irradiation times or in solutions containing initially low $[\text{Fe}^{2+}]_0$, spherical particulates less than 10 nm in size with a narrow size distribution are formed. These particles grow to form larger particles with a dendritic structure upon longer irradiation, but the growth is terminated with particles having a very uniform and narrow size distribution, approximately 60 nm in diameter. Further prolonged irradiation did not change the final particle size, but increases the number of the particles having the final size. The colloidal particles were identified as single-phase γ -FeOOH.

The uniform particle size distribution obtained under γ -irradiation is attributed to a multi-stage process initiated by rapid homogeneous radiolytic oxidation of soluble Fe^{2+} to relatively insoluble Fe^{3+} hydroxides $[\text{Fe}(\text{H}_2\text{O})_{6-n}(\text{OH})_n]^{3-n}$. These hydroxides dehydrate to form amorphous ferric-hydroxide primary particles. Upon longer irradiation, ferrous ion is oxidized by water radiolysis products on the primary particle surface to form γ -FeOOH. The growth of γ -FeOOH is accelerated as the γ -FeOOH layer thickens since γ -FeOOH is more conducting than ferric hydroxide. The ferrous ion required for the growth of γ -FeOOH is supplied by dissolution of other primary particles. The reduction

of γ -FeOOH by water radiolysis products also occurs on the γ -FeOOH surfaces, and the rate increases with time (and particle surface area). Hence the γ -FeOOH particles reach a final uniform size when the ferric reduction rate equals the ferrous oxidation rate on the particle surface. Under irradiation particles grow by radiolytically-induced oxidation and reduction reactions and not by aggregation of smaller particles..

6.6 ACKNOWLEDGEMENTS

Dr. Richard Gardiner at the University of Western Ontario Biotron Facility and Dr. Glynis de Silveira and Mr. Fred Pearson at the Canadian Centre for Electron Microscopy, Brockhouse Institute for Materials Research at McMaster University are thanked for their assistance with TEM imaging and SAED analysis.

The work described herein was funded under an NSERC (Natural Science and Engineering Research Council of Canada) Discovery grant. The support from a Canada Foundation for Innovation New Opportunity grant and an Ontario Research Fund Excellence in Research: Nuclear Ontario grant are greatly acknowledged for the purchase of the UV-Vis absorption and FTIR spectrometers, respectively.

6.7 REFERENCES

- [1] Daub, K., Zhang, X., Noël, J.J., Wren, J.C., "Effects of γ -radiation versus H_2O_2 on carbon steel corrosion", *Electrochim. Acta*, **2010**, 55, 2767-2776.
- [2] Yamamoto, T., Tsukui, S., Okamoto, S., Nagai, T., Takeuchi, M., Takeda, S., Tanaka, Y., "Gamma-ray irradiation effect on corrosion rates of stainless steel, Ti and Ti-5Ta in boiling 9N nitric acid", *J. Nucl. Mater.*, **1996**, 228, 162-167.
- [3] Fujita, N., Matsuura, C., Saigo, K., "Irradiation-enhanced corrosion of carbon steel in high temperature water — in view of a cell formation induced by γ -rays", *Radiat. Phys. Chem.*, **2000**, 58, 139-147.
- [4] Daub, K., Zhang, X., Noël, J.J., Wren, J.C., "Gamma-radiation-induced corrosion of carbon steel in neutral and mildly basic water at 150°C", *Corros. Sci.*, **2011**, 53, 11-16.
- [5] Baxendale, J.H., Fielden, E.M., Keene, J.P., "The pulse radiolysis of aqueous solutions of some inorganic compounds", *Proc. R. Soc. London, Ser. A*, **1965**, 286, 320-336.
- [6] Stuglik, Z., Zagorski, Z.P., "Pulse radiolysis of neutral iron(II) solutions: Oxidation of ferrous ions by OH radicals", *Radiat. Phys. Chem.*, **1981**, 17, 229-233.
- [7] Zehavi, D., Rabani, J., "Pulse radiolytic investigation of O_{aq}^- radical ions", *J. Phys. Chem.*, **1971**, 75, 1738-1744.

- [8] Rush, J.D., Bielski, B.H., "Pulse radiolytic studies of the reactions of HO_2/O_2^- with Fe(II)/Fe(III) ions. The reactivity of HO_2/O_2^- with ferric ions and its implications on the occurrence of the Haber-Weiss reaction.", *J. Phys. Chem.*, **1985**, 89, 5062-5066.
- [9] Jonah, C.D., Miller, J.R., Matheson, M.S., "The reaction of the precursor of the hydrated electron with electron scavengers", *J. Phys. Chem.*, **1977**, 81, 1618-1622.
- [10] Rothschild, W.G., Allen, A.O., "Studies in the radiolysis of ferrous sulfate solutions III: Air-free solutions at higher pH", *Radiat. Res.*, **1958**, 8, 101-110.
- [11] Buxton, G.V., Greenstock, C.L., Helman, W.P., Ross, A.B., "Critical-review of rate constants for reactions of hydrated electrons, hydrogen atoms and hydroxyl radicals (OH/O⁻) in aqueous solution", *J. Phys. Chem. Ref. Data*, **1988**, 17, 513-886.
- [12] Allen, A.O., Hogan, V.D., Rothschild, W.G., "Studies in the radiolysis of ferrous sulfate solutions II: Effect of acid concentration in solutions containing oxygen", *Radiat. Res.*, **1957**, 7, 603-608.
- [13] Allen, A.O., Rothschild, W.G., "Studies in the radiolysis of ferrous sulfate solutions I: Effect of oxygen concentration in 0.8 N sulfuric acid", *Radiat. Res.*, **1957**, 7, 591-602.
- [14] Lin, C.C., "A review of corrosion product transport and radiation field buildup in boiling water reactors", *Progress in Nuclear Energy*, **2009**, 51, 207-224.
- [15] Sawicki, J.A., "Analyses of fuel crud and coolant-borne corrosion products in normal water chemistry BWRs", *J. Nucl. Mater.*, **2011**, 419, 85-96.
- [16] Tsai, T.-L., Lin, T.-Y., Su, T.-Y., Wen, T.-J., Men, L.-C., "Characterization of corrosion products deposited on fuel rods in a boiling water reactor (BWR-6) plant using hydrogen water chemistry (HWC)", *J. Radioanal. Nucl. Chem.*, **2013**, 298, 1235-1244.
- [17] Yeon, J.-W., Choi, I.-K., Park, K.-K., Kwon, H.-M., Song, K., "Chemical analysis of fuel crud obtained from Korean nuclear power plants", *J. Nucl. Mater.*, **2010**, 404, 160-164.
- [18] Henglein, A., Geirsig, M., "Formation of colloidal silver particles: Capping action of citrate", *J. Phys. Chem. B*, **1999**, 103, 9533-9539.
- [19] Ni, Y., Ge, X., Zhang, Z., Ye, Q., "Fabrication and characterization of the plate-shaped $\gamma\text{-Fe}_2\text{O}_3$ nanocrystals", *Chem. Mater.*, **2002**, 14, 1048-1052.
- [20] Belloni, J., Mostafavi, M., Remita, H., Marignier, J.-L., Marie-Odile Delcourt, a., "Radiation-induced synthesis of mono- and multi-metallic clusters and nanocolloids", *New J. Chem.*, **1998**, 22, 1239-1255.
- [21] Chen, S., Liu, Y., Wu, G., "Stabilized and size-tunable gold nanoparticles formed in a quaternary ammonium-based room-temperature ionic liquid under γ -irradiation", *Nanotechnology*, **2005**, 16, 2360.
- [22] Dey, G.R., Remita, H., Mostafavi, M., "Radiolytic reduction of Fe(II) in 2-propanol", *Chem. Phys. Lett.*, **2006**, 431, 83-87.
- [23] Yadav, P., Olsson, R.T., Jonsson, M., "Synthesis and characterization of MnO_2 colloids", *Radiat. Phys. Chem.*, **2009**, 78, 939-944.

- [24] Gracien, E.B., Ruimin, Z., LiHui, X., Kanza Kanza, L., "Effects of pH on the morphology of iron oxides synthesized under gamma-irradiation", *J. Radioanal. Nucl. Chem.*, **2006**, 270, 473-478.
- [25] Abedini, A., Daud, A.R., Hamid, M.A.A., Othman, N.K., "Radiolytic formation of Fe₃O₄ Nanoparticles: Influence of Radiation Dose on Structure and Magnetic Properties", *PLoS ONE*, **2014**, 9, e90055.
- [26] Stookey, L.L., "Ferrozine -a new spectrophotometric reagent for iron", *Anal. Chem.*, **1970**, 42, 779-781.
- [27] Viollier, E., Inglett, P.W., Hunter, K., Roychoudhury, A.N., Van Cappellen, P., "The ferrozine method revisited: Fe(II)/Fe(III) determination in natural waters", *Appl. Geochem.*, **2000**, 15, 785-790.
- [28] Hochanadel, C.J., "Effects of cobalt γ -radiation on water and aqueous solutions", *J. Phys. Chem.*, **1952**, 56, 587-594.
- [29] Boily, J.-F., Gassman, P.L., Peretyazhko, T., Szanyi, J., Zachara, J.M., "FTIR spectral components of schwertmannite", *Environ. Sci. Technol.*, **2010**, 44, 1185-1190.
- [30] Wren, J.C. In *ACS Symposium Series: Nuclear Energy and the Environment*, Chien, W., Mincher, B., Eds., American Chemical Society: Washington, D.C., 2010, p 271-295.
- [31] Joseph, J.M., Choi, B.S., Yakabuskie, P.A., Wren, J.C., "A combined experimental and model analysis on the effect of pH and O₂(aq) on γ -radiolytically produced H₂ and H₂O₂", *Radiat. Phys. Chem.*, **2008**, 77, 1009-1020.
- [32] Yakabuskie, P.A., Joseph, J.M., Wren, J.C., "The effect of interfacial mass transfer on steady-state water radiolysis", *Radiat. Phys. Chem.*, **2010**, 79, 777-785.
- [33] Baes, C.F., Mesmer, R.E. *The hydrolysis of cations*, Robert. E. Krieger Publishing Co.: Malabar, Florida, 1986.
- [34] Fu, D., Wren, J.C., "Preparation and characterization of ferric oxyhydroxide and ferric oxide thin films by direct-hydrolysis deposition", *J. Nucl. Mater.*, **2008**, 374, 116-122.
- [35] Fu, D., Keech, P.G., Sun, X., Wren, J.C., "Iron oxyhydroxide nanoparticles formed by forced hydrolysis: dependence of phase composition on solution concentration", *Phys. Chem. Chem. Phys.*, **2011**, 13, 18523-18529.
- [36] Macary, L.S., Kahn, M.L., Estournès, C., Fau, P., Trémouilles, D., Bafleur, M., Renaud, P., Chaudret, B., "Size effect on properties of varistors made from zinc oxide nanoparticles through low temperature spark plasma sintering", *Adv. Funct. Mater.*, **2009**, 19, 1775-1783.
- [37] Park, J., Lee, E., Hwang, N.-M., Kang, M., Kim, S.C., Hwang, Y., Park, J.-G., Noh, H.-J., Kim, J.-Y., Park, J.-H., Hyeon, T., "One-nanometer-scale size-controlled synthesis of monodisperse magnetic iron oxide nanoparticles", *Angew. Chem. Int. Ed.*, **2005**, 44, 2872-2877.
- [38] Cornell, R.M., Schwertmann, U. *The Iron Oxides: Structure, Properties, Reactions, Occurrences and Uses*, 2nd ed., Wiley-VCH: Weinheim, 2003.

- [39] Fu, D., Zhang, X., Keech, P.G., Shoesmith, D.W., Wren, J.C., "An electrochemical study of H₂O₂ decomposition on single-phase γ -FeOOH films", *Electrochim. Acta*, **2010**, 55, 3787-3796.
- [40] Xu, W., Daub, K., Zhang, X., Noel, J.J., Shoesmith, D.W., Wren, J.C., "Oxide formation and conversion on carbon steel in mildly basic solutions", *Electrochim. Acta*, **2009**, 54, 5727-5738.

CHAPTER 7 THE EFFECT OF INITIALLY DISSOLVED FERROUS IRON ON STEEL CORROSION UNDER γ -IRRADIATION

7.1 INTRODUCTION

Corrosion of reactor structural components releases metallic impurities into the coolant and can lead to the formation of insoluble solids (crud) [1-4]. The deposition of corrosion products on heat exchanger piping can lead to reductions in the heat transfer efficiency of the system. Temporary deposition of crud in the reactor core, where the neutron flux is high, can also promote activity transport if neutron absorption by corrosion products generates radioactive species (e.g., ^{54}Mn , ^{58}Co , ^{59}Fe , ^{60}Co) [5]. Deposition of solids containing these radioactive isotopes outside the biological shielding of the reactor is a health hazard for plant workers.

Corrosion rates are strongly influenced by the presence of chemically reactive species and especially by oxidizing species. In nuclear reactor systems, the γ -radiolysis of water produces highly reactive radicals and molecules which include both oxidizing ($\bullet\text{OH}$, H_2O_2 , O_2) and reducing species ($\bullet\text{e}_{\text{aq}}^-$, $\bullet\text{O}_2^-$, $\bullet\text{H}$) [6-8]. If the radiation field is constant, the irradiated system quickly reaches a steady state in which the concentrations of the water radiolysis products tend to stabilize at low levels. However, due to their high reactivity, these species can effectively control the aqueous redox state, even at low concentrations, and can influence the corrosion kinetics on a metal surface [9-13].

Corrosion products released are often transition metal ions that have multiple stable oxidation states. Thus, redox reactions between these metal ions and water radiolysis products can induce changes to the metal oxidation state, as presented in reaction 7.1 for irradiated ferrous solutions:



Since the solubilities of hydrated metal species also vary considerably depending on their oxidation state [14], these rapid radiolytic reactions of dissolved metal ions can lead to the formation of solid species under some conditions. This behaviour was reported in

Chapter 6, where less soluble Fe^{III} hydroxides (formed by the rapid radiolytic oxidation of Fe²⁺) condensed out of the solution. Growth on these nucleation sites resulted in uniform-sized γ -FeOOH particles; the final particle size was regulated by the radiolytically-induced steady-state redox conditions at the water-solid interface [15].

Just as the steady-state concentrations of water radiolysis products can influence the growth of suspended solids in the solution, they can also impact the oxide structures on a bulk metal surface. The overall impact of these interactions on the chemical system will depend on the precipitation and diffusion behaviour of the oxide species generated. For example, the solubility of the oxide phase can dictate the rate of metal ion release into the solution. This ion release can then, in turn, influence the water radiolysis product concentrations (reaction 7.1). In addition, some of the water radiolysis products can also decompose on metal surfaces without inducing oxidation or reduction of the metal/metal oxide species on the surface (e.g., $\text{H}_2\text{O}_2 \rightarrow \frac{1}{2} \text{O}_2 + \text{H}_2\text{O}$) [16]. Consequently, the net impact of radiolysis on corrosion rates is very difficult to predict.

Most studies on steel corrosion have been performed in pure water with no dissolved corrosion products initially present. In a real environment, corrosion will release ferrous ions from available steel surfaces and the ferrous ion concentration can reach a level near the solubility limit for that ion. Recent electrochemical studies of carbon steel and stainless steel corrosion in our lab show that the presence of ferrous ions in solution does not affect the type of oxide that forms on the steel surface at low potentials, but it does suppress the metal ion dissolution rate [17]. At higher potentials, where Fe²⁺(aq) can oxidize to γ -FeOOH, a thick layer of γ -FeOOH crystallites forms on a corroding steel surface on top of an inner magnetite (for carbon steel) or chromite (for stainless steel) oxide. When the potential at the corroding surface is reduced to a level below the equilibrium potential of the Fe₃O₄/ γ -FeOOH redox reaction, this γ -FeOOH is easily reduced to magnetite. Other studies have also shown that in low oxygen environments, the reduction of corrosion product deposits (such as magnetite and lepidocrocite) can galvanically couple to the metal oxidation [18,19]. Specifically, in wet/dry cycling studies, the reduction of γ -FeOOH was shown to form a Fe²⁺-containing oxide similar to Fe(OH)₂, and this ferrous oxide could be readily oxidized back to γ -FeOOH [20]. Additionally, small iron particulates (< 0.1 μm) have been previously

shown to enhance the solubility of magnetite outside of a radiation field [21]. If irradiation of ferrous solutions leads to continuous formation of γ -FeOOH deposits, then subsequent reduction of the γ -FeOOH may couple with the oxidation of iron in the base metal and the corrosion of steel may be significantly accelerated.

In this work we present the results of experiments to determine the effects of dissolved Fe^{2+} on the radiolysis-driven corrosion of carbon steel and stainless steel. The behaviour of the steels was studied in the presence and absence of γ -radiation over an exposure time of 64 h in ferrous sulphate solutions ranging in concentration from 0 to $5 \times 10^{-4} \text{ mol}\cdot\text{dm}^{-3}$ at pH 6.0. A time-dependent study was also completed for 0 and $5 \times 10^{-4} \text{ mol}\cdot\text{dm}^{-3}$ ferrous solutions that extended to 138 hours of irradiation. Radiolytic gas production, aqueous speciation of metallic species, and coupon surface and particle analyses were performed.

7.2 EXPERIMENTAL PROCEDURE

High-purity iron (II) sulfate was obtained from Sigma-Aldrich (purity $\geq 99\%$) and used without further purification. Deaerated solutions containing dissolved Fe^{2+} in the concentration range 0 to $5 \times 10^{-4} \text{ mol}\cdot\text{dm}^{-3}$ were prepared inside a glove box. The pH of the solution was adjusted to 6.0 using sulphuric acid, as measured with a Mettler Toledo pH meter.

Metal coupons composed of carbon steel (5-mm thick, 10-mm diameter) and stainless steel (5-mm thick, 8-mm diameter) were polished manually with 600 and 1200 grit silicon carbide papers, followed by polishing on a Texmet cloth using a 1 μm MetaDi Supreme diamond paste suspension (Buehler). The coupons were then rinsed with distilled water and sonicated in an acetone/methanol (1:1) mixture for 5 min to remove polishing residues. Due to the large number of coupon samples that were required for each batch of testing, the polishing steps described above were often completed the day prior to test initiation. To minimize any formation of an air-formed oxide over this time period, the coupons were stored in a hexane solution after the polishing and sonication steps were completed.

On the day of testing, the coupons were removed from the hexane storage solvent and rinsed thoroughly with distilled water. The coupons were then transferred into an

Argon-purged glove box for sample preparation. The coupons were placed into specially designed quartz test vials outfitted with sample holders at the bottom. A 10 mL aliquot of the prepared ferrous solution was then added to the test vials such that the coupons were fully immersed in solution and the vials were capped with PTFE silicon septa. A series of test vials were also prepared and sealed without submerged coupons present.

Of the prepared test vials, a small set of reference vials were kept inside the glove box and were not exposed to radiation. The remaining vials were irradiated as described in Section 2.2.2 where the gamma cell provided a uniform absorption dose rate of $1.4 \text{ Gy}\cdot\text{s}^{-1}$ to the ferrous solution. For studies where the initial ferrous concentration was varied, a total irradiation time of 64 h was used. The interactions of the metal coupons with $5 \times 10^{-4} \text{ mol}\cdot\text{dm}^{-3}$ ferrous solutions were also examined as a function of time. Irradiations in this time-dependent study ranged from 21 h to 138 h.

Following irradiation, the concentrations of gas and aqueous phase water radiolysis products were analyzed by gas chromatography and UV-Visible spectrophotometry (described previously in Sections 2.2.3 and 2.2.4). UV-Visible spectrophotometry was also used to analyze for the concentrations of ferrous and ferric species (described previously in Chapter 6) and to monitor the change in the absorbance properties of the irradiated solution as a function of irradiation time [22,23]. All of the spectrophotometric measurements were carried out using a diode array detector (BioLogic Science Instruments).

The coupon surfaces were examined by various surface analytical techniques. Scanning electron microscopy (SEM) was used to view the surface morphology (in a high resolution mode) while energy dispersive X-ray analysis (EDX) was used to obtain information about the general elemental composition of the near-surface. The SEM-EDX analyses were performed using a Hitachi S-4500 field emission SEM equipped with a Quartz XOne EDX system. X-ray photoelectron spectroscopy was also performed to examine the oxidation state characteristics of the coupon surfaces. The XPS spectra were collected with a Kratos AXIS Nova spectrometer. Raman spectroscopy (Renishaw) was also performed on the coupons following irradiation to determine the oxide film compositions by comparing the observed spectra to those of iron oxide standards.

7.2 EXPERIMENTAL RESULTS

7.2.1 Behaviour Observed for Different Initial Ferrous Ion Concentrations

7.2.1.1 Visual Appearance of Solutions and Coupon Surfaces

The appearances of the solutions and coupon surfaces were recorded after 64 h for irradiated and non-irradiated test vials with and without added FeSO_4 . Digital images for tests with $[\text{FeSO}_4]_0 = 2.5 \times 10^{-4} \text{ M}$, shown in Figure 7.1, are representative of the trends observed with other dissolved ferrous sulfate concentrations. For comparison, test vials irradiated without added ferrous sulfate are also shown in Figure 7.1c.





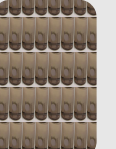




	pH 6.0	Carbon Steel	Stainless Steel	No Coupon
(a)	$[\text{FeSO}_4]_0 = 2.5 \times 10^{-4} \text{ M}$ No Irradiation			
(b)	$[\text{FeSO}_4]_0 = 2.5 \times 10^{-4} \text{ M}$ 64 h Irradiation			
(c)	$[\text{FeSO}_4]_0 = 0 \text{ M}$ 64 h Irradiation			

Figure 7.1: Photographs of the test vials after 64 h for $2.5 \times 10^{-4} \text{ mol}\cdot\text{dm}^{-3} \text{ FeSO}_4$ solutions at pH 6.0 that were (a) not irradiated and (b) irradiated at a dose rate of $1.4 \text{ Gy}\cdot\text{s}^{-1}$. Photographs for pH 6.0 solutions after 64 h of irradiation without initially added iron (c) are also presented.

In all tests where the vials were not irradiated, the solutions remained clear, and there was no evidence of deposits at the bottom of the test vial. The coupon surfaces also retained their mirror finish. For ferrous solutions irradiated without a coupon present or

irradiated with a submerged stainless steel coupon, the solutions remained clear, with a slight yellow tint. A small amount of yellow precipitate was also observed at the bottom of the test vials at the higher dissolved iron concentrations. In contrast, for ferrous solutions irradiated with carbon steel coupons present, there was a dramatic change in the solution colour following irradiation, and a thick orange suspension was observed. Even without ferrous ions initially present, corrosion product deposits were seen at the bottom of the test vials. Hence, for carbon steel systems, irradiation was shown to increase the rate of release of corrosion products relative to non-irradiated tests.

7.2.1.2 *Dissolved Ferrous and Ferric Iron Concentrations*

The concentrations of dissolved ferrous and ferric ions in the solutions, $[\text{Fe}^{2+}]$ and $[\text{Fe}^{3+}]$, measured after 64 h of irradiation are shown in Figure 7.2. The total measured iron concentration in the aqueous phase ($[\text{Fe}^{2+}] + [\text{Fe}^{3+}]$) plotted as a function of the initial dissolved iron concentration ($[\text{Fe}^{2+}]_0$) for the irradiated tests is shown in Figure 7.3.

In the non-irradiated solutions, ferrous ions are the dominant species, irrespective of the presence or type of coupon (not shown). Some oxidation of Fe^{2+} to Fe^{3+} was observed at the highest initial ferrous ion concentration, but this remained less than 10% of the total iron measured. This oxidation was attributed to air ingress into the test vial over the 64 h contact period. For nonirradiated ferrous solutions that were in contact with metal coupons, the total dissolved iron concentration ($[\text{Fe}^{2+}] + [\text{Fe}^{3+}]$) was also nearly the same as $[\text{FeSO}_4]_0$, indicating that dissolution from the metal surface did not occur to a significant extent in the absence of radiation, even after a long contact time.

In the irradiated solutions, the iron species detected after 64 h was predominantly Fe^{3+} (Figure 7.2). This speciation was seen in other work (described in Chapter 6) and is due to the radiolytic oxidation of initially dissolved Fe^{2+} by reaction with $\cdot\text{OH}$ and H_2O_2 . [15]. This conversion to Fe^{3+} leads to a colour change in the test solutions, with the yellow-orange colour characteristic of $\gamma\text{-FeOOH}$ colloid particles. A fraction of the $\gamma\text{-FeOOH}$ particles were observed to settle at the bottom of the vials, and could not be collected into the sampling syringe for speciation analysis. No attempt was made to recover and measure the precipitate due to difficulties in collecting the material from the sample vial surfaces.

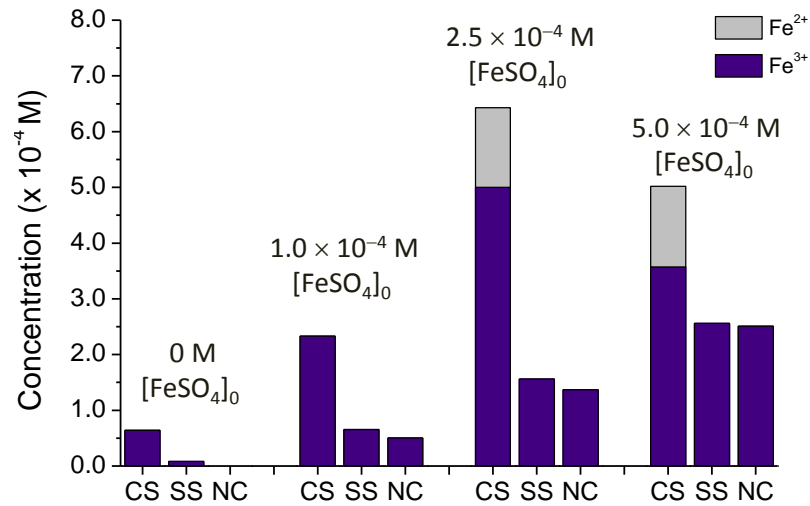


Figure 7.2: Aqueous concentrations of Fe^{2+} (gray) and Fe^{3+} (purple) determined for test solutions at pH 6.0 with various concentrations of initially dissolved ferrous sulfate following 64 h of irradiation at a dose rate of $1.4 \text{ Gy}\cdot\text{s}^{-1}$. The labels CS, SS, and NC represent tests with carbon steel, stainless steel and no coupon.

For all of the $[\text{FeSO}_4]_0$ studied, the aqueous concentrations of iron species in the irradiated solutions containing stainless steel coupons were similar to those detected in irradiated solutions without any coupons present. Furthermore, the total measured iron concentrations for these solutions were lower than $[\text{FeSO}_4]_0$ (Figure 7.3). This trend is consistent with the loss of dissolved iron due to gravitational settling of particles. The stainless steel surface does not experience significant corrosion rates under irradiation (since this would lead to higher detectable levels of Fe^{2+} due to dissolution from the surface).

In tests with carbon steel present, the total iron concentration measured at the end of a test was much higher than the initial concentration (Figure 7.3). Additionally, the deviation of the measured total iron from the initial iron concentration appears to increase for solutions with more initially-dissolved iron. The exception to this trend is the most concentrated solution, where the measured iron concentrations before and after irradiation were almost the same. This apparent change in behaviour is most likely due to

a greater degree of gravitational settling of particles from the solution at higher iron concentrations. This behaviour could also be indicative of particle agglomeration at high concentrations (larger particles will be less likely to remain suspended in the aqueous phase) or an inhibition in the dissolution rate caused by the high $[\text{Fe}^{2+}]$. Unlike the ferrous solutions irradiated with no coupon or with a stainless steel coupon, in carbon steel tests Fe^{2+} continues to comprise a significant fraction of the measured iron at long times (Figure 7.2). These results confirm that the corrosion of carbon steel coupons is accelerated in radiation environments, and this corrosion mainly results in metal dissolution. The results seen in Figure 7.3 seem to further suggest that at sufficiently high $[\text{Fe}^{2+}]_0$, the overall metal dissolution rate may decrease while promoting the precipitation of solids to the bottom of the test vial or onto the coupon surface.

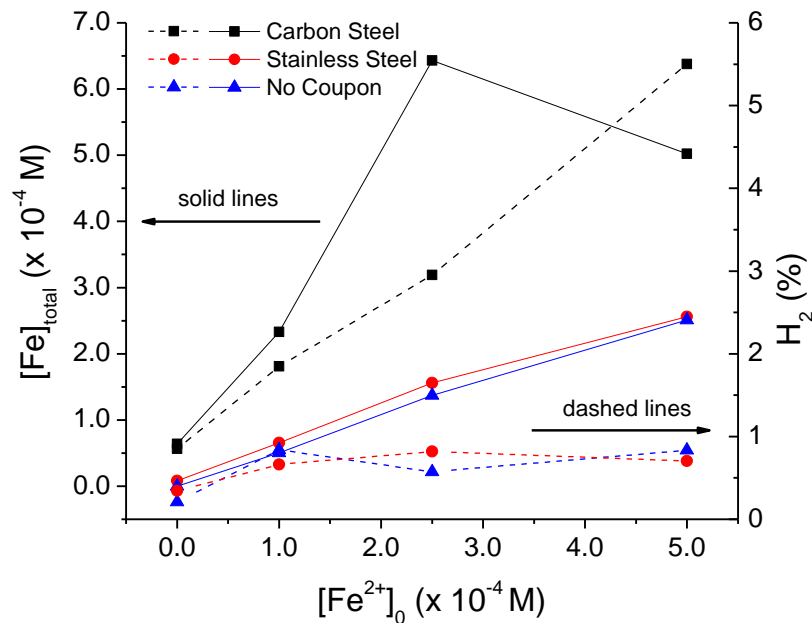


Figure 7.3: The total concentration of iron species measured in the aqueous phase (solid lines) and hydrogen measured in the gas phase (dashed lines) for pH 6.0 ferrous sulfate solutions in contact with carbon steel (■), stainless steel (●) and no coupon (▲) following 64 h of irradiation at a dose rate of $1.4 \text{ Gy}\cdot\text{s}^{-1}$.

7.2.1.3 Gas Phase H_2 and O_2 Concentrations

Hydrogen and oxygen are products of water radiolysis and measurements of their concentrations are often used to gain insight into the radiation chemistry occurring in a chemical system. However, for systems involving a corroding surface, the behaviour of oxygen and hydrogen cannot be tied exclusively to aqueous phase radiolysis reactions. Oxygen can be reduced on a metal surface, and drive the anodic half reaction that results in oxide film formation or the release of metal ions into the aqueous phase. When proton reduction is the cathodic half reaction (which can occur for pH 6.0 water), H_2 can be generated as a product. As a result, separating the influences of radiation chemistry and aqueous corrosion on the gas concentrations is not trivial. However, trends observed in the gas concentrations can be used to support other data.

The concentrations of gaseous O_2 and H_2 in the cover gas for 64 h irradiation tests were analyzed by gas chromatography. In the absence of radiation, the oxygen levels (data not shown) were consistently in the range of 1.2 - 1.3%, regardless of the test conditions (coupon type or $[Fe^{2+}]_0$). As well, in the absence of radiation, no H_2 gas was detected in any of the tests. These observations are consistent with negligible corrosion rates in the absence of a radiation field.

Tests with radiation showed much different behaviour. For a water only test (no added $FeSO_4$ or metal coupon), the oxygen concentration in the gas phase increased from about 1.5% to 2.5% and H_2 could be detected at 0.2%. These increases are due to water radiolysis production of oxygen and hydrogen and their transfer to the gas phase [24]. In solutions containing $FeSO_4$ but no metal coupon, the $[O_2]$ measured in the gas phase was generally lower with irradiation than without, and its concentration decreased with increasing $[Fe^{2+}]_0$ (results not shown). The hydrogen concentrations for irradiated solutions followed the opposite trend; higher levels were observed for ferrous solutions than for irradiated pH 6.0 water. These trends in the concentrations of O_2 and H_2 can be explained by oxidation reactions of dissolved Fe^{2+} with water radiolysis products leading to the formation of ferric oxide species. This radiation-induced redox mechanism has been previously shown to remove oxygen by incorporating it into colloidal ferric oxide particles [15]. This process also results in ferrous iron initially outcompeting H_2 for reaction with $\bullet OH$ (which is the primary removal path for hydrogen in irradiated

systems). Hence, the presence of ferrous ions in the water leads to higher concentrations of H₂.

As observed for iron speciation, the stainless steel and no coupon systems showed similar results for hydrogen (Figure 7.3). Stainless steel does not significantly influence the aqueous phase chemistry of ferrous solutions or participate in any additional corrosion processes that generate H₂. For both systems, moving from pure water to solutions with $1 \times 10^{-4} \text{ mol}\cdot\text{dm}^{-3}$ initially dissolved Fe²⁺ led to an increase in H₂, however further increases in the initial ferrous concentration had no impact. Once the radiolytic conversion of ferrous to ferric species has reached a steady state (which has been shown to be dominated by ferric species at this pH [15]), the removal of hydrogen by •OH can also reach a steady state. Hence, the hydrogen data, in combination with the iron speciation data, suggests that these systems have attained a steady state in the aqueous phase by 64 h of irradiation time, and that the steady state is nearly independent of the initial ferrous concentration.

In contrast, all tests with carbon steel coupons led to evolution of larger quantities of H₂ than was seen with no metal coupon or stainless steel. The hydrogen production also increased with more concentrated ferrous solutions (Figure 7.3). In both cases, the hydrogen behaviour is a consequence of the effective iron concentration. With higher initial dissolved iron, there is more potential for •OH scavenging, allowing hydrogen to build to higher levels. In carbon steel systems, the additional release of ferrous species to the solution by corrosion further increases the total iron concentration in the solution with time, and yields higher levels of hydrogen. Additionally, some contribution of the hydrogen production can arise from the cathodic reaction of water on the carbon steel surface. In ferrous solutions, the radiolytic oxidation of Fe²⁺ species will lead to Fe³⁺ which can hydrolyze. This will drop the pH of the solution, and the rate of proton reduction on the carbon steel surface can initially increase, generating more H₂. Since the stainless steel surface appears to be relatively inert to corrosion under these test conditions ferric ion hydrolysis does not impact H₂ in that system.

7.2.1.4 *Surface Analysis of Steel Coupons*

The oxidation state compositions of the surface layers were analyzed using X-ray photoelectron spectroscopy (XPS). High resolution XPS spectra of Co 2p, Fe 2p, O 1s and C 1s band regions were analyzed by deconvoluting the bands with reference spectra. The detailed description of the XPS analysis method can be found elsewhere [9,10]. A representative XPS survey spectrum along with a high resolution Fe 2p spectrum are shown in Figure 7.4.

Since the O 1s peak does not vary significantly for the different oxides and the Fe peaks are closely spaced, determining the precise contributions of different oxides to the spectra can be difficult [14]. However, comparison of the signal contributions in the 10 nm surface layer (the XPS analysis depth range) from iron in oxide forms ($\text{Fe}(\text{ox})$) and iron in a metallic form (Fe^0) can be reliably performed. A smaller ratio of metallic iron to oxide iron indicates that a thicker oxide film has been formed. The net contributions of these iron species to the Fe 2p spectrum are shown in Figure 7.5 for selected carbon steel tests. For tests in pH 6.0 water with radiation present, carbon steel coupons show a lower metallic iron content in the surface layer compared to tests without irradiation. The ratio decreased even more when ferrous sulfate was initially present in the solution; the metallic Fe contribution was no longer observed. This demonstrates that oxide growth is faster in irradiated systems and that, for a similar irradiation time, the presence of dissolved iron in the solution leads to growth of a thicker oxide layer.

For stainless steel coupons, in addition to the Fe 2p band, the high resolution XPS Cr 2p band was also analyzed. The XPS analysis showed presence of $\text{Cr}(\text{OH})_3$ and Cr_2O_3 in the surface oxide. The ratio of Cr in an oxide form to metallic Cr was independent of the presence of radiation or FeSO_4 in the test solution. Furthermore, metallic Fe could be detected by XPS on the stainless steel coupon surface for all samples, showing that the oxide layer on the coupon was quite thin. Visual inspection also showed that the stainless steel coupons retained their initially polished finish under all experimental conditions studied. These data further confirm that stainless steel corrosion (by metal dissolution or oxide film formation) is negligible for the test solutions examined here.

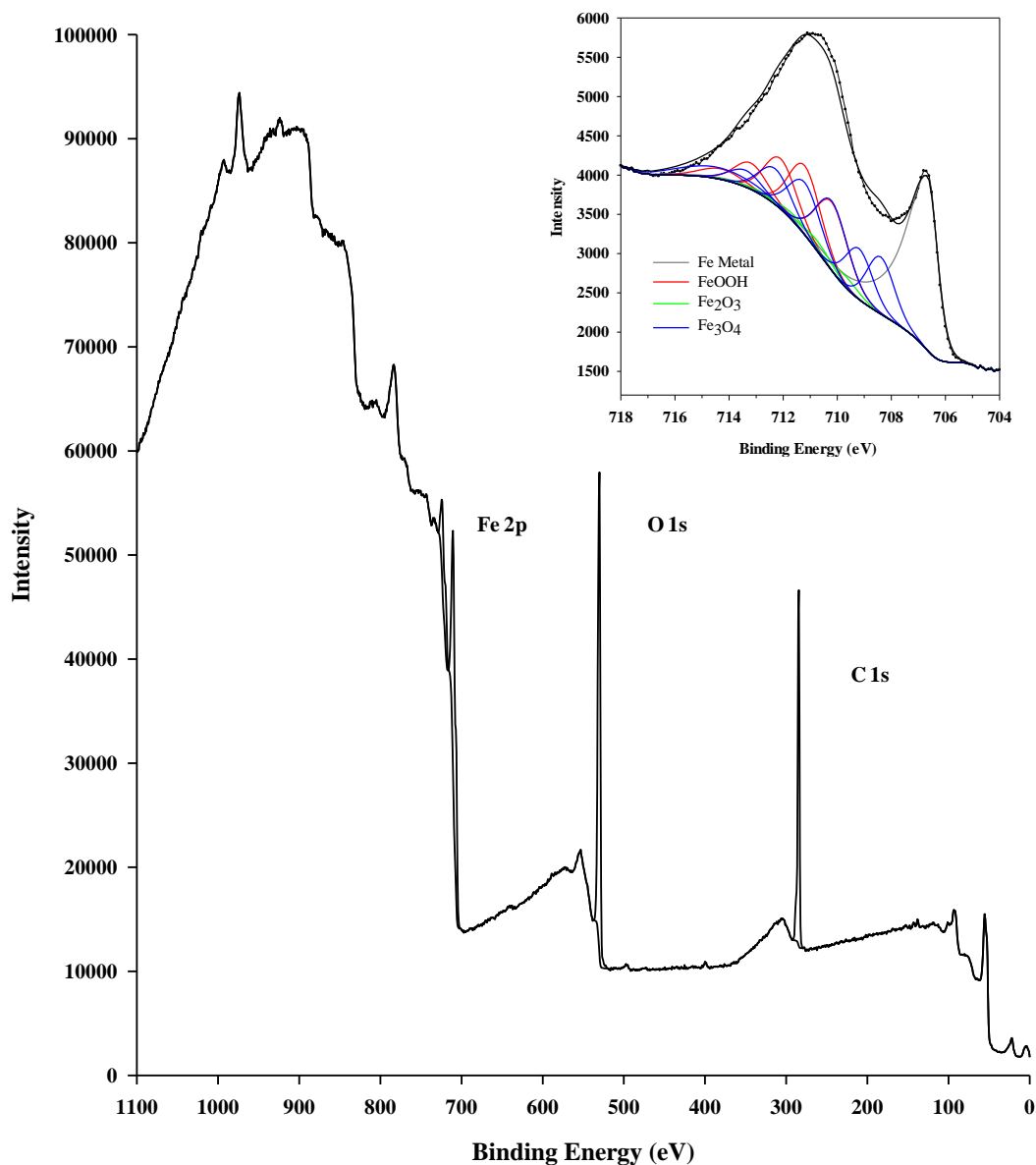


Figure 7.4: A representative survey spectrum and a high resolution Fe 2p band (inset) from the XPS analysis of a carbon steel coupon.

The surface morphology of the carbon steel and stainless steel surfaces were also examined by SEM. Representative images for a 2.5×10^{-4} M FeSO₄ solution following 64 h of irradiation are shown in Figure 7.6. The SEM image shows substantial surface alteration on the carbon steel coupon. The surface morphology for the carbon steel

coupons was independent of the initial $[\text{FeSO}_4]$, but at higher initial $[\text{FeSO}_4]$ precipitates and colloid deposits were more evident. As also demonstrated in the SEM image, EDX spectra showed that the corrosion was not uniform. There was a slight oxygen enrichment in the uppermost ridged areas, and depletion in the lower regions. However, the oxygen signal detected was generally very weak for all samples, appearing as only a small shoulder on the strong iron contributions. This further confirms that the oxide films were thin. No signs of general corrosion on the stainless steel coupon were seen although the surface did show pits.

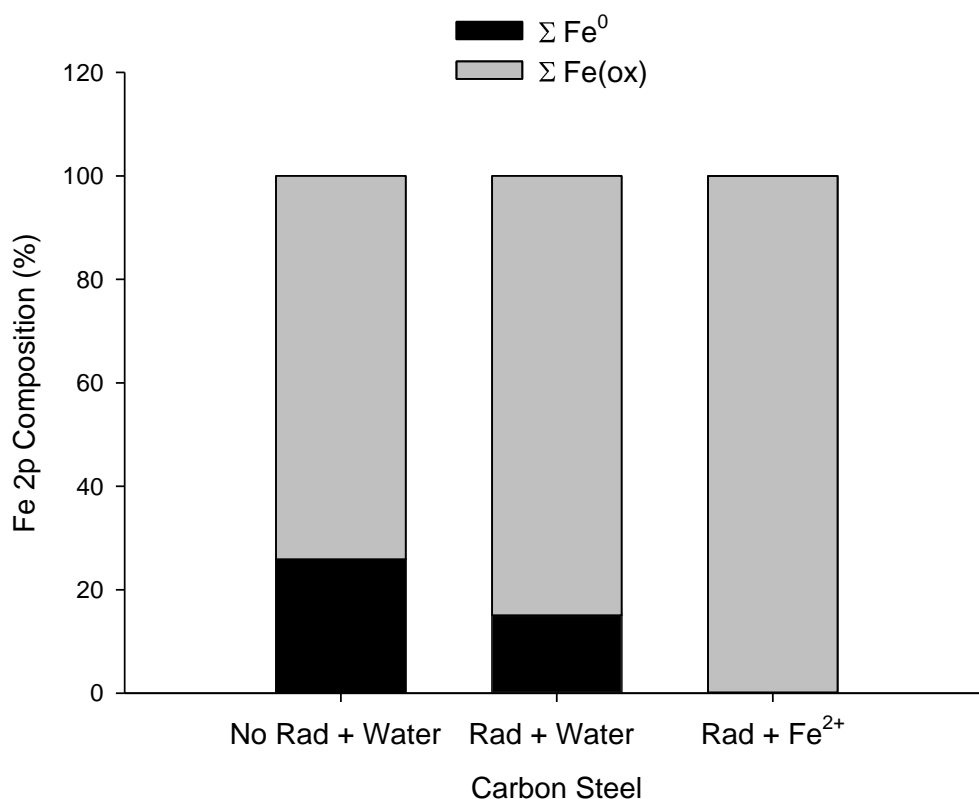


Figure 7.5: XPS analysis results for carbon steel surfaces displaying the relative contributions of metallic Fe^0 and iron oxide phases to the Fe 2p band after 64 h irradiation tests. Carbon steel samples were in contact with: pH 6.0 water without irradiation (left), irradiated pH 6.0 water (middle), and irradiated pH 6.0 FeSO_4 solutions at $2.5 \times 10^{-4} \text{ mol}\cdot\text{dm}^{-3}$.

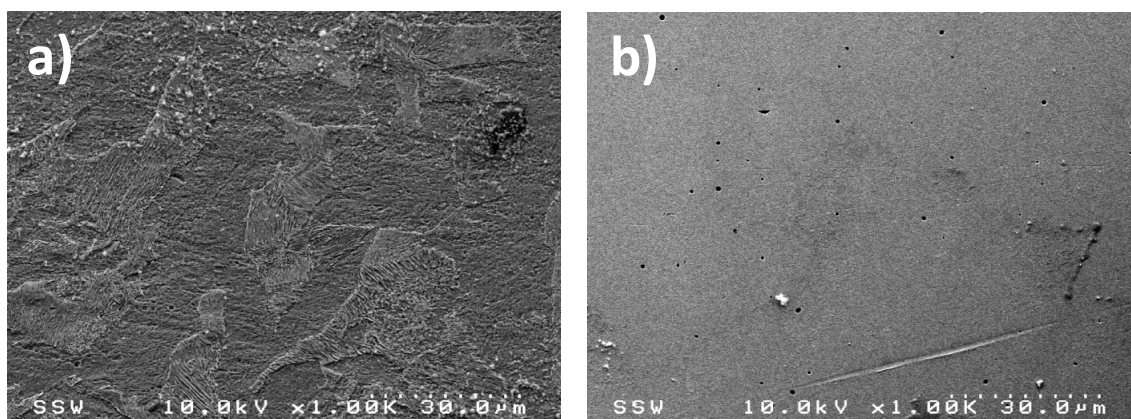


Figure 7.6: The SEM images of (a) a carbon steel coupon and (b) a stainless steel coupon following 64 h of irradiation in 2.5×10^{-4} M $[\text{FeSO}_4]_0$.

7.2.2 Behaviour Observed as a Function of Time

From the experiments, it is clear that stainless steel is relatively inert under our test conditions. In contrast, irradiated carbon steel systems shows high rates of metal ion dissolution, even without iron initially present in the solution, and XPS analyses suggest that the oxide layer thickness increases with radiation and dissolved iron. To examine the kinetic behaviour of the corrosion process, and determine whether a steady state is eventually attained in the aqueous phase iron speciation or the gas phase H_2 production, a time-dependent study was deemed necessary. As a result, a longer term irradiation was performed in solutions of 5×10^{-4} mol·dm⁻³ ferrous sulfate.

7.2.2.1 Visual Appearance of Solutions and Coupon Surfaces with Irradiation

Photographs of the irradiated test solutions for ferrous systems and for carbon steel in contact with pH 6.0 water are shown in Figure 7.7. Once again the appearances of the test solutions resemble those seen after 64 h irradiation tests. Even for the shortest irradiation time, the ferrous solutions with carbon steel present had a thick orange suspension (Figure 7.7b). With further irradiation, the orange colour became even more intense. For pure water tests with carbon steel, ongoing irradiation led to a gradual increase in the intensity of the orange colour, and by 138 h of irradiation, the solution

strongly resembled those of tests with initially dissolved iron (Figure 7.7a). Ferrous solutions irradiated without a coupon or with a stainless steel coupon present remained relatively clear, with a yellow tint (Figure 7.7c and d). The intensity of the yellow colour did not increase noticeably with prolonged irradiation.

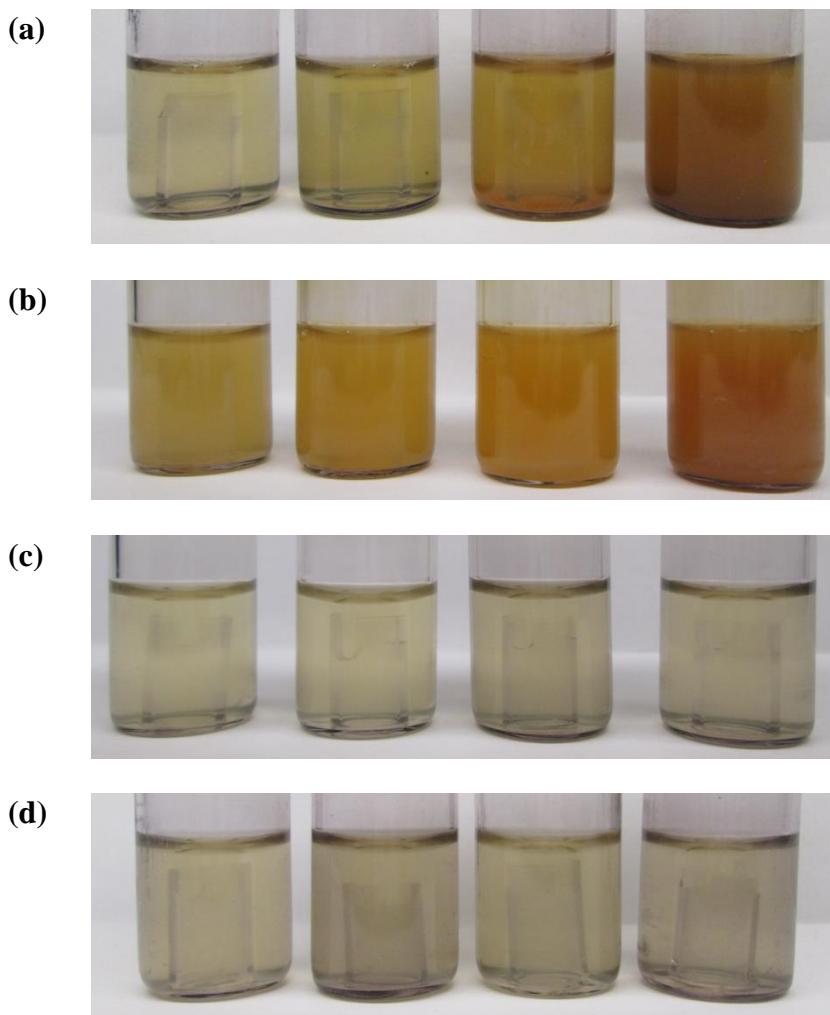


Figure 7.7: Optical images of the irradiated test solutions for carbon steel in (a) water, and (b) 5×10^{-4} M FeSO_4 , and for irradiated 5×10^{-4} M FeSO_4 in contact with (c) a stainless steel coupon, and (d) no coupon. From left to right, the irradiation times increase from 20, 40, 64, to 138 h.

The irradiated coupons were also examined by SEM to determine if any change in morphology occurred with time. Selected images are presented for stainless

steel in Figure 7.8 and for carbon steel in Figure 7.9. Examination of the SEM images for stainless steel irradiated with water and with ferrous solutions showed no remarkable differences. The stainless steel coupons also showed identical characteristics for all test durations. The overall surface remained smooth (some polishing lines still visible) and some pits could be observed.

For carbon steel, the general surface characteristics observed were similar to those presented previously for a 64 h irradiation test. Two main types of morphology can be observed: pearlite regions (the ridged features) and somewhat amorphous regions. These regions were analyzed by EDX, with representative EDX spectra shown in Figure 7.10. Again, the oxygen signal remained weak in comparison to the strong Fe signal originating from iron in the bulk metal and this showed that the oxide layer was relatively thin. There was some indication that the ridged areas have higher oxygen levels and represent areas of (relatively) thicker oxide. The number of these regions observed and the depth of the ridges that they contain both increased with irradiation time, and demonstrate that oxide growth occurs, but very slowly, in these pH 6.0 solutions. Additionally, comparison of the SEM images/EDX spectra indicates that a thicker, amorphous oxide layer forms on the carbon steel in ferrous solutions; the EDX spectrum taken on the overall coupon surface for 64 h tests gave oxygen signals of 1.4 and 2.2 wt. % for water and ferrous solutions, respectively.

Raman spectra of the carbon steel coupon surfaces were also collected to identify the composition of the oxide film. A representative Raman spectrum for a carbon steel test sample is shown in Figure 7.11 along with the spectra of selected iron oxide standards. For all tests, the Raman spectra of the carbon steel coupons have a high background and peaks are not easily defined. It is likely that the oxide layer was too thin to obtain sufficient signals. The general profile was representative of FeOOH oxides, indicating that for tests at pH 6.0, the oxide layer is mainly comprised of these oxy-hydroxide species that generally do not form a compact and protective oxide structure. This can account for the significant dissolution rates observed in carbon steel tests. No significant changes in the spectra were observed with increased irradiation time.

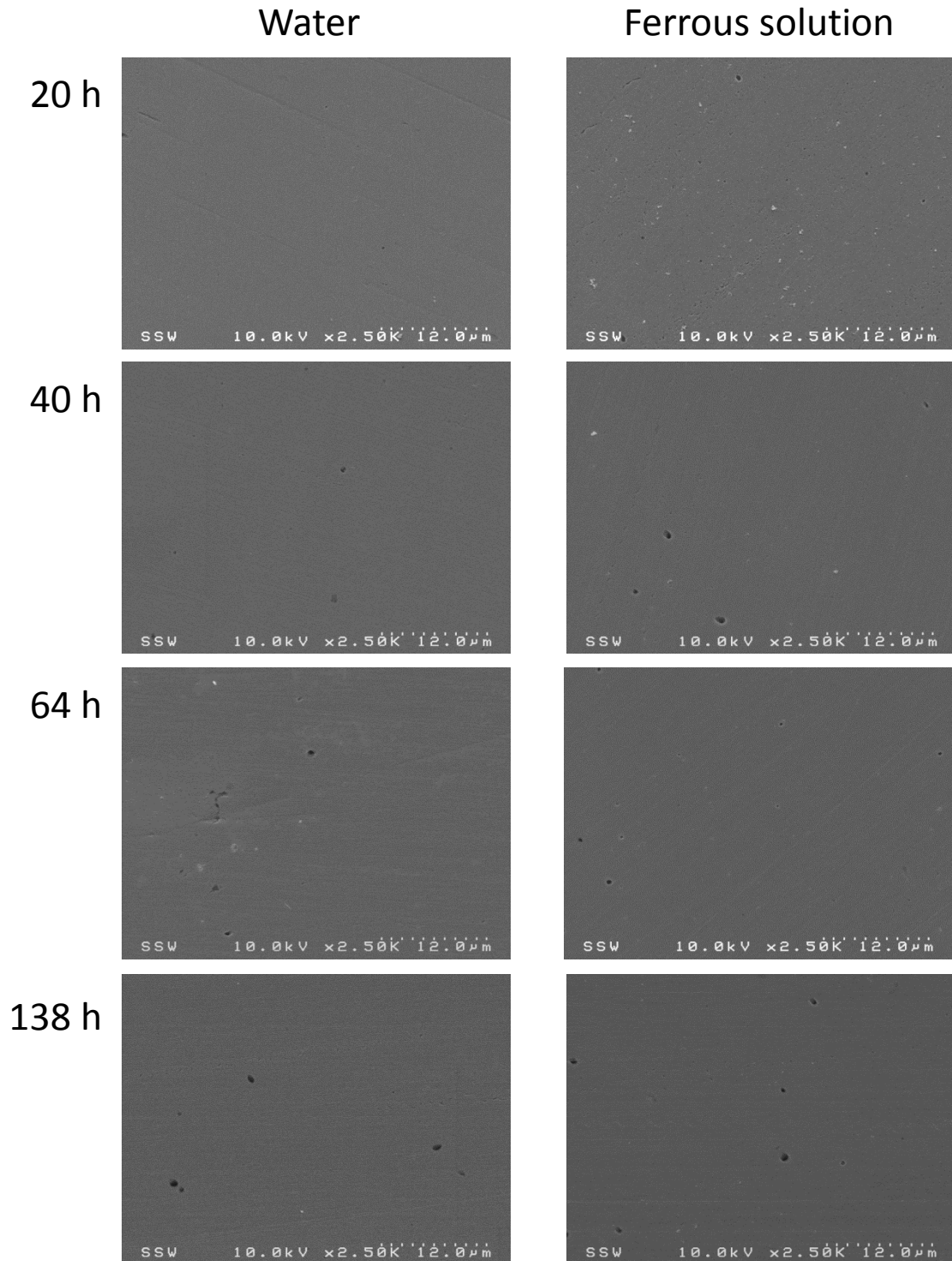


Figure 7.8: SEM images showing the surface morphology of stainless steel coupons irradiated in contact with 5×10^{-4} M FeSO_4 for 20, 40, 64, and 138 h.

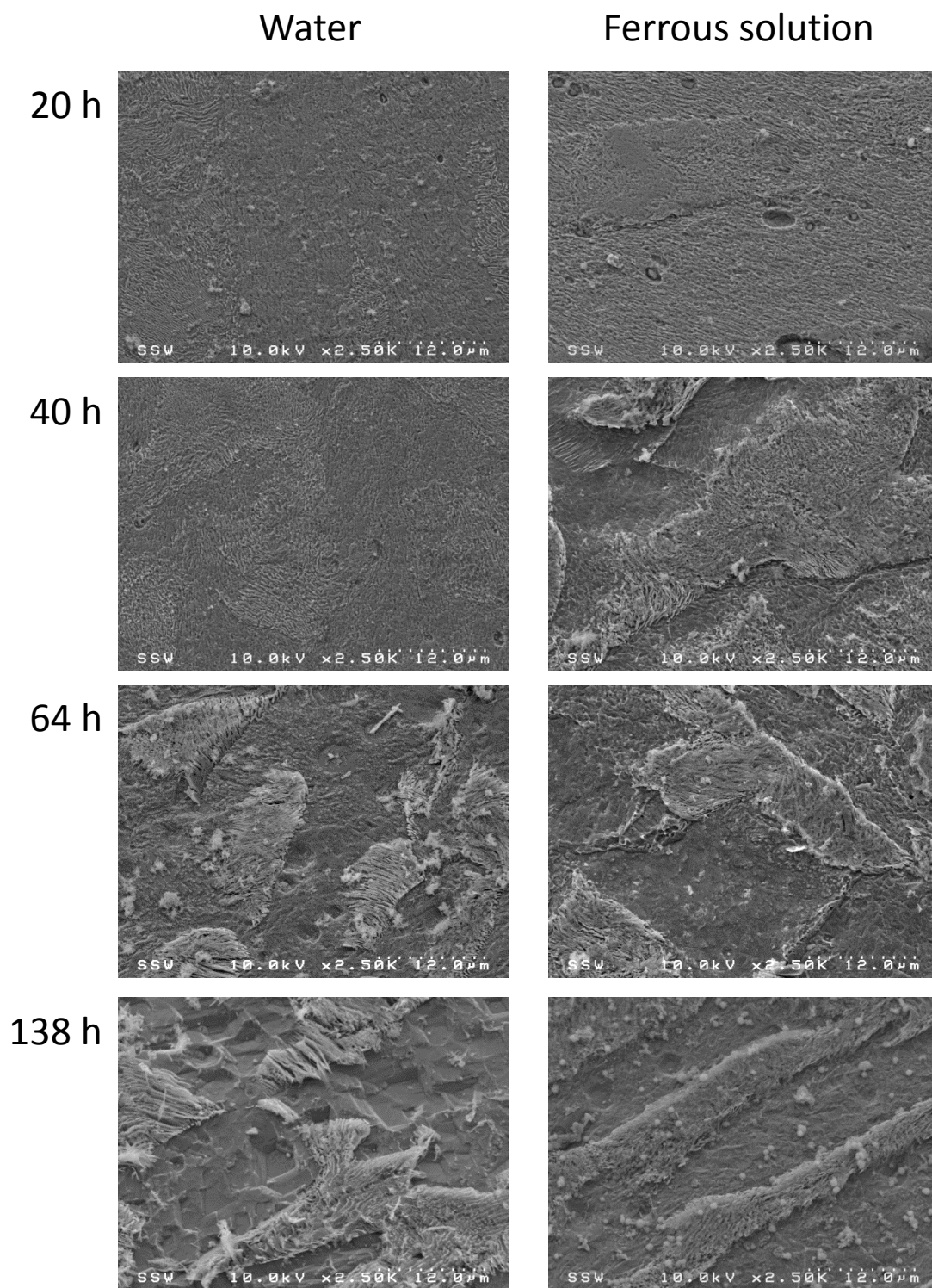


Figure 7.9: SEM images showing the surface morphology of carbon steel coupons irradiated in contact with 5×10^{-4} M FeSO_4 for 20, 40, 64, and 138 h.

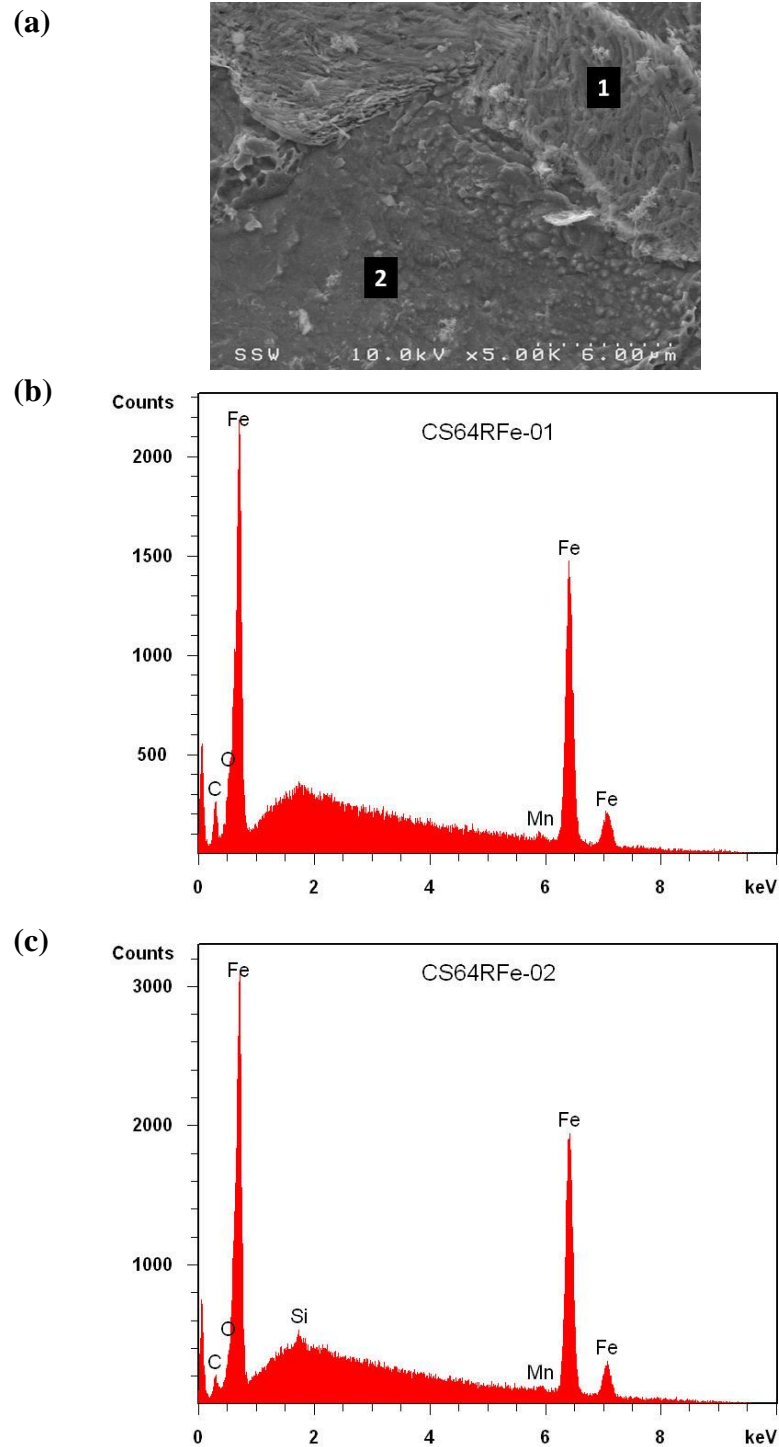


Figure 7.10: (a) An SEM image for a carbon steel coupon irradiated for 64 h in ferrous solution. EDX spectra is shown for the pearlite ridged area (b) and the flatter amorphous region (c).

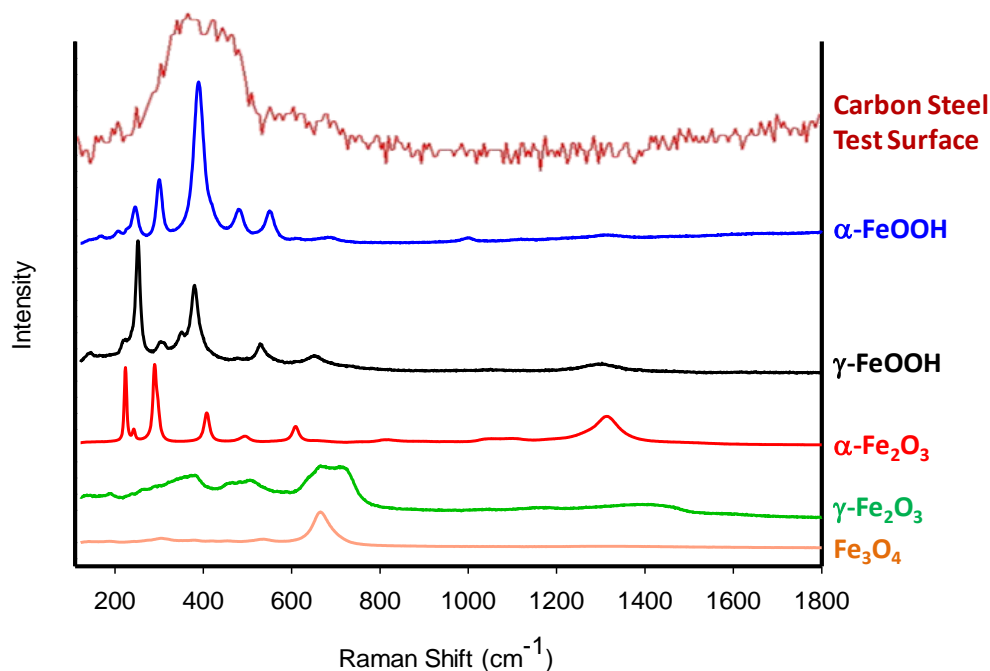


Figure 7.11: The Raman spectra of selected iron oxide standards along with a representative spectra of a carbon steel surface after irradiation in a ferrous solution.

7.2.2.2 Time-Dependent Ferric/Ferrous Behaviour

The ferrous and ferric ion concentrations measured as a function of time for irradiation tests with 5×10^{-4} M FeSO_4 and pH 6.0 water are shown in Figure 7.12 and Figure 7.13, respectively. For all tests without irradiation, the iron remained primarily in the ferrous form, and the total iron concentration was equivalent to that of $[\text{FeSO}_4]_0$.

As observed previously for 64 h irradiations, the dominant iron species detected in all irradiated tests was Fe^{3+} . Once again, the stainless steel and no coupon systems showed comparable behaviour, and the total iron concentrations measured were lower than $[\text{FeSO}_4]_0$, such that only about 80% of the initial iron was detected post-irradiation (Figure 7.12). The loss of mass balance is attributed to formation of insoluble Fe^{3+} and gravitational settling of the particles.

For stainless steel irradiated in pure pH 6.0 water, the level of Fe^{3+} was quite small, even after 138 h of irradiation (Figure 7.13), and the release of iron species from the stainless steel surface is considered to be negligible for all conditions studied.

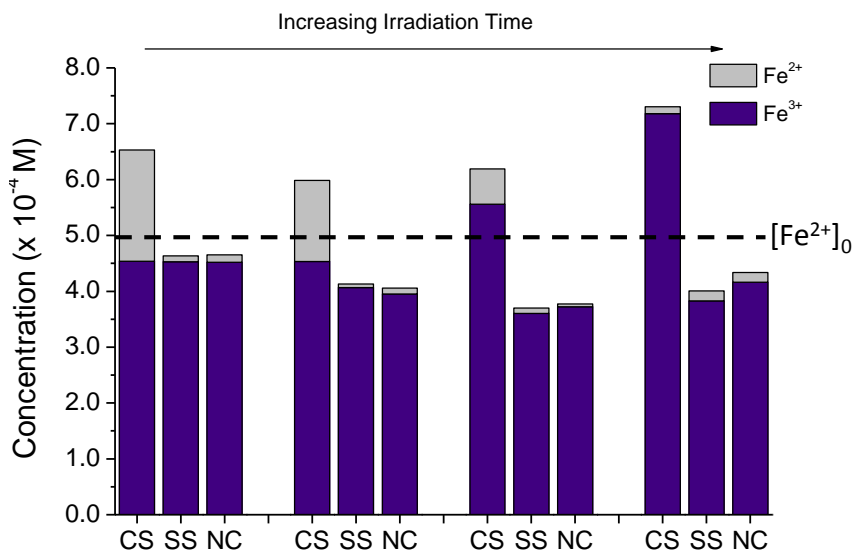


Figure 7.12: The aqueous concentrations of Fe^{2+} (grey) and Fe^{3+} (purple) species measured for tests with carbon steel (CS), stainless steel (SS), or no coupon (NC) in contact with a 5×10^{-4} M FeSO_4 solution as a function of irradiation time (at a dose rate of $1.4 \text{ Gy}\cdot\text{s}^{-1}$). From left to right, the sets of bars represent times of 20, 40, 64, and 138 h.

In tests with carbon steel present, the total iron concentration present at the end of a test was higher than the initial ferrous concentration. Additionally, the contributions of ferrous species to the total signal became greater for irradiations with water at longer times. In ferrous solutions, Fe^{2+} was also detected, but its contribution appears to diminish with time. An additional observation from Figure 7.13 was that, for carbon steel pure water tests, the total dissolved iron increased almost exponentially with time. After 138 h, the total dissolved iron concentration for CS in pure water and for CS irradiated in a 5×10^{-4} M FeSO_4 solution were nearly the same (about 7×10^{-4} M).

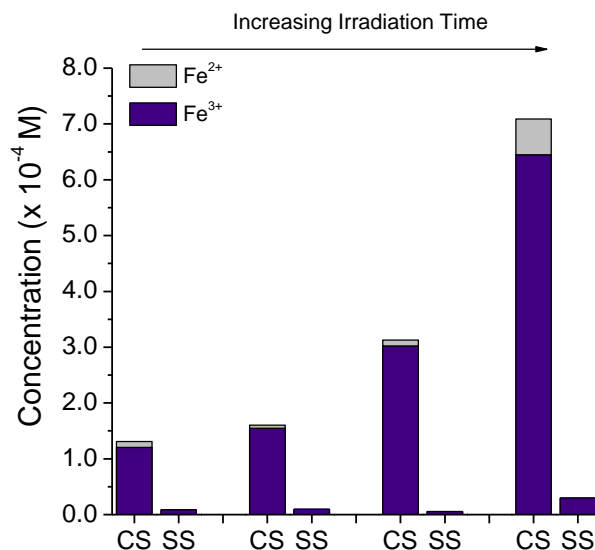


Figure 7.13: The aqueous concentrations of Fe²⁺ (grey) and Fe³⁺ (purple) species measured for tests with carbon steel (CS) and stainless steel (SS) in pure water as a function of irradiation time (at a dose rate of 1.4 Gy·s⁻¹). From left to right, the sets of bars represent times of 20, 40, 64, and 138 h.

It is difficult to predict whether the dissolved metal content in irradiated CS systems would continue to increase well beyond 138 h or whether these systems would begin to approximate the behaviour of irradiations for initially ferrous solutions. It is clear that irradiation increases the corrosion rate of carbon steel (via metal dissolution) in both pure water and ferrous systems. However, the initial presence of high concentrations of ferrous iron seems to suppress the rate of metal dissolution observed at longer irradiation times.

7.2.2.3 Time-Dependent Hydrogen Behaviour

The concentrations of O₂ and H₂ in the cover gas were measured for carbon steel, stainless steel and no coupon tests in pH 6.0 water and in ferrous sulfate solutions. Oxygen results are not shown, but a general decrease from initial levels of around 2-3% to final concentrations of approximately 0.5% for ferrous tests and 1% for water tests was observed. The concentration profiles of hydrogen with time for irradiated tests are shown in Figure 7.14. In all cases, test systems with added FeSO₄ produced more hydrogen than

their pure water equivalents. All tests performed in pure water also appear to have reached a steady state with respect to H_2 , as do ferrous solution tests with no coupon and with a stainless steel coupon. In environments where ferrous iron is present and its solution chemistry remains unaffected by any surfaces present, the dissolved Fe^{2+} competes with H_2 for reaction with $\bullet OH$, which leads to the increased accumulation of H_2 in the system. However, with time, the radiolytic conversion of the initial ferrous species to ferric products reaches an end (with some ongoing radiolytic cycling between redox states), and $\bullet OH$ can contribute more to the removal of H_2 . This allows hydrogen to reach a steady-state concentration.

The H_2 measured in ferrous solutions with carbon steel present increased with time, and did not appear to be approaching a steady state even after 138 h. Despite the fact that the total dissolved iron concentrations after 138 h are about the same for CS + pure water and CS + ferrous solution systems, the final hydrogen concentrations are remarkably different. One possible explanation for this observation is that, with iron initially present, immediate radical scavenging allows faster hydrogen accumulation. Additionally, reaction of Fe^{2+} and $\bullet OH$ leads to an early high concentration of ferric ions whose subsequent hydrolysis can substantially decrease the pH (and increase $[H^+]$) almost immediately in these systems. This may result in proton reduction out-competing other reactions (such as those of H_2O_2 or O_2) at the carbon steel surface and lead to the release of hydrogen as a corrosion product.

When starting with a pure water system, the initial corrosion reactions initiated by the oxygen or hydrogen peroxide generated by water radiolysis will cause an initially slow release of ferrous ions. Even after 20 hours, the total iron concentration detected was less than 20% of the concentration used in the ferrous solution tests (only about 1×10^{-4} M $FeSO_4$ compared to 5×10^{-4} M $FeSO_4$). As a result, the radiolytic scavenging is slower and less H_2 is produced at early times. As well, it is possible that the deposition of particles on the CS surface at low concentrations may promote some metal dissolution from the coupon surface; the reduction of deposited Fe^{III} particles at the surface may couple to the oxidation of Fe^0 to Fe^{2+} in the bulk metal. This can result in ferrous ion dissolution, without generating H_2 , as observed in Figure 7.13 and Figure 7.14. Despite these arguments, eventually the increased iron concentration would be predicted to cause

some increase in the hydrogen production due to the ferric hydrolysis effect, or due to radical scavenging; this was not reflected in our tests under the time frame studied.

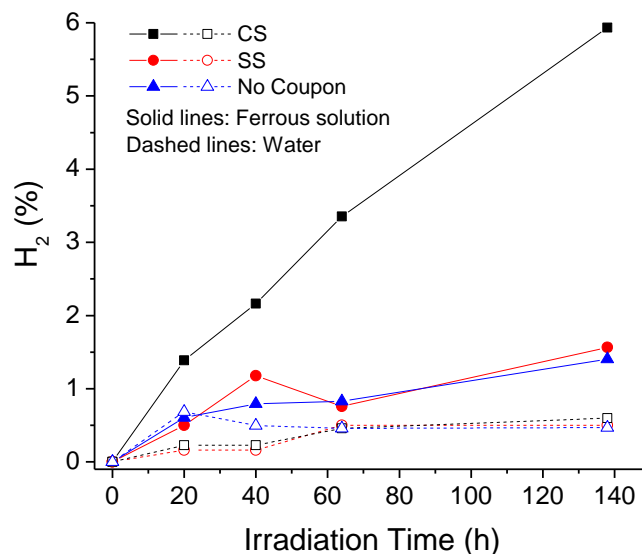


Figure 7.14: The concentrations of hydrogen measured in the gas phase for pH 6.0 5×10^{-4} M FeSO₄ solutions (solid lines) and pH 6.0 water (dashed lines) in contact with carbon steel (■), stainless steel (●) and no coupon (▲) following 64 h of irradiation at a dose rate of 1.4 Gy·s⁻¹.

7.2.2.4 UV-Visible Spectra of Irradiated Solutions

The UV-Visible absorbance spectra of the irradiated 5×10^{-4} mol·dm⁻³ ferrous solutions were collected. For all solutions, the raw spectrum showed very high absorbance values around 300 nm, where the hydrated ferric ion absorbs strongly (data not shown). A shoulder in the spectrum also appears between 350 and 400 nm for all samples; this contribution was also observed for much shorter duration (5 h) tests of irradiated ferrous solutions (see Chapter 6), and was attributed to the scattering of light by the suspended colloid particles. To better observe this colloid peak, all absorbance spectra were normalized to remove the contribution of the hydrated ferric ion. Figure 7.15 shows the normalized spectra for ferrous solutions irradiated absent a coupon

as well as in the presence of a stainless steel coupon. For both cases, the colloid scattering peak seems to have reached a constant value, and its profile does not change with longer irradiation time.

In contrast, the presence of a carbon steel coupon, with or without Fe^{2+} initially present, appears to significantly alter the scattering profile of the colloids formed. The normalized UV-Visible absorbance spectra for deaerated water and $5 \times 10^{-4} \text{ mol} \cdot \text{dm}^{-3}$ ferrous solution, both irradiated in contact with a carbon steel coupon, are presented in Figure 7.16. In both spectra, the peak at 370 nm increases in intensity as irradiation time increases. A similar trend in the light scattering (370 nm) peak was observed for short irradiations of ferrous solutions, and TEM studies showed that the additional amplitude was due to the production of more colloids (but not in conjunction with an increase in particle size) in the system with time (Chapter 6). Similar TEM analyses could not be performed for this study due to unavailability of the instrument. We expect that the explanation for the observed behaviour at longer times is the same. Corrosion product deposits arising from the irradiation of carbon steel in simulated anoxic groundwater (near neutral pH) and analyzed by XRD have been reported to be composed mainly of magnetite and lepidocrocite. This supports a postulate that $\gamma\text{-FeOOH}$ is a likely contributor to the UV-Visible absorption profiles for the deaerated pH 6.0 solutions presented here [25]. Unlike the irradiated ferrous solutions without a coupon or with stainless steel coupons present, a steady state is not reached in the aqueous phase for carbon steel systems. Furthermore, the final intensity of the scattering peak is more than 5 times higher than that observed for stainless steel and no coupon irradiations. This behaviour is attributed to the ongoing release of Fe^{2+} into the solution from the carbon steel. This continuously changes the aqueous phase composition and delays the approach to steady state, while providing additional iron to be converted into a colloidal phase.

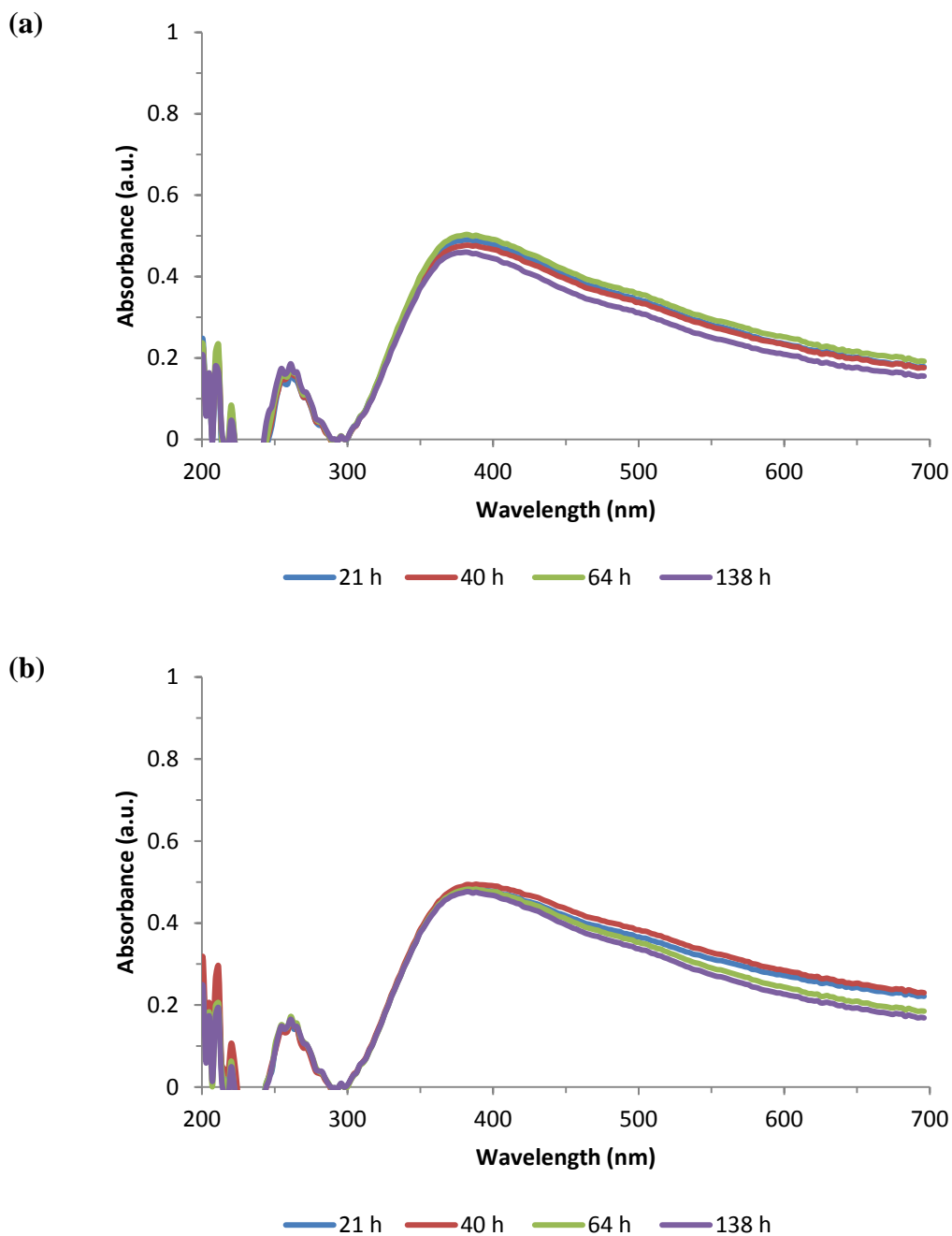


Figure 7.15: The UV-Visible spectra of irradiated $[\text{Fe}^{2+}]_0 = 5 \times 10^{-4} \text{ mol} \cdot \text{dm}^{-3}$ deaerated solutions at pH 6.0 and a dose rate of $1.4 \text{ Gy} \cdot \text{s}^{-1}$ with the absorption contribution of the hydrated ferric ion removed. (a) Ferrous solutions irradiated in the absence of a coupon and (b) ferrous solutions irradiated in contact with a stainless steel coupon.

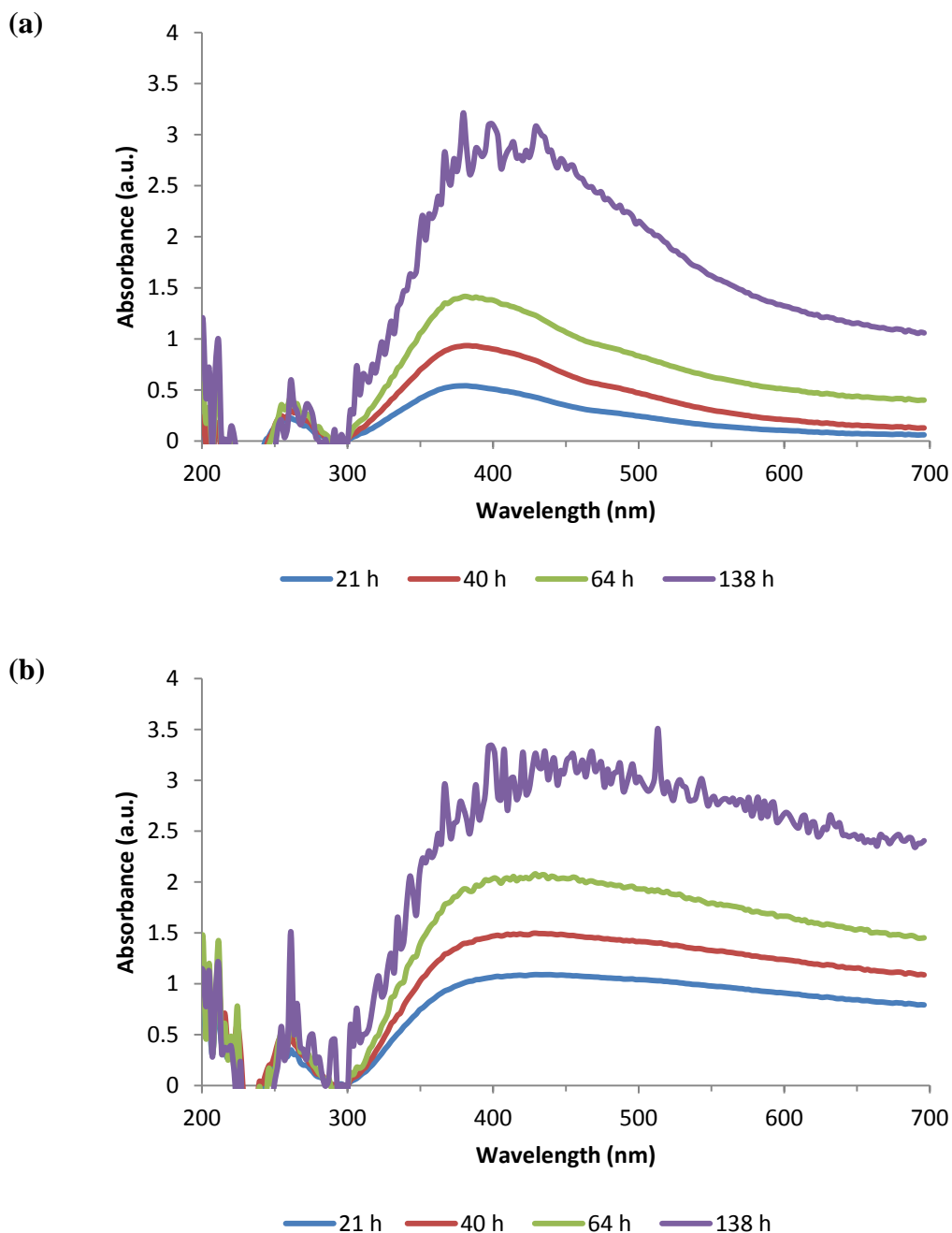


Figure 7.16: The UV-Visible spectra collected for pH 6.0 deaerated (a) water ($[\text{Fe}^{2+}]_0 = 0 \text{ mol}\cdot\text{dm}^{-3}$), and (b) ferrous solution ($[\text{Fe}^{2+}]_0 = 5 \times 10^{-4} \text{ mol}\cdot\text{dm}^{-3}$), that were irradiated in contact with a carbon steel coupon at a dose rate of $1.4 \text{ Gy}\cdot\text{s}^{-1}$. The absorption contribution of the hydrated ferric ion was removed.

Further examination of Figure 7.16 shows some differences between water and ferrous solutions irradiated with carbon steel. The 370 nm scattering peak intensity is smaller (at times < 138 h) for pure water than for solutions with initially dissolved ferrous sulfate. This is expected since colloids can form immediately in the ferrous sulfate solution, while the release of corrosion products from the carbon steel is the only source of iron for the water irradiation tests. The total concentration of iron in the aqueous phase is smaller at early times for initially pure water relative to tests where iron was initially dissolved (Figure 7.12 and Figure 7.13). At 138 h, the intensity of the 370 nm peak is similar for both water and ferrous systems and both profiles are quite noisy. Comparison of Figure 7.16a and Figure 7.16b shows that the normalized spectra for the CS + ferrous solution system does not tail off in intensity after the 370 nm peak, as is observed in the CS + water spectra (as well as the no coupon-ferrous solution and stainless steel-ferrous solution spectra in Figure 7.15).

The peaks in this higher wavelength region have been attributed to the scattering of light by suspended particles, and hence the scattering behaviour can be described by Mie theory. While a detailed light scattering study was not performed here, some conclusions about the particles formed in the test solutions can be made by examination of their relative scattering intensities at these wavelengths (> 500 nm). In Mie theory, the scattering intensity of particles in a medium (at a given scattering angle) is a function of the dimensionless scattering size parameter, x , which relates the particle size to the wavelength of the incident light [26-28]:

$$x = \frac{2\pi r}{\lambda} \quad \text{E7.1}$$

where r is the radius of the spherical particle, and λ is the wavelength of the incident light. In the absorption spectra shown here, an increase in relative absorption equates to an increase in scattering intensity; by relation, this also correlates to an increase in the scattering size parameter, and an increased particle size (at a given wavelength). As a result, the higher absorption observed at $\lambda > 500$ nm for the CS + ferrous solution system relative to all other solutions studied indicates that additional, larger sized particles are

forming. This could be arising from agglomeration of the smaller particles to form larger ones.

7.2.3 Effect of Organic Contamination on Radiolytic Behaviour

From the results presented above, it is clear that the long-term, time-dependent behaviour observed for ferrous solutions that were irradiated on their own or in contact with stainless steel or carbon steel coupons was consistent with results obtained in much shorter duration tests (Chapter 6). However, the results presented were accumulated in a 2nd trial of experiments; the first set of experiments did not successfully reproduce previously observed trends. Prior to beginning the second trial, a detailed interpretation of the data from the 1st trial of tests was performed to determine the cause of this failure.

The first unexpected observation from the 1st trial was a failure to replicate expected solution colour changes. Figure 7.17 shows the results.

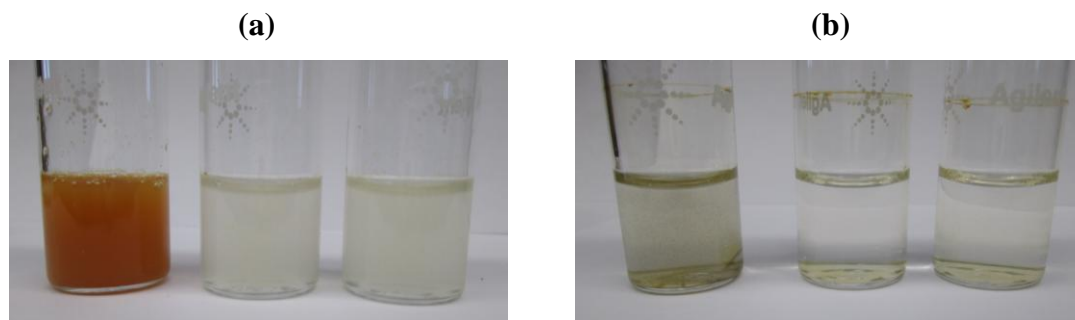


Figure 7.17: Optical images of 1st trial test solutions following 136 h of (a) irradiation at a dose rate of 1.4 Gy·s⁻¹, or (b) no irradiation, with a carbon steel coupon (left), a stainless steel coupon (middle) and no coupon (right), where $[\text{Fe}^{2+}]_0 = 5 \times 10^{-4} \text{ mol}\cdot\text{dm}^{-3}$.

When compared to optical images from the 2nd trial (Figure 7.7), the solutions in the test vials containing carbon steel coupons appear similar. However, the cloudy white solutions in test vials with a stainless steel coupon or no coupon (Figure 7.17) are noticeably different.

Further inconsistencies were observed for gas and aqueous phase analyses. The time-dependent trends in H₂ and O₂ concentrations are shown in Figure 7.18. Similarly, the time-dependent trends in ferrous/ferric speciation for 1st trial irradiated tests are shown in Figure 7.19. While there are some similarities in the trends seen in Figure 7.18 and Figure 7.19 in comparison with the results from the 2nd trial (e.g., H₂ increases while O₂ decreases with irradiation time, solutions irradiated with carbon steel coupons show higher total iron concentrations than [Fe²⁺]₀) there are striking differences. Following 138 h of irradiation, the hydrogen concentration measured in the gas phase was 15% for the carbon steel system in the 1st trial test. This is 2.5 times higher than the concentration observed at the same period for the successful 2nd trial long-term test. Additionally, relative to the 64 h irradiation test for a ferrous solution with a submerged carbon steel coupon presented in Section 7.2.1, Figure 7.18a shows a nearly two-fold increase in hydrogen. An even larger discrepancy exists for the hydrogen measured in vials with stainless steel or no coupon present.

Figure 7.19 also shows peculiar iron speciation behaviour for irradiated solutions; the relative contribution of ferric species to the total measured iron concentration remains ≤ 50% for all irradiation times. This is in stark contrast to the relatively fast and almost complete conversion of iron to ferric species that was observed in previous irradiations involving ferrous solutions.

Processes involving reactions at a surface, such as corrosion, can occasionally be difficult to reproduce with great precision. Slight differences in surface area available for reaction can change the rates observed, small pits at the surface (that are not polished away) can have different local chemical environments than the bulk surface, and some surface reactions may be probabilistic in nature. Hence, while some deviation between different sets of experiments are acceptable for a long-term test involving interfacial reactions, the degree of deviation observed and the fact that all test vials (each containing a different coupon) displayed coordinated trends suggested that the deviations we saw were not due to inconsistencies, but rather reflected a systematic problem.

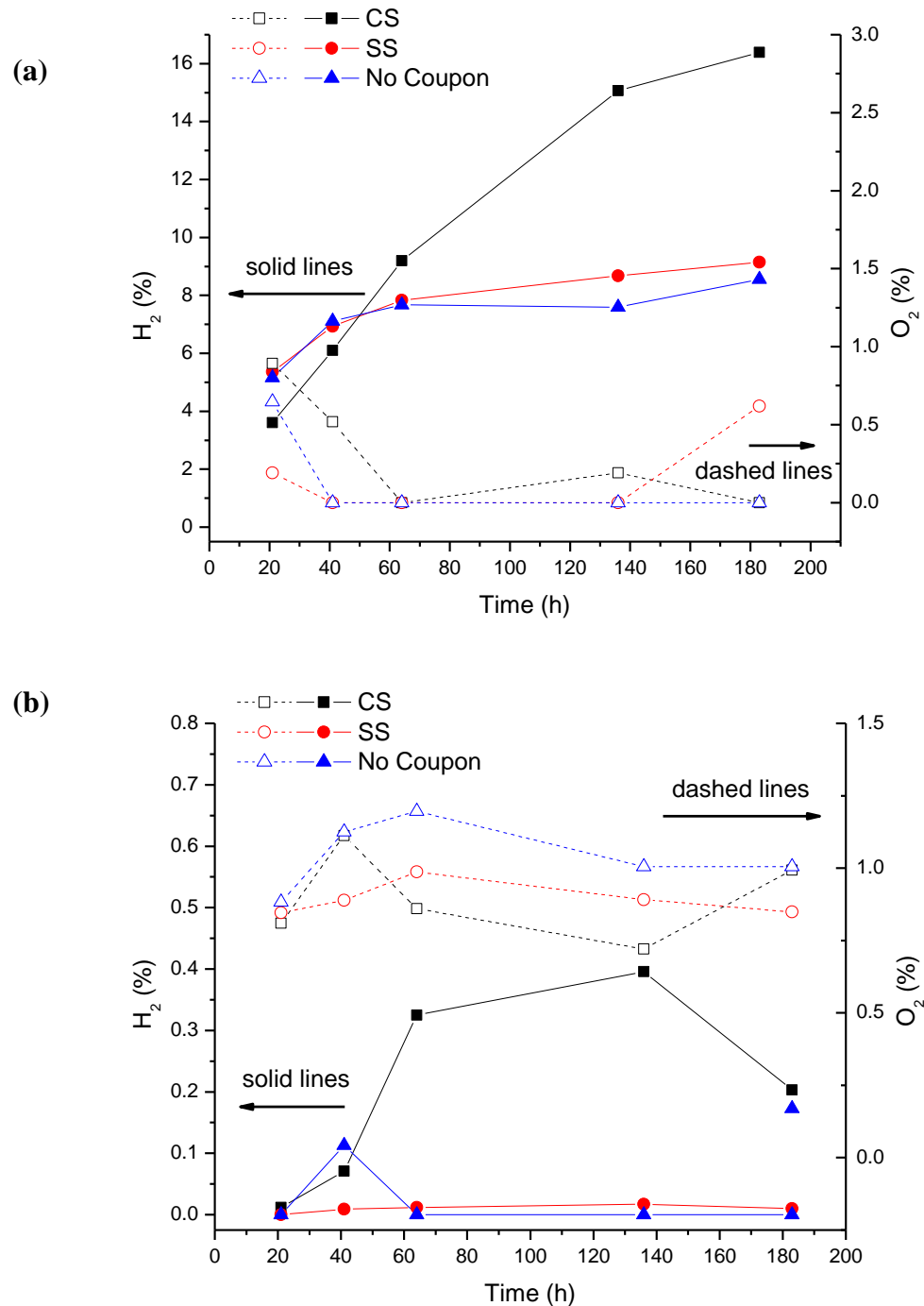


Figure 7.18: The concentrations of H₂ (solid lines) and O₂ (dashed lines) measured in the gas phase for 1st trial test vials containing carbon steel, stainless steel, or no coupon in contact with a 5 × 10⁻⁴ mol·dm⁻³ ferrous solution as a function of (a) irradiation time (at a dose rate of 1.4 Gy·s⁻¹), or (b) contact time outside of a radiation field.

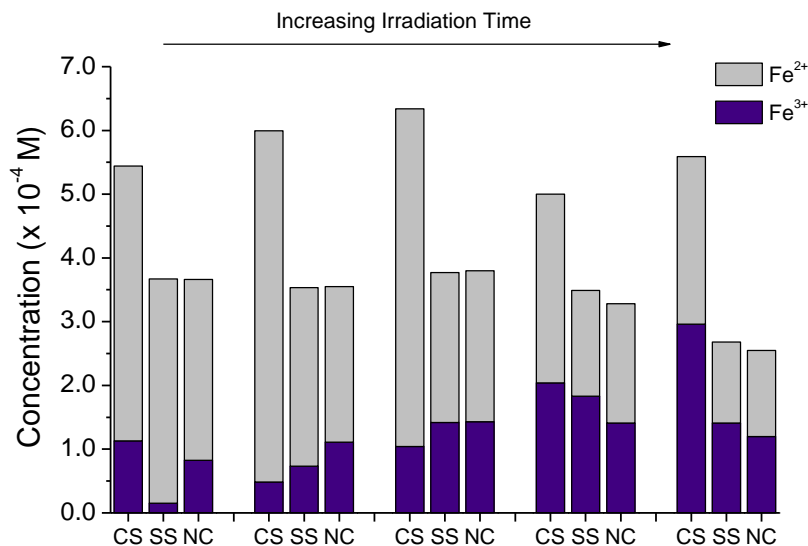


Figure 7.19: The relative concentrations of Fe²⁺ (grey) and Fe³⁺ (purple) species measured in the aqueous phase for test vials containing carbon steel (CS), stainless steel (SS), or no coupon (NC) in contact with a 5×10^{-4} mol·dm⁻³ ferrous solution as a function of irradiation time (at a dose rate of 1.4 Gy·s⁻¹). From left to right, the sets of bars represent times of 21, 41, 64, 138, and 183 hours.

The high H₂ levels seen in the 1st trial tests led us to suspect that organic contamination could have been the source of error. As well, the reduced degree of radiolytic oxidation of ferrous species to ferric species suggested that the dissolved contaminant was a hydrogenated oxidant scavenger. The contaminant was determined to be the hexane solution in which the coupons were stored following polishing, and prior to use. This was further supported by EDX evidence of carbon content on the coupon surfaces. It was believed that the simultaneous transfer of the coupons in the hexane solution with the Ar-purged water and test vials into the glovebox resulted in some hexane either entering the flask holding the water, or contaminating the vials prior to their being filled with the prepared test solution.

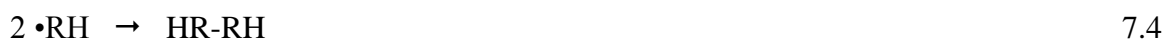
The presence of hexane, even at very low concentrations, led to reducing conditions dominating in the irradiated solution. Straight chain hydrocarbons are known to be effective free radical scavengers, and their presence can effectively suppress net

radiolysis in the aqueous system [6,29]. Unlike the dissolved metal ions which react mainly by oxidation-reduction (electron transfer) processes in the irradiated water, organic solutes react mainly by addition/abstraction mechanisms. For saturated compounds, abstraction will be the initial reaction:

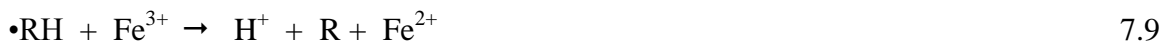


For n-hexane, the reactions with $\cdot\text{H}$ and $\cdot\text{OH}$ have rate constants of 1.4×10^8 and $6.6 \times 10^9 \text{ dm}^3 \cdot \text{mol}^{-1} \cdot \text{s}^{-1}$, respectively [30,31].

The organic radicals ($\cdot\text{RH}$) produced following the initial interaction with water radiolysis products can then undergo polymerization or disproportionation (to form one unsaturated product) reactions. Chain scission of larger organics can also lead to degradation by regenerating organic radicals:



Note that addition reactions of $\cdot\text{H}$ and $\cdot\text{OH}$ with organic radicals are also possible. Stable organic products, such as those generated by reactions 7.4 and 7.5, can then become the reactants in reactions 7.2 and 7.3, and propagate the reaction chain. Hence, even at low concentrations, the effective reactivity of these compounds with radical species can be quite high. With sufficiently long irradiation, organic molecules will eventually degrade to form small volatile molecules, such as CO_2 and H_2 . However, the large volumes of H_2 produced can further scavenge $\cdot\text{OH}$, and maintain a net reducing condition in the system. Additionally, organic radicals formed in the solution by radiolysis could act as one electron reducing agents and reduce any oxidized colloid species (reactions 7.7, 7.8 and 7.9). The radiolytic reduction of colloidal hematite in acidic solutions by propan-2-ol radicals has been reported [32].

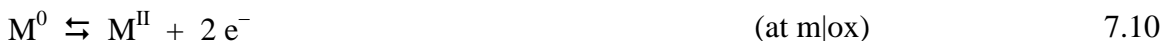


While only a small amount of organic material may have been present in the water, its impact on the radiation chemistry was significant; the organic species competed with ferric and ferrous ions for reaction with the free radicals ($\bullet\text{H}$ and $\bullet\text{OH}$), and the increased hydrogen production further reduced the oxidizing ability of the aqueous solution. The net effect was that the radiolytic oxidation of ferrous iron to ferric iron was significantly reduced in the test with organic contaminants.

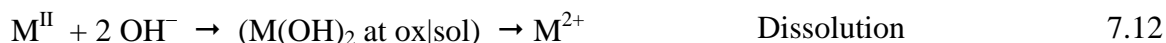
We were fully justified in challenging our 1st trial results and repeating the work to yield the data presented earlier in this chapter. The experience in seeking out the source of non-reproducible data clearly demonstrates the value of fully understanding the mechanism of reactions occurring in a complex system with reactive intermediates. This work also shows that even minor levels of contamination can be very important, and demonstrates that the chemical makeup of experiments and the potential influence that each dissolved solute may have on water radiolysis products must be accurately known.

7.3 MECHANISM OF CORROSION IN IRRADIATED SYSTEMS

Aqueous corrosion is an electrochemical process involving the pairing of two interfacial redox reactions: the oxidation of solid metal species (typically occurring at the metal/oxide interface, m|ox) coupled to the reduction of aqueous species (typically at the oxide/solution interface, ox|sol). If no oxide film is present, the above reactions occur at the metal/solution interface, however for the purposes of this discussion, the presence of an oxide will be considered). These processes are shown in reactions 7.10 and 7.11 for a generic metal, M, and for water reduction:



The rates of the electrochemical half reactions must equal one another for charge balance. Once formed, these M^{II} cations can transport through the oxide layer to the oxide/solution interface. Here, the cations can either dissolve into the solution as M^{2+} or combine with oxygen or hydroxide anions resulting in oxide growth:



Hence, oxidation (corrosion) of a metal occurs through two competing pathways of metal dissolution or oxide growth.

The driving force for a corrosion reaction is related to the difference in the equilibrium potentials of the two coupled half reactions (7.10 and 7.11); a larger potential difference equates to a larger driving force. For a given metal species, the anodic reaction will be constant, hence changes in the corrosion rate must occur due to changes in the aqueous environment, leading to different cathodic reduction pathways. The presence of radiation can have a significant impact on the corrosion rates observed. Radiolytically-generated oxidants such as H_2O_2 and O_2 can participate in reduction reactions at the metal surface (reactions 7.14 and 7.15), offering additional cathodic reactions that can be coupled to the anodic oxidation of the metal (reaction 7.17, shown as a reduction reaction by convention) [14]. The molecular water radiolysis products are more oxidizing than H^+ , which is the only available cathodic reactant in a pH 6.0 non-irradiated system (reaction 7.16). Therefore cathodic reactions involving H_2O_2 and O_2 will preferentially occur in irradiated systems. The net effect is that the coupling of the cathodic and anodic electrochemical half reactions occurs at an increased rate in irradiated systems. The possible cathodic and anodic reactions for carbon steel in water with and without irradiation are represented in Figure 7.20.





While the radiolytic radicals are also capable of undergoing redox reactions with metal species (E° values for $\bullet\text{OH}/\text{H}_2\text{O}$, $\text{H}_2\text{O}/e_{\text{aq}}^{-}$ and $\text{H}^{+}/\bullet\text{H}_{(\text{aq})}$ are +1.9 V, -2.7 V and -2.3 V, respectively for acidic solutions), these types of interactions are more likely to occur on the colloidal particles that are homogeneously distributed in the solution [6,33]. The high reactivity of the radiolytic radicals with ions and molecular products in the aqueous phase limits their lifetime, and consequently, their ability to diffuse to a carbon steel coupon surface for reaction. Hence, it will be the longer-lived molecular products that will drive redox reactions on a metal surface.

The available oxidants in solution are not the only parameters that will determine corrosion behaviour. The solution pH can have an impact on the chemical composition, phase structure and thickness of the oxide that can be formed. Since most oxides are semiconducting in nature, the oxide film can act as a barrier to charge transport. As the oxide grows, the potential drop across the film increases, and this effectively limits the driving force for ongoing metal oxidation. The overall corrosion kinetics depend on the competing rates of metal oxidation and metal dissolution in test solutions and pH has been shown to have a significant impact on the relative contributions of oxide growth and metal dissolution in irradiated systems [10,34,35].

The total solubilities of iron species are much higher at lower pH values than at more alkaline conditions [14,21,36]. Electrochemical studies of metals at pH 10.6, where metal ion solubility is very low, show the growth of thick and compact oxide films. Metal dissolution is negligible in these systems. With time, the growing oxide layer acts as a barrier to further corrosion, and the metal oxidation rate is observed to slow. In contrast, for solutions at pH 6.0, the metal ion solubilities are relatively high. As a result, dissolution proceeds more easily than oxide growth. Since the oxide film remains thin and is comprised mainly of hydrated metal oxides and hydroxides, it does not represent a barrier to corrosion. Hence metal oxidation can continue at a high rate for longer periods of time than at pH 10.6.

7.3.1 Carbon Steel Corrosion in the Absence of Initially Dissolved Fe^{2+}

From the results in Sections 7.2.1 and 7.2.2, the rate of aqueous corrosion on a carbon steel surface in deaerated solutions at pH 6.0 was shown to be accelerated under irradiation. This radiation-induced corrosion is attributed to reactions involving the redox active aqueous species generated by water radiolysis. Consistent with the electrochemical studies at low pH described above, the corrosion mechanism of carbon steel was shown to be dominated by the dissolution of metal ions; the dissolved iron concentration increases with time, while the oxide layer remained very thin, as confirmed by XPS, EDX and Raman analyses.

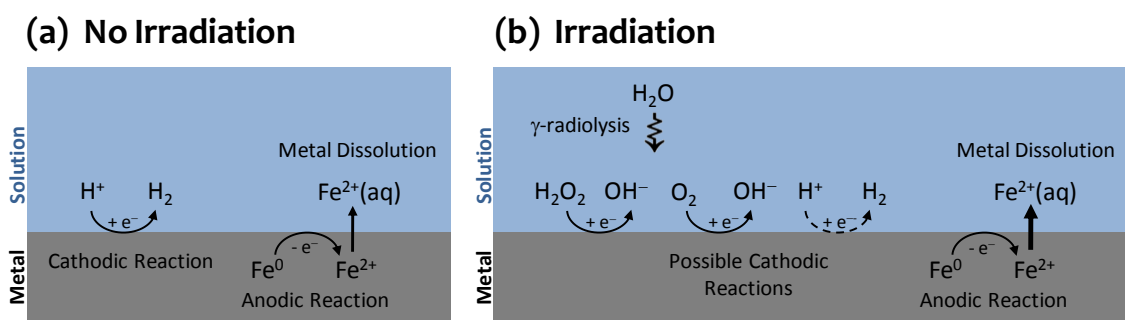


Figure 7.20: Simplified schematic of the cathodic and anodic half reactions that can occur on a carbon steel surface in (a) non-irradiated water, and (b) water subjected to γ -radiation. Note that the anodic reaction can also lead to oxide film formation.

The hydrogen production rate for carbon steel-water systems was low, compared to that seen in ferrous systems. Hydrogen is mainly removed from irradiated systems by its reaction with the water radiolysis product $\bullet\text{OH}$. The radiolytic oxidation of ferrous species will consume $\bullet\text{OH}$, decrease the rate of hydrogen removal, and increase the hydrogen concentration in the system. Hence for systems without any dissolved Fe^{2+} initially present, hydrogen levels are expected to be initially very low because there is no competing $\bullet\text{OH}$ reaction.

While this explanation accounts for low hydrogen values at early times, when the dissolved iron concentration is low, it does not account for low hydrogen levels at longer

times when the total iron concentration is higher. There must be a pathway that allows metal dissolution without generating hydrogen.

One potential explanation involves the reduction of deposits of radiolytically-formed Fe^{III} species (Fe(OH)₃ and γ-FeOOH). When the concentrations of these particles are low (at early irradiation times), their surfaces may act as sites for oxidation/reduction. Reduction (e.g., reaction 7.18) occurring on the particle surface can couple with the anodic oxidation of the metal substrate, Fe⁰ to Fe^{II} and the Fe^{II} dissolves preferentially into the solution at pH 6.0 rather than forming a protective oxide.



The net result is an increase in the Fe²⁺ concentration in solution, without an accompanying cathodic reaction that generates H₂.

7.3.2 Carbon Steel Corrosion in the Presence of Initially Dissolved Fe²⁺

Radiation was shown to increase the metal oxidation rate observed tests in ferrous solutions and this is attributed to the production of radiolytic oxidants that can increase the rate of the cathodic processes. However, when compared to pure water tests, the presence of ferrous ions appears to have suppressed the overall oxidation rate. Ferric/ferrous speciation showed that, although some metal dissolution occurred, the total release was fairly independent of the duration of radiation exposure. Additionally, the amount of iron released from the coupon surface by 138 h was significantly less than that observed in pure water. Upon exposure to γ-radiation the initially-dissolved Fe²⁺ will quickly convert to Fe(OH)₃ and then to γ-FeOOH [15]. Since the solubility of ferric species are many orders of magnitude lower than ferrous species at pH 6.0, these particles can deposit onto the carbon steel surface. Additionally, since the iron is already present at high concentrations (as opposed to a more gradual increase in concentration in the pure water tests), a large area of the coupon surface can be covered by these deposited particles relatively quickly and this can contribute to the slow growth of the oxide layer. Evidence for a thicker oxide layer in ferrous tests compared to pure water tests was observed by XPS, and by EDX at longer times. However, the low signals obtained for

Raman (overall film) and EDX (oxygen signal) demonstrate that the oxide layer is still quite thin even after prolonged irradiation. This behaviour is consistent with a previous electrochemical study on corrosion of carbon steel (with no irradiation), where high concentrations of Fe^{2+} in solution suppressed the Fe^{II} dissolution from the oxidized carbon steel surface, and demonstrated the presence of a thin, hydrated oxide layer [17].

For ferrous solution tests, the hydrogen production was observed to be increased relative to water tests. This is likely due to a combination of radiolytic and corrosion processes. The initial dissolved iron leads to immediate scavenging of the hydroxyl radical with irradiation. This decreases the rates of radiolytic hydrogen removal and allows it to accumulate in the system. Additionally, the high concentrations of ferric species generated by radiolysis can undergo hydrolysis, and decrease the pH. This can lead to proton reduction becoming a significant contributor to the cathodic reactions on the metal surface, generating hydrogen as a corrosion product.

7.3.3 Corrosion of Stainless Steel

In all tests, the stainless steel coupons exhibited negligible corrosion. The surfaces of the irradiated stainless steel coupons do not show significant oxide growth (XPS) or surface damage (SEM), and there was no evidence of iron dissolution from the stainless steel surface (UV-Vis). As result the presence of a stainless steel coupon had no impact on measured concentrations of gaseous O_2 and H_2 or measured ferric and ferrous species concentrations in the test solutions when compared to values for solutions irradiated without a coupon. The inert behaviour of the stainless steel is well known and has been attributed to the presence of a passive Cr oxide layer [9,37,38]. The metal cation and oxygen anion that are injected at the metal/oxide interface and the oxide/solution interface, respectively, must transport through the oxide layer for the corrosion reaction to occur. For stainless steel, the corrosion active metal component is still Fe. The Fe^{II} injected at the metal/oxide interface is either incorporated into the existing Cr_2O_3 oxide layer, slowly converting it to a chromite-like layer (FeCr_2O_4), or transports through the passive chromium oxide until it reaches the oxide/water interface and can dissolve. In this case, the iron dissolution is limited by the rate of Fe^{II} transport through the oxide layer and is less affected by the iron solubility conditions. As a result,

the only redox reactions that occur in tests presented here with a SS coupon present are those between the iron added to the test solutions and the water radiolysis products. As a result, irradiated ferrous solutions with and without a stainless steel coupon show similar gaseous and aqueous phase behaviour.

7.4 CONCLUSIONS

The results of this coupon study show that the presence of radiation alone increases the corrosion rate of carbon steel at pH 6.0. The radiolytically-generated oxidants increase the corrosion potential at the metal surface. Due to the relatively high solubility of ferrous ion at this pH, the metal oxidation contributes mainly to metal dissolution while the oxide film remains very thin. Stainless steel was found to be relatively corrosion resistant at all of the conditions that studied.

Colloid formation was observed for all carbon steel systems, even when iron was not initially dissolved. The ongoing dissolution of Fe^{2+} from the corroding coupon surface resulted in more colloids being formed with time, and a steady-state concentration was not reached within 138 h. Irradiated carbon steel-ferrous solution tests also showed evidence of larger particles being formed. The colloid scattering profiles collected for irradiated ferrous sulfate solutions with and without the presence of a stainless steel coupon were similar; a steady state had already been reached prior to the first sample analysis at 21 h.

The presence of initially dissolved iron in the irradiated solution had a net suppressing effect on the corrosion rate. The mechanism for the suppression of carbon steel corrosion in irradiated ferrous solutions arises from the radiolytic production of insoluble ferric products. A high concentration of these insoluble species can deposit on the coupon surface and contribute to the formation of a thicker (faster growing) amorphous oxide layer. The growth of the oxide layer decreases the potential drop that exists across the film, and decreases the driving force for ongoing corrosion and metal dissolution.

Organic impurities in the aqueous system act as free radical scavengers, competing with metal ions for reaction with $\cdot\text{H}$ and $\cdot\text{OH}$, and suppressed the radiolytic oxidation of ferrous species in the solution. The radiolytic degradation of the organic

material lead to significantly greater hydrogen production relative to that observed in systems absent the organic material.

7.5 ACKNOWLEDGEMENTS

The SEM/EDX images presented in this chapter were collected by Ms. Heather Bloomfield and Dr. Mark Biesinger at Surface Science Western, and Dr. Mark Biesinger also performed the XPS analyses discussed in this chapter. Raman spectra were collected by Dr. Veena Subramanian. Mr. Ryan Morco and Dr. Ahmed Musa are also acknowledged for their help in polishing the experimental coupons used in this study.

7.6 REFERENCES

- [1] Ishigure, K., Fujita, N., Tamura, T., Oshima, K., "Effect of gamma radiation on the release of corrosion products from carbon steel and stainless steel in high temperature water", *Nucl. Technol.*, **1980**, 50, 169-177.
- [2] Sawicki, J.A., "Analyses of fuel crud and coolant-borne corrosion products in normal water chemistry BWRs", *J. Nucl. Mater.*, **2011**, 419, 85-96.
- [3] Tsai, T.-L., Lin, T.-Y., Su, T.-Y., Wen, T.-J., Men, L.-C., "Characterization of corrosion products deposited on fuel rods in a boiling water reactor (BWR-6) plant using hydrogen water chemistry (HWC)", *J. Radioanal. Nucl. Chem.*, **2013**, 298, 1235-1244.
- [4] Yeon, J.-W., Choi, I.-K., Park, K.-K., Kwon, H.-M., Song, K., "Chemical analysis of fuel crud obtained from Korean nuclear power plants", *J. Nucl. Mater.*, **2010**, 404, 160-164.
- [5] Lin, C.C., "A review of corrosion product transport and radiation field buildup in boiling water reactors", *Progress in Nuclear Energy*, **2009**, 51, 207-224.
- [6] Spinks, J.W.T., Woods, R.J. *An Introduction to Radiation Chemistry*, 3rd ed., Wiley-Interscience: New York, 1990.
- [7] Draganic, I.G., Draganic, Z.D. *The Radiation Chemistry of Water*, Academic Press, Inc.: New York, 1971.
- [8] Allen, A.O. *The Radiation Chemistry of Water and Aqueous Solutions*, Van Nostrand Company, Inc.: New York, 1961.
- [9] Knapp, Q.W., Wren, J.C., "Film formation on type-316L stainless steel as a function of potential: Probing the role of gamma-radiation", *Electrochim. Acta*, **2012**, 80, 90-99.
- [10] Behazin, M., Noël, J.J., Wren, J.C., "Combined effects of pH and γ -irradiation on the corrosion of Co-Cr alloy stellite-6", *Electrochim. Acta*, **2014**, 134, 399-410.
- [11] Daub, K., Zhang, X., Noël, J.J., Wren, J.C., "Effects of γ -radiation versus H₂O₂ on carbon steel corrosion", *Electrochim. Acta*, **2010**, 55, 2767-2776.
- [12] Fu, D., Zhang, X., Keech, P.G., Shoosmith, D.W., Wren, J.C., "An electrochemical study of H₂O₂ decomposition on single-phase γ -FeOOH films", *Electrochim. Acta*, **2010**, 55, 3787-3796.

- [13] Zhang, X., Xu, W., Shoesmith, D.W., Wren, J.C., "Kinetics of H₂O₂ reaction with oxide films on carbon steel", *Corros. Sci.*, **2007**, *49*, 4553-4567.
- [14] Cornell, R.M., Schwertmann, U. *The Iron Oxides: Structure, Properties, Reactions, Occurrences and Uses*, 2nd ed., Wiley-VCH: Weinheim, 2003.
- [15] Yakabuskie, P.A., Joseph, J.M., Keech, P., Botton, G.A., Guzonas, D., Wren, J.C., "Iron oxyhydroxide colloid formation by gamma-radiolysis", *Phys. Chem. Chem. Phys.*, **2011**, *13*, 7198-7206.
- [16] Fu, D., Wren, J.C., "Preparation and characterization of ferric oxyhydroxide and ferric oxide thin films by direct-hydrolysis deposition", *J. Nucl. Mater.*, **2008**, *374*, 116-122.
- [17] Wang, L., Daub, K., Qin, Z., Wren, J.C., "Effect of dissolved ferrous iron on oxide film formation on carbon steel", *Electrochim. Acta*, **2012**, *76*, 208-217.
- [18] Kuch, A., "Investigations of the reduction and re-oxidation kinetics of iron(III) oxide scales formed in waters", *Corros. Sci.*, **1988**, *28*, 221-231.
- [19] Sherar, B.W.A., Keech, P.G., Shoesmith, D.W., "Carbon steel corrosion under anaerobic-aerobic cycling conditions in near-neutral pH saline solutions. Part 2: Corrosion mechanism", *Corros. Sci.*, **2011**, *53*, 3643-3650.
- [20] Stratmann, M., Hoffmann, K., "In situ Mössbauer spectroscopic study of reactions within rust layers", *Corros. Sci.*, **1989**, *29*, 1329-1352.
- [21] Tremaine, P.R., LeBlanc, J.C., "The solubility of magnetite and the hydrolysis and oxidation of Fe²⁺ in water to 300°C", *J. Solution Chem.*, **1980**, *9*, 415-442.
- [22] Stookey, L.L., "Ferrozine -a new spectrophotometric reagent for iron", *Anal. Chem.*, **1970**, *42*, 779-781.
- [23] Viollier, E., Inglett, P.W., Hunter, K., Roychoudhury, A.N., Van Cappellen, P., "The ferrozine method revisited: Fe(II)/Fe(III) determination in natural waters", *Appl. Geochem.*, **2000**, *15*, 785-790.
- [24] Yakabuskie, P.A., Joseph, J.M., Wren, J.C., "The effect of interfacial mass transfer on steady-state water radiolysis", *Radiat. Phys. Chem.*, **2010**, *79*, 777-785.
- [25] Čuba, V., Silber, R., Můčka, V., Pospíšil, M., Neufuss, S., Bárta, J., Vokál, A., "Radiolytic formation of ferrous and ferric ions in carbon steel – deaerated water system", *Radiat. Phys. Chem.*, **2011**, *80*, 440-445.
- [26] Wolf, S., Voshchinnikov, N.V., "Mie scattering by ensembles of particles with very large size parameters", *Comput. Phys. Commun.*, **2004**, *162*, 113-123.
- [27] Harris Jr., F.S., "Particle characteristics from light scattering measurements", *Tellus*, **1969**, *21*, 223-229.
- [28] Quirantes, A., Plaza, R., Delgado, A., "Static Light Scattering Study of Size Parameters in Core-Shell Colloidal Systems", *J. Colloid Interface Sci.*, **1997**, *189*, 236-241.
- [29] McCracken, D.R., Rasewych, J.B., Shorter, W.R. "Coolant radiolysis and boiling in water cooled reactors" In *Water Chemistry of Nuclear Reactor Systems*, BNES: London, 1989, Vol. 5, p 107.
- [30] Neta, P., Fessenden, R.W., Schuler, R.H., "An electron spin resonance study of the rate constants for reaction of hydrogen atoms with organic compounds in aqueous solution", *J. Phys. Chem.*, **1971**, *75*, 1654-1666.

- [31] Rudakov, E.S., Volkova, L.K., Tret'yakov, V.P., "Low selectivity of reactions of OH-radicals with alkanes in aqueous solution", *React. Kinet. Catal. Lett.*, **1981**, *16*, 333-337.
- [32] Buxton, G.V., Rhodes, T., Sellers, R.M., "Radiation-induced dissolution of colloidal haematite", *Nature*, **1982**, *295*, 583-585.
- [33] Buxton, G.V., Sellers, R.M., "The radiation chemistry of metal ions in aqueous solution", *Coord. Chem. Rev.*, **1977**, *22*, 195-274.
- [34] Daub, K., Zhang, X., Noël, J.J., Wren, J.C., "Gamma-radiation-induced corrosion of carbon steel in neutral and mildly basic water at 150°C", *Corros. Sci.*, **2011**, *53*, 11-16.
- [35] Musa, A.Y., Behazin, M., Wren, J.C., "Potentiostatic film growth kinetics on Ni-Cr and Co-Cr Alloys: Potential and pH dependences at 25 and 80 C", *Electrochim. Acta*, **2014**, *Accepted*.
- [36] Beverskog, B., Puigdomenech, I., "Revised pourbaix diagrams for iron at 25–300 °C", *Corros. Sci.*, **1996**, *38*, 2121-2135.
- [37] Massoud, T., Maurice, V., Klein, L.H., Seyeux, A., Marcus, P., "Nanostructure and local properties of oxide layers grown on stainless steel in simulated pressurized water reactor environment", *Corros. Sci.*, **2014**, *84*, 198-203.
- [38] Massoud, T., Maurice, V., Klein, L., Marcus, P., "Nanoscale morphology and atomic structure of passive films", *J. Electrochem. Soc.*, **2013**, *160*, C232-C238.

CHAPTER 8 SUMMARY AND FUTURE WORK

8.1 SUMMARY

This thesis examined the influence of various solutes on aqueous phase reactions in irradiated systems. A chemical kinetic model, containing a basic reaction set to describe the radiolytic reactions of water, was expanded to include parameters for the aqueous-to-gas phase interfacial mass transfer of radiolytic gases (H_2 and O_2) as well as a limited reaction set describing reactions of water radiolysis products with nitrogen-containing solutes and their radiolytically-produced derivatives. While radical species can actively participate in the radiation chemistry while the system is contained within the radiation field, their high reactivity leads to their fast removal from the chemical system once the radiation source is removed. As a result, only the more stable products of radiolysis such as H_2O_2 , H_2 and O_2 (for water) or ionic products such as NO_3^- , NO_2^- , Fe^{2+} , and Fe^{3+} (for dissolved solutes) can provide measurable experimental data. To validate the accuracy of the compiled reaction set and the associated rate constants, test results from room temperature experiments were compared to model simulations over a wide range of conditions including solution pH, cover gas volume and aeration, and solute concentration. The kinetic model consistently reproduced the trends of these experiments with reasonable accuracy, and was considered to be sufficiently comprehensive for use as an interpretive tool. The kinetic model was used to simulate the time-dependent concentrations of species that could not be experimentally determined with post-irradiation analysis techniques due to their fast decay (such as the radical species) or because the time scales simulated were too short (< seconds) to analyze effectively. These model predictions could then be interpreted to elucidate the reaction mechanisms that determine the changes in chemical behaviour observed experimentally.

From the modeling results, a distinct change in radiolytic behaviour is observed moving from pH below to pH above the pK_a of $\bullet H$ (9.6). An inverse relationship between the steady-state concentrations of the radical and molecular water radiolysis products is observed such that, at $pH < 9.6$, the concentrations of the radicals are relatively higher, while the concentrations of the molecular products are relatively lower than the corresponding concentrations at $pH > 9.6$. This pH dependence arises from a

shift in the main removal pathway of $\bullet e_{aq}^-$ from reaction with H^+ in more acidic solutions to reactions with O_2 in more alkaline conditions. The reactive intermediate of this reaction, $\bullet O_2^-$, can then undergo reactions with $\bullet OH$ to regenerate O_2 . The net effect is that O_2 , which is only produced as a secondary radiolysis product, can slowly accumulate in the system with time, while constantly scavenging the primary radical species, and the steady states for radiation systems are attained more slowly for alkaline solutions. Regardless of pH, the molecular radiolysis products are mainly removed by their reactions with the primary radiolysis radical products: for H_2O_2 , reaction with both $\bullet e_{aq}^-$ and $\bullet OH$, and for H_2 , reaction with $\bullet OH$ alone. The kinetic analyses presented throughout this thesis have demonstrated that the steady-state molecular product concentrations can be mathematically related to those of the radical species by approximate analytical solutions. Hence at high pH, the radical scavenging by the oxygen cycle leads to reduced removal rates of the molecular products, and their steady-state concentrations are observed to increase.

The initial presence of solutes in water (such as dissolved oxygen, nitrate or nitrite) were shown to impact the steady-state concentrations of the molecular water radiolysis products indirectly through reactions with the radical species, mainly $\bullet OH$ and $\bullet e_{aq}^-$. The added solutes competed with the molecular products for reaction with the radicals. This radical scavenging leads to the accumulation of molecular products in the system. In general, the changes in molecular product concentrations observed upon addition of a solute were greater in more acidic solutions. This behaviour is a consequence of the higher steady-state radical concentrations that exist in pure water at pHs lower than 9.6. At higher pHs, the radical concentrations are already low for pure water, and the additional radical scavenging by the solute species has less impact on the molecular species reactions and steady-state concentrations.

The degree of impact that a solute was observed to have on either H_2O_2 or H_2 depends on whether the solute preferentially removes $\bullet OH$ or $\bullet e_{aq}^-$ from the system. For example, when oxygen is present, hydrogen peroxide is more impacted than hydrogen. This occurs because the removal of H_2 is determined entirely by reaction with $\bullet OH$, but $\bullet OH$ is only removed by an intermediate species in the oxygen cycling mechanism. In contrast, both $\bullet OH$ and $\bullet e_{aq}^-$ control H_2O_2 , and dissolved oxygen directly reacts with

$\bullet e_{aq}^-$. Additionally, for irradiated systems, reactions with the solutes are the main removal paths for the radical species, regardless of pH. Hence, the molecular product concentrations measured at steady state are almost independent of pH; this is not the case for pure water systems.

When the solutes present can form chemically stable products and undergo redox cycling in the irradiated system (e.g., $NO_3^- \rightleftharpoons NO_2^-$, $Fe^{2+} \rightleftharpoons Fe^{3+}$), the speciation of the solute species provides additional insight into the overall redox state of the water. For example, kinetic analysis showed that the nitrate/nitrite ratio could be approximated from the model-predicted concentrations of the radicals $\bullet e_{aq}^-$, $\bullet O_2^-$ and $\bullet OH$ for solutions at either pH 6.0 or 10.6, and with either initially dissolved nitrate or nitrite. Hence, evaluation of the nitrate/nitrite ratio in a chemical system gives a general representation of the relative reducing ($\bullet e_{aq}^-$, $\bullet O_2^-$) and oxidizing ($\bullet OH$) nature of the radicals in solution at a given time. Similarly, for irradiated ferrous solutions, the iron speciation at steady state is dominated by ferric species, and this demonstrates that the aqueous conditions are highly oxidizing.

The formation of uniformly sized γ -FeOOH colloids was observed for irradiated ferrous solutions, and a mechanism for colloid formation was proposed. The fast radiolytic oxidation of hydrated Fe^{2+} to less soluble ferric species leads to the homogeneous condensation of amorphous $Fe(OH)_3$ primary particles. Particle growth is accomplished by redox reactions of ferrous ions on the particle surface, and the final particle size is dictated by the steady-state charge transfer processes at the aqueous-solid interface. Redox reactions at the particle surface are further controlled by the steady-state concentrations of oxidizing and reducing water radiolysis products in the aqueous phase. While the radiolytic interaction of dissolved solutes with radical species usually results in higher observable concentrations of molecular products, H_2O_2 and O_2 were not detected in the iron colloid system. These longer-lived oxidants may actively participate in redox reactions on the particle surface. In particular, catalytic destruction of H_2O_2 may occur on the γ -FeOOH particle surface.

The radiation-induced corrosion of carbon steel was examined in pH 6.0 pure water and ferrous solutions. The rate of carbon steel corrosion was observed to increase with irradiation. This was anticipated since the radiolytically-formed H_2O_2 and O_2 can

increase the corrosion potential at the metal substrate and this increases the rate of the anodic half reaction. Due to the low pH of the solutions, metal ion dissolution dominates over oxide growth, and hence the corrosion rates were easily approximated by monitoring the time-dependent total dissolved iron concentrations. In solutions with dissolved Fe^{2+} , the $\gamma\text{-FeOOH}$ colloids generated by the early radiolytic oxidation of ferrous ions can deposit on the metal coupon surface and contribute to oxide film growth. The result is that the rate of further metal dissolution is suppressed. In contrast, for carbon steel and water systems, the slower release of ferrous ions with time can allow the metal oxidation rate to remain high. Additionally, at early times when the total concentration of colloids is low, the reduction of $\gamma\text{-FeOOH}$ deposits on the coupon surface can couple with the metal oxidation and lead to enhanced metal dissolution.

8.2 FUTURE WORK

This work has added to our understanding of the long-term radiation chemistry occurring in aqueous solutions with dilute dissolved solutes that can be present in irradiated nuclear systems. While many of the results here have been used for validating the kinetic model reaction set, such a model cannot yet be applied to most real reactor systems without further work, since the operational temperatures and pressures of these systems far exceed those used for experimental study in this thesis. With high temperature tests, some additional complications exist. First, the fast thermal degradation of hydrogen peroxide further reduces the number of readily measurable species with which the model predictions can be compared. Additionally, developing an adequate methodology to run the experiments is not trivial. Test vials and seals need to be capable of withstanding the higher pressures arising from water vapour, but cannot be constructed of materials that will interfere with the radiation chemistry to be studied. Finally, at sufficiently high temperatures, the higher concentration of water molecules in the vapour phase requires that gas phase radiolysis be taken into account, and any reaction rate constants with ill studied temperature dependences can bring significant uncertainty into the reaction set.

Of the solutes examined in this thesis, those that could benefit most from further study are transition metal ions. In this thesis, there was no attempt to develop an

extensive model of the radiolysis chemistry of water containing transition metal ions. Significant difficulties arise when trying to model the water radiolysis behaviour of these systems. Appropriate parameters for the related equilibria for the different iron oxides need to be obtained and evaluated. The mass transfer between dissolved and solid-state status of the metal species requires new mass transfer parameters. Additionally, the model cannot include only homogeneous reactions occurring in solution, but also must address heterogeneous reactions at coupon and particle surfaces. The reaction rates between radiolysis products such as $\bullet e_{aq}^-$ or $\bullet OH$ with ferric and ferrous species that are organized in an oxide film will be different from those with hydrated ferric and ferrous ions.

There are also many other avenues to explore with respect to the radiolysis of metal ion solutions. One such area is the formation of mixed-transition metal oxides in a radiation field. Examination of 'crud' from nuclear coolant systems shows that mixed metal oxides can be formed in radiation environments, but this area has not been pursued from a fundamental research standpoint. Additionally, evaluating the effects of changing radiolytic conditions (e.g., moving from net radiolysis to a net reducing condition by saturation with H_2 and back) may provide additional insight into the particle formation mechanism.

In general, adapting the basic water radiolysis model to accommodate more realistic operational temperatures and pressures of reactor systems, and to describe radiolytic behaviour of transition metal species are key topics for further evaluation.

PAMELA A. YAKABUSKIE

EDUCATION

- Ph.D. in Physical Chemistry** 09/2008 – Present
The University of Western Ontario
- B.Sc. Honours Specialization in Chemistry and Biochemistry** 09/2004 – 05/2008
The University of Western Ontario

RELATED WORK EXPERIENCE

- Research Scientist, Canadian Nuclear Laboratories (CNL)
(formerly known as Atomic Energy of Canada Limited)** 01/2014 – Present
- Research experience in an industrial setting with wide ranging subject areas including mechanical materials testing and radiolysis of aqueous systems.
- Graduate Student, The University of Western Ontario** 09/2008 – 01/2014
- Training and experience in the use of a Co-60 gamma irradiation cell.
 - Experience with a number of chromatographic, spectroscopic, and surface analytical techniques.
 - Some experience with the use of high temperature autoclaves (up to 150 °C).
- Visiting Researcher, Notre Dame Radiation Laboratory** 04/2012 – 12/2012
- Research experience using a Van de Graaff electron accelerator to study high temperature escape yields.
 - Gained experience using a radiolysis flow system capable of reaching supercritical conditions to study high temperature escape yields.
- Teaching Assistant, University of Western Ontario** 09/2008 – 04/2012
- Analytical Instrumentation
 - Introductory Chemistry

AWARDS AND ACHIEVEMENTS

2012 – 2014	NSERC PGSD Scholarship
2013	Canadian Nuclear Society R.E. Jervis Award for excellence in research and development carried out by a graduate student in nuclear engineering of related fields
2012	Associate Chair of the Gordon Research Seminar on Radiation Driven Processes in Physics, Chemistry, Biology and Industry
2011 – 2012	Ontario Graduate Scholarship
2010 – 2011	Ontario Graduate Scholarship in Science and Technology
2009	Canadian Society for Chemistry Award for Best Graduate Student Poster, Analytical Chemistry Division
2008	Canadian Nuclear Society Award for Best Undergraduate Student Oral Presentation
2007	Canadian Nuclear Society Scholarship for Undergraduate Summer Research
2004 – 2008	The F.K. Ashbaugh President's Scholarship, The University of Western Ontario's most prestigious entrance scholarship to recognize all around excellence in academics, athletics and the arts.

PUBLICATIONS

1. **Yakabuskie, P.A.**, Joseph, J.M., Keech, P., Botton, G.A., Guzonas, D., Wren, J.C., "Iron oxyhydroxide colloid formation by gamma-radiolysis", *Phys. Chem. Chem. Phys.*, **2011**, *13*, 7198-7206.
2. **Yakabuskie, P.A.**, Joseph, J.M., Stuart, C.R., Wren, J.C., "Long-term γ -radiolysis kinetics of NO_3^- and NO_2^- solutions", *J. Phys. Chem. A*, **2011**, *115*, 4270.
3. **Yakabuskie, P.A.**, Joseph, J.M., Wren, J.C., "The effect of interfacial mass transfer on steady-state water radiolysis", *Radiat. Phys. Chem.*, **2010**, *79*, 777-785.
4. Joseph, J.M., Choi, B.S., **Yakabuskie, P.A.**, Wren, J.C., "A combined experimental and model analysis on the effect of pH and $\text{O}_2(\text{aq})$ on γ -radiolytically produced H_2 and H_2O_2 ", *Radiat. Phys. Chem.*, **2008**, *77*, 1009-1020.